

# IIUM ENGINEERING JOURNAL

**Volume 21**

**Number 1**

**January 2020**



IIUM  
Press

**INTERNATIONAL ISLAMIC UNIVERSITY MALAYSIA**

**ISSN: 1511-788X E-ISSN: 2289-7860**

**<http://journals.iium.edu.my/ejournal>**

# IIUM ENGINEERING JOURNAL

---

## **CHIEF EDITOR**

Ahmad Faris Ismail, IIUM, Malaysia

## **EXECUTIVE EDITOR**

AHM Zahirul Alam, IIUM, Malaysia

## **ASSOCIATE EDITOR**

Nor Farahidah Za'bah, IIUM, Malaysia

## **LANGUAGE EDITOR**

Lynn Mason, Malaysia

## **COPY EDITOR**

Hamzah Mohd. Salleh, IIUM, Malaysia

## **EDITORIAL BOARD MEMBERS**

Abdullah Al-Mamun, IIUM, Malaysia  
Abdumalik Rakhimov, IIUM, Malaysia  
Ali Sophian, IIUM, Malaysia  
Amir Akramin Shafie, IIUM, Malaysia  
Anis Nurashikin Nordin, IIUM, Malaysia  
Erry Yulian Triblas Adesta, IIUM, Malaysia  
Erwin Sulaeman, IIUM, Malaysia  
Hanafy Omar, Saudi Arabia  
Hazleen Anuar, IIUM, Malaysia  
Konstantin Khanin, University of Toronto, Canada  
Ma'an Al-Khatib, IIUM, Malaysia  
Md Zahangir Alam, IIUM, Malaysia  
Meftah Hrairi, IIUM, Malaysia  
Mohamed B. Trabia, United States  
Mohammad S. Alam, Texas A&M University-Kingsville, United States  
Mustafizur Rahman, National University Singapore, Singapore  
Ossama Abdulkhalik, Michigan Technological University, United States  
Razi Nalim, IUPUI, Indianapolis, Indiana, United States  
Rosminazuin AB. Rahim, IIUM, Malaysia  
Waqar Asrar, IIUM, Malaysia

## **AIMS & SCOPE OF IIUMENGINEERING JOURNAL**

The **IIUM Engineering Journal**, published biannually, is a carefully refereed international publication of International Islamic University Malaysia (IIUM). Contributions of high technical merit within the span of engineering disciplines; covering the main areas of engineering: Electrical and Computer Engineering; Mechanical and Manufacturing Engineering; Automation and Mechatronics Engineering; Material and Chemical Engineering; Environmental and Civil Engineering; Biotechnology and Bioengineering; Engineering Mathematics and Physics; and Computer Science and Information Technology are considered for publication in this journal. Contributions from other areas of Engineering and Applied Science are also welcomed. The IIUM Engineering Journal publishes contributions under *Regular papers and Invited review papers*. It also welcomes contributions that address solutions to the specific challenges of the developing world, and address science and technology issues from an Islamic and multidisciplinary perspective.

## **REFEREES' NETWORK**

All papers submitted to IIUM Engineering Journal will be subjected to a rigorous reviewing process through a worldwide network of specialized and competent referees. Each accepted paper should have at least two positive referees' assessments.

## **SUBMISSION OF A MANUSCRIPT**

A manuscript should be submitted online to the IIUM-Engineering Journal website at <http://journals.iium.edu.my/ejournal>. Further correspondence on the status of the paper could be done through the journal website.

---

## INTERNATIONAL ADVISORY COMMITTEE

A. Anwar, United States  
Abdul Latif Bin Ahmad, Malaysia  
Farzad Ismail, USM, Pulau Pinang, Malaysia  
Hanafy Omar, Saudi Arabia  
Hany Ammar, United States  
Idris Mohammed Bugaje, Nigeria  
K.B. Ramachandran, India  
Kunzu Abdella, Canada  
Luis Le Moyne, ISAT, University of Burgundy, France  
M Mujtaba, United Kingdom  
Mohamed AI-Rubei, Ireland  
Mohamed B Trabia, United States  
Syed Kamrul Islam, United States  
Tibor Czigany, Budapest University of Technology and Economics, Hungary  
Yiu-Wing Mai, The University of Sydney, Australia.

Published by:  
IIUM Press,  
International Islamic University Malaysia  
Jalan Gombak, 53100 Kuala Lumpur, Malaysia  
Phone (+603) 6421-5014, Fax: (+603) 6421-6298

Whilst every effort is made by the publisher and editorial board to see that no inaccurate or misleading data, opinion or statement appears in this Journal, they wish to make it clear that the data and opinions appearing in the articles and advertisement herein are the responsibility of the contributor or advertiser concerned. Accordingly, the publisher and the editorial committee accept no liability whatsoever for the consequence of any such inaccurate or misleading data, opinion or statement.

ISSN 1511 - 788X



**IIUM Engineering Journal**  
ISSN: 1511-788X E-ISSN: 2289-7860

# IIUM ENGINEERING JOURNAL

Volume 21, Issue 1, January 2020

<https://doi.org/10.31436/iiumej.v21i1>

## Table of Content

---

<b>EDITORIAL</b> .....	i
<b>CHEMICAL AND BIOTECHNOLOGY ENGINEERING</b>	
NUMERICAL STUDY OF ARGON EFFECT ON NITROGEN SEPARATION FROM AIR BY PRESSURE SWING ADSORPTION .....	1
<i>Abdulbasit Hassan Mahdi, Suhaib Shwish Salih, Heba Sa'ady Ayuob and Tushar Ghosh</i>	
<b>CIVIL AND ENVIRONMENTAL ENGINEERING</b>	
RAINWATER HARVESTING QUALITY ASSESSMENT AND EVALUATION: IIUM CASE STUDY .....	12
<i>Nassereldeen Ahmed Kabbashi, Mohammed Saedi Jami, Nour Hamid Abdurahman and Noor Illi Mohamad Puad</i>	
<b>ELECTRICAL, COMPUTER AND COMMUNICATIONS ENGINEERING</b>	
INVESTIGATION OF MAGNETIC PROPERTIES FOR DIFFERENT COIL SIZES OF DYNAMIC WIRELESS CHARGING PADS FOR ELECTRIC VEHICLES (EV) .....	23
<i>Syasya Azra Zaini, Siti Hajar Yusoff, Amira Aziera Abdullah, Sheroz Khan, Faridah Abd Rahman and Nadia Nazieha Nanda</i>	
STEMMING IMPACT ANALYSIS ON INDONESIAN QURAN TRANSLATION AND THEIR EXEGESIS CLASSIFICATION FOR ONTOLOGY INSTANCES .....	33
<i>Fandy Setyo Utomo, Nanna Suryana and Mohd Sanusi Azmi</i>	
AN ENHANCED PACKET SCHEDULING ALGORITHM FOR THE DOWNLINK COGNITIVE LONG TERM EVOLUTION-ADVANCED .....	51
<i>Huda Adibah Mohd Ramli and Mohamad 'Ismat Hafizi Mansor</i>	
STUDY OF MICROSTRIP PATCH ARRAY ANTENNA FOR SIDE LOBE SUPPRESSION IN THE X-BAND REGION USING UNIFORM, BINOMIAL AND TSCHEBYSCHIEFF EXCITATION METHODS .....	61
<i>Ahmad Alhadi Ruslan, Sarah Yasmin Mohamad, Khairayu Badron, Ahmad Fadzil Ismail, Norun Fariyah Abdul Malek and Farah Nadia Mohd Isa</i>	
PAVEMENT CONDITION ANALYSIS VIA VEHICLE MOUNTED ACCELEROMETER DATA .....	73
<i>Ahmad Jazlan, Muhammad Fahim Rosli, Noor Hazrin Hany Mohamad Hanif, Hasan Firdaus Mohd Zaki, Muhammad Afif Husman, Asan Gani Abdul Muthalif and Deepak Kumar</i>	
PERFORMANCE ANALYSIS OF 5G PATH LOSS MODELS FOR RURAL MACROCELL ENVIRONMENT .....	85
<i>Muhammad Akramuddin Mohd Nordin and Huda Adibah Mohd Ramli</i>	
<b>ENGINEERING MATHEMATICS AND APPLIED SCIENCE</b>	
USING MODIFICATION OF PRIM'S ALGORITHM AND GNU OCTAVE AND TO SOLVE THE MULTIPERIODS INSTALLATION PROBLEM .....	100
<i>Wamiliانا, Mustofa Usman, Warsono, Warsito and Jamal Ibrahim Daoud</i>	
OPTIMIZATION OF THE REGULARIZATION OF THE SOLUTION TO PLATE HEAT TRANSFER PROBLEMS .....	113
<i>Fargana Akter, Abdumalik Rakhimov, Ahsan Ali Khan and Torla Hj Hassan</i>	
PARALLEL PROCESS DISCOVERY USING A NEW TIME-BASED ALPHA++ MINER .....	126
<i>Yutika Amelia Effendi and Riyanarto Sarno</i>	
SOFTWARE, ALGORITHMS AND METHODS OF DATA ENCRYPTION BASED ON NATIONAL STANDARDS .....	142
<i>Rakhmatillo Djuraevich Alov and Mirkhon Mukhammadovich Nurullaev</i>	
NUMERICAL ALGORITHM FOR FINDING OPTIMAL INITIAL CONCENTRATIONS OF CHEMICAL REACTIONS .....	167
<i>Svetlana Mustafina, Andrey Antipin, Evgenia Antipina, Elena Odinkova, Larisa Tuchkina, Konstantin Kolyazov and Sofia Mustafina</i>	
DIABETES CLASSIFICATION BASED ON KNN .....	175
<i>Ameer H. Ali, Mohammed A. T. Alrubei, Laith Falah Mohammed Hassan, Mohannad A. M. Al-Ja'afari and Saif H. Abdulwahed</i>	
ADAPTIVE SYSTEM OF FUZZY-LOGICAL REGULATION BY TEMPERATURE MODE OF A DRUM BOILER .....	182
<i>Siddikov Isamidin Xakimovich, Umurzakova Dilnoza Maxamadjonovna and Bakhrieva Hurshida Askarxodjaevna</i>	

## **MATERIALS AND MANUFACTURING ENGINEERING**

MECHANICAL PROPERTIES, MORPHOLOGY, AND HYDROLYTIC DEGRADATION BEHAVIOR OF POLYLACTIC ACID / THERMOPLASTIC POLYURETHANE BLENDS .....	193
<i>Yose Fachmi Buys, Mimi Syakina Ahmad, Hazleen Anuar, Mudrikah sofia Mahmud and Nur Aimi Mohd Nasir</i>	
STUDY OF PRODUCTIVITY IMPROVEMENT OF MANUAL OPERATIONS IN SOYA SAUCE FACTORY .....	202
<i>Zaharah Wahid, Mohd Radzi Che Daud and Kartini Ahmad</i>	
THE EFFECTS OF SUPERCRITICAL CARBON DIOXIDE ON THE DEGRADATION AND ANTIMICROBIAL PROPERTIES OF PLA BIOCOSPOSITE.....	212
<i>Hazleen Anuar, Siti Nur E'zzati Mohd Apandi, Siti Munirah Salimah Abd Rashid, Fathilah Ali, Yose Fachmi Buys, Mohd Romainor Manshor, Sabu Thomas and Nur Aimi Mohd Nasir</i>	

## **MECHATRONICS AND AUTOMATION ENGINEERING .**

DYNAMIC MODELING OF A SINGLE-LINK FLEXIBLE MANIPULATOR ROBOT WITH TRANSLATIONAL AND ROTATIONAL MOTIONS .....	228
<i>Dermawan Dermawan, Hammad Abbas, Rafiuddin Syam, Zulkifli Djafar and Abdul Kadir Muhammad</i>	

# NUMERICAL STUDY OF ARGON EFFECT ON NITROGEN SEPARATION FROM AIR BY PRESSURE SWING ADSORPTION

ABDULBASIT HASSAN MAHDI<sup>1</sup>, SUHAIB SHWISH SALIH<sup>1\*</sup>, HEBA SA'ADY AYUOB<sup>1</sup>,  
AND TUSHAR GHOSH<sup>2</sup>

<sup>1</sup>Tikrit University, College of Engineering, Department of Chemical Engineering,  
Salahaldin, Iraq.

<sup>2</sup>Department of Nuclear Science & Engineering Institute,  
University of Missouri-Columbia, Missouri, United States.

\*Corresponding author: [sss43b@mail.missouri.edu](mailto:sss43b@mail.missouri.edu)

(Received: 19<sup>th</sup> June 2019; Accepted: 30<sup>th</sup> September 2019; Published on-line: 20<sup>th</sup> January 2020)

**ABSTRACT:** A mathematical model was used to design four modes of two-bed pressure swing adsorption (PSA) process to investigate argon presence in the feed mixture. The effect of operating parameters such as cycle time, pressure equalization, adsorption pressure, and purging flow rate was investigated. The model was validated with experimental data of nitrogen separation from the air by a single bed adsorber on carbon molecular sieve (CMS). A good agreement with experimental data is obtained. In the PSA process, higher purity of nitrogen (99.7%) was detected by mode 4 when the feed mixture was free of argon (O<sub>2</sub>: 21%, N<sub>2</sub>:79%). While the nitrogen purity was only 98.0% in the state of argon presence in the feed mixture (O<sub>2</sub>: 21%, N<sub>2</sub>: 78%, Ar: 1%). The results showed that the cycle time had insignificant effect whereas the pressure equalization and purging at low vacuum pressure had a significant effect on the process performance.

**ABSTRAK:** Model matematik digunakan bagi membina empat mod terdiri daripada tekanan dua-turus proses penyerapan buai (PSA) bagi menyiasat kehadiran argon dalam campuran pakan. Kesan parameter beroperasi seperti masa kitaran, penyamaan tekanan, tekanan penyerapan, dan kadar aliran penyingkiran disiasat. Model matematik tersebut disiasat melalui data eksperimen pemisahan nitrogen dari udara melalui penyerapan turus tunggal pada penapis molekular karbon (CMS). Data eksperimen yang bagus diperoleh. Dalam proses PSA, mod keempat menghasilkan ketulenan nitrogen (99.7%) lebih tinggi apabila campuran pakan bebas argon (O<sub>2</sub>: 21%, N<sub>2</sub>:79%). Sementara itu, ketulenan nitrogen hanya 98.0% apabila terdapat kehadiran argon dalam campuran pakan (O<sub>2</sub>: 21%, N<sub>2</sub>: 78%, Ar: 1%). Kajian menunjukkan masa kitaran memberi kesan tidak signifikan sementara penyamaan tekanan dan penyingkiran pada tekanan vakum rendah mempunyai kesan signifikan terhadap prestasi proses.

**KEYWORDS:** nitrogen separation; PSA; argon; model simulation

## 1. INTRODUCTION

Gaseous nitrogen is used extensively in many industries such as vessel inerting applications, electronics, metals, and food industries due to its inert properties [1]. A variety of separation processes are used to produce commercial nitrogen such as cryogenic distillation, adsorption separation, and membrane separation processes. PSA is one of the most important process in the field of gas separation [2-4]. A carbon molecular sieve

(CMS) is used as an adsorbent for nitrogen separation from air due to the difference in the kinetic adsorption of oxygen and nitrogen [5-7]. Since oxygen is faster than nitrogen to diffuse into the CMS, a kinetic selectivity is created, which allows reaching nitrogen purities as high as 99.999%. The demand for high nitrogen purity, over 99%, in a low and medium amount in the industrial sector has urged a lot of companies to produce nitrogen from atmospheric air by PSA process [8]. Zeolite X-type and perovskite-type ceramic were used as adsorbents instead of the CMS sieve for nitrogen separation from air at high pressure [9-12].

In the last decades, the PSA process was investigated experimentally and theoretically in many studies [13,14]. For instance, a simple linear driving force (LDF) model was created to simulate a single bed PSA process for nitrogen separation from the air on CMS. The feed mixture was assumed to be (O<sub>2</sub>: 21%, and N<sub>2</sub>:79%) [15]. The effect of bed length and pressurizing rate on the single bed PSA performance was studied carefully. The higher performance of the process was observed with a bed length over 1.3 m. The effect of the adsorption/desorption rate constants of oxygen on the nitrogen separation was evaluated through a simulation process and found that the purity varied significantly with cycle time [8,16]. Operating parameters such as feed flow, purge flow, cycle time, adsorption pressure, and bed length on the PSA process performance was studied experimentally and theoretically [17]. Higher purity of nitrogen was observed at short adsorption time. No significant effect of adsorption pressure over 4 bar on the process performance was observed. About 97.6% of nitrogen purity was detected using atmospheric air as a feed [2,3]. The purity was improved from 96% to over 99% by adding a deoxo reactor to the PSA process. The feed mixture only consisted of oxygen and nitrogen [18].

Many previous studies assume that the feed mixture only consists of O<sub>2</sub> and N<sub>2</sub>, but real air consists of argon as well. So, the main objective of this study is to investigate the effect of argon presence in the feed mixture and operating parameters on the nitrogen purity. A mathematical model is introduced to study the nitrogen separation from the air by single bed adsorber on a CMS sieve. Then, it is employed to design four configurations of the two-bed PSA process to deeply investigate the process and compare the four modes.

## 2. MODELING AND SIMULATION

A theoretical study is employed to investigate the nitrogen separation from atmospheric air by PSA process. The numerical study was applied to the following processes:

- a) Single bed adsorber to study the breakthrough time.
- b) Two-bed PSA process with the four different configurations as shown in Table 4.

The first design of the PSA process is represented by the Skarstrom cycle, which involved four steps: pressurizing, producing, depressurizing, and purging steps. Different modifiers are added such as purging by vacuum pump, pressure equalization, and product pressurizing, to improve the performance of the PSA process.

The numerical study of the PSA process was carried out using a simulation program. Finite difference method (FDM) is employed, and axial dimension is discretized into 50 nodes. The purity of oxygen or nitrogen is used as an indication of the process performance. The following assumptions are considered in the numerical study:

- 1- Feed mixture assumed to be (O<sub>2</sub>:21%, N<sub>2</sub>:78%, Ar:1%, and O<sub>2</sub>:21%,N<sub>2</sub>:79%).

- 2- Ideal gas law is applied.
- 3- Isothermal system.
- 4- The flow pattern is described by the axial dispersion plug flow model.
- 5- Radial concentration is neglected.
- 6- Mass Transfer transport is described by a linear driving force (LDF).
- 7- Adsorption equilibrium is fitted with the Langmuir equation.
- 8- Pressure drop along the bed is represented by the Darcy equation.

Overall mass balance:

$$-D_L \frac{\partial^2 c_i}{\partial z^2} + \frac{\partial C}{\partial t} + \frac{\partial(uC)}{\partial t} + \sum_{i=1}^n \rho_p \left( \frac{1-\varepsilon}{\varepsilon} \right) \frac{\partial \bar{q}}{\partial t} = 0 \quad (1)$$

Component (i) mass balance:

$$-D_L \frac{\partial^2 c_i}{\partial z^2} + \frac{\partial(u c_i)}{\partial z} + \frac{\partial c_i}{\partial t} + \rho_p \left( \frac{1-\varepsilon}{\varepsilon} \right) \frac{\partial \bar{q}}{\partial t} = 0 \quad (2)$$

Boundary conditions of each step of the PSA process are presented in Table 1. The boundary conditions of well-known Danckwerts are applied [19]. The adsorption isotherm and adsorption rate parameters of N<sub>2</sub>, O<sub>2</sub>, and Ar on CMS are presented in Table 2. The operating parameters of the single bed adsorber are presented in Table 3. The operation parameters of other modes of PSA process are presented in Table 4.

Table 1: Applied boundary conditions in the simulation process.

Cycle step	Concentration (c <sub>i</sub> )	Velocity (u)
Pressurizing (Pre)	$-D_L(\partial c_i / \partial z) _{z=0} = u(c_i _{z=0-} - c_i _{z=0+})$ $(\partial c_i / \partial z) _{z=L} = 0$	$u _{z=0} = u_{\text{feed}}$ $u _{z=L} = 0$
Adsorption (Ads)	$-D_L(\partial c_i / \partial z) _{z=0} = u(c_i _{z=0-} - c_i _{z=0+})$ $(\partial c_i / \partial z) _{z=L} = 0$	$u _{z=0} = u_{\text{feed}}$
Depressure- Equalization (DepEqu)	$-D_L(\partial c_i / \partial z) _{z=0} = 0$ $-D_L(\partial c_i / \partial z) _{z=L} = 0$	$u _{z=0} = 0$
Depressurizing (Dep)	$D_L(\partial c_i / \partial z) _{z=0} = 0$ $-D_L(\partial c_i / \partial z) _{z=L} = 0$	$u _{z=L} = 0$
Purging (Pur)	$-D_L(\partial c_i / \partial z) _{z=L} = u(c_i _{z=L+} - c_i _{z=L-})$ $-D_L(\partial c_i / \partial z) _{z=0} = 0$	$u _{z=L} = u_{\text{purge}}$
Pressure-Equalization (PreEqu)	$-D_L(\partial c_i / \partial z) _{z=0} = u(c_i _{z=0-} - c_i _{z=0+})$ $(\partial c_i / \partial z) _{z=L} = 0$	$u _{z=0} = 0$

Initial conditions:

$$c_i(z, 0) = c_0; \quad q_i(z, 0) = q_i^*$$

Ideal gas law:

$$\frac{P}{RT} = \sum_{i=1}^n c_i \quad (3)$$



The adsorption rate is described by the LDF equation with concentration-dependent diffusivity:

$$\frac{\partial \bar{q}_i}{\partial t} = \omega_i (q_i^* - \bar{q}_i), \quad \omega_i = \frac{15D_{ei}}{r_c^2} \quad (4)$$

Where:  $D_{ei}/r_c^2 = CP_r^{0.5}(1 + B_i P_i)^2$

The LDF coefficient ( $\omega_i$ ) has been estimated from the fitting between the mathematical model and experimental data of single bed adsorber from the literature survey. The predicted values are presented in Table 2.

The adsorption isotherm for multi-components (oxygen, nitrogen, and argon) are predicted by the Langmuir equation to the n-component mixture:

$$q_i = \frac{q_{mi} B_i P_i}{1 + \sum_{j=1}^n B_j P_j} \quad (5)$$

Where:  $q_{mi} = k_1 + k_2 * T$ , and  $B = k_3 \exp\left(\frac{k_4}{T}\right)$ ,

Table 2: Adsorption equilibrium and adsorption rate parameter [20].

Parameters	O <sub>2</sub>	N <sub>2</sub>	Ar
K <sub>1</sub> *10 <sup>3</sup> (mol/g)	5.817 × 10 <sup>-3</sup>	1.130 × 10 <sup>-2</sup>	9.556 × 10 <sup>-3</sup>
K <sub>2</sub> *10 <sup>5</sup> (mol/g)	-7.512 × 10 <sup>-6</sup>	-2.80 × 10 <sup>-5</sup>	-2.101 × 10 <sup>-5</sup>
K <sub>3</sub> *10 <sup>5</sup> (1/Kpa)	7.984 × 10 <sup>-6</sup>	30.89 × 10 <sup>-5</sup>	6.566 × 10 <sup>-5</sup>
K <sub>4</sub> (k)	1444	359.7	773.8
$\omega_i$ (s <sup>-1</sup> )	0.248	0.001	0.0071

Darcy's equation used to predict pressure drop:

$$-\frac{dP}{dz} = \frac{180\mu(1 - \epsilon)^2}{D_p^2 \epsilon^2} u \quad (6)$$

Where :  $u$  is the superficial gas velocity.

Table 3: Adsorbent and common parameters were used in the single bed process.

Adsorbent	CMS
Type	Pellet
Pellet density $\rho_p$ (kg/m <sup>3</sup> )	800
Bed voidage ( $\epsilon$ )	0.30
Adsorption bed	
Length (m)	1
Diameter (m)	0.0254
Ambient temperature (°C)	25
Adsorption pressure (bar)	7
Product flow rate (liter/min)	1

The performance of the PSA process is indicated by the purity and recovery of nitrogen according to the following equations:

$$Purity(N_2\%) = \frac{\text{amount of } N_2 \text{ produced during adsorption step in the product end}}{\text{amount of total product produced during adsorption step in the product end}} \quad (8)$$

$$Recovery(N_2\%) = \frac{\text{amount of } N_2 \text{ produced during adsorption step in the product end}}{\text{amount of } N_2 \text{ fed during pressurizing, and adsorption steps in the feed end}} \quad (9)$$

Table 4: Operated conditions of the four modes of the PSA process.

The PSA Modes	Pressure (bar)	Product flowrate (liter/min)	Purge flowrate (liter/min)	Vacuum purging (bar)	Cycle step time (sec)
					Pre - Ads - Dep - Pur
2-bed 4-step (mode 1)	2-9	0.1-5	1-6	No	5 - 20 - 5 - 20
					5 - 30 - 5 - 30
					5 - 40 - 5 - 40
					5 - 50 - 5 - 50
					5 - 60 - 5 - 60
					5 - 70 - 5 - 70
2-bed 4-step with vacuum purging (mode 2)	7	0.1-1	1-3	Yes	Pre - Ads - Dep - VacPur
					5 - 80 - 5 - 80
2-bed 6-step with equalization pressure (mode 3)	7	0.1-1	1-6	No	Pre - Ads - DepEq - Dep - Pur - PreEq
					5 - 80 - 5 - 5 - 80 - 5
2-bed 6-step with equalization pressure and vacuum purging (mode 4)		0.1-1	1-3	Yes	Pre - Ads - DepEq - Dep - VacPur - PreEq
					5 - 20 - 5 - 5 - 20 - 5
					5 - 30 - 5 - 5 - 30 - 5
					5 - 40 - 5 - 5 - 40 - 5
					5 - 50 - 5 - 5 - 50 - 5
					5 - 60 - 5 - 5 - 60 - 5
					5 - 70 - 5 - 5 - 70 - 5
					5 - 80 - 5 - 5 - 80 - 5
5 - 90 - 5 - 5 - 90 - 5					
5 - 100 - 5 - 5 - 100 - 5					

### 3. RESULTS AND DISCUSSION

#### 3.1 Single Bed Adsorber

The breakthrough curve of oxygen at the product end of the single bed adsorber for nitrogen separation from the air on CMS is shown in Fig. 1. The effluent flow rate is 1

liter/min. The breakthrough time occurred at 100 s. Thereby, the oxygen purity gradually increased until it reached a stable purity of about 20%. The mass transfer zone (MTZ) is very wide due to the effect of axial dispersion during the pressurizing and producing steps. The predicted results are in good agreement with experimental data obtained by Abdel-Rahman [3].

Figure 2 represents the effect of product pressurizing pressure on the breakthrough time and the amount of nitrogen produced. A little improvement in the breakthrough time and in the amount of nitrogen produced was noticed. That is because the adsorption isotherm of oxygen and nitrogen are closer to each other on the CMS at equilibrium state. So increasing in the product pressurizing pressure leads to increase in the partial pressure of nitrogen in the bed and the most porosities of the adsorbent (CMS) are filled by nitrogen. Therefore, little increases in the breakthrough time may be attributed to increases in adsorbent capacity with pressure and decreased axial dispersion effects.

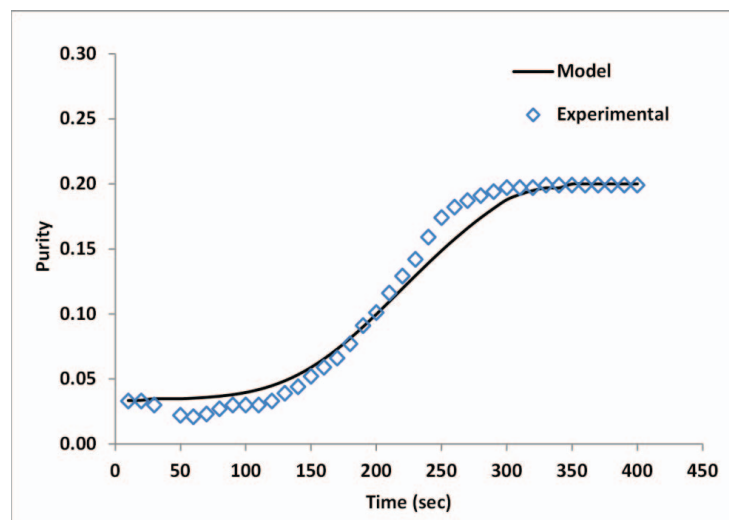


Fig. 1: Fitting between the predicted results and experimental data of oxygen breakthrough curve in the product end of single bed adsorber.

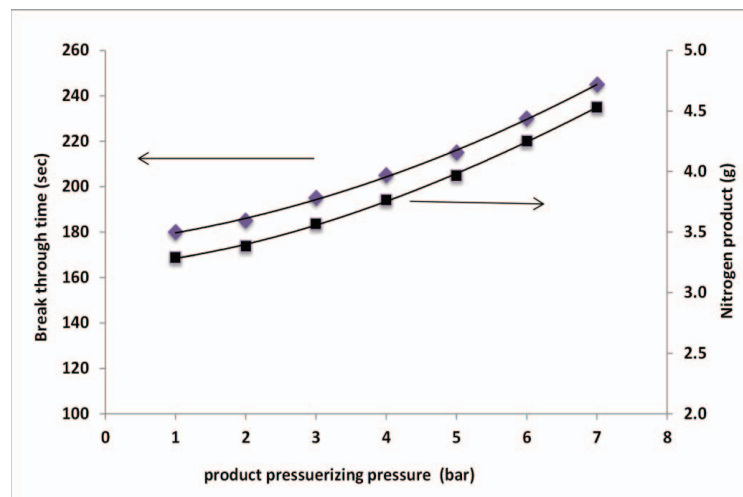


Fig. 2: Effect of product pressurizing pressure on the breakthrough time and amount of produced nitrogen in single bed adsorber.

## 3.2 Two Bed PSA Process

### 3.2.1 Effect of the Ternary Feed Mixture

Figure 3 represents the effect of the argon presence in the feed mixture on the performance of the 2-bed 6-step PSA process (mode 3) at 7 bar pressure, 80 s adsorption time, 1-4 liter/min purge flow rate, and 0.1 liter/min product flow rate. Higher purity of nitrogen, over 99% is observed in the state of a binary feed mixture ( $O_2/N_2$ ) than a ternary feed mixture ( $O_2/N_2/Ar$ ), where the maximum purity was about 95%. According to the LDF coefficient values, oxygen diffuses faster than nitrogen and argon through the CMS porosity, therefore the purity of nitrogen in the product end could not be higher than the purity of the PSA process with the binary feed mixture. Most studies obtained high purity of nitrogen, over 99% when they handled a binary feed mixture.

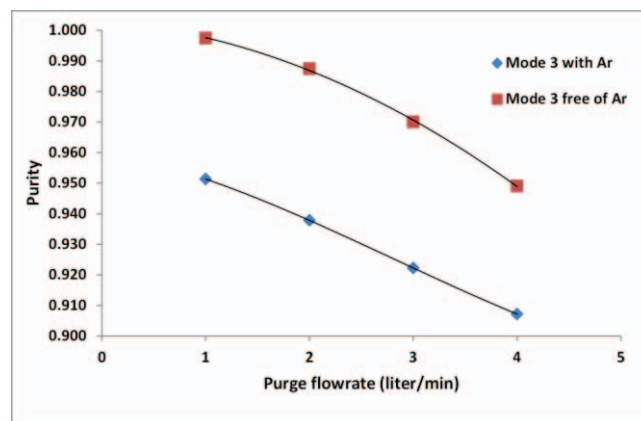


Fig. 3: Effect of argon presence in the feed mixture on the performance of mode 3 of PSA processes.

### 3.2.2 Effect of Adsorption Pressure

Figure 4 shows the effect of adsorption pressure (2-9 bar) on the product purity of 2-bed 4-step PSA processes (mode 2), at purge flow rate of 1 liter/min, product flow rate of 1 liter/min, and adsorption time of 40 s. The purity of nitrogen and argon are increased with increasing adsorption pressure, due to increase in the adsorption capacity of the CMS to adsorb more oxygen. The same trend is detected with the argon component. Only oxygen is adsorbed by CMS, therefore the purity of nitrogen in the product could not be higher due to the argon presence in the feed mixture.

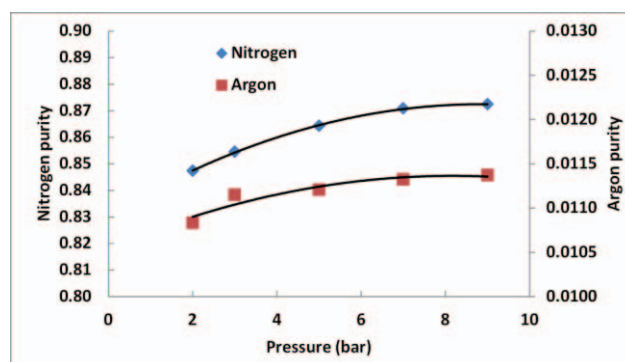


Fig. 4: Effect of adsorption pressure on the purity of the nitrogen and argon in the mode 2 of the PSA process.

### 3.2.3 Effect of Adsorption Time

Figure 5 shows the effect of adsorption time in the range of 40-250 s with two different feed mixtures, at adsorption pressure of 7 bar, purge flow rate of 1 liter/min, and product flow rate of 1 liter/min. Nitrogen purity increased with increasing adsorption time until 100 s and then decreased slightly or kept stable. Nitrogen separation on CMS is kinetically controlled. Increase in the adsorption time over 100 s leads to the system approaching an equilibrium state, causing decreases in the nitrogen purity or keeping it stable. At short adsorption time, the time is not enough to adsorb the whole oxygen molecule by CMS. Maximum uptake is obtained at nearly 100 s. Maximum purity (98%) is detected by mode 3 without argon presence in the feed mixture, while it dropped to 92% with argon presence in the feed mixture.

The production of nitrogen purity by mode 3 regardless of feed mixture components binary or ternary is higher than mode 1. This may be attributed to the effect of the pressure equalization step in mode 3, which contributed to reducing the axial dispersion effect during the pressurizing step. Moreover, the rapid diffusion of oxygen into the CMS led to the adsorption of oxygen rather than argon and nitrogen, where the diffusion rate constant of oxygen is higher than nitrogen and argon as shown in Table 2. CMS is a kind of adsorbent material with pore sizes in the range of 3-5 Å while the diameter of oxygen is (3.46 Å), diameter of nitrogen is (3.64 Å) and the diameter of argon is (3.43 Å). All these reasons lead to kinetic separation of air on CMS. Despite the smaller diameter of argon than other components, low partial pressure of argon in the feed mixture and small diffusion rate constant reduced argon diffusion in the state of the ternary feed mixture. This phenomenon was observed by Jee [20] when they used two ternary feed mixtures (O<sub>2</sub>/Ar/N<sub>2</sub>; 95:4:1 and 90:4:6 vol%) for gas separation on CMS. Nitrogen recovery increased with increasing adsorption time, where the product flow rate increased with increasing the adsorption time. The results are in a good agreement with LaCava [16], Farooq [21], and Mostamand [2].

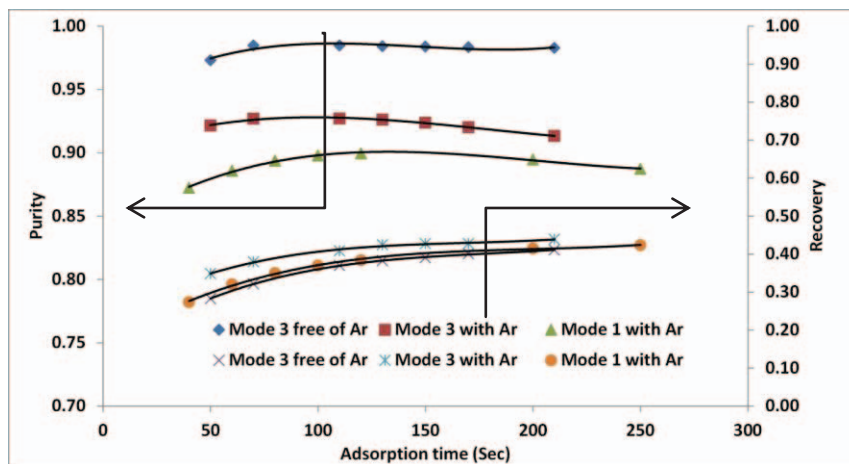


Fig. 5: Effect of the adsorption time on the performance of two modes of PSA process.

### 3.2.4 Effect of Purge Flowrate

Figure 6 shows the effect of purge flow rate for all modes of PSA process on the purity of nitrogen at adsorption time of 80 s, adsorption pressure of 7 bar, and product flow rate of 1 liter/min. In all modes, nitrogen purity was approximately kept constant or decreased slightly with increased purge flow rate until 2 liter/min, and it then decreased

dramatically. The gas used in the purging step is represented as part of the product flow rate during the adsorption step and is enriched with nitrogen. Increasing it over 2 liter/min causes an increase in vapor pressure of nitrogen, after displacing oxygen out of the bed and adsorbing it by CMS. So in the next cycle, nitrogen purity will inevitably drop, because most CMS porosity is filled with nitrogen during the purging step. In addition, both the depressurizing step and low purge flowrate (< 1 liter/min) were enough to expel adsorbed oxygen from CMS porosity. The most out of purge flow rate is observed at low purge flow rate. The results are in agreement with Farooq [21], and Abdel-Rahman [3], and in disagreement with Mostamand [2].

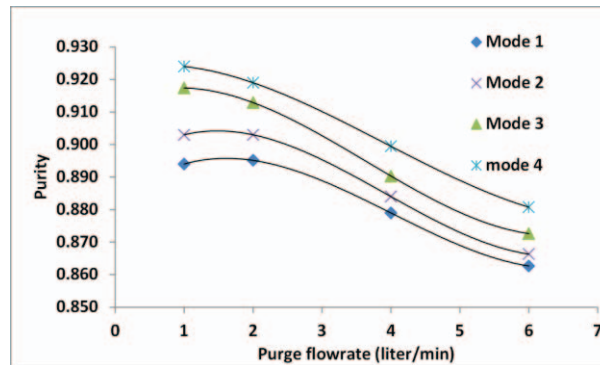


Fig. 6: Effect the purge flow rate on the four modes of the PSA process.

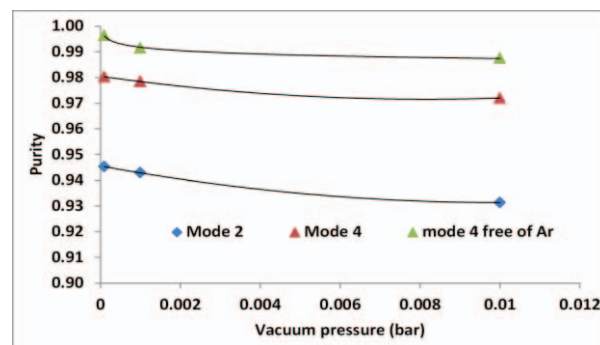


Fig. 7: Effect of vacuum pressure on the performance of two modes of the PSA processes.

### 3.2.5 Effect of Vacuum Pressure

Figure 7 shows the effect of vacuum pressure on the effluent nitrogen purity at adsorption pressure of 7 bar, purge flow rate of 1 liter/min, product flow rate of 0.1 liter/min, and adsorption time of 80 s. All processes have the same trend. High nitrogen purity is detected at a low vacuum pressure (0.0001 bar) and then decreased slightly with increasing vacuum pressure. Purging the adsorbent at low vacuum pressure has a significant effect to clean the adsorbent during the purging step. Increases of vacuum pressure lead to sufficient desorption of CMS to prepare it for the next cycle. Maximum purity, over 99% is observed by mode 4 with the binary feed mixture, while low purity of about 98% is observed with the same mode (mode 4) with the ternary feed mixture. The nitrogen purity produced by mode 4 with a feed mixture that is free of argon is higher than mode 4 with ternary feed mixture and mode 2. This may be attributed to the faster rate of diffusion of oxygen than nitrogen and argon on CMS, the presence of the pressure equalization step, and the purging step at low vacuum pressure, where they contributed to

improving the process performance. It is important to consider the argon presence in the feed mixture, and operation steps to design the PSA unit to produce high purity nitrogen from atmospheric air.

#### 4. CONCLUSIONS

The mathematical model of single bed adsorber is in good agreement with experimental data. The breakthrough time and amount of nitrogen product are increased slightly with increases in product pressurizing pressure. For the PSA process, high purity of nitrogen was not available when argon was present in the feed mixture. High purity of nitrogen over 99% was observed by mode 4 when the feed mixture was free of argon, while the purity decreased to 98% with presence of argon in the feed mixture. Also, the same trend was detected by mode 3, where the purity decreased from 98% to 92% when argon was considered in the feed mixture. Only oxygen is adsorbed by CMS from the feed mixture (O<sub>2</sub>: 21%, N<sub>2</sub>: 78%, Ar: 1%). For different PSA modes, the equalization step in mode 3, and the equalization step with purging step under vacuum pressure in mode 4 are useful to increase the nitrogen purity to 99% in comparison with other modes (mode 1 and mode 2) where the nitrogen purity was about 90%. The best arrangement of all modes from higher to lower nitrogen purity is as follows: mode 4, mode 3, mode 2, and mode 1. For operation parameters, the purities of argon and nitrogen in the product stream increased with increases of adsorption pressure due to increases in adsorption capacity of CMS sieve to adsorb more oxygen. In all modes, the purity of nitrogen increased a few percent between adsorption times of 50 – 100 s. Also, the purity of nitrogen decreased about 4% with increases of purge flow rate from 1 to 6 liter/min, and optimum purge flow rate was between 1 and 2 liter/min.

#### ACKNOWLEDGEMENT

The authors would like to thank the Chemical Engineering Department at the University of Tikrit, Iraq for allowing them working in their laboratories.

#### REFERENCES

- [1] Nicholas AF, Mohd ZH, Zulkarnain Z, Tumirah K. (2019) Activated Carbon for shape stabilized Phase Change Material. *Technology and Applications of carbon nanomaterials*, 279-308.
- [2] Mostamand A, Mofarahi M. (2011) Simulation of a single bed pressure swing adsorption for producing nitrogen. In *International Conference on Chemical, Biological and Environment Sciences (ICCEBS'2011) Bangkok*.
- [3] Abdel-Rahman ZA, Mhdi AH, Auob HS. (2016) Parametric study for nitrogen separation from air by pressure swing adsorption using carbon molecular sieve. *Tikrit Journal of Engineering Science*. 23 (2), 1-9
- [4] Carreon MA. (2018) Molecular sieve membranes for N<sub>2</sub>/CH<sub>4</sub> separation. *Journal of Material Research*, 33(1): 32-43.
- [5] Lemcoff NO. (1999) Nitrogen separation from air by pressure swing adsorption. *Studies in Surface Science and Catalysis*. 120: 347-370.
- [6] Reid CR, O'koye IP, Thomas KM. (1998) Adsorption of gases on carbon molecular sieves used for air separation. *Spherical Adsorptives as Probes for Kinetic Selectivity*. 14(9): 2415-2425.

- [7] Vivo-Vilches JF, Agustín FP, Francisco JM, Francisco C, Christophe S, Ana MR, Alexander F, Alirio ER. (2018) From Carbon Molecular Sieves to VOCs filters: Carbon gels with tailored porosity for hexane isomers adsorption and separation, *Microporous and Mesoporous Materials*, 270: 161-167.
- [8] Shirley AI, Lemcoff NO. (2002) Air separation by carbon molecular sieves. *Adsorption*. 8: 147–155.
- [9] Kim J-D. (1995) Production of high-purity nitrogen from air by pressure swing adsorption on zeolite X. *Separation Science and Technology*, 30: 347-368.
- [10] Reynolds SP, Ebner AD, Ritter JA. (2006) Enriching psa cycle for the production of nitrogen from air. *Ind. Eng. Chem. Res.*, 45: 3256-3264.
- [11] Yang J, Lee CH. (1998) Adsorption dynamics of a layered bed PSA for H<sub>2</sub> recovery from coke oven gas. *Aiche Journal*, 44: 1325-1334.
- [12] Xu M, Wu HC, Lin YS, Deng S. (2018) Simulation and optimization of pressure swing adsorption process for high-temperature air separation by perovskite sorbents. *Chemical Engineering Journal*, 354: 62-74.
- [13] Mate VIA, Dobladez JAD, Alvarez-Torrellas S, Larriba M, Rodriguez AM. (2019) Modeling and simulation of the efficient separation of Methane/Nitrogen mixtures with [Ni<sub>3</sub>(HCOO)<sub>6</sub>] MOF by PSA. *Chemical Engineering Journal*, 361: 1007-1018.
- [14] Moran A, Talu O. (2018) Limitations of Portable Pressure Swing Adsorption Processes for Air Separation. *Industrial & Engineering Chemistry Research*, 57(35): 11981-11987.
- [15] Farooq S, Ruthven DM. (1990) A comparison of linear driving force and pore diffusion models for a pressure swing adsorption bulk separation process. *Chemical Engineering Science*, 45: 107 – 115.
- [16] LaCava AI, Lemcoff NO. (1996) Single bed pressure swing adsorption process to generate high purity nitrogen. *Gas Separation & purification*, 10(2): 113-115.
- [17] Makarem MA, Mofarahi M, Jafarian B, Lee CH. (2019) Simulation and analysis of vacuum pressure swing adsorption using the differential quadrature method. *Computers & Chemical Engineering*, 121: 483-496.
- [18] Vaduva M, Stanciu V. (2006) Separation of nitrogen from air by selective adsorption of carbon molecular sieves. *U.P.B. Sci. Bull.*, 68: 2-10.
- [19] Jee JG, Lee J-S, Lee CH. (2001) Air separation by a small-scale two-bed medical O<sub>2</sub> pressure swing adsorption. *Industrial & engineering chemistry research*, 40: 3647-3658.
- [20] Jee JG, Kim MB, Lee CH. (2005) Pressure swing adsorption processes to purify oxygen using a carbon molecular sieve. *Chemical Engineering Science*, 60: 869 - 882.
- [21] Farooq S, Rathor MN, Hidajat K. (1993) A predictive model for a kinetically controlled pressure swing adsorption separation process, *Chemical Engineering Science*, 48(24): 4129–4141.



## RAINWATER HARVESTING QUALITY ASSESSMENT AND EVALUATION: IIUM CASE STUDY

NASSERELDEEN AHMED KABBASHI<sup>1</sup>, MOHAMMED SAEDI JAMI<sup>1</sup>, NOUR HAMID  
ABDURAHMAN<sup>2</sup> AND NOOR ILLI MOHAMAD PUAD<sup>1</sup>

<sup>1</sup>*Department of Biotechnology Engineering, Faculty of Engineering,  
International Islamic University Malaysia,  
P.O Box 10, 50728 Kuala Lumpur, Malaysia*

<sup>2</sup>*Faculty of Chemical and Natural Resources Engineering,  
Universiti Malaysia Pahang, Gambang, Pahang, Malaysia.*

*\*Corresponding author: nasreldin@iium.edu.my*

*(Received: 11<sup>th</sup> April 2019; Accepted: 16<sup>th</sup> October 2019; Published on-line: 20<sup>th</sup> January 2020)*

**ABSTRACT:** This study focuses on rainwater harvesting quality at the Faculty of Engineering, International Islamic University Malaysia (IIUM). As development is progressing over the years in Malaysia, there is also an increasing number of environmental issues and those issues are getting worse day by day. At present, Malaysia is blessed with plentiful annual rainfall that represents approximately 314 mm of monthly rainfall but there is no evidence that this rainwater is redirected for daily usage. To pursue a more sustainable development, rainwater harvesting has been recognized as one innovative solution. The IIUM Gombak campus is located in a hillside area that is a suitable study area to perform rainwater harvesting, which can be used as an alternative water supply in the future and reduce utility bills for water used on the campus. Firstly, a suitable study area for rain water harvesting around KOE, IIUM was determined before collection of data to determine the storage capacity needed. This study includes the estimation of rainwater quantity that can be harvested in one year. The quality of rainwater in terms of biochemical oxygen demand (BOD), chemical oxygen demand (COD), pH, total suspended solid (TSS), turbidity, and microbial count were studied. Data analysis showed that the values of BOD, COD, pH, TSS, turbidity, and microbial count were in the range of 2 - 3.2 mg/l, 22.5 - 42.5 mg/l, 5.9 - 6.5, 20 mg/l, 9 -11 NTU, and between 200 - 260 cfu/ml, respectively. This indicates that the harvested rainwater is acceptably clean but not suitable to be used as drinking water.

**ABSTRAK:** Fokus kajian ini adalah pada kualiti air hujan yang ditadah di Fakulti Kejuruteraan, Universiti Islam Antarabangsa Malaysia (UIAM). Sejalan dengan pembangunan pesat di Malaysia, isu alam sekitar juga semakin bertambah dan menjadi semakin teruk hari ke hari. Pada masa sama, ketika ini Malaysia dirahmati dengan hujan yang mencurah setiap tahun, dengan kuantiti bulanan sebanyak 314 mm air hujan dan tidak ada bukti penggunaan air hujan ini bagi kegunaan harian dsb. Bagi memenuhi keperluan kelangsungan pembangunan, penadahan air hujan dikenal pasti sebagai satu penyelesaian inovatif. Kampus UIAM Gombak terletak di kawasan pinggir bukit yang sesuai bagi menjalankan kajian tadahan air hujan. Ianya boleh digunakan sebagai bekalan air alternatif pada masa depan dan mengurangkan bil utiliti bekalan air dalam kampus. Terlebih dahulu, kawasan kajian yang sesuai dikenal pasti berdekatan Fakulti Kejuruteraan, UIAM bagi mengumpul air hujan sebelum data dikumpulkan bagi mengenal pasti kapasiti pengumpulan yang diperlukan. Kajian ini juga menganggar kuantiti air hujan yang boleh ditadah dalam satu tahun. Kualiti air hujan dikaji dari segi keperluan oksigen biokimia

(BOD), keperluan oksigen kimia (COD), pH, jumlah pepejal terampai (TSS), kekeruhan dan bilangan mikrob. Analisis data mendapati nilai BOD, COD, pH, TSS, kekeruhan dan bilangan mikrob berada dalam julat 2 - 3.2 mg/l, 22.5 – 42.5 mg/l, 5.9 - 6.5, 20 mg/l, 9 - 11 NTU dan antara 200 -260 cfu/ml, masing-masing. Ini menunjukkan air hujan yang ditadah adalah boleh diterima sebagai bersih tetapi tidak sesuai dijadikan sebagai air minuman.

---

**KEYWORDS:** *rainwater harvesting; water quality analysis; Moringa oleifera; disinfectant*

## 1. INTRODUCTION

Water harvesting is a practice that has been used to increase the effectiveness of water and make use of it. Water harvesting systems direct water, from a great normal watershed or man-made collection, into a small puddling basin. The water can then be stored in subversive tanks or be used directly for irrigation or family purposes. In the modern period, water harvesting has been neglected, particularly in developed countries, due to technical achievements in the fields of water treatment and distribution. But, in recent years, water harvesting in modern-urban environments has turned into an essential practice. Municipal areas are being cemented and built, resulting in the decrease of groundwater renewal area. As a result, a great quantity of good water that rains over the municipality is inhibited from refreshing aquifers as it is absorbed into the public drainage system.

The water crisis is hitting a current civilization that already needs to decrease its major expenditures: energy utilization and water use. The sometimes indiscriminate utilization of water wealth flies in the face of water deficiencies and scarcity occurring in several countries. Less than 1% of the water on the globe is potable. The water from rain, melting snow, and fog has always been considered to have important potential to contribute to supply, even though these types of water need to be treated in order to meet the legal requirements for consumption, with chemical, microbiological, and sometimes accurate bacteriological reports. The most important factor in the planet's wellbeing report card is the quality and quantity of potable water reserves: partial accessibility, patchy distribution, and rising contamination levels are growing concerns aggravated by booming world population, increased use per capita, water mismanagement and the lowering of water aquifers due to unnecessary removal.

Ruhela [1], declared that fresh surface water is routinely restocked by rainfall, but added that the one factor that most determines the availability of good and sufficient fresh water supply is the ever-increasing population. In Malaysia, Wong [2] highlighted that in November and December, during the North-East Monsoon, Malaysia received the maximum rainfall for the year. The difference in temperatures in certain places, for example cold temperatures in central Asia, will result in a change in atmospheric pressure that causes strong winds and heavy rainfall on the east coast of peninsular Malaysia near the South China Sea. The maximum average rainfall recorded in one month is 314 mm in December, which represented 14 percent of the average rainfall for one year. This proves that Malaysia is blessed by a sufficient, accessible supply of fresh water.

Rainwater harvesting is a process for inducing, collecting, storing, and conserving local surface run off water for various purposes such as drinking, washing, and irrigation. There are 3 types of surfaces that allow the process of harvesting rainwater: rooftops, water bodies, and storm drains [3]. Several factors that need to be considered before implementing water harvesting are rainfall intensity and distribution, the type of soil and the depth of soil, water resources, infrastructure and socio-economic conditions, environmental and ecological impacts, and the terrain and topography profile [4].

Water quality, on the other hand, generally refers to the characteristics and condition of water according to certain units of measurement. Water is divided into a few classes based on its usage and it can be determined to be good and safe for use if it meets the minimum requirements set by the Department of Environment (DOE) of Malaysia.

In Malaysia for instance, water harvesting can fulfill two purposes: to stockpile surplus water owing to rain and to supplement established water sources, usually during periods of water deficiency [2]. During droughts, water harvesting is vital to meet domestic water requirements for human use. Whether rainwater harvesting technology is used as the source of non-potable or potable water, it can be managed to supplement existing sources. In addition, the fast expansion of population is another factor aggravating water shortages. A sluggish economy paired with water scarcity causes the need for potable or non-potable water for drinking and sanitation to proportionally increase.

There are a few treatments that can be used to treat the rainwater harvested from the roofs, such as filtration and UV treatment [6]. *Moringa oleifera* seeds can be used as a disinfectant that can remove microbes in water and act as a coagulant [7]. The main objective of this study is to estimate the volume of rainwater that can be harvested from the roof of one building (E0) at the Faculty of Engineering, IIUM over the course of one year. An additional aim is to analyze and characterize the harvested rainwater in terms of BOD, COD, pH, TSS, turbidity and microbial count to determine its suitable application or usage.

### 1.1 Present Rainwater Harvesting (RWH)

RWH consists of rainwater collection from large surfaces, mainly rooftops [8,9,10], and storage of the water under or above ground in reservoirs. Based on the water quality, which is mainly affected by the quality and state of the water collection surfaces and the delivery systems, the water can be used for drinking, domestic uses, and irrigation. RWH is a renewable source of clean water that is ideal for domestic and small scale agricultural uses and the greater attraction of a rainwater harvesting system is its low cost, accessibility, and simple maintenance at the household level [11]. RWH can promote significant water saving in residences in different countries. For an example, in Germany, Herrmann [12] reported that a potential saving of potable water in a house might vary from 30% to 60%, depending on the demand and size of the rainwater collection area. In Newcastle, Australia, RWH would save 60% of potable water [13] and in Brazil, Ghisi [14] concluded that a potential water saving by using water harvesting was in the range of 34% to 92%, with an average of 69%. Abdulla [11] indicated a potential water saving of up to 20% of drinking water by applying RWH at urban environment in Jordan.

### 1.2 Water Quality Analysis

Water from any source, whether harnessed or harvested from ground water or rainwater, has its own quality. Therefore, it is important to begin by analyzing the water's quality before it can be used for drinking or for irrigation. There are many variables that make up the water quality analysis such as the total suspended solid, the chemicals present, and the oxygen demand of the water tested. It is important to determine the water quality so that a proper water treatment process can be carried out to fulfill the specific water quality requirement for a specific usage. These requirements have been set by either the Department of the Environment (DOE) or Ministry of Health (MOH) in Malaysia. In Malaysia, Juhair et al [15] asserted that, according to Malaysia's DOE (1997), there are six variables that need to be included in water quality data to develop a Water Quality Index. These six variables are dissolved oxygen (DO), biochemical oxygen demand (BOD), chemical oxygen demand (COD), suspended solids (SS), ammonical nitrogen (AN) and pH. The standard

requirement of the DOE for different types of water class is shown in Table 1 and the applications allowed for each class are shown in Table 2.

Table 1: DOE Water Quality Index Classification\*

Parameter	Unit	Class				
		I	II	III	IV	V
<b>Ammonical nitrogen</b>	mg/l	< 0.1	0.1 – 0.3	0.3 – 0.9	0.9 – 2.7	> 2.7
<b>Biochemical oxygen demand</b>	mg/l	< 1	1 – 3	3 – 6	6 – 12	> 12
<b>Chemical oxygen demand</b>	mg/l	< 10	10 -25	25 – 50	50 – 100	> 100
<b>Dissolved oxygen</b>	mg/l	> 7	5 – 7	3 – 5	1 – 3	< 1
<b>pH</b>		> 7	6 – 7	5 – 6	< 5	> 5
<b>Total suspended solid</b>	mg/l	< 25	25 - 50	50 - 150	150-300	> 300

(\* adapted from the National Water Quality Standards)

Table 1: DOE Water Quality Index Classification\*

CLASS	USES
<b>Class I</b>	Conservation of natural environment. Water Supply I - Practically no treatment necessary. Fishery I - Very sensitive aquatic species.
<b>Class IIA</b>	Water Supply II - Conventional treatment. Fishery II - Sensitive aquatic species.
<b>Class IIB</b>	Recreational use body contact.
<b>Class III</b>	Water Supply III - Extensive treatment required. Fishery III - Common, of economic value and tolerant species; livestock drinking.
<b>Class IV</b>	Irrigation
<b>Class V</b>	None of the above.

(\* adapted from the National Water Quality Standards)

## 2. MATERIALS AND METHODS

This study was conducted in three parts according to the objectives of the project. The E0 building in the Faculty of Engineering was set as the study area where the rainwater was harvested. A high density polyethylene (HDPE) tank with down pipes and conveyance pipes, depending on the site assessment and calculation of water demand, were installed in the E0 building to collect and store the harvested rainwater.

### 2.1 Preparation of Water Storage Tank

Fresh rainwater was the main raw material for this study and it was collected from the roof of IIUM's Faculty of Engineering Building (E0). A downpipe which connected with gutter of the roof was chosen to install a high density polyethylene (HDPE) tank for the rainwater storage. Figure 1 shows the location of the rainwater harvest at IIUM.



Fig. 1: The study area (adapted from <https://www.google.com.my/maps>).

A downpipe (Fig. 2) that connected with the gutter of the roof was used to harvest the rainwater. An HDPE tank holding roughly 80 gallons was purchased together with 3 inch polyvinyl chloride (PVC) lay-flat flexible water hose pipe for the installation of the tank. The tank was installed with a PVC water tap to collect the samples in the E0 building near the staff parking area.

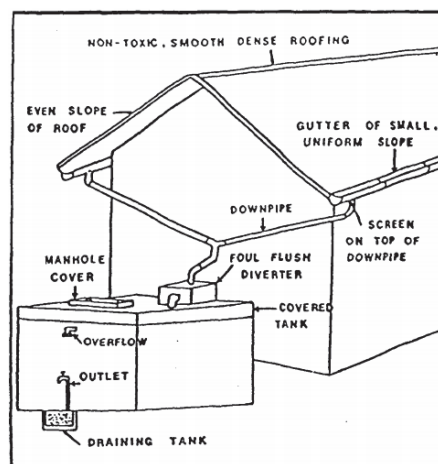


Fig. 2: Roof rainwater harvesting system.

## 2.2 Estimation of the Rainwater Quantity

The external length and width of the E0 building beneath the roof were measured, and divided into several individual rectangles. The tank was designed to meet the necessary water demand throughout the dry season. Eq. (1) was used to obtain the required storage capacity:

$$\text{Required storage capacity} = \text{demand} \times \text{dry period} \quad (1)$$

The average volume of rainwater collected in an hour of rain was calculated based on Eq. (2).

$$V_R = I \times H_{ra} \times C \quad (2)$$

Where

$V_R$  = amount of water that can be harvested ( $m^3$ );  $I$  = rainfall intensity (mm);  $H_{ra}$  = catchment area ( $m^2$ );  $C$  = runoff coefficient.

The volume of rainfall that can be harvested from IIUM was estimated using Eq. (1). Eq. (2) can be interpreted as the volume of rainfall that can be harvested per hour and is based on the area of catchment, the rainfall intensity, and the runoff coefficient. Since this study focused specifically on rainwater harvesting by roof catchment, the data for the surface area of the roof at Faculty of Engineering E0 building and the entire roof of IIUM were obtained from the Development Division of IIUM (Table 3).

Table 3: Total surface area of roof in IIUM

Location	Surface Area of the Roof ( $m^2$ )
Faculty of Engineering	19,302
IIUM (Gombak Campus)	
All Faculties, Mahallah's and Other Buildings in IIUM	726,986

The runoff coefficient was determined from the roof's material. Different types of material used for the roof will have different runoff coefficients. Table 4 shows the runoff coefficient for the roof catchment area. Based on Table 4, the runoff coefficient for roof in IIUM was set to 0.80 since it is made of tiles.

Table 4: The runoff coefficient for roof catchment (UNEP, 2009)

Roof's Material	Runoff Coefficients
Tiles	0.8 – 0.9
Corrugated metal sheets	0.7 – 0.9

The rainfall intensity data was obtained from the on-line hydrological data from the Department of Irrigation and Drainage Malaysia for Klang Gate Dam area. From the cumulative rainfall data, the average rainfall intensity in a month is between 100-200 mm/hour taken in December as the reference. Figure 3 illustrates the hyetograph obtained for cumulative rainfall per hour for a period of a month.

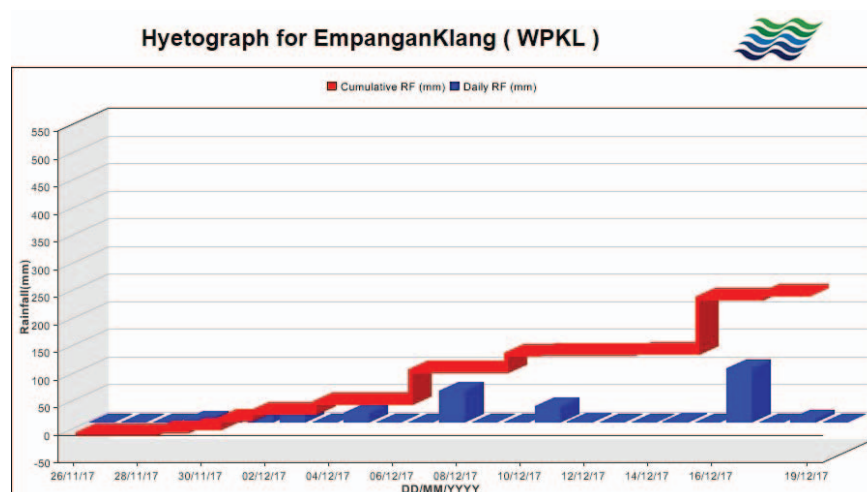


Fig. 3: Hyetograph of rainfall in Klang Gate Dam station (obtained from <http://infobanjir.water.gov.my>).

### 2.3 Sample Collection and Analysis

Samples were taken from a downpipe in the E0 building for every 5 minutes of rainfall over a 30-minute period. The samples were analyzed according to the parameters selected (BOD, COD, pH, TSS, turbidity and microbial count). The BOD and COD test were conducted according to the standard operating procedure by the American Public Health Association (APHA). The concentration of COD in the water was analyzed using a spectrophotometer at the 600 nm wavelength. In addition, digestion solution and sulfuric acid reagent were prepared prior to the COD analysis. The sample's pH and turbidity were both analyzed by HACH pH meter and turbidity meter. Microbial count was measured by incubating the 100 µl samples in nutrient agar for 48 hours at 37°C.

### 2.4 Preparation of *Moringa oleifera* Seeds

Dry seeds of *Moringa oleifera* were bought from a local supplier before the wings and coat of the seeds were separated manually. The seeds were grounded into powder form using a domestic blender and sieved through a 210 µm sieve. The powdered form of *Moringa oleifera* seeds was defatted using a Soxhlet extractor. About 10 g of powdered seeds was placed in the thimbles and 170 ml of hexane was poured into the thimbles as well as the solvent. It was run for 90 minutes and the powdered seeds in the thimbles were dried and weighed. The defatted powder was added into a beaker containing 1000 ml of distilled water. The solution was mixed using a stirrer at 85 rpm for different periods of mixing time set for experiment optimization [16].

#### 2.4.1 Optimization of Disinfectant Preparation

The disinfectant preparation procedure was optimized based on two factors, the dosage of powdered seed (mg/ml) and the mixing time. The mixing speed was fixed at 85 rpm. Design Expert software was used for experimental design and statistical analysis using a Response Surface Methodology (RSM). The percentage of bacterial removal was set as the response of this study. The dosage of seeds in the beaker was varied from 2.75 mg/ml to 3.75 mg/ml while the mixing time was varied from 21 minutes to 41 minutes [16].

#### 2.4.2 Treatment of Rainwater Using *Moringa oleifera*

In each optimization run, 1 ml of *Moringa oleifera* extracts was added into 10 ml of rainwater sample. A blank sample was prepared as the control by adding 10 ml of rainwater without any disinfectant. The mixture was mixed and incubated without agitation for 2 hours. Each sample was diluted with distilled water before it was pipetted onto the agar in a petri dish. It was then incubated at 37 °C for 48 hours. The bacterial count was calculated and the data of each run was compared with the control.

## 3. RESULTS AND DISCUSSION

### 3.1 Estimation of Rainfall Quantity

The volume of rainfall that can be harvested at IIUM was estimated using Eq. (1). The equation stated that the volume of rainfall that can be harvested per hour is calculated based on the area of catchment, the rainfall intensity and the runoff coefficient. The study was done specifically on rainwater harvesting by roof catchment, thus, the data for the surface area of the roof in the Faculty of Engineering and the entire IIUM roof was obtained. The estimated volume of rainwater that can be harvested in the Faculty of Engineering and the entire IIUM (Gombak campus) is 37000 m<sup>3</sup> per year and 1395 × 10<sup>3</sup> m<sup>3</sup> per year, respectively. The result was in line with a study carried out in Sarawak that reported that water demand for their study was 4.32 m<sup>3</sup> per day.

### 3.2 Water Quality Analysis

The BOD obtained was in the range of 2.0 – 3.2 mg/l. Contamination that occurred on the roof and along the downpipe by elements such as dried leaves, dead animals, or animal waste, contributed to the high BOD. This is due to the consumption of dissolved oxygen in the water by the bacteria that degrade these contaminants. It may also be due to the contamination occurring along the downpipe being flushed exponentially in the first few minutes of rainfall.

The concentration of COD was in the range of 22.5 – 42.5 mg/l. Since IIUM is located near the Karak Highway, pollutants from the vehicles contribute to the high concentration of COD as well as chemicals from bird droppings and chemicals from the roof itself. The amount of TSS is contributed from the impurities that formed on the catchment roof and along the downpipe to the rainwater harvesting tank. The average concentration of TSS in the rainwater collected was 20 mg/l. The readings of concentration of TSS for every five minutes of samples were quite similar and since there are not many impurities in the rainwater harvested, the concentration of TSS is low. Figure 4 shows the concentration of BOD, COD, and TSS in the rainwater against the times of sampling.

The pH of the rainwater harvested in IIUM was in the range of 5.9 – 6.5. The pH value changed after a few minutes of rainfall where a low pH value was recorded in the first 10 minutes. The result indicates the rainwater is acidic in the early minutes of rainfall. This is because the first flush of rainfall carries the trapped carbon dioxide gas from vehicle activities as well as other gases in the air [4]. The average turbidity of rainwater was rather low, in which the highest recorded turbidity for harvested rainwater was 11.21 NTU. The low turbidity indicates that the clarity of rainwater is high since there are less particles or matter suspended in the water [1]. Microbial count was performed with the aim to determine the existence of microbial matter in the harvested rainwater. The recorded microbial count in 1 ml of water sample is in the range of 200 – 260 colony-forming units (CFU). This is the result of two major contamination sources: animals and the environment of the catchment area itself. These include the waste produced by birds or animals and dead organisms [6].

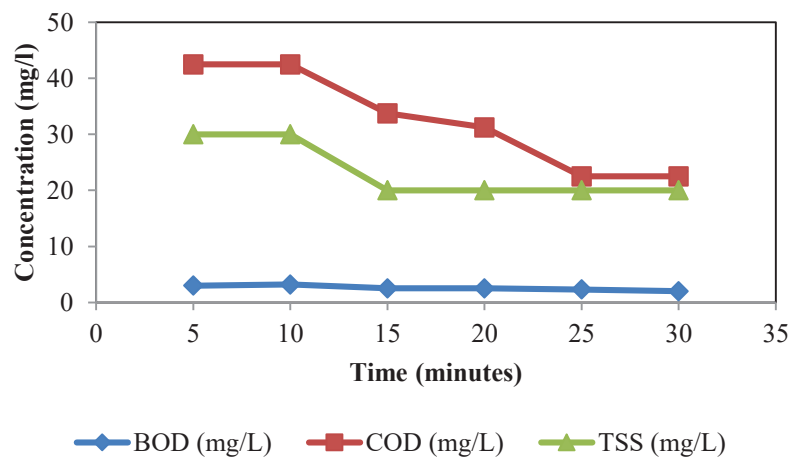


Fig. 4: The graph of water quality against time.

### 3.3 Optimization of Disinfectant Preparation

The optimization was done for the preparation of the disinfectant by using Design Expert 6.0.8. Two factors were tested by using Central Composite Design (CCD) under RSM. The aim of the optimization is to obtain the highest percentage of microbial removal



by varying the mixing time and the dosage use in the preparation of disinfectant. A total of 10 runs with two central points were set for the experiment, as shown in Table 5.

Table 5: Experimental design for optimization

Run	Mixing time (min)	Dosage (mg/ml)	Microbial removal (%)
1	21	3.25	65.9
2	41	3.25	59.5
3	31	2.75	65.4
4	41	3.75	65.4
5	31	3.75	66.8
6	31	3.25	65.9
7	21	3.75	67.3
8	21	2.75	77.1
9	41	2.75	54.1
10	31	3.25	66.3

From the data obtained, ANOVA was used to represent the relationship between the parameters and the response as well as the effect of individual parameters. The final equation obtained from ANOVA is as in Eq. (3):

$$\text{Microbial Removal (\%)} = + 65.37 - 5.22A + 0.48B + 5.28AB \quad (3)$$

Where, A and B are the mixing time (in minutes) and the dosage (mg/ml), respectively. The model is significant, as the Model *F-Value* was 18.23. Furthermore, the value of *Prob > F* was less than 0.05, thus proving the model was significant. The R-squared for the model was 0.9011, which means that 90.11% of total variation in microbial removal is attributed to the experimental value. Figure 5 shows the effect of both mixing time and dosage during the preparation of *Moringa oleifera* as disinfectant on the microbial removal during treatment of rainwater. De-fatted powdered seeds of *Moringa oleifera* at 2.75 g/liter of distilled water and 21 minutes of mixing time was able to achieve the best percentage of microbial removal of 75.38%. According to Suarez [17], around 2 mg/ml of *Moringa oleifera* used had the highest inhibition, which is acceptable.

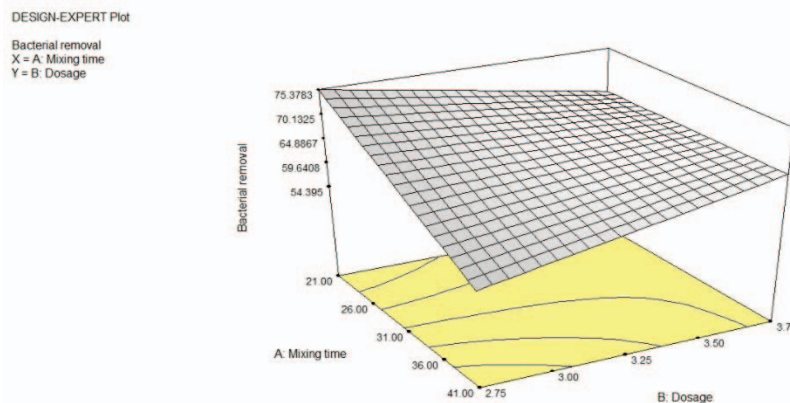


Fig. 5: Effect of mixing time and dosage on microbial removal in 3-D.

#### 4. CONCLUSION

In this study, the three main objectives were to estimate the volume of rainwater that can be harvested in a year, to characterize the rainwater harvested, and to treat the rainwater using *Moringa oleifera*. The volume of rainwater that can be harvested from the roof at

IIUM is  $1395 \times 10^3 \text{ m}^3$  per year. Analysis done on BOD, COD, pH, TSS, turbidity, and microbial count indicates that the rainwater complies with the Class III standard in the water quality index set by the DOE. The rainwater harvested from the rooftop is non-potable and is not safe to consume as drinking water but it is suitable to be used for gardening, flushing, or cleaning processes. From the data obtained, the quality of rainwater harvested from the rooftop improved as the time increased. This proved the importance of having a first-flush concept on the rainwater harvesting system. The treatment process using *Moringa oleifera* as disinfectant improved the quality of the rainwater in terms of removing some of the microbial component. An amount of 2.75 mg/ml of seeds dissolved and mixed with distilled water at 85 rpm for 21 minutes is the optimum parameter to prepare the disinfectant. Harvested rainwater in KOE-IIUM still needs another type of treatment to improve and utilize the water for more than cleaning and flushing.

From the study conducted, there are a few recommendations that could be made for further study. First, analyze and compare the quality of the rainwater harvested from roof catchment and harvested directly from the sky by prepare an open tank to collect the rainwater. Furthermore, install a first-flush device along the downpipe so that the quality of the rainwater store in the tank is improved.

## REFERENCES

- [1] Ruhela, M., Bhutiani, R., & Anand, A. (2004) Rain water harvesting. Journal-Geological Society of India, 85(9): 1259-1261. Retrieved from [http://www.currentscience.ac.in/cs/Downloads/article\\_id\\_085\\_09\\_1259\\_1261\\_0.pdf](http://www.currentscience.ac.in/cs/Downloads/article_id_085_09_1259_1261_0.pdf).
- [2] Wong, C. L., Venneker, R., Uhlenbrook, S., Jamil, a. B. M., & Zhou, Y. (2009) Variability of rainfall in Peninsular Malaysia. Hydrology and Earth System Sciences Discussions, 6(4): 5471–5503. <https://doi.org/10.5194/hessd-6-5471-2009>.
- [3] Prinz, D., & Singh, A. (2000) Technological potential for improvements of water harvesting. Gutachten Für Die World Commission on Dams, Retrieved from [http://web.stanford.edu/~cbauburn/basecamp/dschool/homeproject/water\\_harvesting\\_improvements\\_technology.pdf](http://web.stanford.edu/~cbauburn/basecamp/dschool/homeproject/water_harvesting_improvements_technology.pdf).
- [4] Evans, C. A., Coombes, P. J., & Dunstan, R. H. (2006) Wind, rain and bacteria: The effect of weather on the microbial composition of roof-harvested rainwater. Water Research, 40(1): 37–44. <https://doi.org/10.1016/j.watres.2005.10.034>.
- [5] Boers, T. M., & Ben-Asher, J. (1982) A review of rainwater harvesting. Agricultural Water Management, 5(2): 145–158. [https://doi.org/10.1016/0378-3774\(82\)90003-8](https://doi.org/10.1016/0378-3774(82)90003-8).
- [6] Despina, C., Farahbakhsh, K., & Leidl, C. (2009) Assessment of rainwater quality from rainwater harvesting systems in Ontario, Canada. Journal of Water Supply: Research and Technology - AQUA, 58(2): 117–134. <https://doi.org/10.2166/aqua.2009.013>.
- [7] Bichi, M. H., Agunwamba, J. C., & Muyibi, S. A. (2012) Optimization of operating conditions for the application of *Moringa oleifera* (Zogale) seeds extract in water disinfection using response surface methodology, 11(92): 15875–15887. <https://doi.org/10.5897/AJB12.1341>.
- [8] Liaw, C. H., & Chiang, Y. C. (2014) Dimensionless analysis for designing domestic rainwater harvesting systems at the regional level in Northern Taiwan. Water (Switzerland), 6(12): 3913–3933. <https://doi.org/10.3390/w6123913>.
- [9] Sharma, A.K., Begbie, D. and Gardner, T. (2015) Rainwater Tank Systems for Urban Water Supply: Design, Yield, Energy, Health Risks, Economics and Social Perceptions. IWA Publishing, London.
- [10] Charters, F. J., Cochrane, T. A., & O’Sullivan, A. D. (2016) Untreated runoff quality from roof and road surfaces in a low intensity rainfall climate. Science of the Total Environment, 550: 265–272. <https://doi.org/10.1016/j.scitotenv.2016.01.093>.

- 
- [11] Fayez Abdulla & A.W. Al-Shareef. (2009) Roof Rainwater Harvesting Systems for Household Water Supply in Jordan. *Desalination*. 243(1-3):195-207. <https://doi.org/10.1016/j.desal.2008.05.013>
- [12] Herrmann T, Schmida U. (2000) Rainwater utilization in Germany: efficiency, dimensioning, hydraulic and environmental aspects. *Urban Water*, 1(4): 307-316.
- [13] Cook, S., Sharma, A. and Chong, M. (2013) Performance Analysis of a Communal Residential Rainwater System for Potable Supply: A Case Study in Brisbane, Australia. *Water Resources Management*, 27: 4865-487.
- [14] Ghisi E. (2006) Potential for potable water savings by using rainwater in the residential sector of Brazil. *Building and Environment*, 41(11): 1654-1666.
- [15] Juahir, H., Zain, S. M., Yusoff, M. K., Hanidza, T. I. T., Armi, A. S. M., Toriman, M. E., & Mokhtar, M. (2011) Spatial water quality assessment of Langat River Basin (Malaysia) using environmetric techniques. *Environmental Monitoring and Assessment*, 173(1-4): 625-641.
- [16] Bichi, M. H., Agunwamba, J. C., & Muyibi, S. A. (2012) Optimization of operating conditions for the application of *Moringa oleifera* (Zogale ) seeds extract in water disinfection using response surface methodology, 11(92): 15875-15887. <https://doi.org/10.5897/AJB12.1341>.
- [17] Suarez M, Entenza J, Doerries C, Meyer E, Bourquin L, Sutherland J, Marison I, Moreillon P, Mermod N (2003) Expression of a plant-derived peptide harboring water-cleaning and antimicrobial activities. *Biotech Bioeng* 81(15):13-20. Retrieved from [https://www.researchgate.net/publication/237077424\\_Genetic\\_diversity\\_and\\_population\\_structure\\_of\\_Moringa\\_oleifera](https://www.researchgate.net/publication/237077424_Genetic_diversity_and_population_structure_of_Moringa_oleifera)

## INVESTIGATION OF MAGNETIC PROPERTIES FOR DIFFERENT COIL SIZES OF DYNAMIC WIRELESS CHARGING PADS FOR ELECTRIC VEHICLES (EV)

SYASYA AZRA ZAINI, SITI HAJAR YUSOFF\*, AMIRA AZIERA ABDULLAH,  
SHEROZ KHAN, FARIDAH ABD RAHMAN AND NADIA NAZIEHA NANDA

*Department of Electrical and Computer Engineering, Faculty of Engineering,  
International Islamic University Malaysia,  
P.O Box 10, 50728 Kuala Lumpur, Malaysia*

*\*Corresponding author: sityusoff@iium.edu.my*

*(Received: 14<sup>th</sup> March 2019; Accepted: 22<sup>nd</sup> October 2019; Published on-line: 20<sup>th</sup> January 2020)*

**ABSTRACT:** Electric vehicles (EV) have been introduced in the recent years due to public awareness of the effect of gas emission from traditional cars and the extinction of petroleum natural resources. For charging EV, dynamic wireless charging is considered in this paper. This is because it is more convenient and saves charging time since it charges the electric vehicle while moving. The main challenge of this process is to maintain a high amount of power transfer from primary to secondary coil. One of the factors contributing to a good power transfer is the size of the coil [1]. There are various designs of coil for wireless charging of electric vehicles (EV). Among the most common designs are circular pad (CP), rectangular pad (RP), double-D pad (DDP), and double-D quadrature pad (DDQP). In this paper, circular pad (CP) is chosen for use, due to its simplicity in design and good electrical and magnetic properties. Three different coil pair sizes are tested to find the most suitable coil pair for the primary and secondary pads that has the maximum power transfer and is least sensitive to misalignment. The magnetic properties have been investigated to obtain the highest value of magnetic flux. The geometry design of the pads and simulation was done using COMSOL Multiphysics software. From the simulation, it was found that the unsymmetrical coil pair gives high magnetic strength when the outer diameters of the primary and secondary coils have the same value.

**ABSTRAK:** Kendaraan Elektrik (EV) telah diperkenalkan sejak beberapa tahun ini hasil kesedaran awam tentang kesan pembebasan gas dari kenderaan lama dan pengurangan sumber asli petroleum. Kajian ini berkaitan pengecas dinamik tanpa wayar bagi mengecas EV. Ini kerana pengecas ini lebih sesuai dan jimat masa mengecas kerana kenderaan elektrik dicas ketika bergerak. Cabaran utama proses ini adalah mengekalkan pemindahan tenaga yang tinggi daripada gegelung primer kepada gegelung sekunder. Salah satu faktor bagi mendapatkan pemindahan tenaga yang tinggi adalah saiz gegelung wayar [1]. Terdapat pelbagai bentuk gegelung bagi mengecas kenderaan elektrik (EV) tanpa wayar. Antaranya adalah pad membulat (CP), pad segiempat tepat (RP), pad berganda-D (DDP), dan pad kuadratur berganda-D (DDQP). Kajian ini telah menggunakan pad membulat (CP) kerana reka bentuknya yang ringkas dan ia mempunyai sifat elektrik dan magnetik yang baik. Tiga pasang gegelung berbeza telah diuji bagi mendapatkan pasangan gegelung pad primer dan sekunder yang paling sesuai di mana ianya mempunyai pemindahan tenaga maksima dan paling kurang sensitif pada ketidakjajaran. Sifat magnet telah diuji bagi mendapatkan nilai fluks magnet tertinggi. Rekabentuk geometri pad dan simulasi telah dijalankan menggunakan perisian Multifizik COMSOL. Hasil simulasi mendapati pasangan gegelung yang tidak simetri telah menghasilkan kekuatan magnetik tertinggi apabila diameter luaran gegelung primer dan sekunder mempunyai nilai sama.

**KEYWORDS:** electric vehicle (EV); magnetic properties; wireless power transfer; inductive charging; circular coil

## 1. INTRODUCTION

Electric vehicles (EV) have been introduced in 2012 due to public awareness of the effect of gas emission from traditional cars and the extinction of petroleum natural resources [2]. Malaysia's government also supports electric vehicles by offering full exemption of tax for EV. Besides, the fact that EV and plug-in hybrid EV produce smaller carbon dioxide (CO<sub>2</sub>) than traditional vehicles and lower the cost of ownership over lifetimes has attracted manufacturers and researchers alike to study more about this topic [3]. In developed countries, EV sales are rising rapidly due to their advantages.

In wireless charging systems, several components are needed to ensure that power is transferred efficiently from the grid to the car battery, as shown in Fig. 1. The wireless charging process will begin from the DC input, which is the main source power. Then, the DC power will pass through an inverter and compensation to convert it from DC to AC power. For wireless charging, the transmitter coil and receiver coil are used as a medium to transmit and receive power using an air gap channel. After that, the received power will go through the same process with the help of a converter before reaching the car battery. Many types of converter can be used, such as AC/AC matrix converters [4,5], T-type direct converters, and many more.

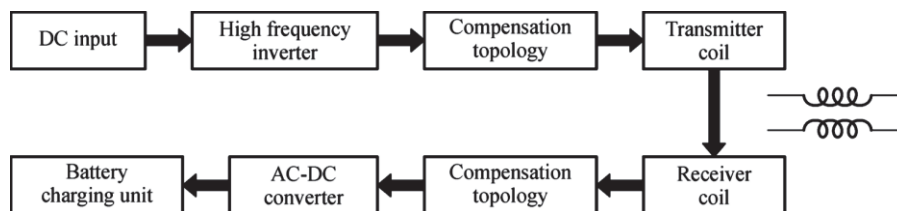


Fig. 1: Basic block diagram of wireless charging EV system [6].

There are various designs of coil for the wireless charging of electric vehicles (EV). Among the most common design are circular pad (CP), rectangular pad (RP), double-D pad (DDP), and double-D quadrature pad (DDQP) [7,8]. Each of the pad designs has its own benefit for its specific requirements and applications. Among the designs are:

### a) Circular Pad (CP)

Circular pad design is the most widely used due to its simplicity in design and manufacturing [9]. Besides that, CP design also has good electrical and magnetic properties to transfer power efficiently [10]. In terms of misalignment, CP design has the same tolerance in all directions [8] due to its circular shape. However, researchers are still trying to reduce the misalignment effect in order to improve the performance of wireless charging. Polarized circular pads have mostly been implemented in static EV charging applications [8]. Despite that, CP has a problem with the increasing of the air gap. This is because the diameter of the coil will get four times larger when the air gap increases once. This is due to the 1:4 ratio of the primary flux path and diameter of coil [8,11]. Due to this limitation, other designs of coil were introduced.

b) *Rectangular Pad (RP)*

Rectangular pad (RP) is another basic coil design for wireless charging. It is suitable in dynamic charging due to its cost effectiveness. Besides that, RP is also popular because of its capability to transfer power and its reasonable cost of materials [12]. In order to optimize the power transfer between coils, a ferrite bar has been used and attached to the rectangular coil. Wang et al. tested a variety of lengths of ferrite bar on the rectangular coil in order to improve the coupling coefficient and mutual inductance between two coils [13]. From the simulation, it can be concluded that longer ferrite bars can transfer more power than shorter bars.

c) *Double-D Pad (DDP)*

Besides circular and rectangular pad, Double-D pad (DDP) is also among the popular designs for wireless EV charging. This is due to a better performance and its interoperability with different secondary topologies [7]. Even though DDP has a higher tolerance of misalignment, it only covers the horizontal component. Therefore, the Double-D Quadrature pad (DDQP) was invented to have a high tolerance in both horizontal and vertical components [8]. The DDQP design is a combination of DD pad and rectangular pad (RP). This pad has high misalignment tolerance especially when it is placed at the secondary side [14]. Nonetheless, this design leads to increased costs due to the increase in number of coils. Figure 2 below shows the design of DDP and DDQP coils.

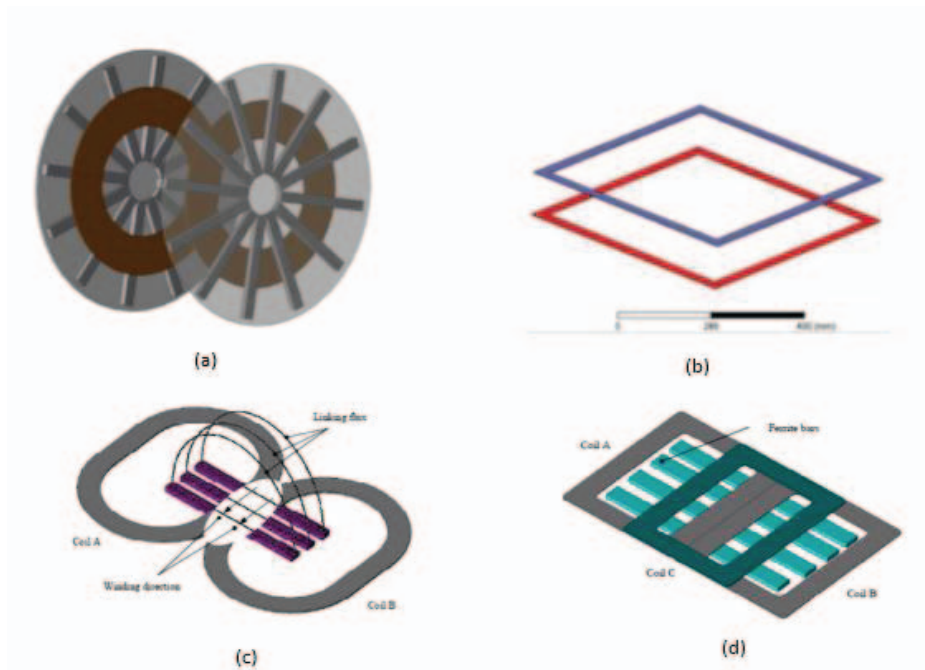


Fig. 2: Different charging pads (a) CP (b) RP (c) DDP (d) DDQP.

Among many pad designs, circular couplers are the most usable because of their magnetic properties [15]. However, different sizes of circular pad would give different performance in terms of magnetic properties. Therefore, this paper would design and discuss different pairs of circular-circular coil pads that give highest magnetic strength between the primary and secondary coils.

This paper is organized as follows: Section II presents the methodology consisting of the design for each coil pair. Then, Section III discussed the simulation results using COMSOL Multiphysics software. Finally, the paper concludes in Section IV.

## 2. METHODOLOGY

In this project, three different circular pairs of coils have been investigated to decide which pair gives the maximum power transfer. The secondary coil, or the receiving side, is set to the same value in all three designs, while the primary, or transmitting side, is varied to compare the effect on power transfer. Proper matching of coil parameters such as the diameter of the primary and secondary coils, distance between two coils, and mutual inductance between them, allow the maximum power transmission through the link. Therefore, this paper proposed the best design for circular coils in order to obtain high magnetic strength. In all coil pairs, ‘P’ represents the primary coil and ‘S’ represents the secondary coil. Detailed explanations about the three different coils will be discussed below.

- a)  $P_1$ -S  
 For this type of coil, the inner diameter as well as the outer diameter of primary coil are kept smaller than the secondary coil.
- b)  $P_2$ -S  
 For this coil-pair, the inner diameter of the primary coil is kept smaller than the inner diameter of the secondary coil and the outer diameter of the primary coil is kept the same as the outer diameter of the secondary coil.
- c)  $P_3$ -S  
 For this type of coil pair, the outer diameter of primary coil is larger than secondary coil and diameter of inner primary coil is less than inner diameter of secondary coil.

Table 1 listed the value parameters that were used in this project. Figure 3 also shows a clear illustration of the three coil pairs designed. The primary coil is placed at the bottom, whereas secondary coil is placed at the top in order to replicate a real EV system. For real EV, the primary coil is attached to the road while the secondary coil attached below the car.

Table 1: Geometry parameters of designed coils

Coil	$D_{out}$ (cm)	$D_{in}$ (cm)
S	28	21.4
$P_1$	24	6
$P_2$	28	12
$P_3$	32	12

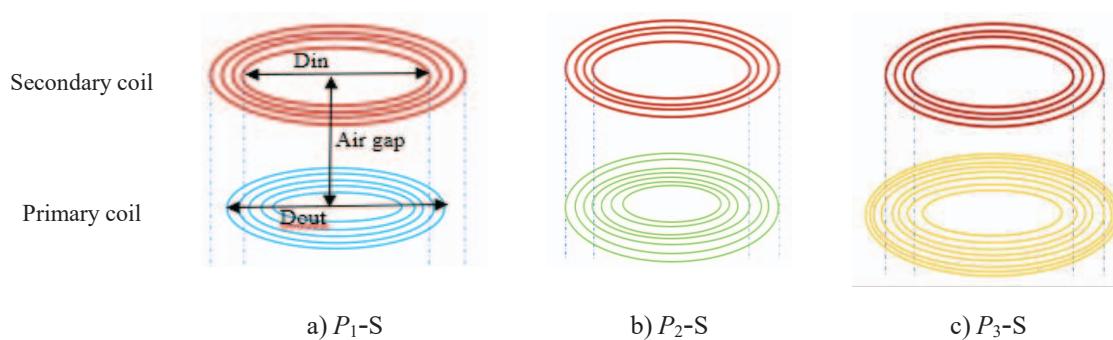


Fig. 3: Different coil pairs.

Figure 4 below shows the primary and secondary coil sketch in COMSOL Multiphysics before running the simulation. The air gap between the primary coil and secondary coil is fixed at 16 cm.

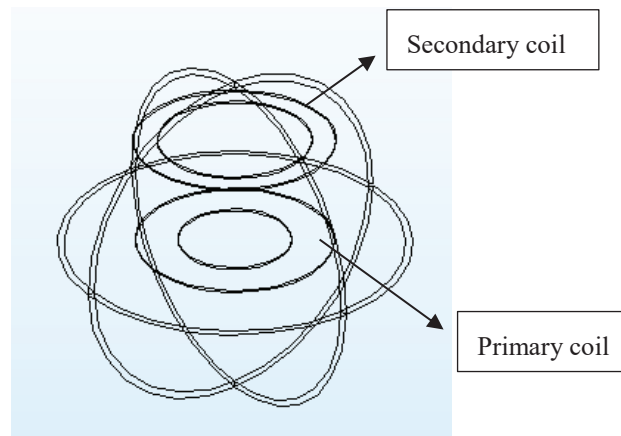


Fig. 4: Primary and secondary coil drawn in COMSOL Multiphysics.

After the simulations for all three pairs were done, another simulation is performed to vary the inner diameter while fixing the outer diameter for the best primary coil. The coil design that gives the highest magnetic field norm and magnetic flux density norm will be simulated again by varying the inner diameter of primary coil in order to find the most suitable parameter for the primary coil.

### 3. SIMULATION RESULTS

There are three designs of coil pair that were tested in the COMSOL Multiphysics software. Each coil has a fixed number of turns,  $N$ , and an air gap with no misalignment condition. The secondary coil is also fixed for all the three tests. The diameter of the secondary coil is chosen based on the best design achieved from Aditya [1]. The diameter of the primary coil is the only varying parameter for this simulation. The simulation results are shown below.

#### 3.1 Magnetic Field Characteristic

In each coil pair, different values of magnetic field have been identified. The figures below show the behaviour of magnetic fields around the coils. The red colour indicates a strong magnetic field while the blue colour indicates the lowest field strength. In each simulation, there is a colour legend that states the maximum and minimum magnetic fields. Different ranges of colour show different values of magnetic field inside the coil.

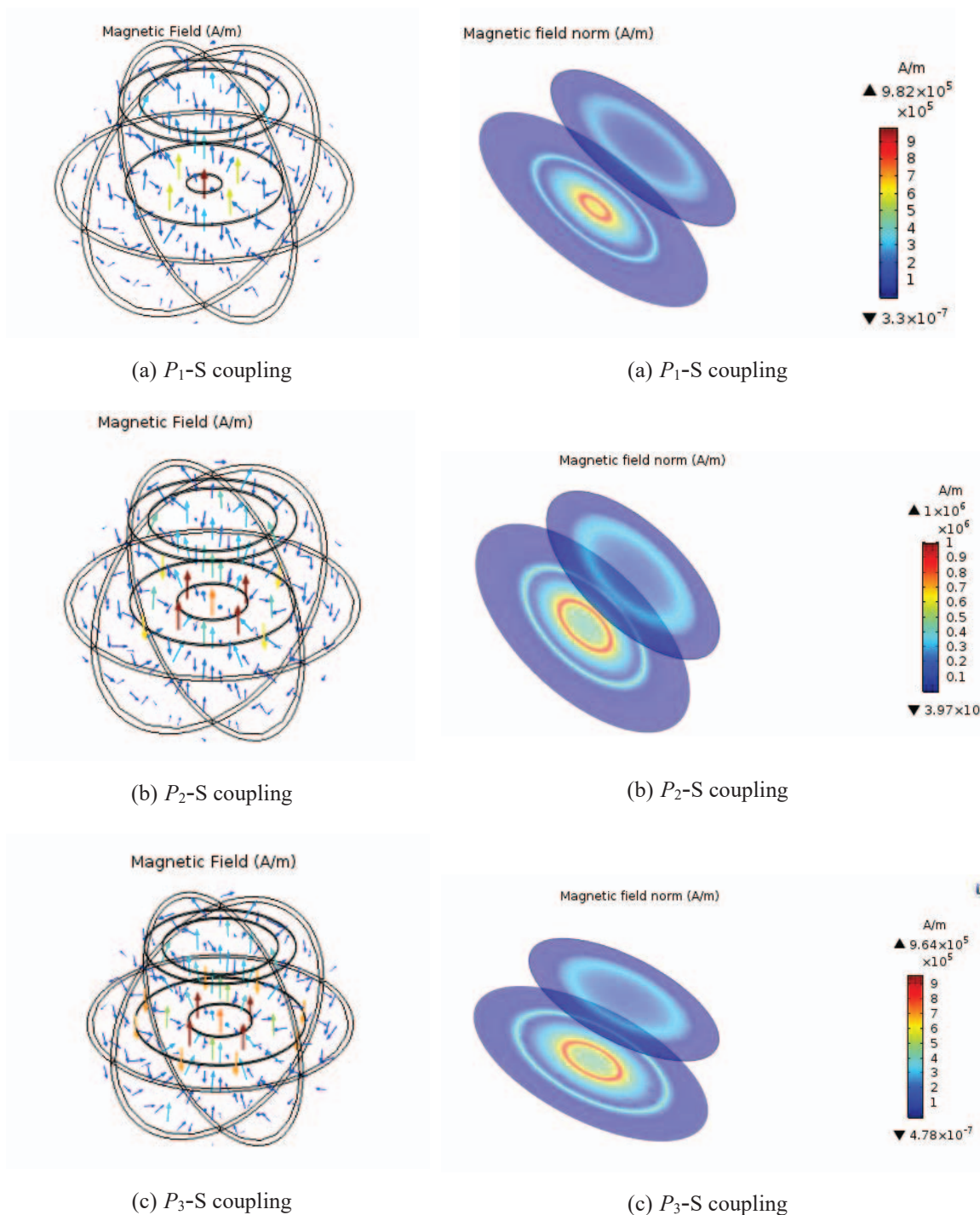
Table 2 shows the magnetic field characteristics for all coil pairs. This simulation is done to observe the behaviour of the magnetic fields between the primary and secondary coils. From the simulation, it can be seen that the behaviour of the magnetic fields is quite similar for all pairs since there are no misalignments involved.

However, table 2 only shows the behaviour of the magnetic fields. In order to know the magnitude of magnetic fields, the magnetic fields norm have been simulated. The maximum normal magnetic field value for the first, second, and third pairs are  $9.82 \times 10^5$  (A/m),  $1.0 \times 10^6$  (A/m) and  $9.64 \times 10^5$  (A/m), respectively. Normal magnetic fields represent the magnitude for the magnetic fields between two coil pairs. Table 3 shows the magnetic field norms for each coil pair.



Table 2: The magnetic field behaviour for each coil pair

Table 3: The magnetic field norms for each coil pair

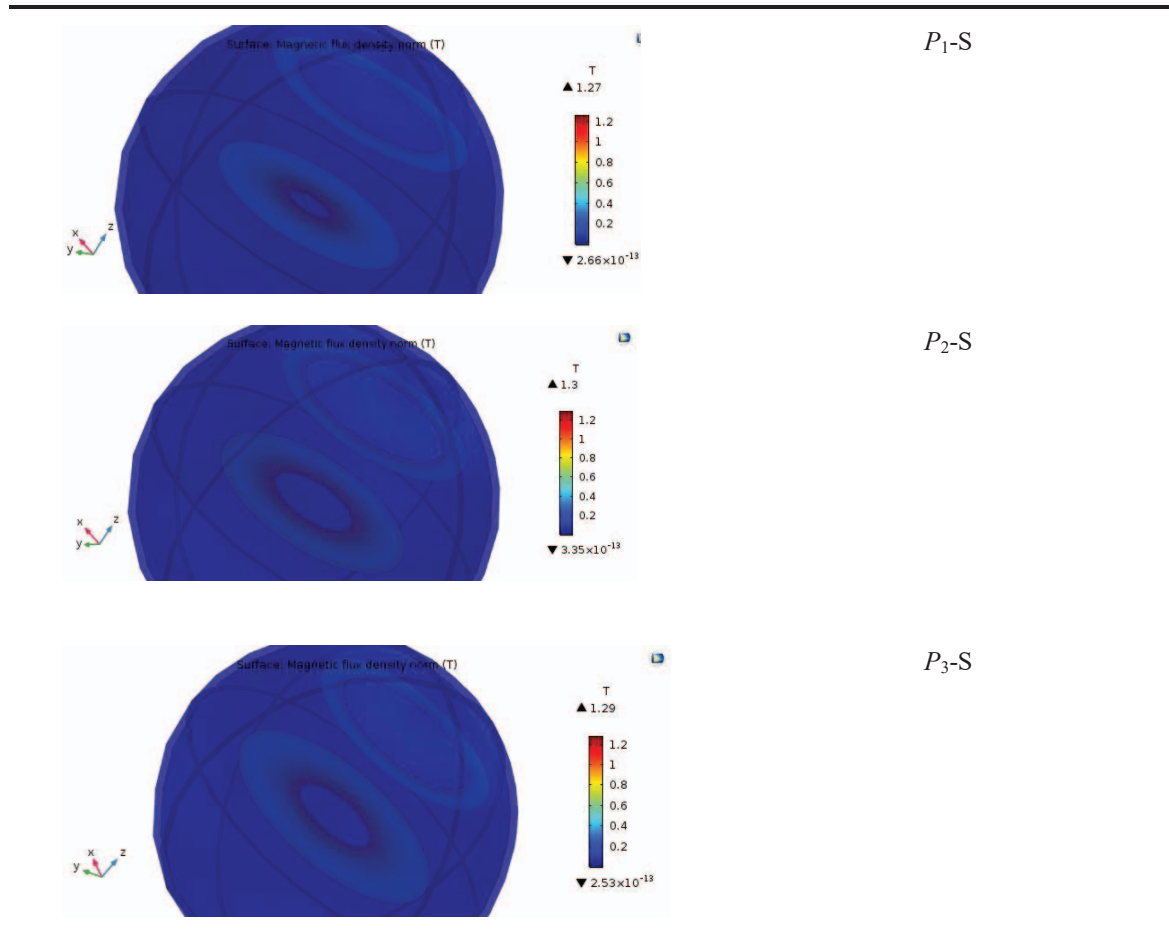


From the table above,  $P_2$ -S gives the highest magnetic field norm with  $1.0 \times 10^6$  A/m. So, high magnetic strength between  $P_2$ -S coils will provide better power transfer between the primary and secondary coils. There is no specific range of magnetic field and magnetic flux density needed for good performance of wireless charging. However, a magnetic field induces electrical charge movement, producing an electric current. Therefore, a high value of magnetic field and magnetic flux density produces more current and thus improves the charging process for the electric vehicle (EV).

### 3.2 Magnetic Flux Density Characteristic

Table 4 below shows the simulation of the magnetic flux density for all three coil pairs. The blue colour around the coil represents the air environment.

Table 4: The magnetic flux density norm for each coil pair



The simulation shows that the  $P_2$ -S coupling pair gives the highest magnetic flux density norm, which is 1.3 T. The strengths of the magnetic flux density norms in descending order are  $P_2 > P_3 > P_1$ . Therefore, the  $P_2$ -S coil pair is chosen for use in EV charging since it has high strength of magnetic field and magnetic flux density norm between the two coils.

### 3.3 Simulations Varying the Inner Diameter of $P_2$ Coils

In the previous simulation,  $P_2$ -S has been proven to provide the highest magnetic field norm and magnetic flux density. Therefore, in this section, the  $P_2$ -S design is further simulated to find the most suitable parameter for the primary coil. The inner diameter for the  $P_2$  coil is varied between 12 cm, 16 cm, and 20 cm while maintaining the outer diameter of 28 cm. Table 5 shows the value of varying the  $P_2$  inner diameter.

Table 6 shows the simulation results for the  $P_2$  coil by varying the inner diameter of the primary coil. The parameter for the coil was shown in Table 1. From the simulation results, it can be seen that the magnetic field behaviour for larger inner diameter of primary coil is higher. It can be seen  $P_{2c}$ -S has more arrows compared to the other two designs.

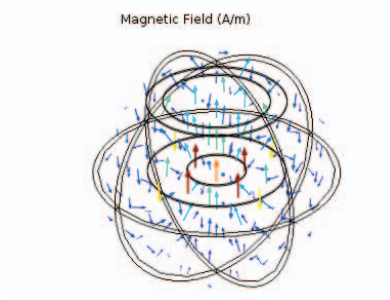
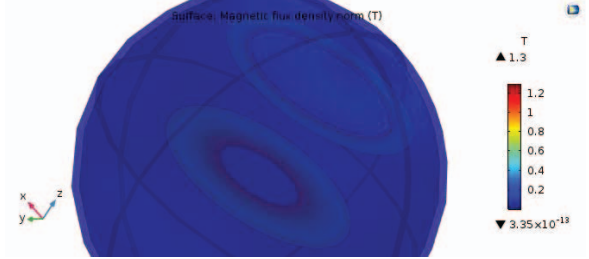
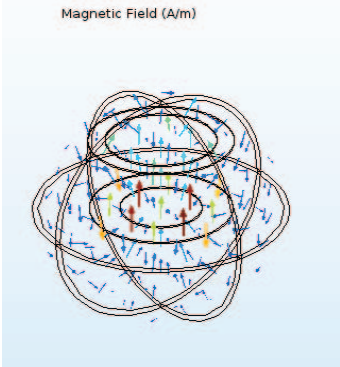
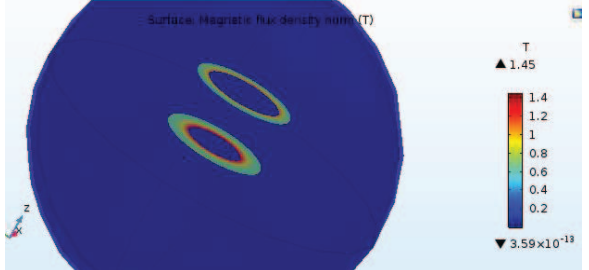
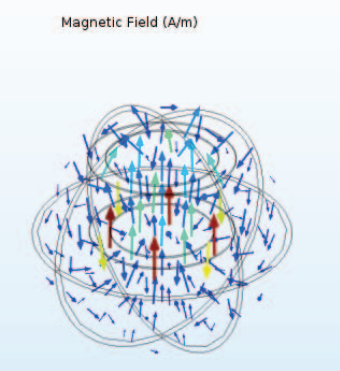
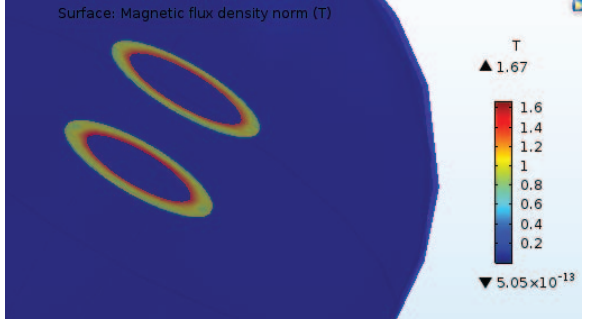
Arrows inside the coil and air region indicate the amount of magnetic field flow between the two coils. The sphere line in this simulation represents the air region.

Furthermore, as the magnetic field arrow increases, the magnetic flux density value also increases. As can be seen from Table 6,  $P_{2c}$ -S has the highest magnetic flux density value of 1.67 T. Therefore,  $P_{2c}$ -S will produce the highest power transfer between primary and secondary coils.

Table 5: Geometry parameters varying the inner diameter for  $P_2$  coils

Coil	$D_{out}$ (cm)	$D_{in}$ (cm)
$S$	28	21.4
$P_{2a}$	28	12
$P_{2b}$	28	16
$P_{2c}$	28	20

Table 6: Simulation results varying the inner diameter for  $P_2$  coils

Coil pair	Magnetic field behaviour	Magnetic flux density
$P_{2a} - S$		
$P_{2b} - S$		
$P_{2c} - S$		

According to the International Commission on Non-Ionizing Radiation Protection (ICNIRP) 2010 guidelines, the reference level for magnetic fields is 27  $\mu\text{T}$  for frequencies between 3 kHz to 10 MHz [16, 17]. However, the value achieved from this simulation is in the range of 1.3 T to 1.67 T and it exceeds the reference level. Therefore, it shows that several improvements need to be done before it can be used by the public. High magnetic flux density is useful to increase the effectiveness of power transfer. But, if the value exceeds the maximum value set by ICNIRP, it might be harmful for the public.

#### 4. CONCLUSION

This paper has successfully investigated the effect of unsymmetrical pad couplers on the magnetic flux density in air environment. Three pairs of unsymmetrical pad couplers were designed and simulated using COMSOL Multiphysics software in order to analyse the magnetic properties for each pair. The primary coil is varied by the diameter of the coil while secondary coil's parameter is kept constant. From the results, similar values of the coil's outer diameter will give a strong magnetic field and magnetic flux density. The simulation done in COMSOL Multiphysics shows that the second coil pair ( $P_2$ -S) that has an outer diameter of 28 cm has the highest magnetic field and magnetic flux density norm, which is  $1.0 \times 10^6$  A/m and 1.3 T, respectively. Another simulation was done to find the best inner diameter of the primary coil ( $P_2$ ). The results show that  $P_{2c}$ -S gives the highest magnetic flux density of 1.67 T. Therefore, high magnetic field and magnetic flux density will provide high power transfer between the primary and secondary coils. Thus, the  $P_{2c}$ -S coil pair is chosen for use in EV wireless charging. However, further research can explore a coil pair that is safe for use by the public and obeys the standards given by ICNIRP.

#### ACKNOWLEDGEMENT

This work was partially supported by Ministry of Higher Education Malaysia (Kementerian Pendidikan Tinggi) under Fundamental Research Grant Scheme (FRGS) number FRGS17-038-0604.

#### REFERENCES

- [1] K. Aditya, V. K. Sood, and S. S. Williamson. (2017) Magnetic characterization of unsymmetrical coil pairs using archimedean spirals for wider misalignment tolerance in ipt systems. *IEEE Transaction on Transportation Electrification*, 3(2): 454–463.
- [2] R. Bosshard and J. W. Kolar. (2016) Inductive Power Transfer for Electric Vehicle Charging. *IEEE Power Electronics Magazine*: 22–30.
- [3] Malaysian Green Technology Corporation "Low Carbon Mobility" [<https://www.greentechmalaysia.my/services/low-carbon-mobility/>]
- [4] S. Yusoff, L. De Lillo, P. Zanchetta, and P. Wheeler. (2012) Predictive Control of a direct AC/AC matrix converter power supply under non-linear load conditions. 15th International Power Electronics and Motion Control Conference Expo. EPE-PEMC 2012 ECCE Europe: 1–6.
- [5] S. Yusoff, L. De Lillo, P. Zanchetta, P. Wheeler, P. Cortés, and J. Rodríguez. (2012) Predictive control of a direct AC/AC matrix converter for power supply applications. 6th IET International Conference on Power Electronics, Machines and Drives (PEMD 2012): A92–A92.
- [6] P. S. R. Nayak and D. Kishan. (2018) Performance analysis of series/parallel and dual side LCC compensation topologies of inductive power transfer for EV battery charging system. *Front. Energy*: 1–14. <https://doi.org/10.1007/s11708-018-0549-z>
- [7] C. Liu, C. Jiang, C. Qiu. (2017) Overview of Coil Designs for Wireless Charging of Electric

- Vehicle. IEEE PELS Workshop on Emerging Technologies: Wireless Power Transfer (WoW): 15–18.
- [8] A. Ahmad, M. S. Alam, S. Member, and R. Chabaan. (2018) A Comprehensive Review of Wireless Charging Technologies for Electric Vehicles. *IEEE Transaction on Transportation Electrification*, 4(1): 38–63.
- [9] M. Mohammad and S. Choi. (2018) Optimization of ferrite core to reduce the core loss in double-D pad of wireless charging system for electric vehicles. *Conference Proceedings - IEEE Applied Power Electronics Conference and Exposition (APEC)*: 1350–1356.
- [10] A. Tejada, C. Carretero, J. T. Boys, and G. A. Covic. (2017) Ferrite-Less Circular Pad with Controlled Flux Cancellation for EV Wireless Charging. *IEEE Transactions on Power Electronics*, 32(11): 8349–8359.
- [11] M. Budhia, G. Covic, and J. Boys. (2010) A new IPT magnetic coupler for electric vehicle charging systems. *IECON Proceedings- Industrial Electronics Conference*: 2487–2492.
- [12] W. Chen, C. Liu, C. H. T. Lee, and Z. Shan. (2016) Cost-effectiveness comparison of coupler designs of wireless power transfer for electric vehicle dynamic charging. *Energies Journal*: 1–13.
- [13] S. Wang, Y. Guo, and D. Dorrell. (2017) Analysis of Rectangular EV Inductive Charging Coupler. *12th IEEE Conference Industrial Electronics and Applications*: 285–291.
- [14] L. Xiang, Y. Sun, Z. Ye, Z. Wang, and S. Zhou. (2016) Combined primary coupler design and control for EV dynamic wireless charging system. *IEEE PELS Workshop on Emerging Technologies: Wireless Power, WoW 2016*: 174–179.
- [15] M. Budhia, S. Member, J. T. Boys, G. A. Covic, and S. Member. (2013) Development of a Single-Sided FluxMagnetic Coupler for Electric Vehicle IPT Charging Systems. *IEEE Transactions on Industrial Electronics*, 60(1): 318–328.
- [16] S. Li and C. C. Mi. (2014) Wireless Power Transfer for Electric Vehicle Applications. *IEEE Journal of Emerging and Selected Topics in Power Electronics*, 3(1): 4–17.
- [17] K. A. Grajski, R. Tseng, and C. Wheatley. (2012) Loosely-Coupled Wireless Power Transfer: Physics, Circuits, Standards. *IEEE MTT-S International*: 9–14.

## STEMMING IMPACT ANALYSIS ON INDONESIAN QURAN TRANSLATION AND THEIR EXEGESIS CLASSIFICATION FOR ONTOLOGY INSTANCES

FANDY SETYO UTOMO<sup>1,2\*</sup>, NANNA SURYANA<sup>2</sup> AND MOHD SANUSI AZMI<sup>2</sup>

<sup>1</sup>Department of Information System, Faculty of Computer Science,  
Universitas AMIKOM Purwokerto, Purwokerto, Indonesia.

<sup>2</sup>Center for Advanced Computing Technology (C-ACT),  
Faculty of Information and Communications Technology,  
Universiti Teknikal Malaysia Melaka, Melaka, Malaysia.

\*Corresponding author: [fandy\\_setyo\\_utomo@amikompurwokerto.ac.id](mailto:fandy_setyo_utomo@amikompurwokerto.ac.id)

(Received: 29<sup>th</sup> May 2019; Accepted: 7<sup>th</sup> October 2019; Published on-line: 20<sup>th</sup> January 2020)

**ABSTRACT:** The current gap that appears in the Quran ontology population domain is stemming impact analysis on Indonesian Quran translation and its exegesis (Tafsir) to develop ontology instances. The existing studies of stemming effect analysis were performed in various languages, datasets, stemming methods, cases, and classifiers. However, there is a lack of literature that studies the stemming influence on instance classification for Quran ontology with different datasets, classifiers, Quran translations, and their exegesis in Indonesian. Based on this problem, our study aims to investigate and analyse the stemming impact on instance classification results using Indonesian Quran translation and their exegesis as datasets with multiple supervised classifiers. Our classification framework consists of text pre-processing, feature extraction, and text classification stage. Sastrawi stemmer was used to perform stemming operation in the text pre-processing stage. Based on our experiment results, it was found that Support Vector Machine (SVM) with Term Frequency-Inverse Document Frequency (TF-IDF) and stemming operation owns the best classification performance, i.e., 70.75% for average accuracy and 71.55% for average precision in Indonesian Quran translation dataset on 20% test data size. While in 30% test data size, SVM and TF-IDF with stemming process own the best classification performance, i.e., 67.30% for average accuracy and 68.10% for average precision in Ministry of Religious Affairs Indonesia dataset. Furthermore, in this study, it was also discovered that the Backpropagation Neural Network has the most precision and accuracy reduction due to the negative impact of stemming operations.

**ABSTRAK:** Jurang semasa yang muncul dalam domain populasi ontologi Quran adalah punca analisis kesan bendungan pada terjemahan Quran Bahasa Indonesia dan Tafsir bagi membangunkan ontologi kata dasar. Kajian lalu terhadap analisis kesan bendungan telah dijalankan dalam pelbagai bahasa, set data, kaedah bendungan, kes dan pengkelasan. Walau bagaimanapun, terdapat kekurangan kesusasteraan yang mengkaji kesan bendungan dalam bidang pengkelasan ontologi Quran dengan set data berbeza, pengkelasan, penterjemahan Quran dan Tafsir dalam Bahasa Indonesia. Oleh itu, kajian ini bertujuan bagi menyasiat dan menganalisa kesan bendungan terhadap dapatan pengkelasan menggunakan terjemahan Quran dan Tafsir Bahasa Indonesia sebagai set data dengan pelbagai pengkelasan yang diselia. Kaedah pengkelasan kajian ini terdiri daripada pra-pemprosesan teks, ciri pengekstrakan, dan peringkat pengkelasan teks. Pembendung Sastrawi digunapakai bagi menjalankan operasi pembendungan pada peringkat pra-pemprosesan teks. Hasil eksperimen menunjukkan Mesin Vektor Sokongan (SVM), Frekuensi Dokumen Terma Frekuensi-Berbalik (TF-IDF) dan operasi pembendungan memberikan keputusan pengkelasan yang terbaik, iaitu purata ketepatan pada 70.75% dan

purata kejituan pada 71.55% terhadap 20% saiz data ujian penterjemahan Quran dalam Bahasa Indonesia. Sementara itu, SVM, TF-IDF dan proses pembendungan memberikan prestasi pengkelasan terbaik, iaitu, purata ketepatan pada 67.30% dan purata kejituan pada 68.10% terhadap 30% saiz data ujian dari set data Kementerian Hal Ehwal Agama Indonesia. Kajian ini juga mendapati Rangkaian Neural Rambatan Belakang menghasilkan pengurangan ketepatan dan kejituan yang paling tinggi disebabkan oleh kesan negatif operasi pembendungan.

---

**KEYWORDS:** *K-nearest neighbor; neural network; ontology learning; ontology population; support vector machine*

## 1. INTRODUCTION

The Quran (Al-Quran) is a Muslim sacred book that contains God's revelations received by the holy prophet Muhammad (*sallallahu 'alaihi wa sallam*). This holy book contains knowledge, instruction, and scientific facts. Quran consists of several thematic topics or themes such as morals, criminal law, private law, worship, previous nations, the Quran, and faith. These topics aim to guide humankind to reach blessedness in the world and hereafter. The knowledge inside the Holy Quran n could be stored and represented by ontology. There are two approaches to build an ontology, i.e., non-automated and automated process [1]. This automatic process is also known as the ontology population. The non-automated process is usually crafted by a human, such as an ontology engineer or expert in a particular domain, whereas the ontology population is a technique to build an ontology by learning the concepts, relationships, and instances from the text. The standard techniques to conduct the ontology population are lexico-syntactic patterns, classification based on similarity, supervised methods, and knowledge-based and linguistic methods [2].

In the ontology, instances are defined as members of a class [3–5]. Based on earlier research by [6, 7, 8–10], they classified the Quran verses based on thematic topics for the Quran ontology. In their case, thematic topics are concepts or classes, while Quran verses are the instances. Based on their case, our study also adopts the definition of thematic topics as a class and Quran verses as instances. The aim of instances classification is to map the Quran verses into their themes in order for users to have knowledge and better understanding by seeing the entire picture of a particular topic in the Quran.

Stemming is one of the phases in text pre-processing which applies a natural language processing technique for removing affixes from words in order to transform them into their stems [11–13]. The aim of the stemming operation in text classification is to reduce the dimensionality of feature space to provide efficiency within the text classification processing [14,15]. There are several previous studies that employed a stemming operation in the text pre-processing stage to support the instances classification process. Studies by [16–18] performed verse classification for English Quran translation by applying a stemming operation in the pre-processing stage. To classify the verses, research conducted by [16,17] used Back-propagation Neural Network (BPNN) as a classifier, while [18] used three classifiers, i.e., Support Vector Machine (SVM), k-Nearest Neighbour (k-NN), and Naive Bayes (NB). However, their research did not study the stemming impact on classification results. A different approach to performing Quran verse classification was conducted by [19]. In their experiment, they learned the impact of the stemming operation to classify the English Quran verse translations using Hamming Loss as a measuring instrument. As a result, they found stemming was not able to improve Multinomial Naive Bayes performance to classify the instances according to the topics.

To date, the study of stemming impact analysis on instance classification is still a gap that needs to be bridged in the Quran ontology population research field. There is a lack of literature that studies the stemming impact on instance classification with different datasets, Quran translations, and classifiers. Based on this gap, our study aims to investigate and analyse the stemming impact on instance classification results on several datasets and supervised classifiers. Our research contribution is to provide knowledge toward stemming impact on instance classification results in Quran ontology population domain using Indonesian Quran translation and Indonesian Quran exegesis as the dataset.

The rest of the paper is structured as follows: Section 2 presents the study of related work. Section 3 describes our research methodology. Section 4 discusses our experiment results. Finally, we conclude our study results in Section 5.

## 2. RELATED WORKS

Study to investigate and analyse the stemming impact has been conducted by several previous researchers for some languages and cases. Research by [20] explains the stemming effect on the Arabic text classification. They used *Shereen Khoja's* stemmer and Term Frequency-Inverse Document Frequency (TF-IDF) as a feature selection model. Their dataset consisted of 1100 documents from trusted websites. Then, they classified the entire document into 9 classes, i.e., Agriculture, art, economics, health and medicine, law, politics, religion, science, and sports. Naïve Bayes, SMO (Sequential Minimal Optimization), and Decision Tree (J48) were used as classifiers. The dataset was split 66% for training data and 34% for test data. After two test modes using Percentage Split (PS) and k-fold Cross Validation (CV), it was found that stemming had a negative impact on the classification accuracy of the three classifiers. On PS and CV test mode, J48 had the most significant accuracy decrease from 76.3% to 64.2% in PS mode, and 69.69% to 62.6% in CV mode. Similar research conclusion was also obtained by [21] in their research. They performed Arabic text classification using three datasets that were taken from two trusted sources. The first dataset consisted of 1800 documents with six classes, the second dataset had 1500 documents with five classes, and the third dataset had 1200 documents with four classes. The datasets were split into 70% for training data and 30% for test data on each dataset. Bag of Words (BoW) with sorted and ratio was used for feature selection. They applied the Frequency Ratio Accumulation Method (FRAM) as a classifier, while to transform the words into their root form, they employed Information Science Research Institute's (ISRI) stemmer [22] and *Tashaphyne* stemmer [23]. Experimental results in the entire dataset demonstrated that stemming had a negative impact on the classification accuracy. The most significant accuracy decrease was found in the second dataset from 97.33% to 88.89% with the ISRI stemmer and 95.33% with the *Tashaphyne* stemmer.

Besides Arabic, other studies have studied stemmer impact in another language and dataset. Research by [24] conducted an Indonesian Tweet Classification using 2000 tweets divided into three datasets, i.e., a first dataset with 1500 tweets, second dataset with 1750 tweets, and third dataset with 2000 tweets. They classified the tweets into 2 classes, namely positive and negative tweets. There were 1074 positive and 926 negative tweets. Support Vector Machine (SVM) and Naïve Bayes were used as classifiers. To convert the words into their root form, they applied *Nazief and Adriani's* algorithm. This algorithm is clearly described by [25] in their research. They used BoW and TF-IDF for feature selection in their study. Experimental results on the three datasets demonstrated that stemming had a negative impact on the classification accuracy. The most significant accuracy decrease was seen in the third dataset with BoW as a feature selection and Naïve Bayes as a classifier from 89%



to 85.5%. Furthermore, a study by [19] conducted a multi-label classification on topics of Quranic verses in English translation by Shakir. They used BoW for feature selection, Multinomial Naive Bayes as a classifier, 5-fold cross-validation to evaluate the system, and Hamming Loss as a metric measurement. According to their experiment results, the classification rate without stemming was 0.125 of Hamming Loss, while it was 0.135 using stemming. Based on their research results, it can be concluded that stemming has a negative impact on the classification accuracy.

Different results for English text classification were obtained by [26]. They classified the US Congress data collection document with 60% for training data and 40% for test data. Lovin, Porter, Yet Another Suffix Stripper (YASS), GRAPh based Stemmer (GRAS), Statistic Based Stemmer (SNS), and High Precision Stemmer (HPS) were used as stemmers. As a result of text classification by SVM using all stemmers, it was concluded that stemming had a positive impact on the classification accuracy. All stemmers could improve the precision, recall, and f-measure values. The most significant value increase was seen with Porter as a stemmer from 62.1% to 68.3% for precision, 62.9% to 65.3% for recall, and 61% to 65.4% for f-measure.

### 3. METHODOLOGY

This section is structured as follows: Sub-Section 3.1 discusses the framework for instance classification in this study that was taken from earlier studies. Sub-Section 3.2 provides the collection of datasets used in this investigation. Our experimental configuration is shown in sub-section 3.3. Finally, the experiment test scenario is defined in Sub-Section 3.4.

#### 3.1 Framework Adopted

Based on earlier studies by [19–21, 24, 26], we have adopted their framework for classifying Quranic verses and Quran exegesis instances in our studies. Their framework includes several phases, i.e. text pre-processing, feature extraction, and text classification. Figure 1 presents the instance classification framework in our research. The text pre-processing phase is presented in Sub-Section 3.1.1, whereas Sub-Section 3.1.2 describes the feature extraction and text classification phase.

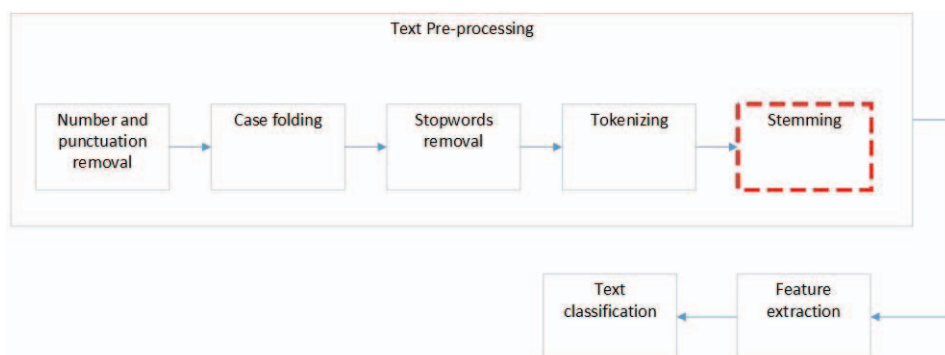


Fig. 1: Instances classification framework.

##### 3.1.1 Text Pre-Processing Phase

The pre-processing phase input is text from Indonesian Quran translation and their exegesis in Indonesian. This phase is aimed at preparing the text in an appropriate format to be processed in the next step. First, it removes the number and punctuation from the text. Then, to prevent ambiguity in term identification, any capital letters discovered are

substituted by lower case letters. Common words deemed to have no significance are removed from the sentences in the stop word removal stage after the case-folding procedure. This stage used Tala's stop word list [27] consisting of 757 words. Moreover, in the tokenization phase, the sentence was then divided into words. Tokenization is a process where the text is fragmented into an array of words.

Subsequently, the array of words is used as an input for the stemming phase. Stemming is an operation to remove affixes from the word to convert into their root form. We applied Sastrawi stemmer to perform stemming operation for the Indonesian language text. This stemmer is accessible at <https://pypi.org/project/Sastrawi/>. Sastrawi has work procedures based on the fundamental concept from Nazief and Adriani's stemmer. This stemmer algorithm was described by Asian in [25]. However, there are several modifications on Sastrawi to optimize the stemming operation results. To remove any derivational suffixes, Sastrawi has added the adopted foreign suffix rule {"-is," "-isme," "-isasi"} into the Nazief and Adriani's stemmer origin rule. Furthermore, Sastrawi also has added and modified prefix disambiguation rules to remove complex derivational prefixes {"be-," "te-," "me-," or "pe-"}. Sastrawi stemmer is the optimization result from Nazief and Adriani's algorithm. This stemmer was improved by Confix Stripping (CS) algorithm, Enhanced Confix Stripping (ECS) algorithm, and Modified ECS algorithm [28-29]. Table 1 shows the prefix disambiguation rules that have added and modified in the Sastrawi stemmer.

Table 1: Prefix disambiguation rules

Modified Rules			
Rule	Construct	Return	Modified By
5	beC <sub>1</sub> erC <sub>2</sub> ...	be-C <sub>1</sub> erC <sub>2</sub> ... where C <sub>1</sub> != 'r'	Sastrawi
12	mempe...	mem-pe...	[25]
14	men{c d j s t z}...	men-{c d j s t z}...	Sastrawi
16	meng{g h q k}...	meng-{g h q k}...	[25]
17	mengV...	meng-V...   meng-kV...   mengV-... where V='e'   me-ngV...	Sastrawi
18	menyV...	meny-sV...   me-nyV...	[30]
19	mempA...	mem-pA... where A != 'e'	[31]
29	pengC...	peng-C...	[31]
30	pengV...	peng-V...   peng-kV...   (pengV-... if V='e')	[31]
31	penyV...	peny-sV...   pe-nyV...	[30]
Deleted Rules			
Rule	Construct	Return	Deleted By
33	peCerV...	per-erV... where C!={r w y l m n}	Sastrawi
New Rules			
Rule	Construct	Return	Added By
35	terC <sub>1</sub> erC <sub>2</sub> ...	ter-C <sub>1</sub> erC <sub>2</sub> ... where C <sub>1</sub> != 'r'	[25]
36	peC <sub>1</sub> erC <sub>2</sub> ...	pe-C <sub>1</sub> erC <sub>2</sub> ... where C <sub>1</sub> != {r w y l m n}	[25]
37	CerV...	CerV   CV	[30]
38	CeIV...	CeIV...   CV...	[30]
39	CemV...	CemV...   CV...	[30]
40	CinV...	CinV...   CV...	[30]
41	kuA...	ku-A...	Sastrawi
42	kauA...	kau-A...	Sastrawi

Based on Table 1, the letter 'C' is a consonant; the letter 'V' is a vowel, and the letter 'A' means any letter. There are 40 prefix disambiguation rules on Sastrawi stemmer, where 32 of these rules were taken directly from Nazief and Adriani's stemmer, and about ten rules were from 32 rules in Nazief and Adriani's stemmer that were modified by several sources.

Sastrawi stemmer has applied the procedure to solve the suffix removal failure that was adopted from [31], for improving the stemming results. This procedure was used to handle

the suffix removal problem that arises from the Nazief and Adriani's stemmer. Finally, the array of words that contain the key terms in the basic form is used as an input on the feature extraction stage.

### 3.1.1 Feature Extraction and Text Classification Phase

Text feature extraction is a method for extracting and selecting text to represent it in a specific form. We used the Bag of Words (BoW) and Term Frequency-Inverse Document Frequency (TF-IDF) model in this research to conduct feature extraction. Bag of Words is an extraction model that could represent text as an unordered set of words and ignore grammatical structure [32]. This model has the representation of a sparse vector that includes appearance for each word in a document. Hereinafter, TF-IDF is a statistical model representing the meaning of a word on a collection by comparing the occurrence of a word in a document with its appearance in another document [33]. Mathematically, the TF-IDF approach can be written in Eq. (1) as follows:

$$TF.IDF = tf_c^r \times \log(N/df^r) \tag{1}$$

Where  $tf_c^r$  is the number of occurrences that term  $r$  appeared in a document  $c$ ,  $N$  is the number of entire documents in the corpus, and  $df^r$  is the number of documents in which term  $r$  appears.

Here is an example to describe the difference between BoW and TF-IDF. Suppose our dataset consists of two Quran verses taken from Indonesian Quran translation. These verses are:

- *Dan jika kamu ditimpa sesuatu godaan syaitan maka berlindunglah kepada Allah* (Surah Al-A'raf: 200)
- *Sesungguhnya syaitan itu tidak ada kekuasaannya atas orang-orang yang beriman dan bertawakkal kepada Tuhannya* (Surah An-Nahl: 99)

After the stop word list and stemming operation are performed on the data set, these are the verses final results after both operations have been conducted.

- *timpa goda syaitan lindung allah* (Surah Al-A'raf: 200)
- *sungguh syaitan kuasa orang orang iman bertawakkal tuhan* (Surah An-Nahl: 99)

The BoW model was built for comparing a set of documents. Based on the data set, the model has two rows, i.e. Surah Al-A'raf: 200 as  $V_1$  and An-Nahl: 99 as  $V_2$ .

	timpa	goda	syaitan	lindung	allah	sungguh	kuasa	iman	bertawakkal	tuhan	orang
$V_1$	1	1	1	1	1						
$V_2$			1			1	1	1	1	1	2

Based on Eq. (1), the BoW model then modified into a TF-IDF model. The model transformation result is shown below.

	timpa	goda	syaitan	lindung	allah	sungguh	kuasa	iman	bertawakkal	tuhan	orang
$V_1$	0,3	0,3	0	0,3	0,3						
$V_2$			0			0,3	0,3	0,3	0,3	0,3	<b>0,6</b>

Finally, after feature extraction and selection has been conducted, further the BoW and TF-IDF data are divided into training and test sets. We employed the Back-propagation

Neural Network (BPNN), Support Vector Machine (SVM), and k-Nearest Neighbor (k-NN) classifier to classify the instances. The instances are classified into one of the classes by those classifiers. We utilized three classes, i.e., morals, Al-Quran, and previous nation in our study that taken from thematic topics within Al-Quran Cordoba [34].

### 3.2 Dataset Collection

We utilized two sources to create the dataset, i.e., the data from *Tanzil* project (<http://tanzil.net>) to build the Indonesian Quran translation and *Quraish Shihab* exegesis corpus; and the data from the Ministry of Religious Affairs Indonesia (<https://quran.kemenag.go.id/>) to develop Quran exegesis corpus. In our study, we utilized several Quran surahs and thematic topics for developing corpus. Table 2 presents the thematic topic number with their names and the total of Quran verse, which is connected to their thematic topic that was used to develop our corpus.

Table 2: Thematic topics and total of Quran verses

Thematic Topic ID	Thematic Topic Name	Total of Quran Verses
1	Morals	218
2	Al-Quran	183
3	Previous Nation	127

Based on Table 2, we employed 528 of Quran verses from Indonesia Quran translation and their exegesis. Table 3 presents the Quran surah, a total of verses inside the surah, and their thematic topic that are utilized to build the corpus.

Table 3: Surah name, total of verses, and their thematic topic

Topic ID	Al-Baqarah	Ali Imran	An-Nisa'	Al-An'am	Al-A'raf	At-taubah	An-Nahl	Taha
1	51	40	47	13	21	28	14	4
2	59	29	25	20	16	8	18	8
3	13	28	12	10	37	4	5	18
<b>Sum</b>	<b>123</b>	<b>97</b>	<b>84</b>	<b>43</b>	<b>74</b>	<b>40</b>	<b>37</b>	<b>30</b>

For this study, we utilized Quran verses that are categorized by Al-Quran Cordoba into a single thematic topic. We used two datasets, i.e. Indonesian Quran translation and Quraish Shihab exegesis corpus to observe stemming impact toward the accuracy level of the classifier on both datasets.

### 3.3 Experimental Setup

We employed two operational frameworks to classify the instances. Figure 2 presents the framework that utilized the BoW approach for classification, while Fig. 3 shows the framework that used TF-IDF to classify the instances.

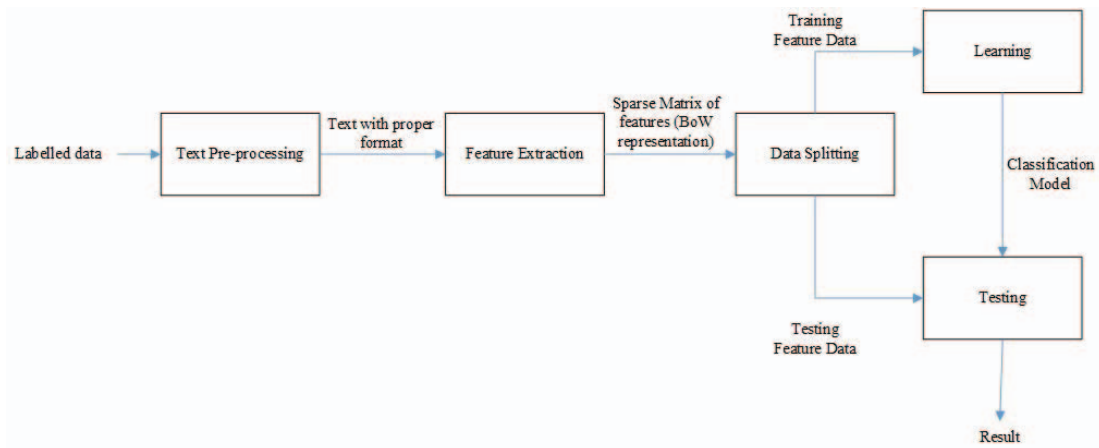


Fig. 2: Framework with BoW approach.

Figure 2 shows that the BoW model follows the feature extraction phase. Furthermore, the data is divided into training and test feature data. The dimensions of both feature data will be presented in Sub-chapter 3.4. For the text pre-processing stage, we used two scenarios, i.e., pre-processing without stemming operation and with the stemming process.

As shown in Fig. 3, BoW model representation is converted into the TF-IDF model. Further, the TF-IDF representation divided into training and test feature data. We developed the operational framework and tested the model performance in Python programming environment. Similar to the previous operational framework, we used two scenarios, i.e., pre-processing without stemming operation and with the stemming process on the text pre-processing stage.

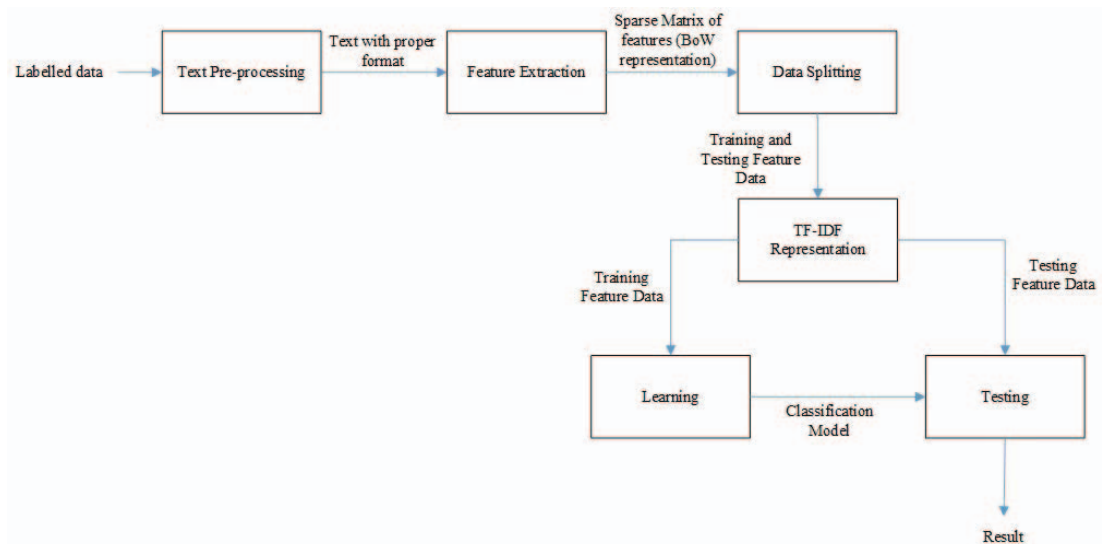


Fig. 3: Framework with TF-IDF approach.

### 3.4 Test Scenario

We applied several test data sizes to investigate and analyse the stemming operation impact on instance classification with different feature selection models, i.e., BoW and TF-IDF. The test data size for each thematic topic is shown in Table 4.

Table 4: The size of the test data for each topic

Size of test data	Topic 1: Morals (data)	Topic 2: Al-Quran (data)	Topic 3: Previous Nation (data)	Sum (data)
20%	44	37	25	106
30%	66	55	38	159

As shown in Table 4, there are two test scenarios to investigate and analyse the impact of the stemming operation on instance classification performance. We utilized the precision, recall, and accuracy metric for measuring the classification results in this study.

### 3.5 Metric for Evaluation

In this study, we used various evaluation metrics to measure classification results, i.e. average accuracy, average precision, precision, and recall. Table 5 presents the metric for evaluation and their evaluation focus which is used in this research.

Table 5: The evaluation metric for instance classification

Metrics	Formula	Evaluation Focus
Precision	$\frac{tp}{tp + fp}$	The ratio between the positive patterns that are correctly predicted from the total predicted data in a positive class
Recall	$\frac{tp}{tp + fn}$	Measure the fraction of positive patterns that are correctly classified
Average Accuracy	$\frac{\sum_{i=1}^l \frac{tp_i + tn_i}{tp_i + fn_i + fp_i + tn_i}}{l}$	The average effectiveness of all class from a classifier
Average Precision	$\frac{\sum_{i=1}^l \frac{tp_i}{tp_i + fp_i}}{l}$	The average of all class precision

where  $tp$  is true positive,  $fp$  is false positive,  $fn$  is false negative,  $tp_i$  are true positive for  $C_i$ ,  $tn_i$  are true negative for  $C_i$ ,  $fn_i$  are false negative for  $C_i$ , and  $fp_i$  are false positive for  $C_i$ .

In our experiment, we used average accuracy and average precision to measure the impact of the stemming operation in all approaches toward classification results for all datasets. While to measure the effect of stemming operation in all methods toward classification results for each theme within all datasets, we used the precision and recall metric.

## 4. RESULTS AND ANALYSIS

First, we utilized the Indonesian Quran translation (IQT) corpus as a dataset in our experiment. This experiment applied the test scenario based on Table 4. Figure 4 presents the experiment results for the average precision and average accuracy measurement in all approaches.

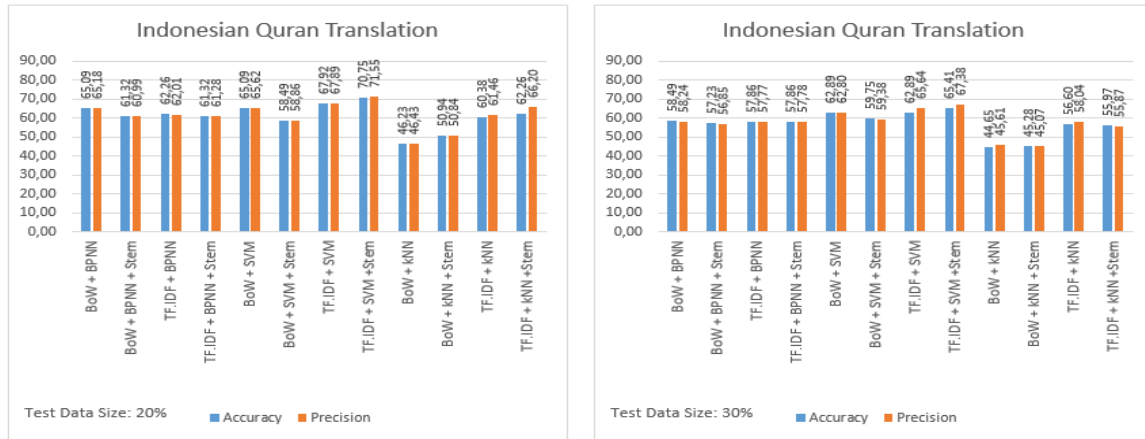


Fig. 4: Measurement average precision and average accuracy on IQT dataset.

As shown in Fig. 4, the stemming operation has a negative impact on BoW/TF-IDF with BPNN approaches for both test data sizes. However, the stemming process has a positive effect on the TF-IDF with SVM approach for both test data sizes. Furthermore, on BoW/TF-IDF with k-NN methods also have a positive impact from the stemming operation on 20% test data size. The TF-IDF with SVM and stemming approach has the highest average precision and average accuracy value on both test data sizes. Hereinafter, Figure 5 shows the experiment results with Quraish Shihab exegesis as a corpus.

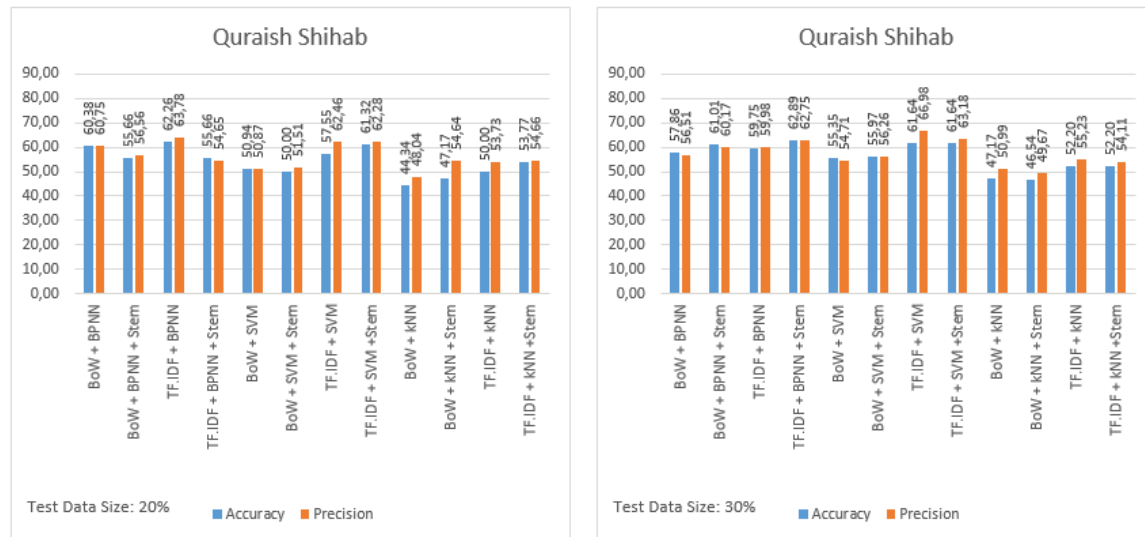


Fig. 5: Measurement average precision and average accuracy on the Quraish Shihab dataset.

Based on Fig. 5, it can be concluded that the stemming operation has a negative impact for BoW/TF-IDF with BPNN approach and BoW with SVM approaches on 20% test data size. Similar to the previous dataset, the BoW/TF-IDF with k-NN methods have a positive impact from stemming operation on 20% test data size. Otherwise, the stemming process has a positive effect for BoW/TF-IDF with BPNN approach and BoW with SVM approaches on 30% test data size. Also, the BoW/TF-IDF with k-NN methods has a negative effect from stemming operation on 30% test data size. Furthermore, Fig. 6 describes the experimental results with the Ministry of Religious Affairs Tafsir as a corpus.

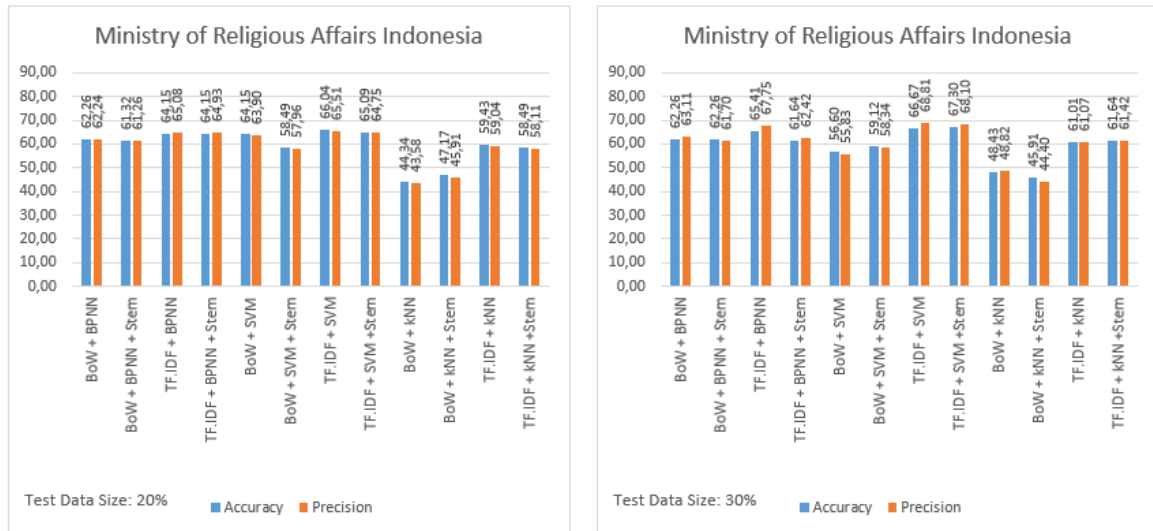


Fig. 6: Measurement of average precision and average accuracy on Ministry of Religious Affairs dataset.

As shown in Fig. 6, it was found that the stemming process has a negative impact on BoW/TF-IDF with BPNN/SVM approaches on 20% test data size. Furthermore, the stemming process also has a negative impact on BoW/TF-IDF with BPNN approaches on 30% test data size. While the BoW/TF-IDF with SVM approaches on 30% test data size has a positive impact from stemming operation.

Figure 7 shows the performance measurement of classification results for Morals class on IQT dataset with 20% and 30% test data size.

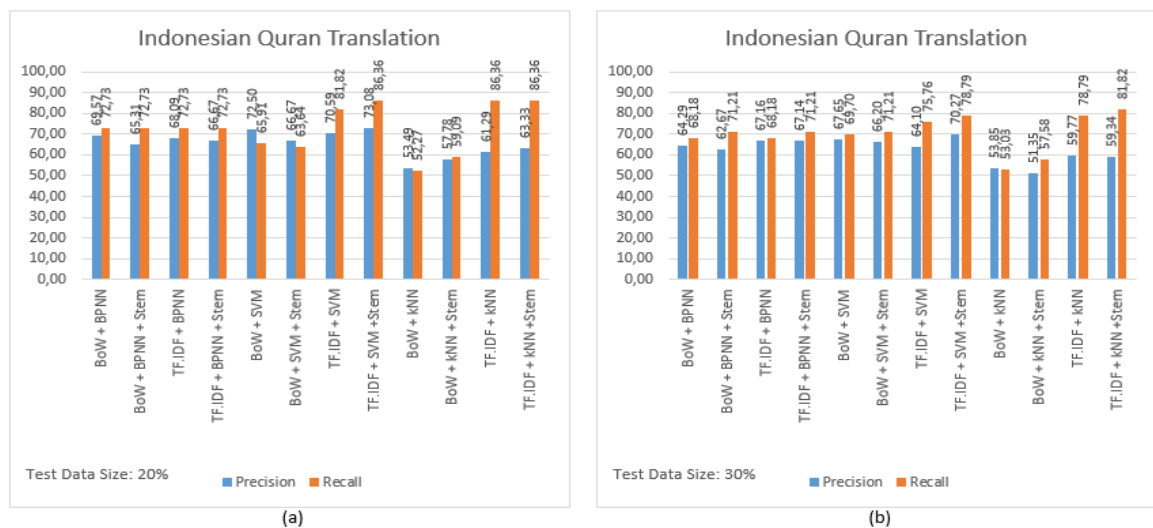


Fig. 7: (a) Morals class on IQT corpus with 20% test data size; (b) Morals class on IQT corpus with 30% test data size.

As shown in Fig. 7, it was found that the stemming operation has provided negative results for BoW/TF-IDF with BPNN and BoW with SVM approaches on both test data sizes since there is a decrease in precision value. However, the stemming process has provided positive results for TF-IDF with SVM and BoW/TF-IDF with k-NN approaches on both test data size since there is an increase in precision and recall value.



Figure 8 presents the performance measurement of classification results for Al-Quran class on IQT dataset with 20% and 30% test data size.

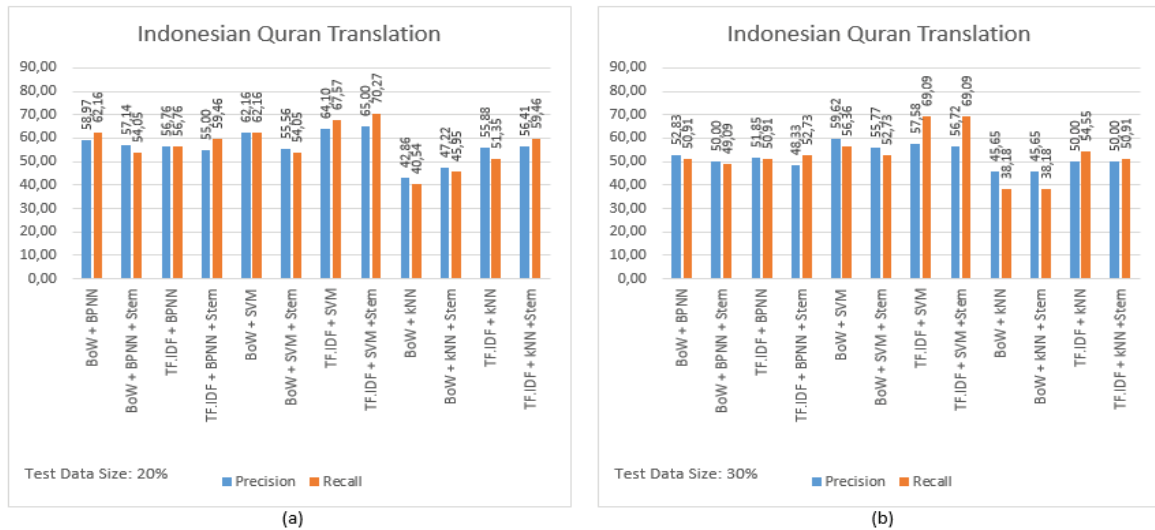


Fig. 8: (a) Al-Quran class on IQT corpus with 20% test data size; (b) Al-Quran class on IQT corpus with 30% test data size.

Based on Fig. 8, similar to the previous class, the stemming process has provided negative results for BoW/TF-IDF with BPNN and BoW with SVM approaches on both test data size since there is a decrease in precision value. While the stemming operation has provided positive results for TF-IDF with SVM and BoW/TF-IDF with k-NN approaches on 20% test data size since there is an increase in precision values.

Figure 9 describes the performance measurement of classification results for previous nation class on IQT dataset with 20% and 30% test data size.

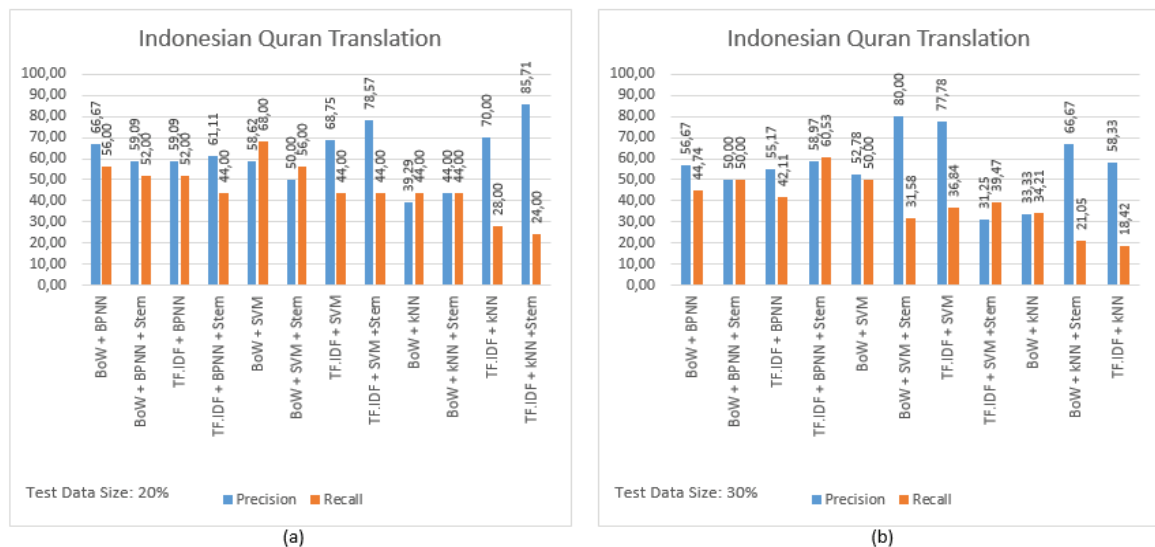


Fig. 9: (a) Previous nation class on IQT corpus with 20% test data size; (b) Previous nation class on IQT corpus with 30% test data size.

According to Fig. 9, it was found that the stemming operation provides a negative impact for BoW/TF-IDF with BPNN and SVM approaches on 20% test data size since there is a decrease in precision and recall values.

Figure 10 describes the performance measurement of classification results for morals class on Quraish Shihab Tafsir dataset, Fig. 11 shows the results for Al-Quran class, while Fig. 12 presents the results for the previous nation class.

As shown in Fig. 10, the stemming process provides a positive impact for BoW/TF-IDF with k-NN and TF-IDF with SVM approaches on 20% test data size since there is an increase in precision and recall values. Furthermore, Fig. 11(a) shows that stemming operation provides a negative impact for BoW/TF-IDF with BPNN and BoW with SVM approaches since there is a decrease in precision values, otherwise Fig. 11(b) presents that the stemming operation provides a positive impact for BoW/TF-IDF with BPNN and BoW with SVM approaches since there is an increase in precision and recall values.

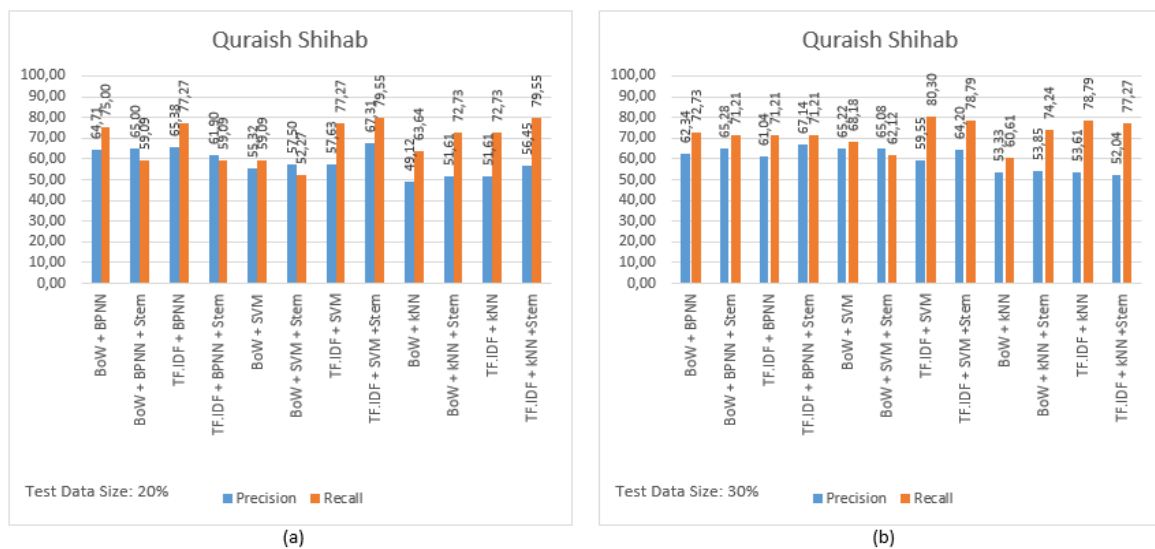


Fig. 10: (a) Morals class on Quraish Shihab Tafsir corpus with 20% test data size; (b) Morals class on Quraish Shihab Tafsir corpus with 30% test data size.

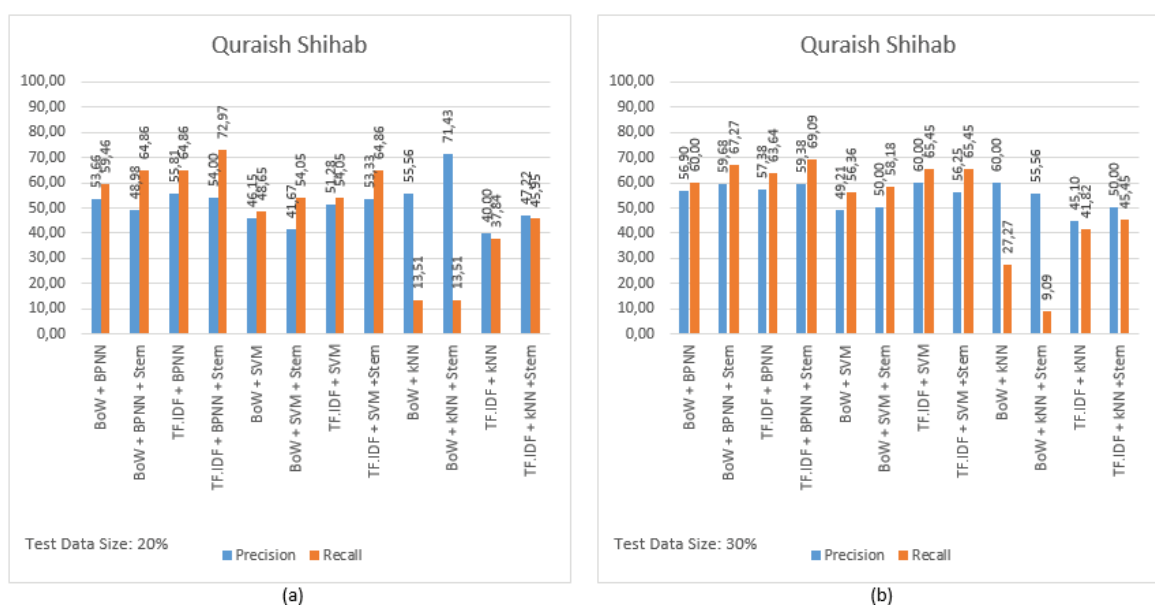


Fig. 11: (a) Al-Quran class on Quraish Shihab Tafsir corpus with 20% test data size; (b) Al-Quran class on Quraish Shihab Tafsir corpus with 30% test data size.

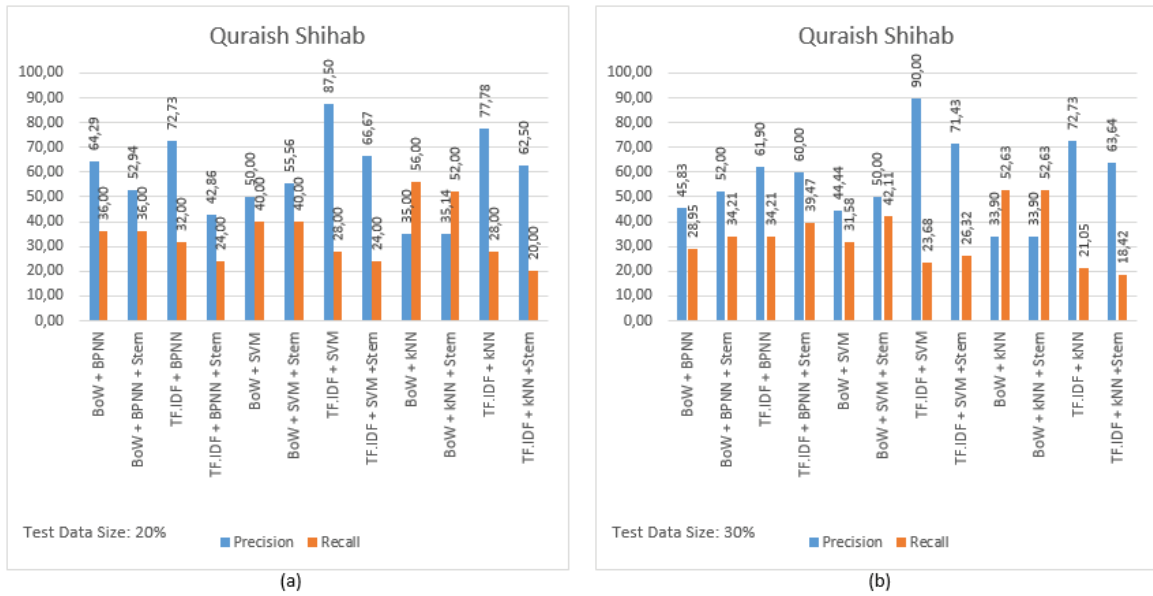


Fig. 12: (a) Previous nation class on Quraish Shihab Tafsir corpus with 20% test data size; (b) Previous nation class on Quraish Shihab Tafsir corpus with 30% test data size.

Figure 13 shows the performance measurement of classification results for morals class on Ministry of Religious Affairs Indonesia dataset, Fig. 14 presents the results for Al-Quran class, while Fig. 15 provides the results for the previous nation class.

As shown in Fig. 13(a), it was found that the stemming operation provides a negative impact for BoW with BPNN/SVM approaches since there is a decrease in precision and recall values. This result is inverse compared to classification results for Al-Quran class with BoW, and BPNN/SVM approaches, as shown in Fig. 14(b). Furthermore, the stemming process also provides a negative impact on all approaches to classify the instances in previous nation class, as shown in Fig. 15(a) and (b).

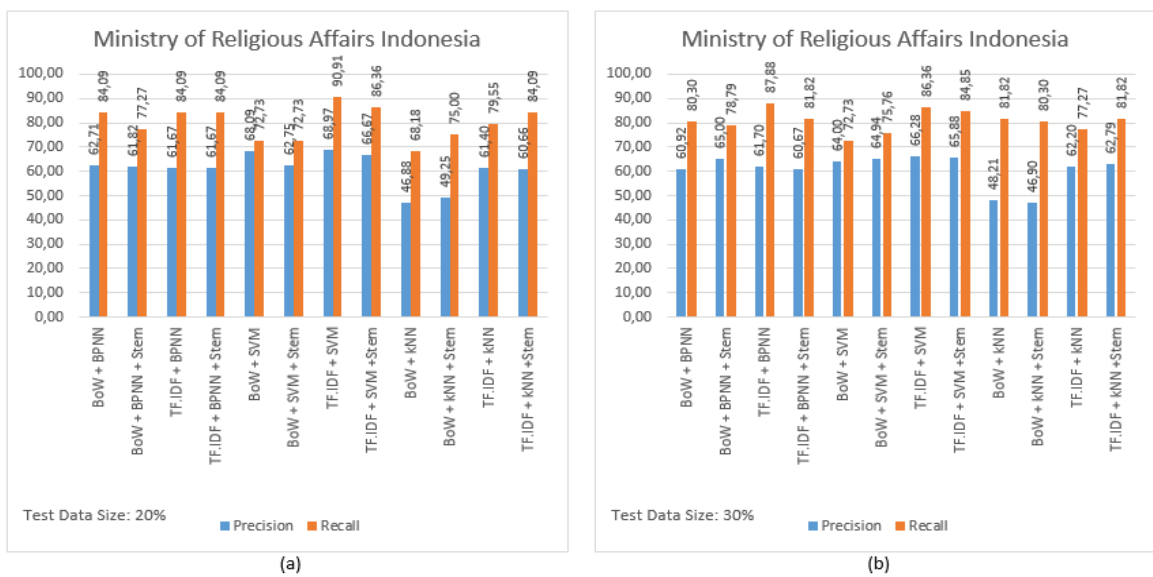


Fig. 13: (a) Morals class on Ministry of Religious Affairs Tafsir corpus with 20% test data size; (b) Morals class on Ministry of Religious Affairs Tafsir corpus with 30% test data size.

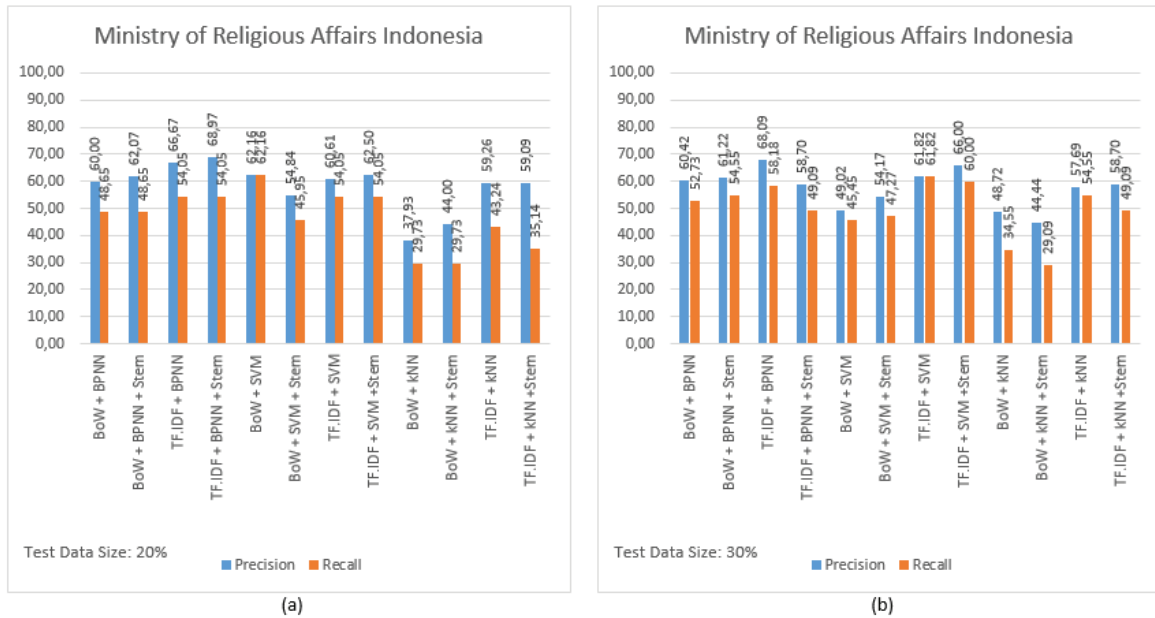


Fig. 14: (a) Al-Quran class on Ministry of Religious Affairs Tafsir corpus with 20% test data size; (b) Al-Quran class on Ministry of Religious Affairs Tafsir corpus with 30% test data size.

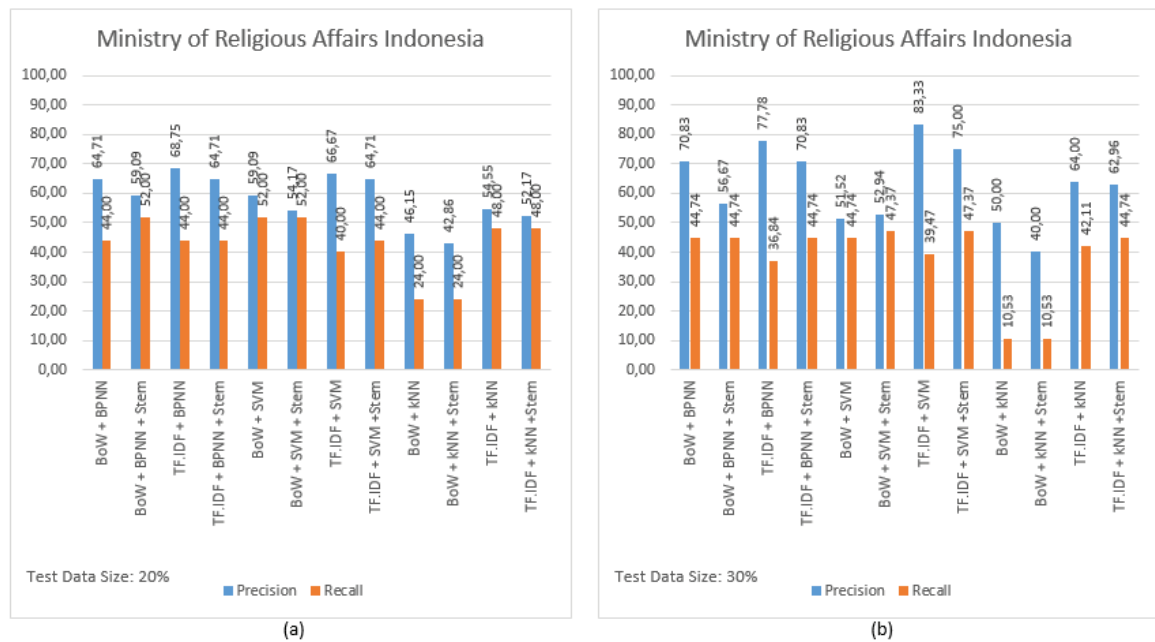


Fig. 15: (a) Previous nation class on Ministry of Religious Affairs Tafsir corpus with 20% test data size; (b) Previous nation class on Ministry of Religious Affairs Tafsir corpus with 30% test data size.

## 5. CONCLUSIONS

Based on our experimental results, as shown in Fig. 4 to Fig. 6, it was found that the stemming operation provides positive outcomes for k-NN with BoW approach to perform instance classification on 20% test data size. Furthermore, in this test data size, it was also found that the stemming process supplies a negative influence for instance classification

with SVM and BoW, BPNN and BoW, and BPNN with TF-IDF. SVM and TF-IDF with stemming operation own the best classification performance, i.e., 70.75% for average accuracy and 71.55% for average precision in IQT dataset. While in the 30% test data size, it was found that stemming operation provides a negative impact on precision for k-NN with BoW approach to classify the instances. However, the stemming process was able to provide a positive effect on accuracy for instance classification with SVM and TF-IDF. SVM and TF-IDF with stemming process own the best classification performance, i.e., 67.30% for average accuracy and 68.10% for average precision in Ministry of Religious Affairs Indonesia dataset. In this study, it was also discovered that the BPNN has the most average precision and average accuracy reduction due to the negative impact of stemming operations.

## ACKNOWLEDGEMENT

The authors would like to thank the financial support from Universitas AMIKOM Purwokerto; and Center for Advanced Computing Technology (C-ACT), Faculty of Information and Communications Technology, Universiti Teknikal Malaysia Melaka (UTeM) for their assistance in this research.

## REFERENCES

- [1] Utomo FS, Suryana N, Azmi MS. (2019). New Instances Classification Framework on Quran Ontology Applied to Question Answering System. *TELKOMNIKA*, 17(1): 139–146. <http://dx.doi.org/10.12928/telkomnika.v17i1.9794>
- [2] Cimiano P. (2006). *Ontology Learning and Population from Text: Algorithms, Evaluation and Applications*. New York, Springer Science & Business Media. doi: 10.1007/978-0-387-39252-3
- [3] Xian G, Li J, Kou Y, Luo T, Huang Y. (2018). Construction and Application of Upper Country Ontology Based on OWL and SKOS. In *Proceedings of the 2nd International Conference on Computer Science and Application Engineering: 22-24 October 2018; Hohhot*. pp 1–6. doi: 10.1145/3207677.3278056
- [4] Buranarach M, Supnithi T, Thein YM, Ruangrajitpakorn T, Rattanasawad T, Wongpatikaseree K, Lim AO, Tan Y, Assawamakin A. (2016). OAM: An Ontology Application Management Framework for Simplifying Ontology-Based Semantic Web Application Development. *International Journal of Software Engineering and Knowledge Engineering*, 26(1): 115–145. doi: 10.1142/s0218194016500066
- [5] Mitzias P, Riga M, Kontopoulos E, Stavropoulos TG, Andreadis S, Meditskos G, Kompatsiaris I. (2016). User-Driven Ontology Population from Linked Data Sources. In *Communications in Computer and Information Science*. Volume 649. Edited by Ngonga Ngomo AC., Křemen P. Prague, Springer; 31–41.
- [6] Hakkoum A, Raghay S. Advanced Search in the Qur'an using Semantic modeling. (2015). In *IEEE/ACS 12th International Conference of Computer Systems and Applications (AICCSA): 17-20 November 2015; Marrakech*. pp. 1–4. doi: 10.1109/AICCSA.2015.7507259
- [7] Periamalai NSHA, Mustapha A, Alqurneh A. (2016). An Ontology for Juz' Amma based on Expert Knowledge. In *7th International Conference on Computer Science and Information Technology (CSIT): 13-14 July 2016; Amman*. pp. 1–5. doi: 10.1109/CSIT.2016.7549480
- [8] Zailani SAM, Omar NA, Mustapha A, Rahim MHA. (2018). Fasting ontology in pillars of Islam. *Indonesian Journal of Electrical Engineering and Computer Science*, 12(2): 562–569. doi: 10.11591/ijeecs.v12.i2.pp562-569
- [9] Ta'a A, Abed QA, Ali BM, Ahmad M. (2016). Ontology-Based Approach for Knowledge Retrieval in Al-Quran Holy Book. *International Journal of Computational Engineering Research (IJCER) Ontology-Based*, 6(3): 8–15.

- [10] Afifi M, Safee M, Saudi MM, Pitchay SA, Ridzuan F, Basir N, Saadan K, Nabila F. (2018). Hybrid Search Approach for Retrieving Medical and Health Science Knowledge from Quran. *International Journal of Engineering & Technology*, 7: 69–74. doi: 10.14419/ijet.v7i4.15.21374
- [11] Jabbar A, Iqbal S, Khan MUG, Hussain S. (2018). A survey on Urdu and Urdu like language stemmers and stemming techniques. *Artificial Intelligence Review*, 49(3): 339–373. doi: 10.1007/s10462-016-9527-1
- [12] Jabbar A, Iqbal S, Akhuzada A, Abbas Q. (2018). An improved Urdu stemming algorithm for text mining based on multi-step hybrid approach. *Journal of Experimental and Theoretical Artificial Intelligence*, 30(5): 703–723. <https://doi.org/10.1080/0952813X.2018.1467495>
- [13] Kassim MN, Jali SHM, Maarof MA, Zainal A. (2019). Towards stemming error reduction for Malay texts. *Lecture Notes in Electrical Engineering*, 481: 13–23. doi: 10.1007/978-981-13-2622-6\_2
- [14] Uysal AK, Gunal S. (2014). The impact of preprocessing on text classification. *Information Processing and Management*, 50(1): 104–112. <http://dx.doi.org/10.1016/j.ipm.2013.08.006>
- [15] Sharma D, Jain S. (2015). Evaluation of Stemming and Stop Word Techniques on Text Classification Problem. *International Journal of Scientific Research in Computer Science and Engineering*, 3(2): 1–4.
- [16] Hamed SK, Ab Aziz MJ. (2018). Classification of Holy Quran Translation using Neural Network Technique. *Journal of Engineering and Applied Sciences*, 13(12): 4468–4475. doi: 10.3923/jeasci.2018.4468.4475
- [17] Hamed SK, Ab Aziz MJ. (2016). A question answering system on Holy Quran translation based on question expansion technique and Neural Network classification. *Journal of Computer Science*, 12(3): 169–177. doi: 10.3844/jcssp.2016.169.177
- [18] Rostam NAP, Malim NHAH. (in press). Text categorisation in Quran and Hadith: Overcoming the interrelation challenges using machine learning and term weighting. *Journal of King Saud University - Computer and Information Sciences*. <https://doi.org/10.1016/j.jksuci.2019.03.007>
- [19] Pane RA, Mubarak MS, Huda NS, Adiwijaya. (2018). A Multi-label Classification on Topics of Quranic Verses in English Translation using Multinomial Naive Bayes. In *Proceedings of the 6th International Conference on Information and Communication Technology (ICoICT): 3-5 May 2018; Bandung*. pp. 481–484. doi: 10.1109/ICoICT.2018.8528777
- [20] Wahbeh A, Al-Kabi M, Al-Radaideh Q, Al-Shawakfa E, Alsmadi I. (2011). The Effect of Stemming on Arabic Text Classification. *International Journal of Information Retrieval Research*, 1(3): 54–70. doi: 10.4018/ijirr.2011070104
- [21] Sallam RM, Mousa HM, Hussein M. (2016). Improving Arabic Text Categorization using Normalization and Stemming Techniques. *International Journal of Computer Applications*, 135(2): 38–43. doi: 10.5120/ijca2016908328
- [22] Taghva K, Elkhoury R, Coombs J. (2005). Arabic Stemming without a Root Dictionary. In *Proceedings of the International Conference on Information Technology: Coding and Computing (ITCC): 4-6 April 2005; Las Vegas*. pp. 152–157. doi: 10.1109/ITCC.2005.90
- [23] Tashaphyne: Arabic Light Stemmer [<https://pypi.org/project/Tashaphyne/>].
- [24] Hidayatullah AF, Ratnasari CI, Wisnugroho S. (2016). Analysis of Stemming Influence on Indonesian Tweet Classification. *TELKOMNIKA*, 14(2): 665–673. doi: 10.12928/telkomnika.v14i2.3113
- [25] Asian J. (2007). Effective Techniques for Indonesian Text Retrieval. PhD thesis. RMIT University, School of Computer Science and Information Technology.
- [26] Singh J, Gupta V. (2017). A systematic review of text stemming techniques. *Artificial Intelligence Review*, 48(2): 157–217. doi: 10.1007/s10462-016-9498-2
- [27] Tala FZ. (2003). A Study of Stemming Effect on Information Retrieval in Bahasa Indonesia. Master Thesis. Universiteit van Amsterdam, Institute for Logic, Language and Computation.
- [28] Kusumaningrum R, Adhy S, Suryono S. (2018). WLOUDVIZ: Word Cloud Visualization of Indonesian News Articles Classification based on Latent Dirichlet Allocation. *TELKOMNIKA*, 16(4): 1752–1759. doi: 10.12928/telkomnika.v16i4.8194

- [29] Darmawiguna IGM, Pradnyana GA, Santyadiputra GS. (2019). The Development of Integrated Bali Tourism Information Portal using Web Scrapping and Clustering Methods. *Journal of Physics: Conference Series*, 1165(1): 1–10. doi: 10.1088/1742-6596/1165/1/012010
- [30] Tahitoe AD, Purwitasari D. (2010). Implementasi modifikasi enhanced confix stripping stemmer untuk bahasa indonesia dengan metode corpus based stemming. Undergraduate Thesis. Institut Teknologi Sepuluh November (ITS), Informatics Engineering Department.
- [31] Arifin AZ, Mahendra IPAK, Ciptaningtyas HT. (2009). Enhanced confix stripping stemmer and ants algorithm for classifying news document in indonesian language. *Proceeding of International Conference on Information & Communication Technology and Systems (ICTS)*. pp. 149-158.
- [32] Schneider MJ, Gupta S. (2016). Forecasting sales of new and existing products using consumer reviews: A random projections approach. *International Journal of Forecasting*, 32(2): 243–256. doi: 10.1016/j.ijforecast.2015.08.005
- [33] Chen G, Xiao L. (2016). Selecting publication keywords for domain analysis in bibliometrics: A comparison of three methods. *Journal of Informetrics*, 10(1): 212–223. <http://dx.doi.org/10.1016/j.joi.2016.01.006>
- [34] Kurnia I, Sopian T, Suryana Y, Makbul, Nugraha S, Al-Ghifari, MM, Abdullah R. (2012). *Al-Qur'an CORDOBA*, 1st ed. Bandung, Cordoba: Internasional - Indonesia.

# AN ENHANCED PACKET SCHEDULING ALGORITHM FOR THE DOWNLINK COGNITIVE LONG TERM EVOLUTION-ADVANCED

HUDA ADIBAH MOHD RAMLI, MOHAMAD ISMAT HAFIZI MANSOR

*Department of Electrical and Computer Engineering,  
International Islamic University Malaysia,  
P.O. Box 10, 50728 Kuala Lumpur, Malaysia.*

*\*Corresponding author: hadibahmr@iium.edu.my*

*(Received: 18<sup>th</sup> June 2019; Accepted: 30<sup>th</sup> July 2019; Published on-line: 20<sup>th</sup> January 2020)*

**ABSTRACT:** A packet scheduling algorithm known as Enhanced Maximum-Largest Weighted Delay First (EM-LWDF) is proposed in this paper. It aims to maximize the number of Real Time (RT) and Non Real Time (NRT) users that meet their desired Quality of Service (QoS) in the cognitive Long Term Evolution-Advanced (LTE-A). This cognitive LTE-A allows its Component Carriers (CCs) to be combined with licensed CCs from another system. This enables the LTE-A to further expand the available bandwidth for packet transmission. The EM-LWDF algorithm decides the priority of each user on the basis of the desired QoS of each packet, the urgency of each packet, channel quality and the average throughput. The potential of this algorithm is validated via computer simulation where it is able to simultaneously maximize more users that meet their desired QoS in realistic RT and NRT multimedia of the downlink cognitive LTE-A.

**ABSTRAK:** Algoritma penjadualan paket yang dikenali sebagai Enhanced Maximum-Largest Weighted Delay First (EM-LWDF) dicadangkan dalam kertas ini. Ia bertujuan untuk memaksimumkan bilangan pengguna Real Time (RT) dan Non Real Time (NRT) yang memenuhi Kualiti Perkhidmatan yang dikehendaki (QoS) dalam system kognitif Long Term Evolution-Advanced (LTE-A). Kognitif LTE-A ini membolehkan Carrier Component (CC) untuk digabungkan dengan CC berlesen dari sistem lain. Ini membolehkan LTE-A untuk memperluaskan jalur lebar yang tersedia bagi penghantaran paket. Algoritma EM-LWDF menentukan keutamaan setiap pengguna berdasarkan QoS yang dikehendaki dari setiap paket, kecemasan setiap paket, kualiti saluran dan purata penghantaran. Potensi algoritma ini disahkan melalui simulasi komputer di mana ia dapat memaksimumkan lebih banyak pengguna yang memenuhi QoS yang dikehendaki mereka dalam realistik RT dan NRT multimedia dari downlink sistem kognitif LTE-A.

**KEYWORDS:** *maximum-largest weighted delay first (M-LWDF); packet scheduling; long term evolution-advanced; quality of service; real time and non-real time*

## 1. INTRODUCTION

The introduction and evolution of various Real Time (RT) and Non-Real Time (NRT) multimedia content have drastically increased the number of wireless subscriptions. It should be noted that RT content are sensitive to delay whereas NRT is a loss-sensitive multimedia content. To address this scenario, Long Term Evolution-Advanced (LTE-A) that promises a significant increase in the data speed whilst maximizing the number of users that meet their desired Quality of Service (QoS) was standardized. Such increase in the data speed is



achieved via Carrier Aggregation (CA) method. This method combines a number of Component Carriers (CCs) of the same or different frequency bands.

Given the current escalating demand on the multimedia contents, the limited CCs of the LTE-A will soon be saturated. To offload some portion of the CCs usage, integrating the CCs of the LTE-A with other licensed CCs via Cognitive Radio (CR) seems a feasible solution. It should be noted that the Federal Communication Commission reported in its study that some portions of licensed CCs are heavily utilized while other portions of the CCs licensed to Digital Video Broadcast (DVB) and TV systems are lightly used [1]. This allows more available CCs to be exploited for use by the LTE-A users. CR is a technology that allows unlicensed users (for example, LTE-A users) to opportunistically utilize the vacant portions of the licensed CCs and quickly release these portions when licensed users (such as DVB users) become active.

Transmission of multimedia content takes place via packet-switched technology. Therefore, packet scheduling is of significant importance in the LTE-A. A large number of packet scheduling algorithms have been developed. For example, the most popular conventional Maximum Largest Weighted Delay First (M-LWDF) [2] algorithm was developed to meet the desired QoS of the RT multimedia content in the single-user legacy wireless systems that have only one CC. The M-LWDF chooses a downlink user to receive its packets based on Eq. (1).

$$\mu_k(i) = a_k * RT_k(i) * \frac{cq_k(i)}{AT_k(i)} \quad (1)$$

$$a_k = \frac{\log \delta_k}{TB_k} \quad (2)$$

$$AT_k(i+1) = \left(1 - \frac{1}{t_c}\right) AT_k(i) + I_k(i+1) * \frac{1}{t_c} * cq_k(i+1) \quad (3)$$

where  $\mu_k(i)$  is the priority of user  $k$  at time  $i$ ,  $a_k$  is the desired QoS of user  $k$ ,  $\delta_k$  is the content-dependent packet loss threshold of user  $k$ , and  $TB_k$  is the content-dependent buffer delay threshold of user  $k$ . It should be noted that the maximum residence time of RT/NRT content in the buffer at the base station is determined by content-dependent buffer delay threshold.  $RT_k(i)$  is the residence time of the Head-of-Line (HOL) packet at the base station of user  $k$  at time  $i$ ,  $cq_k(i)$  is the channel quality of user  $k$  at time  $i$ ,  $AT_k(i)$  is the average throughput of user  $k$  at time  $i$ ,  $t_c$  is a time constant and  $I_k(i+1)$  is an indicator of the event where packets of user  $k$  were transmitted at time  $k+1$ .

It can be observed in Eq. (1) that the packet scheduler in these single-user legacy wireless systems chooses only one user to receive its packets at each time. Moreover, in this system, all of the available bandwidth in a CC is used to transmit the packets to this user. This is contrary to packet scheduling in multi-user wireless systems that allows more than one user to receive its packets at each time.

Similarly in the multi-user wireless systems, a number of extensions of the well-known M-LWDF versions are available. This includes the algorithms developed in [3-5] that exploited the Resource Block (RB), the average throughput and the packet residence time to further improve the multi-user wireless performance. It should be noted that an RB is the smallest unit of radio resource in LTE-A. It contains twelve subcarriers of 15 kHz bandwidth

each and is of one ms interval. For example, the Modified Maximum-Largest Weighted Delay First (MM-LWDF) algorithm discussed in [3] uses Eq. (4) when determining the priority of each user on each RB, on each CC and at each time.

$$\mu_{k,l,m}(i) = a_k * RT_k(i) * \frac{cq_{k,l,m}(i)}{\sum_{l=1}^{l=CC_{max}} AT_{k,l}(i)} \quad (4)$$

where  $\mu_{k,l,m}(i)$  is the priority of user  $k$  on CC  $l$  on vacant RB  $m$  at time  $i$ ,  $a_k$  is the desired QoS of user  $k$  as defined in Eq. (2),  $RT_k(i)$  is the residence time of the HOL packet at the base station of user  $k$  at time  $i$ ,  $cq_{k,l,m}(i)$  is the channel quality of user  $k$  on CC  $l$  on vacant RB  $m$  at time  $i$ ,  $AT_{k,l}(i)$  is the average throughput of user  $k$  on CC  $l$  at time  $i$  (as defined in Eq. (3)) and  $CC_{max}$  is the total number of licensed CCs.

Besides the extended versions of the M-LWDF, other studies that investigated the packet scheduling algorithms in the literature include [6-14]. Based on our study, it was observed that the majority of these conventional multi-user packet scheduling algorithms offer to meet the desired QoS of either for RT packets or NRT packets. Those PS algorithms that were developed for simultaneous support of both RT and NRT were computationally expensive, did not consider a realistic RT and NRT traffic, or require further performance investigation if these algorithms were to be implemented in the downlink cognitive LTE-A.

Due to the limitations of the conventional packet scheduling algorithms and motivated by the work in [3], this paper proposed an enhancement of the MM-LWDF known as an Enhanced M-LWDF (EM-LWDF) with the intention to provide support for more RT and NRT users that meet their desired QoS. The EM-LWDF algorithm takes the desired QoS of each packet (either RT or NRT), the channel quality, the average throughput and the urgency of each packet into consideration when scheduling packets on each RB and on each CC.

The remaining parts of this paper are structured as follows: Section II explains in detail the proposed EM-LWDF algorithm, thereafter followed by the description of the simulation environment in Section III. Results are analytically discussed in Section IV whereas Section V marks the conclusions of the paper.

## 2. ENHANCED MAXIMUM-LARGEST WEIGHTED DELAY FIRST (EM-LWDF) ALGORITHM

The co-existence of the downlink LTE-A and DVB system as shown in Fig. 1 is considered in this paper. It should be noted that the base station of the LTE-A is known as eNodeB. It is assumed that the DVB system has a total of two licensed CCs of 3 MHz bandwidth each. The CCs of the LTE-A are not taken into account as this paper aims to investigate the impact on cognitive LTE-A performance for opportunistic use of the vacant portions of the licensed DVB CCs via CR.

The EM-LWDF algorithm aims to simultaneously provide satisfactory QoS for both RT and NRT multimedia contents for more users. Therefore, to achieve its intention, the proposed algorithm selects the packets that maximize Eq. (5) at each time, on each licensed CC and on each vacant RB.

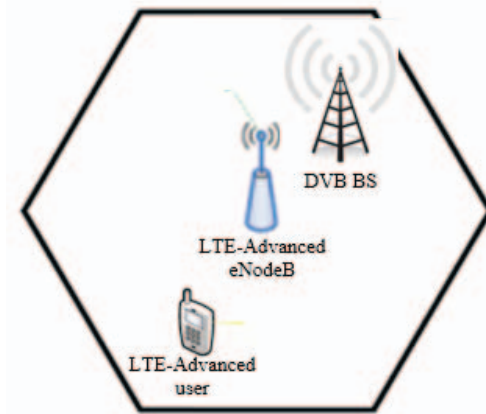


Fig. 1: Downlink cognitive LTE-A topology [15].

$$\mu_{k,l,m}(i) = a_k * \frac{TB_{ki}(i)}{TB_k - RT_{ki}(i)} * \frac{cq_{k,l,m}(i)}{\sum_{l=1}^{CC_{max}} AT_{k,l}(i)} \quad (5)$$

where  $\mu_{k,l,m}(i)$  is the priority of user  $k$  on CC  $l$  on vacant RB  $m$  at time  $i$ ,  $a_k$  is the desired QoS of user  $k$  as defined in Eq. (2), and  $TB_k$  is the content-dependent buffer delay threshold of user  $k$ .  $RT_k(i)$  is the residence time of the HOL packet at the eNodeB of user  $k$  at time  $i$ ,  $cq_{k,l,m}(i)$  is the channel quality of user  $k$  on CC  $l$  on vacant RB  $m$  at time  $i$ ,  $AT_{k,l}(i)$  is the average throughput of user  $k$  on CC  $l$  at time  $i$  (as defined in Eq. (3)) and  $CC_{max}$  is the total number of licensed CCs.

The EM-LWDF has the following similarities with the MM-LWDF. It takes into account the desired QoS of each user, channel quality on each licensed CC and on each vacant RB as well as the average throughput on each licensed CC when making scheduling decisions. The desired QoS allows the EM-LWDF as well as the MM-LWDF to give a slightly higher priority for delay-sensitive RT packets whereas the channel quality enables the multiuser diversity to be exploited (i.e. a user with a good channel quality is favoured for packet transmission over the ones located at the cell edge. This allows the user to receive more packets as the channel quality on vacant RB used for packet transmission is good). If only the channel quality is accounted, then it will starve other users of poor channel qualities. Therefore, the average throughput on each licensed CC is accounted so as to increase fairness among the users by increasing the chances to users whose packets were not selected in the previous time to be scheduled in the consecutive time.

The main difference between the EM-LWDF and the MM-LWDF is the exploitation of the residence time of the HOL. In this case, the MM-LWDF only considers the packets that have resided the longest at the eNodeB ( $RT_k(i)$ ) whereas the EM-LWDF considers the outcome of  $\frac{TB_k}{TB_k - RT_k(i)}$  so as to ensure that the most urgent packets are given a higher priority

than the packets that have resided the longest at the eNodeB. This is one of the attempts made so as to reduce the number of discarded packets for violation of the content-dependent buffer delay threshold and hence reduce the RT and NRT packet loss

### 3. SIMULATION ENVIRONMENT

The performance of the proposed EM-LWDF algorithm was evaluated on the basis of a Packet Loss Ratio (PLR) metric given that it is the most important metric when evaluating the QoS of multimedia performance. Definition of the PLR metric is given as follows:

$$PLR = \frac{\sum_{k=1}^K \sum_{i=1}^T \text{discard\_packet}_k(i)}{\sum_{k=1}^K \sum_{i=1}^T \text{arrive\_packet}_k(i)} \quad (6)$$

where  $\text{discard\_packet}_k(i)$  is the size of discarded packets of user  $k$  at time  $i$ ,  $\text{arrive\_packet}_k(i)$  is the size of packets that arrived at the eNodeB buffer of user  $k$  at time  $i$ ,  $K$  is the total number of users, and  $T$  is the total simulation time.

The performance evaluation was conducted via a computer simulation and the simulation was run for a sufficient length of time to get stable results. The downlink cognitive LTE-A was modelled to contain only one eNodeB. This eNodeB is located at the centre of a cell of 450 m radius. Users are assumed to have uniform distribution within the cell and move at 30 km/h speed. A total of two DVB CCs of 3 MHz bandwidth is assumed and these CCs are of 700 MHz and 704 MHz bandwidths. Given that this paper aims to investigate the performance improvement due to RT and NRT multimedia scheduling in the cognitive LTE-A system, the CCs of the LTE-A are not taken into account in this performance evaluation.

The content-dependent buffer delay threshold for RT and NRT contents are capped at 50 ms and 200 ms respectively. RT and NRT packets are discarded and considered as loss packets if their residence times exceed these thresholds. The PLR threshold for RT multimedia content is limited to  $10^{-3}$  whereas  $10^{-6}$  is the limiting PLR threshold for the NRT content. These thresholds are considered acceptable 3GPP thresholds. Moreover, it is assumed that the RT users are streaming video with 256 kbps average data speed whereas the NRT users are browsing the web. It was assumed that the system has a variable number of RT and NRT users (i.e. 50:50, 75:25 and 25:75) to allow for the collection of more accurate simulation results.

### 4. RESULTS AND DISCUSSION

To assess the EM-LWDF, its performance was evaluated and compared with the well-known Single-User M-LWDF [2] (also referred to as (Single Carrier M-LWDF, SC-MLWDF) and MM-LWDF [3] algorithms. The SC M-LWDF was selected as the benchmark given its popularity and ability to meet the desired multimedia QoS in the single-user wireless systems. Moreover, to investigate M-LWDF in the multi-carrier wireless system, MM-LWDF was considered for benchmarking the EM-LWDF. The results are divided into three subsections for different distribution of RT and NRT cognitive LTE-A users.

#### 4.1 50:50 RT and NRT Cognitive LTE-A Users

RT PLR of the EM-LWDF, SC M-LWDF and MM-LWDF algorithms with increasing number of cognitive LTE-A users is illustrated in Fig. 2. As previously discussed in Section 3, the desired RT QoS is met if the PLR is kept below  $10^{-3}$  (see Threshold line in the figure). The figure depicts that the EM-LWDF outperforms the SC M-LWDF and MM-LWDF in maximizing the number of cognitive LTE-A users at the required RT PLR. Table 1 shows that the EM-LWDF supports 185% and 9.6% more cognitive LTE-A users over the SC M-

LWDF and MM-LWDF algorithms respectively. This improvement can be considered significant as the RT users are streaming video at 256 kbps average data speed.

The NRT PLR performance with increasing number of cognitive LTE-A users of the EM-LWDF, SC M-LWDF and MM-LWDF are demonstrated in Fig. 3. When compared with the RT, the NRT content is more sensitive to lost packets. It requires its PLR to be maintained below  $10^{-6}$  threshold. The figure demonstrates that with increasing number of cognitive LTE-A users, the EM-LWDF has a comparable performance with the MM-LWDF whereas the SC M-LWDF is the worst. However, the threshold of  $10^{-6}$  threshold is exceeded by all three PS algorithms even for a small number of cognitive LTE-A users. This can be considered as acceptable because of the vacancy of the RBs in the downlink cognitive LTE-A (vacant RBs can only be used by the cognitive LTE-A users when licensed DVB users are not active and these cognitive LTE-A users have to compete for these scarce vacant RBs among themselves).

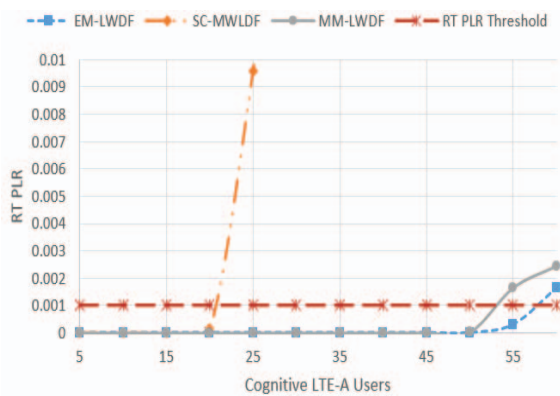


Fig. 2: RT PLR vs Cognitive LTE-A Users 50:50.

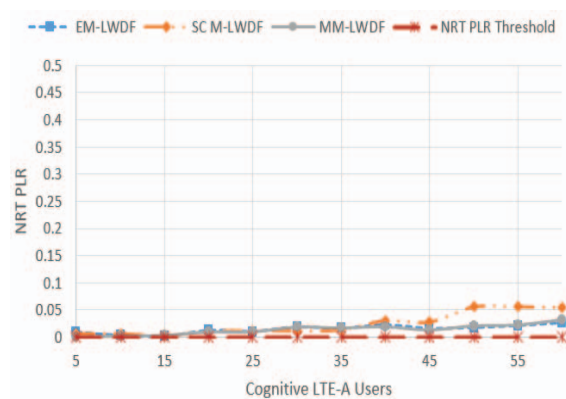


Fig. 3: NRT PLR vs Cognitive LTE-A Users 50:50.

Table 1: Maximum number of cognitive LTE-A users with satisfied QoS of RT contents (50:50)

PS Algorithms	Maximum number of cognitive LTE-A users	Percentage of improvement over benchmark PS algorithms
EM-LWDF	57	-
SC M-LWDF	20	185%
MM-LWDF	52	9.6%

#### 4.2 75:25 RT and NRT Cognitive LTE-A Users

In Fig. 4, the RT PLR performance of EM-LWDF, SC M-LWDF and MM-LWDF are illustrated where 75% of the system capacity is RT cognitive LTE-A users and the remaining 25% is the NRT cognitive LTE-A users. The figure implies that EM-LWDF and MM-LWDF have a significantly greater number of RT cognitive LTE-A users that met the required RT PLR compared to SC M-LWDF. Based on Table 2, the EM-LWDF supports 200% and 15.4% more RT cognitive LTE-A users compared to SC M-LWDF and MM-LWDF, respectively. In comparison with the data in Table 1, the EM-LWDF improves 15% and 5.8% more RT users compared to SC M-LWDF and MM-LWDF respectively in maximizing RT cognitive LTE-A users at the required RT PLR.

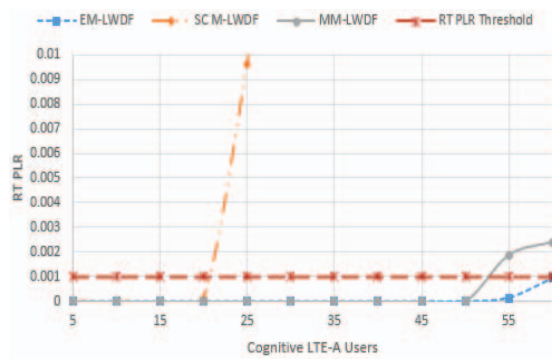


Fig. 4: RT PLR vs Cognitive LTE-A Users 75:25.

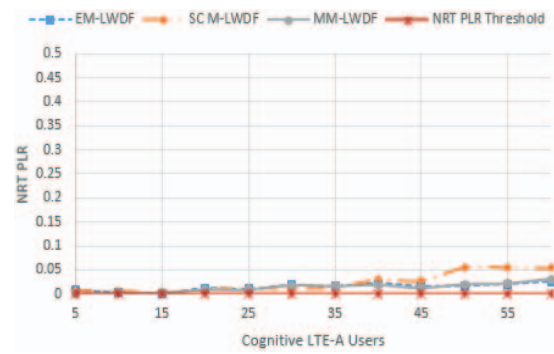


Fig. 5: NRT PLR vs Cognitive LTE-A Users 75:25.

Table 2: Maximum number of cognitive LTE-A users with satisfied QoS of RT contents (75:25)

PS Algorithms	Maximum number of cognitive LTE-A users	Percentage of improvement over benchmark PS algorithms
EM-LWDF	>60	-
SC M-LWDF	20	200%
MM-LWDF	52	15.4%

The NRT PLR performance of EM-LWDF, SC M-LWDF and MM-LWDF when the distribution of RT and NRT cognitive LTE-A users is 75:25 is shown in Fig. 5. It is demonstrated in the figure that similar to the results achieved in sub-section 4.1, all algorithms exceed the NRT PLR threshold. This is due to the NRT contents being more sensitive to packet loss as compared to the RT. However, the figure shows that the EM-LWDF has comparable performance as MM-LWDF while the SC M-LWDF significantly lags behind both algorithms.

### 4.3 25:75 RT and NRT Cognitive LTE-A Users

The RT PLR performance of EM-LWDF, SC M-LWDF and MM-LWDF with 25:75 distributions of RT and NRT cognitive LTE-A users are demonstrated in Fig. 6. It can be seen in the figure that EM-LWDF achieves similar performance compared to MM-LWDF and significantly outperforms the SC M-LWDF algorithm. Table 3 shows that EM-LWDF supports the same number of RT users as MM-LWDF and 130.8% more RT users compared to SC M-LWDF. The SC-MLWDF supports more users (i.e. 26 in 25:75 RT and NRT cognitive LTE-A users distribution as compared to 20 in 75:25 RT and NRT cognitive LTE-A users distribution) because there are smaller number of RT users as compared to NRT users competing for the scarce vacant RBs.

Finally, the NRT PLR that indicates similar performances as in Fig. 3 and Fig. 5 are provided in Fig. 7. The NRT PLR threshold of  $10^{-6}$  is more sensitive compared to the RT PLR threshold of  $10^{-3}$  thus resulting in all of the three algorithms exceeding the NRT PLR threshold. However, EM-LWDF still manages to achieve comparable performance compared to MM-LWDF whereas the performance of the SC M-LWDF significantly degraded. Though the results indicate a fluctuation trend, this does not affect the overall performance of each algorithm given that the scale is very small.

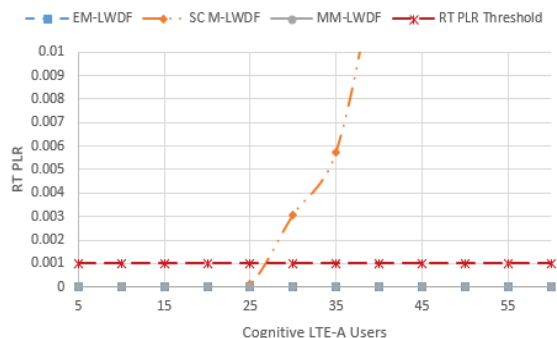


Fig. 6: RT PLR vs Cognitive LTE-A Users 25:75.

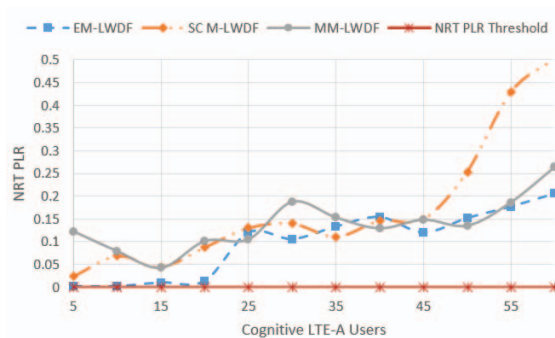


Fig. 7: NRT PLR vs Cognitive LTE-A Users 25:75.

Table 3: Maximum number of cognitive LTE-A users with satisfied QoS of RT contents (25:75)

PS Algorithms	Maximum number of cognitive LTE-A users	Percentage of improvement over benchmark PS algorithms
EM-LWDF	>60	-
SC M-LWDF	26	131%
MM-LWDF	>60	0%

The substantial improvement (especially in maximizing the number of cognitive LTE-A users with the desired RT QoS) of the EM-LWDF over the SC M-LWDF is because the SC M-LWDF assigns all of the vacant RBs to a selected user at each time and on each licensed CC. At a time, a number of vacant RBs in a licensed CC may not be utilized if the packets of the chosen user in the eNodeB buffer have all been transmitted. On the contrary, the EM-LWDF allows efficient use of the vacant RBs at each time and on each licensed CC, by selecting a cognitive LTE-A user for packet transmission on each vacant RB.

The RT PLR of EM-LWDF is slightly better than the MM-LWDF because the algorithm always prioritizes cognitive LTE-A users with the most urgent packets (i.e. the residence time of the packets are approaching the content dependent-buffer delay threshold). This is one of the attempts made so as to reduce the RT PLR where it avoids RT packets from being discarded due to delay violation in the consecutive scheduling time. Even though there is a slight improvement achieved by the EM-LWDF as compared to the MM-LWDF, the EM-LWDF does not introduce any new complexity in its algorithm given that the information of  $TB_k$  and  $RT_k$  are available at the eNodeB packet scheduler. Based on the results obtained in this performance evaluation it can be concluded that when compared with benchmark PS algorithms, the implementation of EM-LWDF in the downlink cognitive LTE-A system is more suited.

## 5. CONCLUSION

An enhanced packet scheduling algorithm known as EM-LWDF is proposed in this paper. The EM-LWDF algorithm was developed to prioritize the user with most urgent packet instead of the user with the packet that has waited the longest. In order to validate this improvement, several performance comparisons have been conducted. The results demonstrated that the proposed algorithm outperforms SC M-LWDF in supporting more

cognitive LTE-A users at the required RT PLR where it supports 185%, 200%, and 131% more cognitive LTE-A users in 50:50, 75:25, and 25:75 distributions of RT and NRT cognitive LTE-A users. The EM-LWDF algorithm also slightly outperforms MM-LWDF algorithm where it supports 9.6% and 15.4% more cognitive LTE-A users at required RT PLR in 50:50 and 75:25 distributions of RT and NRT cognitive LTE-A users and provides similar performance in the 25:75 situation. EM-LWDF achieves this feat without introducing any new complexity in its algorithm as compared to the MM-LWDF. Future works include enhancement of the EM-LWDF such that the desired QoS of the RT and NRT multimedia content can be simultaneously met. Additionally, the performance of the EM-LWDF will be compared with other packet scheduling algorithms that were developed for downlink cognitive LTE-A that simultaneously support RT and NRT multimedia contents. Performance evaluation of the EM-LWDF in multiple hexagonal cells taking the mobility and handover into account as well as with larger number of users (not capped at 60) will also be a part of future study.

## ACKNOWLEDGEMENT

This research is funded by the Kementerian Pendidikan Malaysia under the Grant ID of FRGS/1/2019/TK04/UIAM/02/2.

## REFERENCES

- [1] Osa V, Herranz C, Monserrat JF, Gelabert X. (2012) Implementing Opportunistic Spectrum Access in LTE-Advanced. *EURASIP Journal on Wireless Communications and Networking*, 2012(1): 1-17.
- [2] Andrews M, Kumaran K, Ramanan K, Stolyar A, Whiting P, Vijayakumar R. (2001) Providing Quality of Service over a Shared Wireless Link. *IEEE Communications Magazine*, 39(2): 150-154.
- [3] Ramli HAM. (2014) Performance of Maximum-Largest Weighted Delay First Algorithm in Long Term Evolution-Advanced with Carrier Aggregation. 2014 IEEE Wireless Communications and Networking Conference (WCNC): 1415-1420.
- [4] Aiyetoro G, Takawira F. (2015) A New User Scheduling Scheme in LTE/LTE-A Networks using Cross-Layer Design Approach. *MILCOM 2015 - 2015 IEEE Military Communications Conference*: 1-5.
- [5] Aiyetoro G, Takawira F. (2014) A Cross-Layer Based Packet Scheduling Scheme for Multimedia Traffic in Satellite LTE Networks. 2014 6th International Conference on New Technologies, Mobility and Security (NTMS): 1-6.
- [6] Bahreyni MS, Sattari-Naeini V. (2014) Fairness Aware Downlink Scheduling Algorithm for LTE Networks. *Journal of Mathematics and Computer Science*, 11(2): 53-63.
- [7] Alfayly A, Mkwawa IH, Sun L, Ifeakor E. (2015) QoS-driven LTE downlink scheduling for VoIP application. 2015 12th Annual IEEE Consumer Communications and Networking Conference (CCNC): 603-604.
- [8] Chung YL, Jang LJ, Tsai Z. (2011) An Efficient Downlink Packet Scheduling Algorithm in LTE-Advanced Systems with Carrier Aggregation. 2011 IEEE Consumer Communications and Networking Conference (CCNC): 632-636.
- [9] Mnif K, Masmoudi A, Kamoun L. (2014) Adaptive Efficient Downlink Packet Scheduling Algorithm in LTE-Advanced System. *The 2014 International Symposium on Networks, Computers and Communications*: 1-5.
- [10] Li J, Xu B, Xu Z, Li S, Liu Y. (2006) Adaptive Packet Scheduling Algorithm for Cognitive Radio System. *International Conference on Communication Technology*: 1-5.
- [11] Mansor MIH, Ramli HAM, Asnawi AL, Isa FNM, (2017) Simulation of Packet Scheduling in Cognitive Long Term Evolution-Advanced. *Indonesian Journal of Electrical Engineering & Computer Science* 8(2): 533-540.



- [12] Zhang Y, Zhang Y, Teng Y, Song M (2014) An Efficient Carrier Scheduling Scheme in Cognitive LTE-Advanced System with Carrier Aggregation, IEEE 25th Annual International Symposium on Personal, Indoor, and Mobile Radio Communication (PIMRC): 1970-1974.
- [13] Vijayarani R, Nithyanandan L, (2017) Dynamic Slot-Based Carrier Scheduling Scheme for Downlink Multimedia Traffic Over LTE Advanced Networks with Carrier Aggregation. Turkish Journal of Electrical Engineering & Computer Sciences, 25(4): 2796-2808.
- [14] Kaur R, Kaur N, (2016) A Delay Reduced Scheduling Approach for Fast Spectrum Access in Cognitive Radio. International Journal of Engineering Development and Research, 4(2) 1946-1955.
- [15] Ramli HAM, Isa FNM, Asnawi AL, Jusoh AZ, Azman AW, (2019) Urgency-Aware Scheduling Algorithm for Downlink Cognitive Long Term Evolution-Advanced. IEEE 89th Vehicular Technology Conference (VTC2019-Spring): 1-6.

# STUDY OF MICROSTRIP PATCH ARRAY ANTENNA FOR SIDE LOBE SUPPRESSION IN THE X-BAND REGION USING UNIFORM, BINOMIAL AND TSCHEBYSCHIEFF EXCITATION METHODS

AHMAD ALHADI RUSLAN, SARAH YASMIN MOHAMAD\*,  
KHAIRAYU BADRON, AHMAD FADZIL ISMAIL,  
NORUN FARIHAH ABDUL MALEK AND FARAH NADIA MOHD ISA

*Department of Electrical and Computer Engineering, Faculty of Engineering,  
International Islamic University Malaysia,  
P.O. Box 10, 50728 Kuala Lumpur, Malaysia*

*\*Corresponding author: smohamad@iium.edu.my*

*(Received: 20<sup>th</sup> August 2019; Accepted: 30<sup>th</sup> October 2019; Published on-line: 20<sup>th</sup> January 2020)*

**ABSTRACT:** In this paper, a microstrip patch array antenna is designed and simulated to operate in the X-band frequency region at 9.5 GHz. For X-band communication transmission, it is necessary to suppress the side lobe radiation pattern of the antenna as much as possible to avoid the transmission being intercepted and/or received by undesirable neighbouring satellites. The geometrical design of the microstrip patch array antenna is simulated and executed using CST Microwave Studio (CST MWS) in order to study the effects of various antenna parameters such as  $S_{11}$ , gain, directivity, side lobe level, and angular width. It is shown that the proposed antenna exhibits a low side lobe level of -14.2 dB with an acceptable high gain and directivity of 16.5 dB and 17.7 dB, respectively. The antenna configuration also has a size of only 285 mm × 59.275 mm which is much more compact and lightweight compared to the standard reflector antennas that are used for most X-band communication transmission.

**ABSTRAK:** Kajian ini berkaitan antena cantuman barisan jalurmikro yang direka dan disimulasi beroperasi pada 9.5 GHz frekuensi daerah jalur-X. Pada transmisi komunikasi jalur-X, corak radiasi sisi-lobus antena perlu ditahan sebanyak mungkin bagi mengelak transmisi dipintas dan/atau diterima oleh satelit tetangga yang tidak di ingini. Rekaan geometri antena cantuman barisan jalurmikro disimulasi dan diuji menggunakan perisian CST Studio Gelombang Mikro (CST MWS) bagi mengkaji pelbagai kesan parameter antena seperti  $S_{11}$ , gandaan, keterarahan, tahap sisi-lobus dan lebar sudut. Didapati bahawa antena yang dicadangkan mempunyai tahap sisi-lobus -14.2 dB yang rendah dengan gandaan tinggi yang boleh diterima dan keterarahan sebanyak 16.5 dB dan 17.7 dB, masing-masing. Tatabentuk antena mempunyai saiz 285 mm × 59.275 mm yang kompak dan ringan berbanding antena pemantul piawai, di mana telah digunakan pada kebanyakan jalur-X transmisi komunikasi.

**KEYWORDS:** *array antenna; microstrip antenna; side lobe suppression; X-band communication*

## 1. INTRODUCTION

Microstrip antennas are used for many communication applications and systems due to several advantages. These types of antennas offer benefits in terms of flexibility,

simplicity, and size [1]. Microstrip antennas are usually compact and very lightweight, making them easily portable compared to other types of antennas such as satellite parabolic dishes or reflector antennas, which are more massive and hefty [2]. They also possess a planar structure and provide low fabrication costs [3]. Moreover, reflector antennas have high side lobe levels that make it possible for other parties to intercept the transmitted signals.

In terms of radiation pattern, most microstrip antennas exhibit a directional pattern, where its radiation intensity is mostly directed in a single direction [4]. These accumulated advantages make it very useful in developing and improving communication systems. Nevertheless, despite all these advantages, microstrip antennas also present some drawbacks. While offering a possible compact size structure, the gain and directivity of the antenna is quite low compared to other directional antennas. This, however, can be solved by improvising the microstrip antennas to operate as an array. Array antennas are a group of single element antennas that are arranged and connected in a regular structure [5]. One of the benefits of using the array configurations are the increase in directivity and gain that cannot be achieved using a single element antenna [6].

In this paper, the microstrip patch array antenna is proposed for use in the X-band communication frequency range (8-12 GHz) [7], specifically at 9.5 GHz. The antenna is expected to be compact, portable, exhibit fairly high gain/directivity, and able to reduce the side lobe radiation pattern. As explained earlier, currently used antennas such as parabolic dish antennas have high side lobe levels, as illustrated in Fig. 1. For an excellent X-band communication, the side lobe radiation must be suppressed as much as possible to avoid the transmission being intercepted and/or received by undesirable neighbouring satellites. It should also be noted that much research has been carried out and is still ongoing in order to develop and improve this type of antenna to give better performance [2, 8-12] (summary of recent work can be seen in Table 6). In this project, our proposed microstrip patch array antenna is shown to be able to provide a low side lobe level, with a fairly high gain and directivity, and a compact and lightweight structure.

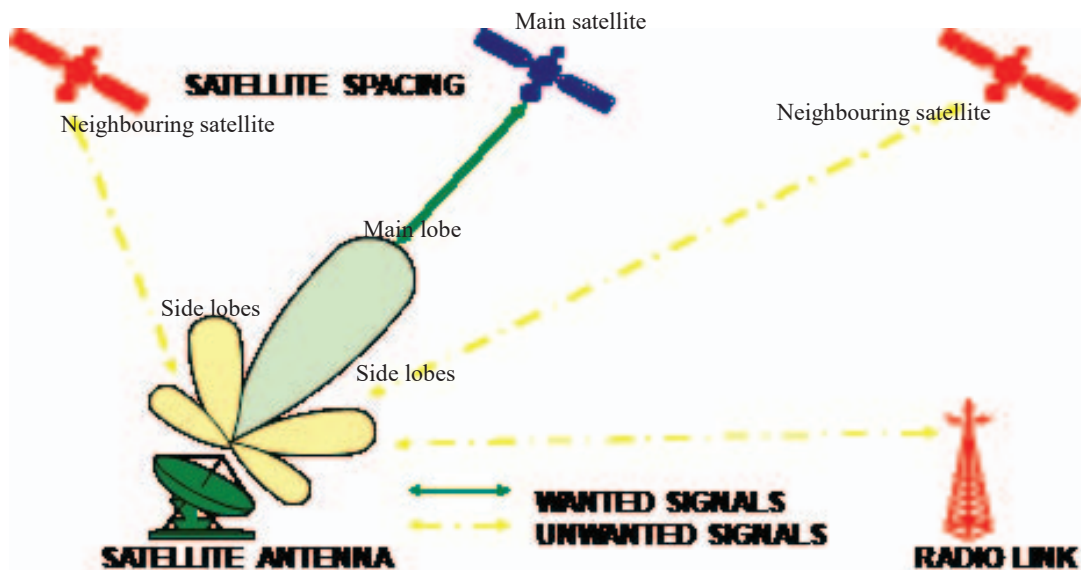


Fig. 1: Parabolic dish antenna radiation pattern with high side-lobe levels.

## 2. DESIGN OF THE MICROSTRIP PATCH ANTENNA

This paper focused on the design of a microstrip patch array antenna for X-band satellite communication. The antenna is designed to work in the X-band region, specifically at 9.5 GHz.

### 2.1 Design of the Single Element Microstrip Patch Antenna

The microstrip patch antenna is initially designed and simulated as a single element (Fig. 2) using a specialized microwave tool, the Computer Simulation Technology (CST) Microwave Studio. The optimized parameters of the antenna are shown in Table 1. The Rogers' RT/duroid 5880 is used as the substrate with a dielectric constant of  $\epsilon_r = 2.2$ , loss tangent of  $\delta = 0.0009$  and thickness of  $t = 1.574$  mm. The ground plane is designed to be larger than the substrate in order to ensure that the direction of the main beam is set to 0 deg. and also to reduce the back lobe radiation [3].

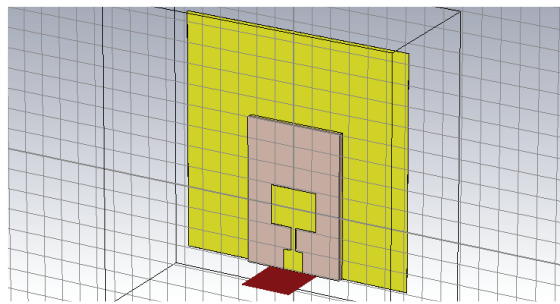


Fig. 2: The single element microstrip patch antenna.

Table 1: Parameters of the single element microstrip patch antenna.

Parameters	Optimized value
Resonant frequency	9.5 GHz
Width of patch	12.163 mm
Length of patch	9.318 mm
$\lambda/4$ feeding line width	1.344 mm
50 $\Omega$ feeding line width	5.044 mm
Dielectric material	RT/duroid 5880
Dielectric constant	2.2
Dielectric height	1.574 mm
Dielectric length	35.275 mm
Dielectric width	25 mm
Ground length	59.275 mm
Ground width	60 mm

### 2.2 Design of the Microstrip Patch Array Antenna

The microstrip patch antenna is further improved to be an array with ten elements (Fig. 3) in order to increase the gain and directivity. The ten elements are selected for the array implementation since the array produced the most optimal results in terms of gain and directivity when the elements are increased. The design parameters for the microstrip patch array antenna are shown in Table 2. The spacing between the patch is set at two different spacing,  $s = 0.5\lambda$  and  $s = 0.75\lambda$ , to compare the effect of these parameters to the simulation performances.

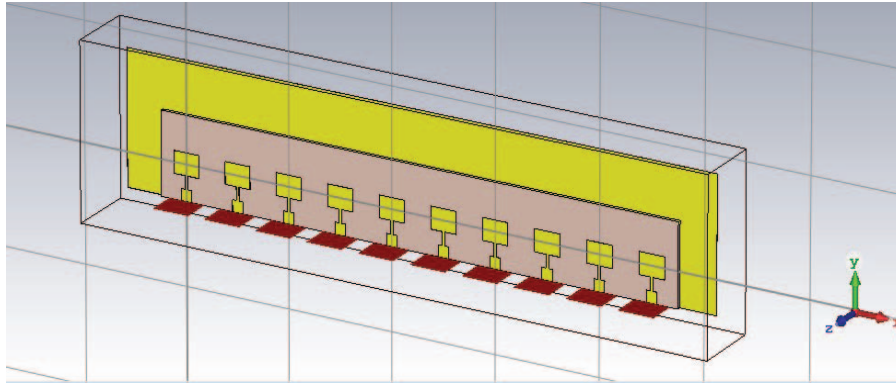


Fig. 3: The microstrip patch array antenna with ten elements.

Table 2: Parameters of the microstrip patch array antenna

Parameters	Optimized value
Resonant frequency	9.5 GHz
Width of patch	12.163 mm
Length of patch	9.318 mm
$\lambda/4$ feeding line width	1.344 mm
50 $\Omega$ feeding line width	5.044 mm
Dielectric material	RT/duroid 5880
Dielectric constant	2.2
Dielectric height	1.574 mm
Dielectric length	35.275 mm
Dielectric width	250 mm
Ground length	59.275 mm
Ground width	285 mm

### 3. SIMULATED RESULTS

#### 3.1 Simulated Results of the Single Element Microstrip Patch Antenna

The simulated results of the single element microstrip patch antenna using the CST Microwave Studio Software are presented. From Fig. 4, it can be observed that the resonant frequency of the microstrip patch antenna is 9.5 GHz with a  $S_{11}$  parameter of -39.11 dB. This proves that the designed antenna radiated well in the intended resonant frequency. Next, the side-lobe level is shown to be -12.345 dB (Fig. 5). It is also observed that the angular width of the microstrip patch antenna is very wide (74.1 deg.). This is inconvenient for the intended satellite communication in the X-band, which requires the beam width to be small enough for the transmission of data. This issue can be solved with an array antenna. Moreover, based on Fig. 6, it is observed that the microstrip patch antenna radiated in a directional pattern, where the gain and directivity of the antenna are 7.44 dB and 8.54 dB, respectively at the main lobe direction of 0 deg. The gain and directivity will be further improved by improvising the single element antenna to be working as an array (results in Section 3.2). The simulated results of the single element microstrip patch antenna in terms of gain (dB), directivity (dB), side-lobe level (dB) and angular width (deg.) are summarized in Table 3.

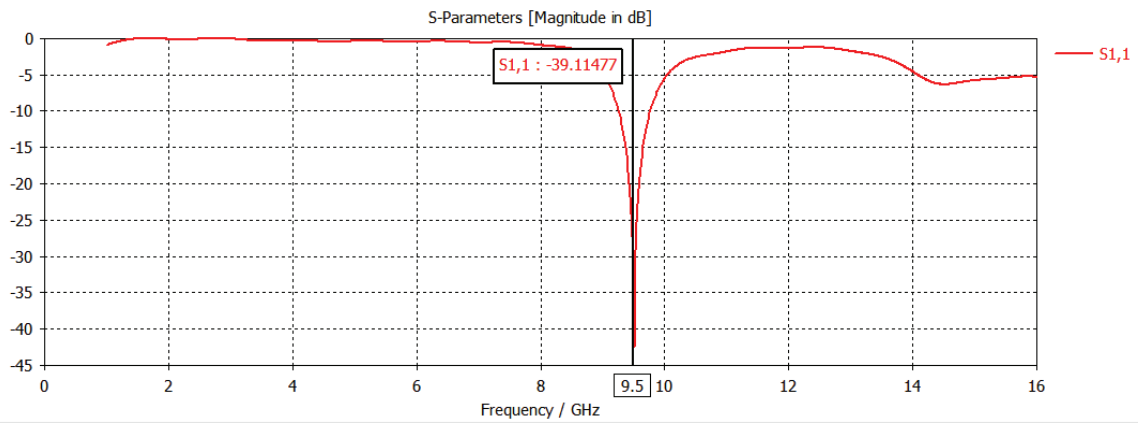


Fig. 4: Return loss for the single element microstrip patch antenna.

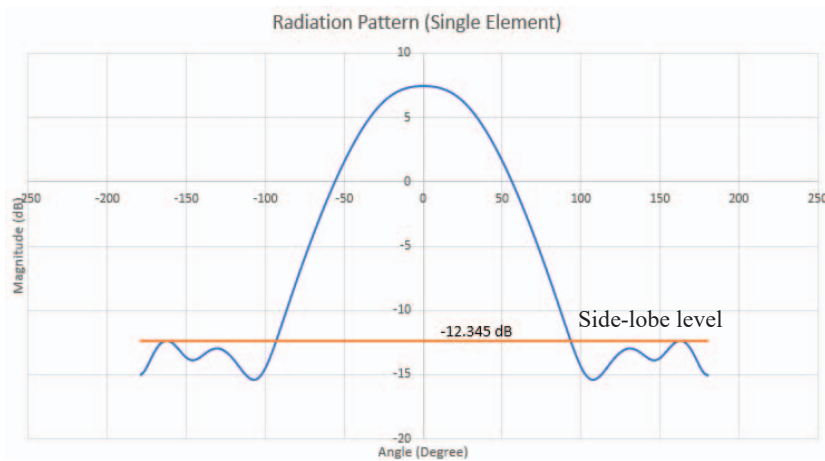


Fig. 5: Side-lobe level for the single element microstrip patch antenna.

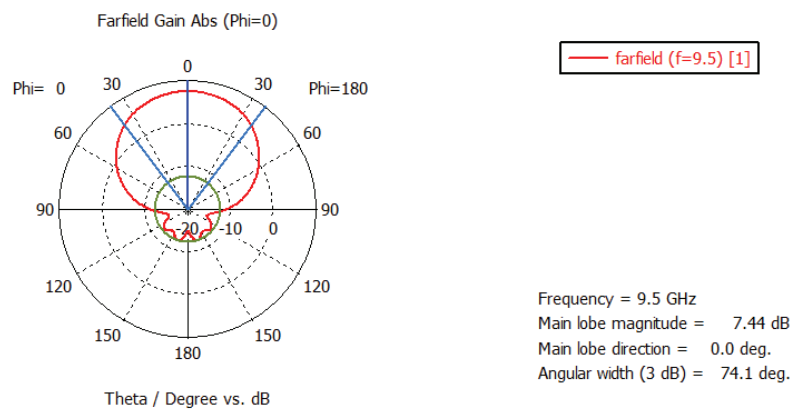


Fig. 6: Radiation pattern for the single element microstrip patch antenna.

Table 3: Simulated results of the single element microstrip patch antenna in terms of gain (dB), directivity (dB), side-lobe level (dB) and angular width (deg.).

Parameters	Optimized value
Gain (dB)	7.44
Directivity (dB)	8.54
Side-lobe level (dB)	-12.345
Angular width (deg.)	74.1

### 3.2 Simulated Results of the Microstrip Patch Array Antenna

As mentioned earlier, the single element antenna is then improved to work as an array with ten elements (Fig. 3) in order to improve some of its performance characteristics. Three types of excitation methods (uniform, binomial, and Tschebyscheff) are applied to the microstrip patch array antenna, which radiates in a directional pattern and is suitable for use in X-band satellite communication. The simulation was run for two different spacings between the patches, i.e.  $s = 0.5\lambda$  and  $s = 0.75\lambda$ , to observe the effect of spacing on the overall performances of the antenna. Figures 7 to 9 show the simulated return loss for the array antenna using uniform, binomial, and Tschebyscheff excitation signals. All three excitation methods resonated well at the targeted frequency of 9.5 GHz. Among the three excitation methods, the Tschebyscheff and binomial signals provided the best return loss with  $S_{11} = -24.56$  dB, followed by the uniform signal with  $S_{11} = -16.46$  dB.

Table 4 shows the simulated results of the microstrip patch array antenna using uniform, binomial, and Tschebycheff excitation methods for the two different spacings. The gain (dB), directivity (dB), side lobe level (dB) and angular width (deg.) of the array antenna can be observed for each method. It can be seen that the uniform signal excitation produced the highest gain of 17.3 dB ( $s = 0.75\lambda$ ) and 15.5 dB ( $s = 0.5\lambda$ ), followed by Tschebycheff with 16.5 dB ( $s = 0.75\lambda$ ) and 14.6 dB ( $s = 0.5\lambda$ ). The binomial amplitude excitation produced the lowest gain among the three with 14.5 dB ( $s = 0.75\lambda$ ) and 12.6 dB ( $s = 0.5\lambda$ ). Furthermore, among the three different types of excitation, the uniform signal excitation produced the highest directivity for both spacings between the patches with 18.5 dB ( $s = 0.75\lambda$ ) and 16.8 dB ( $s = 0.5\lambda$ ). This is followed by Tschebycheff with 17.7 dB ( $s = 0.75\lambda$ ) and 16 dB ( $s = 0.5\lambda$ ), and binomial amplitude excitation with the lowest directivity among the three, with 15.8 dB ( $s = 0.75\lambda$ ) and 14 dB ( $s = 0.5\lambda$ ).

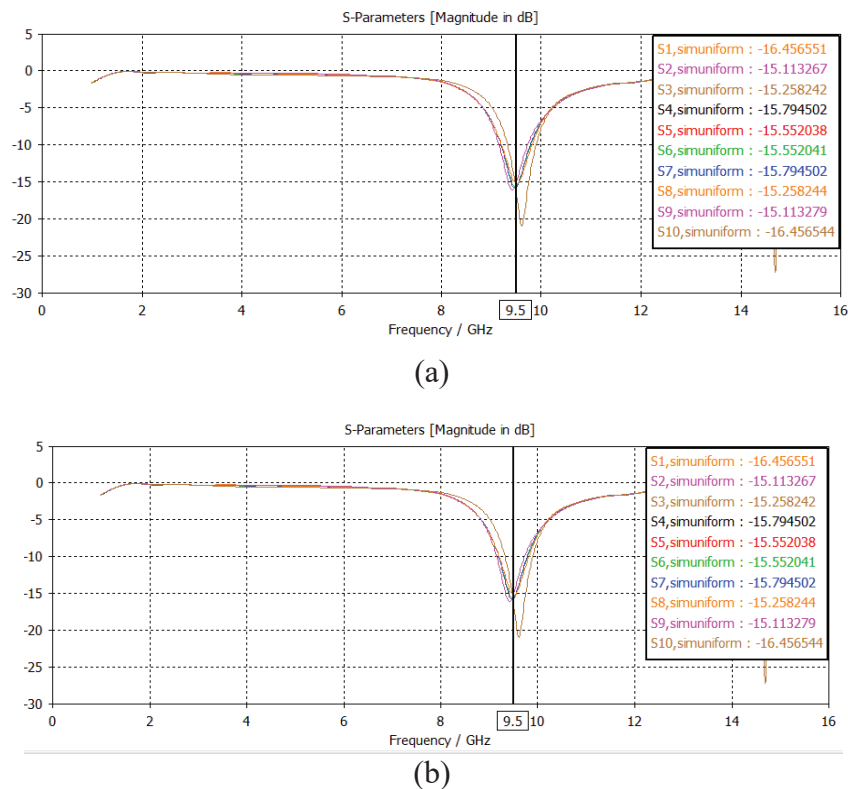


Fig. 7: Return loss for uniform excitation signal with (a)  $s = 0.5\lambda$  and (b)  $s = 0.75\lambda$ .

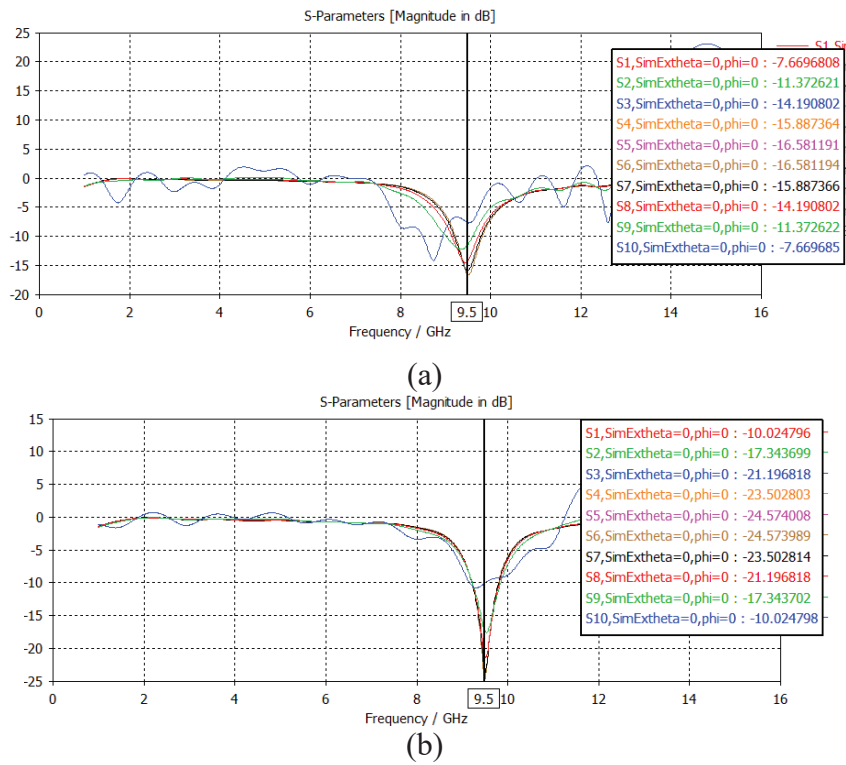


Fig. 8: Return loss for binomial excitation signal with (a)  $s = 0.5\lambda$  and (b)  $s = 0.75\lambda$ .

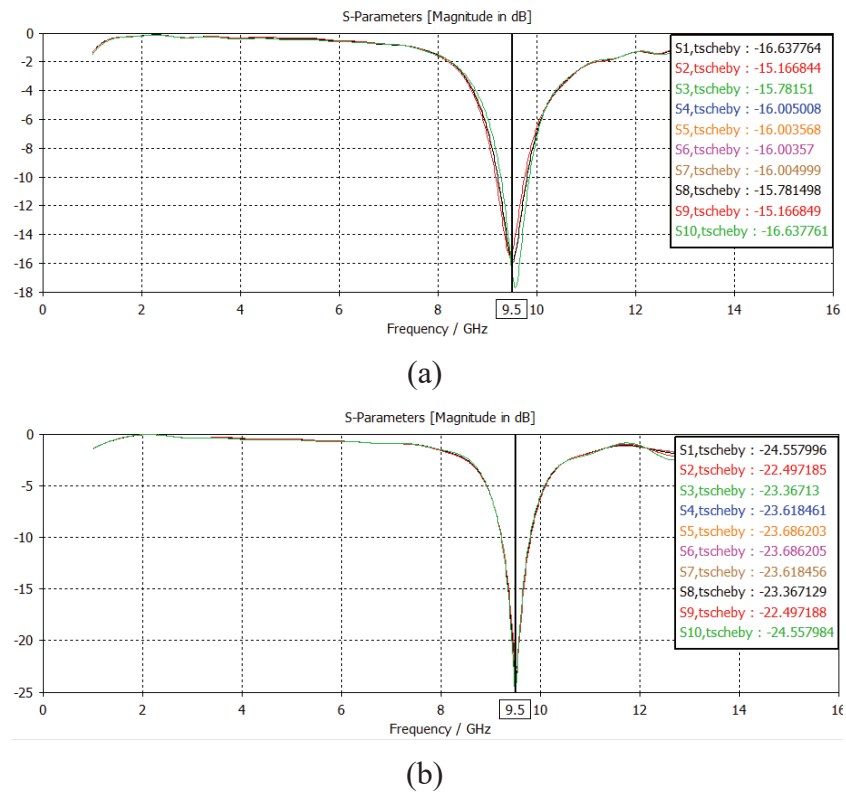


Fig. 9: Return loss for Tschebyscheff excitation signal with (a)  $s = 0.5\lambda$  and (b)  $s = 0.75\lambda$ .



Table 4: Simulated results of the microstrip patch array antenna in terms of gain (dB), directivity (dB), side lobe level (dB) and angular width (deg.) using uniform, binomial and Tschebycheff excitation signals with  $s = 0.5\lambda$  and  $s = 0.75\lambda$ .

Excitation method	Uniform		Binomial		Tschebyscheff		
	Spacing (mm)	$0.5\lambda$	$0.75\lambda$	$0.5\lambda$	$0.75\lambda$	$0.5\lambda$	$0.75\lambda$
Gain (dB)		15.5	17.3	12.6	14.5	14.6	16.5
Directivity (dB)		16.8	18.5	14	15.8	16	17.7
Side lobe level (dB)		2.2	4.2	-55.6	-32.1	-17.3	-14.2
Angular width (deg.)		10.0	6.7	19.9	13.3	12.8	8.6

In terms of side lobe level, binomial amplitude excitation exhibits the lowest level with -55.6 dB ( $s = 0.5\lambda$ ) and -32.1 dB ( $s = 0.75\lambda$ ) as shown in Fig. 11. This is followed by Tschebycheff with -17.3 dB ( $s = 0.5\lambda$ ) and -14.2 dB ( $s = 0.75\lambda$ ) as shown in Fig. 12. The uniform excitation signal exhibits the highest level of side lobes (which resulted the poorest performance) with 2.2 dB ( $s = 0.5\lambda$ ) and 4.2 dB ( $s = 0.75\lambda$ ) as shown in Fig. 10.

Furthermore, in terms of beam width, binomial amplitude excitation produces the widest angular width with 19.9 deg. ( $s = 0.5\lambda$ ) and 13.3 deg. ( $s = 0.75\lambda$ ) among the three amplitude excitation methods. It should be noted that the beam width of the main lobe must be as narrow as possible in the X-band satellite communication system. Therefore, uniform and Tschebycheff methods are more preferable than the binomial method in this case.

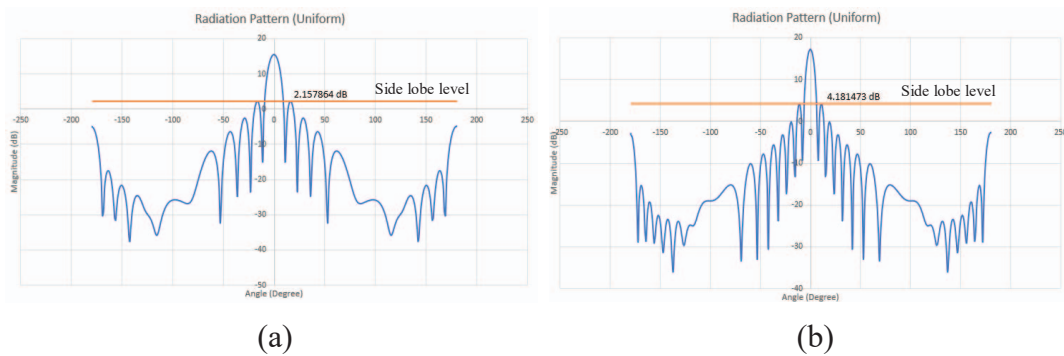


Fig. 10: Side lobe level for uniform excitation signal with (a)  $s = 0.5\lambda$  and (b)  $s = 0.75\lambda$ .

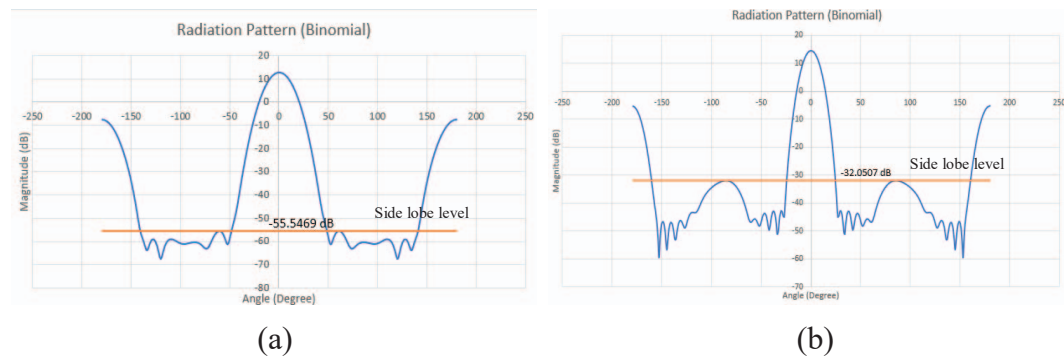


Fig. 11: Side lobe level for binomial excitation signal with (a)  $s = 0.5\lambda$  and (b)  $s = 0.75\lambda$ .

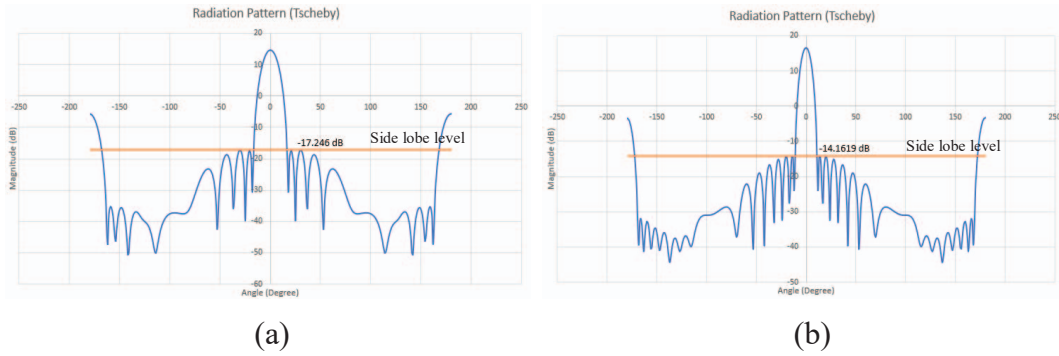


Fig. 12: Side lobe level for Tschebyscheff excitation signal with (a)  $s = 0.5\lambda$  and (b)  $s = 0.75\lambda$ .

Table 5 shows the radiation pattern of the microstrip patch array antenna with uniform, binomial, and Tschebyscheff excitation methods, at two different spacings of  $s = 0.5\lambda$  and  $s = 0.75\lambda$ . Based on these results, the uniform and Tschebyscheff amplitude excitation methods produced the narrowest beam width, which is parallel to their high directivity and gain. However, they also produced the highest side lobe levels, which could risk the signal to be intercepted by neighbouring satellites through the side lobes. The binomial excitation method produced the widest beam width among the three, but with better side lobe level suppression, which will reduce the risk for the signal being intercepted.

Table 5: Radiation pattern of the microstrip patch array antenna with uniform, binomial and Tschebyscheff excitation signal, at two different spacing of  $s = 0.5\lambda$  and  $s = 0.75\lambda$ .

Excitation Method	Radiation Pattern	
	$s = 0.5\lambda$	$s = 0.75\lambda$
Uniform		
Binomial		
Tschebyscheff		

Table 6 concludes the contribution of this work in comparison to previous work done by others [2, 8-12]. By observing the side lobe level of each proposed antenna in the previous work, we can assume that the produced range of side lobe level is in between -10 dB to -20 dB. Through this research, we have proven that the side lobe level can be improved using three different excitation methods. In this work, the side lobe level improved from 4.2 dB to -32.1 dB using binomial excitation and from 4.2 to -14.2 dB using Tschebycheff. Unfortunately, this is gained at the cost of reduced gain and directivity by changing the excitation method from a uniform method to a non-uniform method (binomial and Tschebycheff).

Table 6: Contribution of this work in comparison with previous work [2, 8-12].

Authors	Antenna proposed	No. of element	Freq. band	Resonant freq. (GHz)	Size (mm)	Gain (dB)	Side lobe level (dB)
Chaurasia et al. (2017)	Microstrip antenna	1	X	11	30 (W) × 35 (L)	10.38	N/A
Mao et al. (2017)	Dual-band shared-aperture CP array antenna	4×4	X	8.2	110 (W) × 110 (L)	17.5	-15
		2×2	C	5.3	110 (W) × 110 (L)	14.5	-12.5
Huang et al. (2017)	Circularly-polarized (CP) planar patch antenna array	16×6	Ku	-	340 (W) × 137 (L)	26.4	N/A
Suryana and Madiawati (2016)	Antenna microstrip array	2×16	Ku	14	20 (W) × 5 (L)	17.91	N/A
			Ku	12	20 (W) × 5 (L)	18.69	N/A
So and Chan (2016)	Circularly polarized patch antenna array	16×16	Ku	12	N/A	> 30	N/A
Chen and Yan (2016)	Microstrip phased array antenna	8×12	K	24	N/A	25	-18
This work (tschebycheff)	Microstrip patch array antenna	1×10	X	9.5	285 (W) × 59.275 (L)	16.5	-14.2
This work (binomial)	Microstrip patch array antenna	1×10	X	9.5	285 (W) × 59.275 (L)	14.5	-32.1
This work (uniform)	Microstrip patch array antenna	1×10	X	9.5	285 (W) × 59.275 (L)	17.3	4.2

Practically, implementing the non-uniform excitation method would be difficult to achieve and maintain due to its variation in the excitation amplitude, especially for the

binomial excitation method compared to the Tschebycheff excitation method as in Table 7.

Table 7: Uniform, Tschebyscheff and binomial excitation coefficients.

	Uniform	Tschebyscheff (with major-to- minor lobe ratio of 30 dB)	Binomial
Port1	1	2.5177	1
Port2	1	4.2036	9
Port3	1	6.5436	36
Port4	1	8.5866	84
Port5	1	9.78006	126
Port6	1	9.78006	126
Port7	1	8.5866	84
Port8	1	6.5436	36
Port9	1	4.2036	9
Port10	1	2.5177	1

#### 4. CONCLUSION

In conclusion, a microstrip patch array antenna for side lobe suppression has been developed for use in X-band communication at 9.5 GHz. The antenna performance such as  $S_{11}$ , gain, directivity, side lobe level and angular width have been investigated and discussed. The antenna was first designed as a single element and further modified to work as an array in order to increase the gain and directivity, and also to reduce the beam width, which is convenient for transmission of data for specific satellite communication in the X-band region. Furthermore, the proposed array antenna has been simulated using three different signal excitation methods, which are uniform, binomial, and Tschebyscheff, at two different spacing of  $s = 0.5\lambda$  and  $s = 0.75\lambda$ . Based on the radiation pattern produced, the Tschebycheff amplitude excitation method provides the best antenna performance compared to the other two excitation methods. The proposed antenna configuration has met all the objectives set (i.e. having low side-lobes level of -14.2 dB, an acceptable high gain of 16.5 dB, a directivity of 17.7 dB, an angular width of 8.6 deg., and a compact structure of 285 mm  $\times$  59.275 mm), which is convenient for mobility purposes. Therefore, it can be summarized that our microstrip patch array antenna can be an alternative choice for a future X-band antenna to replace the currently used reflector antennas that are massive, heavy, and produce very high side lobe levels.

#### ACKNOWLEDGEMENT

This research was supported by International Islamic University Malaysia and Ministry of Education Malaysia through Fundamental Research Grant Scheme for Research Acculturation of Early Career Researchers FRGS-RACER (RACER19-053-0053) (RACER/1/2019/TK04/UIAM//1).

## REFERENCES

- [1] Balanis CA. (2016) *Antenna Theory - Analysis and Design*. Hoboken, John Wiley & Sons, Inc.
- [2] Chaurasia RK, Mathur V, Saini AK, Mukherji R. (2017) Design and analysis of microstrip antenna for X-Band communication. *IUP Journal of Telecommunications*, 9(3): 38-43.
- [3] Mohamad S, Cahill R. (2017) Spiral Antenna with reconfigurable HIS using liquid crystals for monopulse radar application. In *Proceedings of the IEEE Conference on Antenna Measurements and Applications (CAMA)*; pp 55-58.
- [4] Mohamad S, Cahill R, Fusco V. (2015) Tri-band HIS Backed Spiral Antenna for Wireless LAN Applications. *Microwave and Optical Technology Letters*, 57(5):1116–1121.
- [5] Balanis CA. (2012) *Advanced Engineering Electromagnetics*. Hoboken, John Wiley & Sons, Inc.
- [6] Rahman DA, Mohamad S, Abdul Malek NF, Rahman DA, Zabri SN. (2018) A wideband mm-wave printed dipole antenna for 5G applications. *Indonesian Journal of Electrical Engineering and Computer Science*, 10(3): 943-950.
- [7] Ahmad Mustafa A M, Mohamad S, Abdul Malek NF, Mohd Isa FN, Md. Rafiqul Islam. (2018) A wideband circularly-polarized spiral antenna for Cube Sat application. *Journal of Telecommunication, Electronic and Computer Engineering*, 10(1-8): 17-20.
- [8] Mao CX, Gao S, Wang Y, Chu QX, Yang XX. (2017) Dual-band circularly polarized shared-aperture array for C-/X- band satellite communications. *IEEE Transaction and Propagation*, 65(10): 5171-5178.
- [9] Huang J, Lin W, Qiu F, Jiang C, Lei D, Guo YJ. (2017) A low profile, ultra-lightweight, high efficient circularly-polarized antenna array for Ku band satellite applications. *IEEE Access*, 5: 18356-18365.
- [10] Suryana J, Madiawati H. (2016) Design and implementation of mobile antenna VSAT with microstrip array based at Ku band frequency. In *Proceedings of the 10<sup>th</sup> International Conference on Telecommunication Systems Services and Applications (TSSA)*.
- [11] So KK, Chan CH. (2016) Circularly polarized patch antenna array for satellite communication in Ku band. In *Proceedings of the IEEE 10<sup>th</sup> European Conference on Antennas and Propagation (EuCAP)*; pp. 1-4.
- [12] ChenLJ, Yan MJ. (2016) Design of 24 GHz microstrip phased array antennas with low side-lobe. In *Proceedings of the IEEE International Conference on Electronic Information and Communication Technology*.

## PAVEMENT CONDITION ANALYSIS VIA VEHICLE MOUNTED ACCELEROMETER DATA

AHMAD JAZLAN<sup>1\*</sup>, MUHAMMAD FAHIM ROSLI<sup>1</sup>, NOOR HAZRIN HANY MOHAMAD HANIF<sup>1</sup>, HASAN FIRDAUS MOHD ZAKI<sup>1</sup>, MUHAMMAD AFIF HUSMAN<sup>1</sup>, ASAN GANI ABDUL MUTHALIF<sup>2</sup> AND DEEPAK KUMAR<sup>3</sup>

<sup>1</sup>Smart Structures, System and Control Research Lab S<sup>3</sup>CRL,  
Department of Mechatronics Engineering, Faculty of Engineering,  
International Islamic University Malaysia, P.O. Box 10, 50728 Kuala Lumpur, Malaysia.

<sup>2</sup>Department of Mechanical and Industrial Engineering, College of Engineering,  
Qatar University, P.O. Box: 2713 - Doha, Qatar.

<sup>3</sup>School Department of Electrical Engineering,  
Motilal Nehru National Institute of Technology, Allahabad, 211004, India.

\*Corresponding author: [ahmadjazlan@iium.edu.my](mailto:ahmadjazlan@iium.edu.my)

(Received: 26<sup>th</sup> August 2019; Accepted: 27<sup>th</sup> November 2019; Published on-line: 20<sup>th</sup> January 2020)

**ABSTRACT:** Road anomalies and irregularities such as potholes and uneven surfaces are a common hazard in South East Asia and developing countries. Such hazards pose a threat to the safety and well-being of both civilians going about their daily routine and tourists who are exploring the city. Since bicycles and rickshaws are still a common mode of transport used by both civilians and tourists in many South East Asian countries, it is essential to improve the overall quality and smoothness of pavements which are traversed by these vehicles. Management of international sporting and recreational events also require satisfactory road and pavement conditions. Before pavement conditions can be improved, it is an essential prerequisite to obtain comprehensive information about road irregularities such as the location and also severity of the road irregularity (depth of the potholes and height of bumps). In this paper, we propose a method for obtaining mathematical models that represent the overall condition of the pavements that are part of a commonly traversed cycling route. Such mathematical models and coefficients can be stored in the cloud of an Internet of Things (IOT) data analytics systems subsequently leading to identification of regions with severe road irregularities.

**ABSTRAK:** Kerosakan pada permukaan jalan raya merupakan salah satu faktor risiko kemalangan yang berlaku secara meluas di negara Asia Tenggara dan negara membangun yang lain. Memandangkan kenderaan seperti beca dan basikal masih diguna pakai secara meluas di negara membangun, adalah mustahak untuk membaiki pulih kerosakan jalan raya. Pengurusan sukan antarabangsa dan rekreasi juga memerlukan keadaan jalan dan laluan pejalan kaki yang baik. Sebelum kerja membaiki pulih dapat dilakukan, maklumat lengkap mengenai tahap kerosakan jalan raya dan lokasi kerosakan diperlukan. Dalam kajian ini satu kaedah telah diperkenalkan untuk mendapatkan persamaan matematik yang menggambarkan keadaan sebenar permukaan jalan raya, di mana sebahagiannya merupakan laluan berbasikal yang selalu digunakan. Model matematik dan pekali ini boleh di simpan dalam sistem analisis data awan Internet Benda (IOT) kemudiannya dapat mengenal pasti kawasan jalan yang rosak dan tidak rata.

---

**KEYWORDS:** road quality monitoring; accelerometer; vibrations; envelope detection

## 1. INTRODUCTION

Cycling is increasingly becoming a preferred means of transport in developing countries due to the awareness of the benefits of daily physical activity and also the awareness of the importance of environmental preservation. In Kuala Lumpur, dedicated cycling lanes have been recently constructed to cater to the increasing number of Malaysian cyclists. Dedicated cycling lanes are a norm in developed countries such as Australia, the UK, and many parts of Europe. Ensuring the smoothness and quality of the roads and pavements is essential for the ride comfort and safety of cyclists and even pedestrians. Uneven surfaces and road irregularities may lead to trips and falls, thus endangering both cyclists and pedestrians alike. Before the local City Council utilizes materials, resources and manpower to repair uneven and irregular road surfaces, it is essential to obtain an overall representation of the condition of the pavements or roads in order to devise an optimal strategy for repair works that efficiently utilize existing resources and manpower.

In this paper, we develop mathematical models that represent the overall condition of a pavement by utilizing vertical Z-axis accelerometer data that have been collected by a sensor package mounted onto the handle of a bicycle. The Z-axis accelerometer data corresponds to vertical vibration of the bicycle, which directly corresponds to the condition of the road. A sensor package consisting of a combination of an ADXL 335 MEMS Accelerometer, an Arduino Nano Microcontroller, and an SD card (for data storage) are mounted onto a bicycle and the subsequent accelerometer data, reflecting the condition of the pavement, are collected and stored in the SD card for further offline data processing and analysis. Mathematical models that describe the condition of the pavement can then be obtained. The location of the pavement irregularity can be estimated with a mathematical model that represents the pavement condition and also takes into consideration the sampling rate used for the accelerometer measurements together with the distance traversed and time taken to reach the destination.

## 2. EXISTING WORK

Existing work regarding road quality analysis utilizing accelerometer data have focused primarily on the road quality analysis of larger roads such as highways. Therefore, in our study, in order to address the current research gap, we have chosen to analyse the road quality of pavements meant for cyclists and pedestrians that cannot be traversed by larger vehicles such as cars and trucks. Nevertheless we describe herewith recent work on road quality analysis to equip the reader with some background knowledge about the current state of the art.

Chenglong et al. developed a system to calculate the International Roughness Index (IRI) in real time based on road quality information collected from wireless accelerometer data and also vehicle position information collected from GPS data [1]. ZigBee and 3G based wireless communication was utilized to transfer information collected from the accelerometers and GPS to a central computer. Field tests conducted in selected locations in Zhejiang demonstrated the feasibility of the proposed system to deliver real-time road quality information.

Xiao Li and Goldberg described the usage of citizen sensing or mobile crowd-sensing in which the public can utilize their smartphones, which have a variety of sensors, in order to collect data in the form of spatial series of the geo-referenced Z-axis accelerations of the road surface [2]. The collected data was then used to compute two novel assessment indexes that represent the road quality.

Harikrishnan and Gopi proposed a method to monitor road surfaces, detect potholes and humps, and predict severity by analysing the vertical vibration signals obtained as the vehicle moved along a particular road [3]. The inbuilt accelerometer inside the smartphone is used to capture the vehicle vibrations in which the z-axis reading corresponds to the vehicle vertical vibrations. A Gaussian model-based mining algorithm has been proposed for detecting road abnormalities. The X-Z ratio filtering had been applied for event classifying and discriminating potholes and humps. A severity estimation algorithm has been proposed that utilized the relation between vertical acceleration and relative vertical displacement of the vehicle. Wickramaratne, Garg and Bauer had developed a simplified approach towards characterizing road surface conditions from vertical acceleration measurements based on a signal transmission model that captures the complete system dynamics of the vehicle suspension system [4].

Mukherjee and Majhi had demonstrated the feasibility of using smartphones placed inside the vehicles in characterisation of road bumps. However, they highlighted that the smartphone's capability of discerning different types of speed bumps while travelling in heterogeneous vehicles is still an open problem [5].

### 3. MAIN WORK

The block diagram of the proposed methodology is shown in Fig. 1. Firstly, vibration signals that reflect the condition of the pavement are collected using a combination of an accelerometer, microcontroller, and SD card that have been mounted onto a bicycle. Alternatively, a portable Data Acquisition Device (DAQ), such as the NI-6008/6009 by National Instruments, together with a laptop could also have been used to record vibration signals from the output of the ADXL 335 accelerometer with a superior sampling rate. However, at this stage of the study, we desired to have a small, light, portable, and detachable package for measuring the vibration signals that reflect the condition of the pavement.

#### 3.1 Data Acquisition

##### 3.1.1 Accelerometer Sensor Package

For this system, we have developed an Accelerometer Sensor Package that consists of an ADXL 335 Microelectromechanical Systems (MEMS) accelerometer, an Arduino Nano Microcontroller, a Micro SD card that is used together with an SPI ICSP Micro SD Card Adapter for data storage, and a 9V rechargeable battery for power supply, as shown in Fig. 2. The ADXL 335 is a tri-axial accelerometer which is capable of measuring vibrations along the X, Y, and Z axes. This combination of components were selected to ensure that the package is small, light, and can be easily fitted onto the handlebar, frame, or any other suitable position on the bicycle that can effectively capture the vibrations generated as the bicycle travels on both smooth and bumpy pavements. In this experiment, the bicycle speed will be monitored using an app installed on a smartphone. Figure 2 shows the Accelerometer Sensor Package together with its components whereas Fig. 3 shows the placement of the ASP and smartphone on the handlebar of the bicycle.



Although the ADXL 335 MEMS accelerometer is capable of measuring vibrations along the X, Y, and Z axes, in this study we are primarily concerned with the vibrations generated along the Z axis since the vibrations recorded along the Z axis correspond to vertical vibrations of the bicycle as the bicycle is traveling along the pavement which corresponds to the degree of smoothness of the pavement. The sampling rate of the Arduino Nano microcontroller is set at 50 samples per second. This selected sampling rate adheres to the Nyquist criteria in order to prevent signal aliasing.

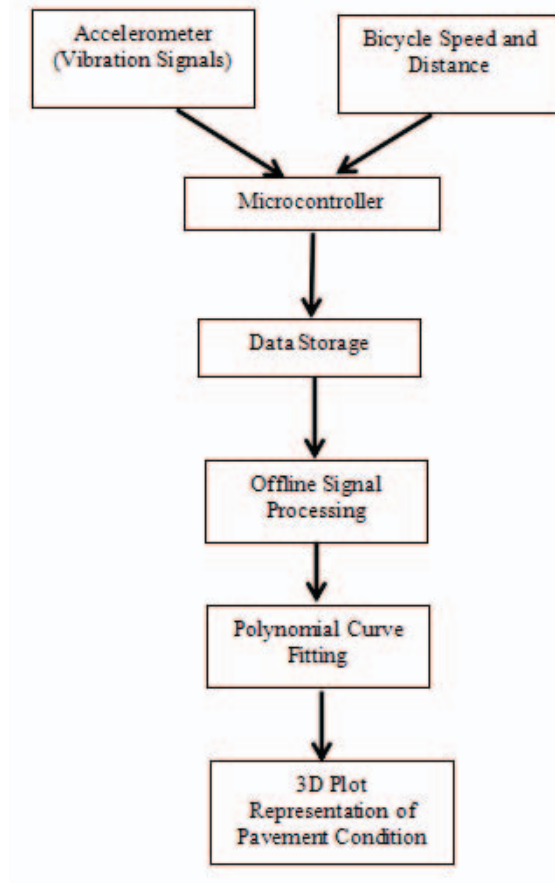


Fig. 1: Block diagram of the proposed methodology for pavement condition monitoring.

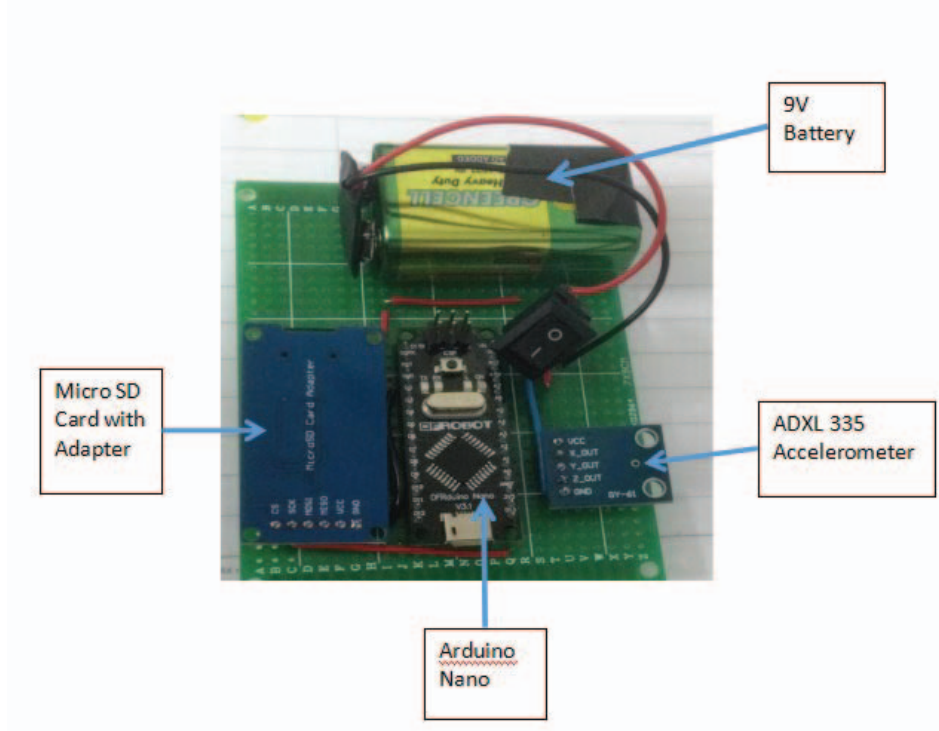


Fig. 2: Accelerometer sensor package.

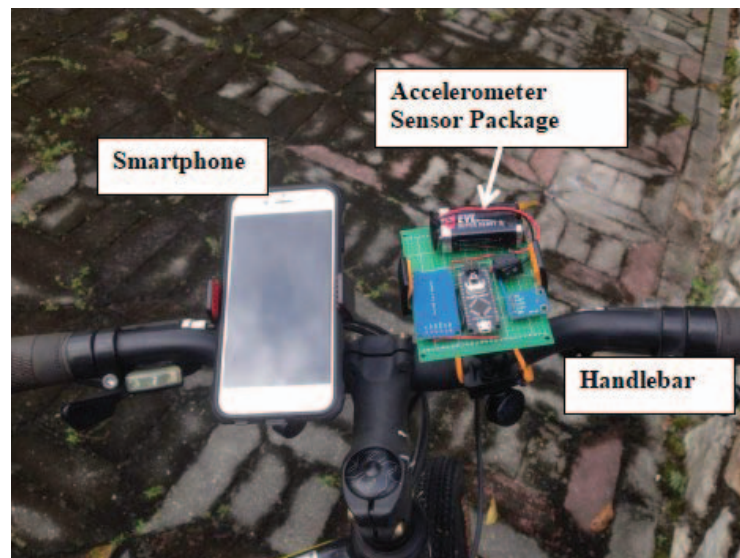


Fig. 3: Accelerometer Sensor Package and smartphone placement on bicycle handlebar.

### 3.1.2 Vibration Data Collection

In this study, pavements located on two separate cycling routes were chosen for the vibration data measurement and analysis. The first cycling route consists of a smooth pavement, as shown in Fig. 4 (left), whereas the second cycling route consists of an uneven pavement with irregularities due to branching roots from a nearby tree, as shown in Fig. 4 (right). The distance travelled by the bicycle on both routes was set to 50 meters. The width of the road was 1.5 meters.

In this study, we are primarily concerned with the acceleration data recorded along the vertical Z axis since this data best reflects the pavement condition. Accelerometer data

from the X and Y coordinates are discarded in this study. During the bicycle ride in each region, the speed of the bicycle was fixed at 5km/h and the distance travelled was 45 meters. An app installed on the smartphone was used to keep track of the speed of the bicycle and also of the distanced travelled by the cyclist. Fig. 5 shows the pavement that has been divided into 10 regions. Each region will be traversed by the bicycle and data corresponding to the overall pavement condition in each region has been collected.



Fig. 4: Smooth pavement (left) and uneven pavement with irregularities (right).

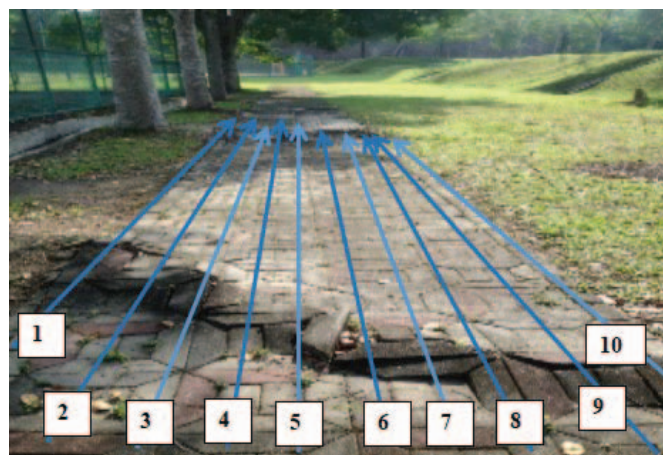


Fig. 5: Division of pavement into 10 regions which will be traversed by the bicycle.

### 3.2 Signal Processing

In order to extract meaningful information regarding the condition of the pavement in each of these 10 regions traversed by the bicycle from the accelerometer data, the raw accelerometer data needs to be processed in order to reveal the presence of significant irregularities on the pavement such as potholes and bumps and also the severity of the irregularity. For example deeper potholes or higher bumps on the pavement will result in higher amplitudes of the accelerometer data collected. This is one of the advantages of analyzing the condition of the pavement with accelerometer data compared to computer vision based methods. Computer vision based methods are able to accurately detect the location of a road anomaly whatever the depth or severity but the irregularity cannot be fully captured and analyzed using computer vision based methods alone [6-10].

### 3.2.1 Envelope Detection

The accelerometer data collected from each of the regions (Region 1 to Region 10) reflects the condition of the pavement, as shown in Fig. 6 to Fig. 10. All the raw data have been full wave rectified to eliminate all the negative values in the results. In this paper an envelope detection method that consists of a combination of calculating the absolute value of the raw accelerometer data (full wave rectification) combined with low pass filtering with a very low cut off frequency is implemented to obtain an envelope of the raw accelerometer data. The amplitude of the enveloped signal is a representation of the severity of the irregularity. A low pass filter was designed in order to complete the envelope detector design. Figure 11 shows the magnitude response for a 51st order FIR low pass filter with a cut off frequency of 13 Hz that was used for the envelope detection method and was designed using the Matlab filter design toolbox.

### 3.2.2 Offset Correction

Before envelope detection is performed, another preprocessing method known as offset correction is required. Offset correction is required since the accelerometer is highly sensitive even to minute variations in the evenness of the pavement, which are insignificant to our analysis and do not correspond to significant irregularities of the pavement such as bumps and potholes. Therefore, baseline accelerometer measurements are required. Baseline measurements are obtained by logging accelerometer measurements while the bicycle is travelling on a smooth pavement with no significant irregularities. The accelerometer data obtained by any other accelerometer measurement will then be subtracted with the average of the baseline measurements resulting in offset correction. Offset correction ensures that insignificant accelerometer readings that represent minute variations in the pavement are discarded from the analysis of the pavement condition. From test rides conducted on a smooth road, it was found that the highest signal amplitude is  $0.2 \text{ m/s}^2$ . Therefore, all collected data will be subtracted by this value resulting in the offset corrected results shown in Fig. 12 to Fig. 14. The offset corrected data gives a better indication of which parts of the pavement contain significant irregularities such as potholes and bumps.

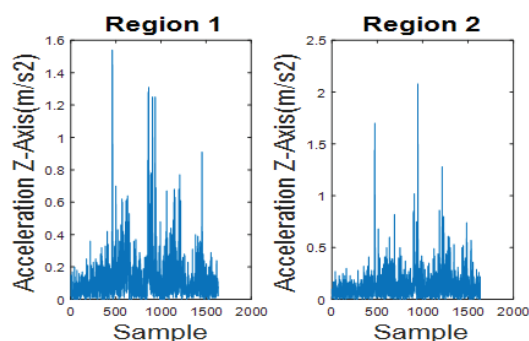


Fig. 6: Rectified accelerometer data for regions 1-2.

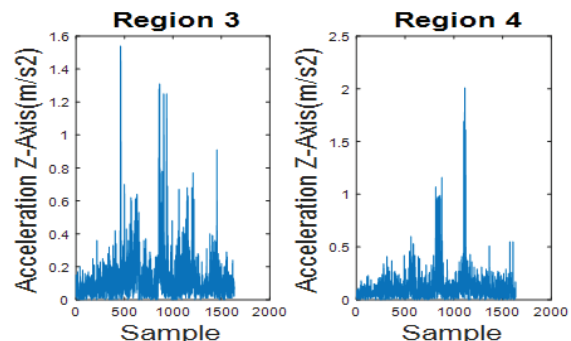


Fig. 7: Rectified accelerometer data for regions 3-4.

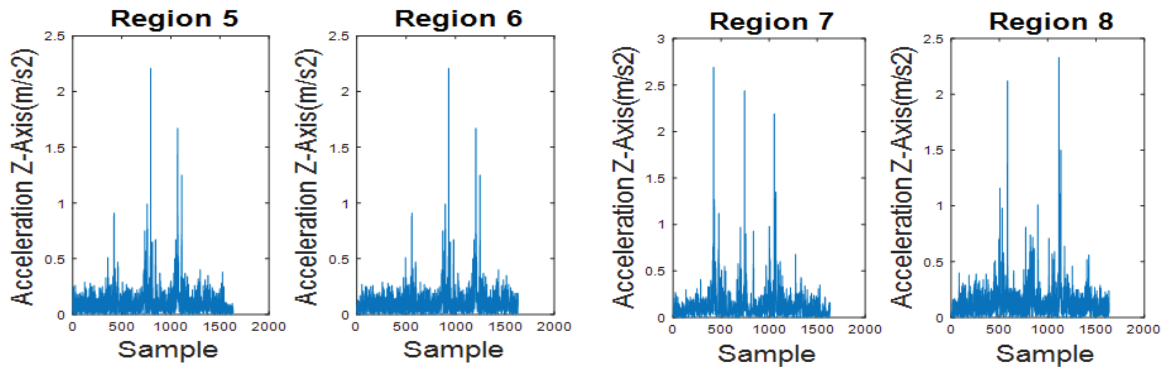


Fig. 8: Rectified accelerometer data for regions 5-6.

Fig. 9: Rectified accelerometer data for regions 7-8.

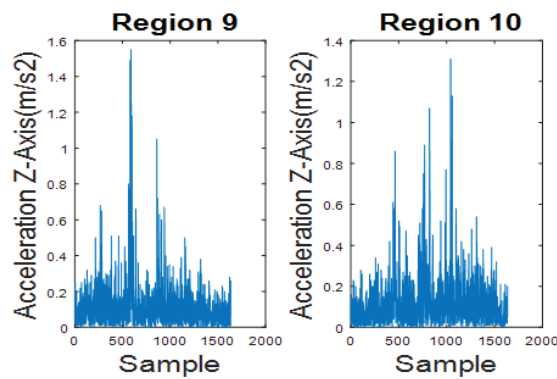


Fig. 10: Rectified accelerometer data for regions 9-10.

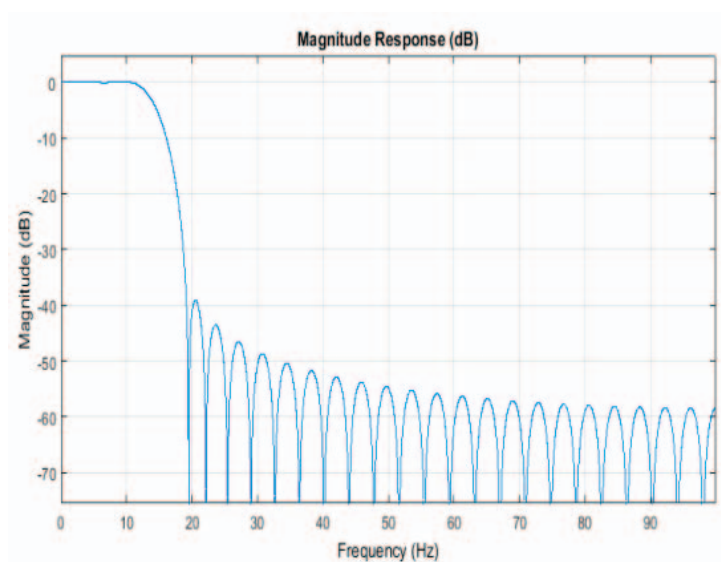


Fig. 11: Magnitude response of FIR low pass filter used for envelope detection.

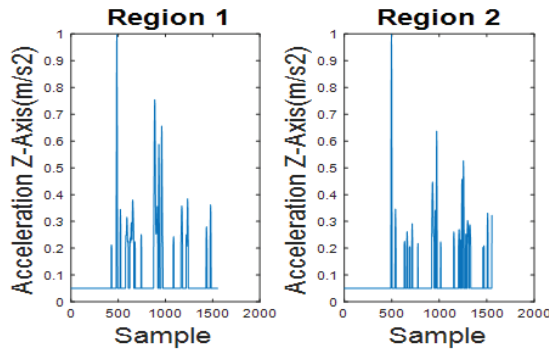


Fig. 12: Offset corrected accelerometer data for regions 1-2.

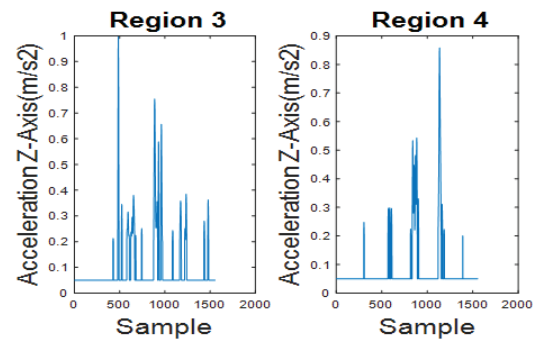


Fig. 13: Offset corrected accelerometer data for regions 3-4.

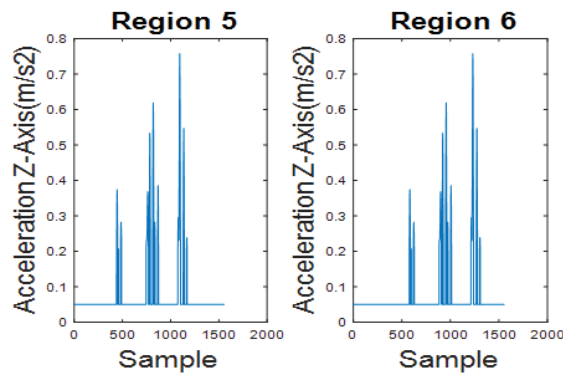


Fig. 14: Offset corrected accelerometer data for regions 5-6.

### 3.2.3 Polynomial Curve Fitting

Polynomial curve fitting can be utilized in order to obtain a mathematical polynomial model that represents the condition of the pavement at each of the regions from 1 to 10. Polynomial curve fitting has been applied to all of the data presented in Fig. 6 to Fig. 8 resulting in polynomial functions that reflect the condition of the pavement. The polynomial functions that correspond to each of the regions are represented by  $Y_1(s)$  to  $Y_{10}(s)$  as shown below.

$$Y_1(s) = 0.00000015s^{60} \dots - 0.0003s^2 + 0.0033s - 0.357 \quad (1)$$

$$Y_2(s) = 0.00000021s^{60} \dots - 0.001s^2 + 0.0103s + 0.0274 \quad (2)$$

$$Y_3(s) = 0.00000011s^{60} \dots - 0.0003s^2 + 0.0033s + 0.0357 \quad (3)$$

$$Y_4(s) = 0.00000001s^{60} \dots - 0.001s^2 + 0.0155s - 0.0363 \quad (4)$$

$$Y_5(s) = 0.00000005s^{60} \dots - 0.0001s^2 - 0.0053s + 0.0907 \quad (5)$$

$$Y_6(s) = 0.00000003s^{60} \dots + 0.0009s^2 - 0.0134s + 0.1167 \quad (6)$$

$$Y_7(s) = 0.00000009s^{60} \dots + 0.0011s^2 - 0.0185s - 0.1516 \quad (7)$$

$$Y_8(s) = 0.00000005s^{60} \dots + -0.0003s^2 + 0.0056s + 0.0189 \quad (8)$$

$$Y_9(s) = 0.00000004s^{60} \dots + 0.0018s^2 - 0.0287s + 0.1963 \quad (9)$$

$$Y_{10}(s) = 0.00000008s^{60} \dots + 0.0004s^2 + 0.0036s + 0.0455 \quad (10)$$

Figure 15 shows the rectified and offset corrected accelerometer data from Region 5, together with the graph of the polynomial approximation function of this data. From these graphs it becomes apparent that there are three significant irregularities of the road that could be due to uneven surfaces due to branching roots, potholes, or other road/pavement construction factors such as uneven bricks. Upon obtaining the polynomial approximation together with prior knowledge of the speed of the bicycle, the sampling rate used for the accelerometer data collection, and the distance of the road, we can determine the location of the irregularity and subsequently manpower and resources can be effectively utilized for the pavement/road repair works. Finally, the processed accelerometer data, either by envelope detection or polynomial approximation, can be extrapolated and combined to form a 3D plot that is an overall representation of the condition of the pavement, as shown in Fig. 16 and Fig. 17.

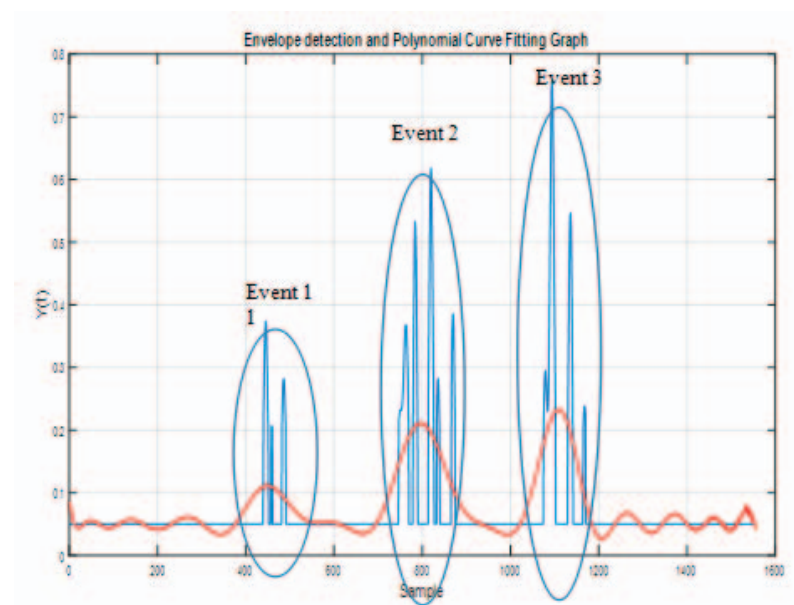


Fig. 15: Processed accelerometer data indicating 3 pavement irregularities together with corresponding polynomial approximation.

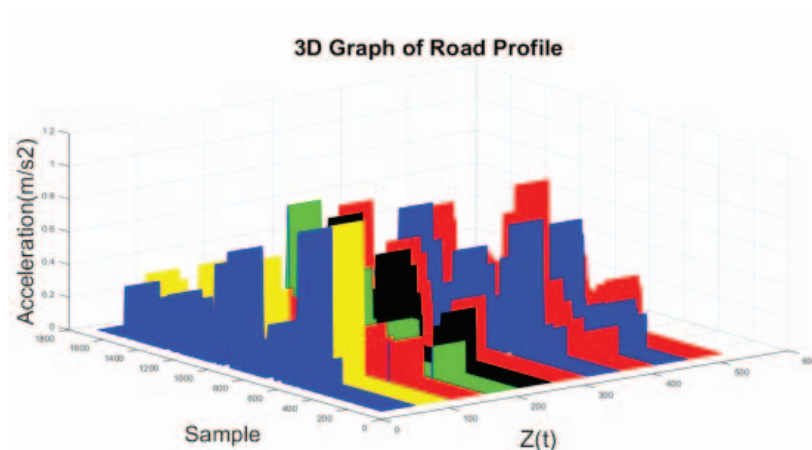


Fig. 16: 3D plot of pavement condition - extrapolated envelope detection data.

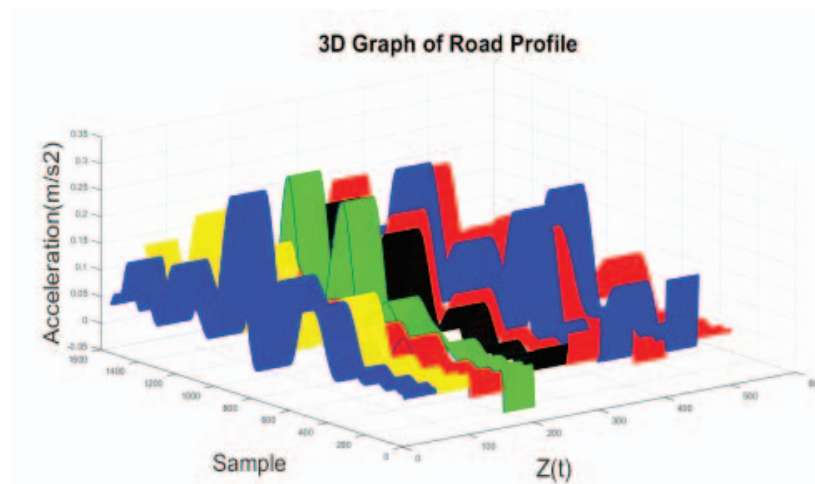


Fig. 17: 3D plot of pavement condition - extrapolated polynomial approximation data.

#### 4. CONCLUSION

In conclusion, a method for obtaining mathematical models that represent the overall pavement conditions has been proposed using bicycle-mounted accelerometer data. The proposed method based on accelerometer data is advantageous compared to image processing methods since the severity of the irregularity can be effectively captured by accelerometers. For future work, the proposed technique can be further extended by placing Accelerometer Sensor Packages on multiple bicycles or vehicles that are traversing the same route. Each Accelerometer Sensor Package can be equipped with an antenna to send the collected data to a gateway resulting in a complete Internet of Things (IOT) application.

#### ACKNOWLEDGEMENT

The authors would like to thank the Ministry of Education Malaysia for funding this research project under the Fundamental Research Grant Scheme - Grant No: FRGS19-057-0665 and FRGS16-053-0552 and also the International Islamic University Malaysia for funding this research under the Research Initiative Grant Scheme - Grant No: RIGS17-152-0727.

#### REFERENCES

- [1] Liu C, Wu D, Du Y, Li S. (2016) Application of vehicle mounted accelerometers to measure pavement roughness. *International Journal of Distributed Sensor Networks*, 12(6):1-8.
- [2] Li X, Goldberg DW. (2018) Towards a mobile crowdsensing system for road surface assessment. *Computers, Environment and Urban Systems*, 69: 51-62.
- [3] Harikrishnan PM, Gopi VP. (2018) Vehicle vibration signal processing for road surface monitoring. *IEEE Sensors Journal*, 17(16): 5192-5197.
- [4] Wickramaratne T, Garg V, Bauer P. (2018) On the use of 3-D accelerometers for road quality assessment. *Proceedings of the 2018 IEEE 87th Vehicular Technology Conference (VTC Spring)*, Porto, pp. 1-5.
- [5] Mukherjee A, Majhi S. (2016) Characterisation of road bumps using smartphones. *European Transport Research Reviews*, 8(13):16-20.
- [6] Ryu S-K, Kim T, Kim Y-R. (2015) Image-based pothole detection system for ITS service and road management system. *Mathematical Problems in Engineering*, 968361, pp. 1-10.



- 
- [7] Wang P, Hu Y, Dai Y, Tian M. (2017) Asphalt pavement pothole detection and segmentation based on wavelet energy field. *Mathematical Problems in Engineering*, 1604130, pp. 1-13
  - [8] Fernandez C, Fernandez-Llorca D, Sotelo MA. (2017) A hybrid vision-map method for urban road detection. *Journal of Advanced Transportation*, 7090549, pp. 1-21.
  - [9] Jo Y, Ryu S. (2015) Pothole Detection System Using a Black-box Camera. *Sensors*, 15(1): 29316-29331.
  - [10] Fernández C, Fernández-Llorca D, et al. (2012) Free space and speed humps detection using lidar and vision for urban autonomous navigation. *Proceedings of the 2012 IEEE Intelligent Vehicles Symposium*, pp. 698-703.

## PERFORMANCE ANALYSIS OF 5G PATH LOSS MODELS FOR RURAL MACROCELL ENVIRONMENT

MUHAMMAD AKRAMUDDIN MOHD NORDIN AND HUDA ADIBAH MOHD RAMLI

*Department of Electrical and Computer Engineering, Faculty of Engineering,  
International Islamic University Malaysia,  
P.O. Box 10, 50728 Kuala Lumpur, Malaysia.*

*\*Corresponding author: hadibahmr@iium.edu.my*

*(Received: 27<sup>th</sup> September 2019; Accepted: 27<sup>th</sup> November 2019; Published on-line: 20<sup>th</sup> January 2020)*

**ABSTRACT:** 5G networks are expected to use the Millimeter Wave (mmWave) frequency band and this frequency provides wider bandwidth allowing a better quality of service to be offered to the users. However, the mmWave frequencies may lead to a higher path loss due to several factors including blockages, rain and atmosphere. Therefore, to allow optimal positioning of the 5G base stations, the study of path loss model in this 5G mmWave frequencies is crucial. This paper investigates the 5G path loss models as well as their parameters that are most suitable for cross-polarized antennas under rural macrocell environment in Malaysia. Path loss models namely Close In Free Space Reference Distance Path Loss Model (CI) model, and Alpha Beta Gamma (ABG) or Floating Intercept (FI) Model along with their parameters achieved from the previous studies were evaluated by comparing the parameters and models that are closest to the sampled path loss when using antennas that have different patterns and polarizations in an open-source simulator. Results obtained indicate that FI model can be adapted to the majority of the environment where this model showed the lowest Root Mean Square Error (RMSE). The study of path loss models by using advanced simulator or field measurement, and studies on other rural areas from other states in Malaysia will be considered in future works.

**ABSTRAK:** Rangkaian 5G dijangka menggunakan jalur frekuensi Gelombang Milimeter (mmWave) dan frekuensi ini menyediakan jalur lebar yang lebih lebar membolehkan kualiti servis yang lebih baik untuk para pengguna. Walau bagaimanapun, frekuensi mmWave mungkin menyebabkan kehilangan penyebaran yang tinggi disebabkan beberapa faktor seperti halangan, hujan dan atmosfera. Oleh itu, untuk membolehkan stesen pangkalan 5G berada dalam kedudukan optimum, kajian model kehilangan penyebaran dalam frekuensi mmWave untuk rangkaian 5G ini sangat penting. Kertas ini menyiasat beberapa model kehilangan penyebaran rangkaian 5G serta parameter yang paling sesuai untuk antenna polarisasi-silang dalam persekitaran sel makro luar bandar di Malaysia. Model-model kehilangan penyebaran iaitu Model Kehilangan Penyebaran Berdekatan Ruang Bebas Bersama Rujukan Jarak (CI), dan Model Alpha, Beta, Gamma (ABG) atau dipanggil Model Pintasan Apungan (FI) telah dinilai dengan membandingkan beberapa parameter dan model yang paling hampir dengan kehilangan penyebaran yang sudah disampel apabila menggunakan antenna yang mempunyai corak dan polarisasi yang berbeza melalui simulator sumber-terbuka. Kajian ini mendapati bahawa model FI boleh diadaptasi ke persekitaran majoriti di mana model ini menunjukkan prestasi statistik punca min ralat kuasa dua (RMSE) yang terendah. Kajian model-model kehilangan penyebaran ini akan mempertimbangkan penggunaan simulator yang canggih atau

pengukuran lapangan, dan juga kawasan luar bandar di negeri-negeri lain di Malaysia untuk kerja masa akan datang.

---

**KEYWORDS:** 5G networks; path loss modelling; rural macrocell

## 1. INTRODUCTION

The Fifth Generation (5G) network is expected to provide a better quality of multimedia services for significantly larger number of mobile phone users [1,2]. To achieve this expectation, the standardization bodies proposed the Millimeter wave (mmWave) frequencies (i.e. the frequency range of 3 GHz to 300 GHz) to be used for the 5G given that the lower range of frequencies are mostly congested [2,3]. However, it was found in a number of studies that the mmWave has implementation issues especially in terms of path loss. For example, the study conducted by [4] shows that path loss in mmWave frequency at shorter distance under non-line of sight (NLOS) condition is above 100 dB. This indicates that mmWave frequencies is very sensitive to certain factors such as rain, atmosphere and blockages [5]. Based on this observation and given the importance of path loss in the network planning for optimal installation of 5G base stations, path loss needs to be accurately modelled.

There are a number of well-known path loss models proposed for use in the 5G networks. The basic path loss models include Close-in Free Space with Reference Distance (CI), and Alpha, Beta, Gamma (ABG) or Floating Intercept (FI) [1,6]. The majority of the other path loss models are derived by modifying the values of the path loss parameters of these basic models. However, it is difficult to obtain the optimal values of path loss parameters due to several factors such as different areas and countries, environment, and type of antennas. This lead to inaccurate optimal values of path loss parameters been established. Given this limitation, this paper will focus on finding the optimal values of path loss parameters in Malaysia context.

Besides the limitation previously stated, another limitation include the existing studies did not highlight the type of antenna polarization been used as well as the line of sight (LOS) or NLOS conditions been assumed. For instance, research conducted in [4] focus on different polarizations at LOS condition but fail to state the antenna polarization type use at NLOS condition. Another example is the work in [7] that do not mentioned the antenna polarization type been used. Given the newly stated limitation, this paper will be investigate on the 5G path loss model for the case of cross-polarized antennas. Cross-polarized antennas can be described as a polarization type where the transmitter transmits different polarization to the receiving antenna. According to [8], multiple and reconfigurable polarization of antennas (which includes cross-polarized antennas) will be used for 5G network implementation. Therefore, this shows the importance to study on 5G path loss model for cross-polarized antennas.

Besides the limitations on antenna polarizations, limited studies have been conducted in rural macrocell areas. Only research in [9] and [10] focused in this type of area. However, these two researches focused for CI model and its modification only. There could be possibility that FI or ABG models could be suitable for this area. Therefore, this research will utilizes these path loss models to identify whether these models are suitable for rural macrocell areas in Malaysia. Rural macrocell can be defined as larger coverage of cell sizes for undeveloped and less populated areas[11]. Although most 5G path loss studies were conducted in urban areas, the study for rural areas seems to be important as 5G network will also be implemented in rural areas in near future. Hence, by combining

all the limitations of the existing studies, this paper will investigate the performance of 5G path loss models based on their optimal values of path loss parameters for cross-polarized antennas in Malaysia's rural macrocell environment. It should be noted that identification of the optimal values of the path loss parameters will be based on the values achieved from previous studies [4,6,7,9,10,12-14].

The remaining sections of this paper is described as follows. Section 2 explains the well-known path loss for 5G networks followed by Section 3 that highlights on the research methodology. Section 4 analyzes the results obtained while conclusion and improvements of this research are discussed in Section 5.

## 2. WELL-KNOWN PATH LOSS MODELS FOR 5G NETWORKS

The basic path loss models investigated in this paper are Close-In Free Space Reference Distance Path Loss Model (CI) and Floating Intercept or Alpha-Beta-Gamma Model (FI or ABG). Each model is described next.

### 2.1 Close-In Free Space Reference Distance Path Loss Model (CI)

The first basic path loss model for 5G networks is CI path loss model where this model depends on the frequency and it is obtained by applying the CI reference distance upon law made by Friis as below [1]

$$PL^{CI}(f_c, d_{3D})[dB] = FSPL(f_c, 1m) + 10n \log_{10}(d_{3D}) \quad (1)$$

where,  $n$  is the path loss exponent (PLE) found by measured data error minimization to Eq. (1), where  $d_{3D}$  is the separation distance and it is must greater  $> 1m$  and  $FSPL(f_c, 1m)$  is the free space path loss equation at 1m given as below

$$FSPL [dB] = 32.4 + 20 \log_{10}(f_c) \quad (2)$$

where  $f_c$  is the carrier frequency.

The CI model is simple and accurate as it requires to optimize the PLE value only and it offers similar prediction of path loss to the measured path loss [6,13]. As an evidence, results obtained in [10] showed that when modelling the path loss at LOS settings using CI model, the result were almost identical to the measured path loss and hence indicating CI model is very accurate model under LOS. However, the weakness of this model is that the transmitter power needs to be standardized so that same PLE can be achieved at the same frequency [15].

### 2.2 Floating Intercept or Alpha-Beta-Gamma Model (FI or ABG)

The ABG model is determined by finding the best fit values for error minimization between model and the measured data. This is by introducing the  $\alpha$ ,  $\beta$ , and  $\gamma$  parameters. The equation for this model is as follows [6]

$$PL^{ABG}(f_c, d)[dB] = 10\alpha^{ABG} \log_{10}(d) + \beta^{ABG} + 10\gamma^{ABG} \log_{10}(f_c) \quad (3)$$

where  $\alpha^{ABG}$  and  $\gamma^{ABG}$  are coefficients indicating the path loss dependence on distance and frequency, respectively,  $\beta^{ABG}$  is an optimized offset path loss value in dB,  $d$  is separation distance between receiver and transmitter in meters and  $f_c$  is the carrier frequency in GHz. When  $\gamma^{ABG}$  is 0, this model becomes Floating Intercept (FI) as follows:

$$PL^{FI}(f_c, d)[dB] = \alpha^{FI} + 10\beta^{FI} \log_{10}(d) \quad (4)$$

where  $\alpha^{FI}$  and  $\beta^{FI}$  are the same parameter described as  $\beta^{ABG}$  and  $\alpha^{ABG}$  respectively.

Sun et al. state that ABG or FI offers slightly improved accuracy of measured path loss [14]. Whereas [6] shows that ABG or FI model able to give good prediction at short range compared to CI model. However, the good prediction at short range only works at specific measurement range. Furthermore, ABG or FI model is difficult as it requires optimization of two or three parameters compared to CI.

### 2.3 Related Works Using CI and FI or ABG Models

A number of studies extended the basic path loss models for use in the outdoor 5G networks. For example, Third Generation Partnership Project (3GPP) and 5G Channel Model (5GCM) proposed their own path loss based derived from the CI and ABG models [1]. The advantage of their proposed path loss model is that the model can be used in the frequencies ranging from 6 GHz to 100 GHz and without modification on the values of the path loss parameters (i.e. PLE). However, this proposed model assumed the usage of omnidirectional antennas. It should be noted that the directional antennas will be considered for implementation in the 5G networks [8]. Directional antenna is the antenna pattern that makes an antenna to transmit or receive signal at a specific directions. While omnidirectional antenna is defined as an antenna patterns that make an antenna to transmit and receive signal at all directions.

Rappaport et al. [1] stated that the predicting of path loss on the basis of omnidirectional antenna as a replacement for directional antennas is not effective unless understanding on the modelling of the directional antenna patterns and true spatial and temporal multipath channel statistics are achieved. Zhao et al. [7] argues that similar parameter values of PLE,  $\alpha$ , and  $\beta$  cannot be achieved under LOS condition when the CI and FI or ABG models are utilized for different antenna patterns. This might be due to the antenna gain of the omnidirectional antenna is independent as compared to the directional antennas and therefore lead to the omnidirectional antenna obtained lower path loss. Consequently, the results obtained by Zhao et.al support the argument made by Rappaport et al. with respect to the ineffectiveness for assuming the omnidirectional antennas as the replacements for directional antennas [1,7]. Given that the polarization method was not mention in the Zhao et.al, this becomes one of the limitations of their work.

To address the limitation faced by Zhao et al., [4] investigated the impact of using cross polarized antennas on path loss. This paper compares [4] and [7] given that these two works use similar frequency and identify that cross-polarized antenna requires higher parameter values of PLE,  $\alpha$ , and  $\beta$ . This is probably due to higher path loss obtained by cross-polarized antennas in [4] compared to the unknown polarization used in [7]. This indicates that different antenna polarization requires different parameters values of PLE,  $\alpha$  and  $\beta$ . This research [4] however, did not mention the polarization use for NLOS condition and investigation of antenna polarization in NLOS condition is important given the sensitivity of mmWave to blockages.

In regards to path loss study for rural macrocell areas, research in [10] investigated CI path loss model at 73 GHz frequency at rural macrocell area and obtained PLE of 2.16 and 3.04 for LOS and NLOS respectively. When the results obtained in [10] are compared with [4], it is observed that the PLE obtained in [10] is slightly lower than in [4] although the research in [10] uses higher frequency than the research in [4]. This is probably due to higher transmitter height used in [10] which causes the path loss measured in [10] to be lower than [4]. Nevertheless, the researchers in [10] used unknown polarization and focus

at CI model only. Better results can be obtained if known polarization and other models are used.

### 3. RESEARCH METHODOLOGY

This chapter describes the methodology used for this research. The methodology of this research begins with the description on how the path loss samples is collected and ends with how the path loss models are benchmarked using Root Mean Square Error (RMSE) calculation.

#### 3.1 Research Flow

The research begins with the collection of path loss samples by using a simulator called NYUSIM [15]. This software is very popular given that several researches had used this software for 5G path loss study as discussed in [16] and [17]. This is probably because NYUSIM is an open-source simulator and provides samples that are similar to field measurements of signal levels as claimed in [15]. Thus, these advantages motivates the usage of NYUSIM for this research. For further information on how NYUSIM works, it can be referred in [15].

Due to the time constraint and given the main aim of this research, this paper only considers path loss (PL) figure (the values obtained from the figure will become the path loss samples) in Power Delay Profile (PDP) output, though a number of output were generated from the software. One of the disadvantages of the NYUSIM is that only the PL figure of CI model was generated. This does not fulfil the aim of this paper where investigation of other basic path loss models need to be conducted. Therefore, additional results of other basic path loss models described in Section 2 will be plotted by using MATLAB software.

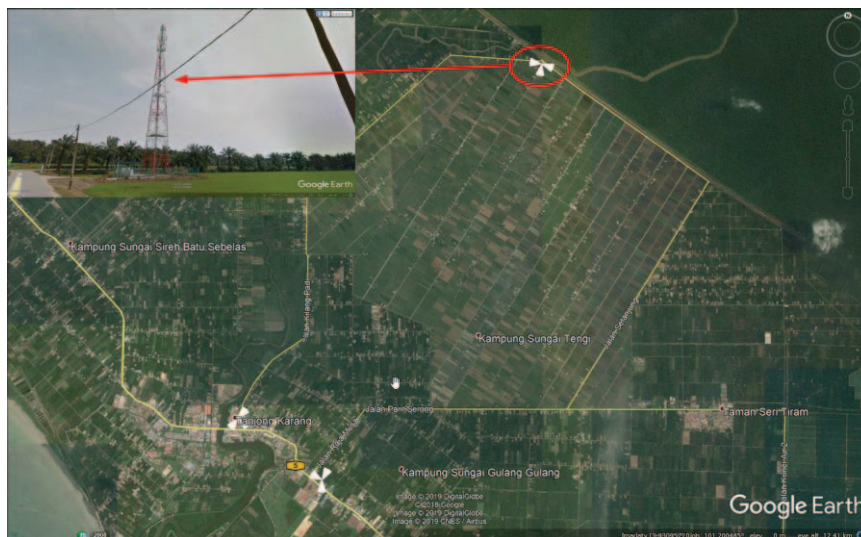


Fig. 1: Location for path loss samples collection for rural macrocell area.

Besides that, another disadvantage of NYUSIM is that this simulator is not a map-based channel simulator. This may lead to inaccurate values of path loss sample collection. Furthermore, these inaccurate values may contradict to the one of the NYUSIM's advantages which is to provide samples that are similar to field measurements. Therefore, a thorough geographical studies were conducted to identify the rural macrocell area in Malaysia to be as the reference location for collecting path loss samples. Based on the

assistance of Google Earth, the chosen location is depicted in Fig. 1 where it is located in Tanjong Karang, Selangor. The reason for choosing this area is because this area is not similar to other rural areas in Malaysia where it is not covered by dense foliage. Therefore, input parameter of foliage loss provided by NYUSIM can be ignored for collecting path loss samples for this location. This is because, when testing the performance of NYUSIM, it is found out that less number of output samples especially for PDP output can be taken from this simulator when higher rain rate and foliage loss are considered for path loss study.

Table 1 describes the relevant parameters that will be used for processing path loss samples. This table has been categorized into two categories which are Channel Parameters, and Antenna Properties. It should be noted that some of the parameters used were based on weather websites on 6th April 2019, guidelines from Ericsson and International Telecommunication Union (ITU), some parameters in [13] and what is provided by NYUSIM [18-20].

Table1: Simulation parameters for path loss samples collection [13,18-20]

Environment	Rural Macrocell
Location	Tanjong Karang, Selangor
Channel Parameters	
Frequency (GHz)	40
Scenario	RMa
Conditions	LOS and NLOS
Distance (m)	100 to 10000
TX Power (dBm)	40 dBm
Antenna Height (m)	35
Barometric Pressure (mbar)	1011
Humidity (%)	88
Temperature (°C)	26
Rain Rate (mm/hr)	90
Polarization	Cross Polarized
Number of RX Locations	20
Antenna Properties	
Array Type	Uniform Rectangular Array
Number of TX Antenna Elements, Nt	16
Number of RX Antenna Elements, Nr	16
Number of TX Element Per Row, Wt	8
Number of RX Antenna Elements Per Row, Wr	8
TX Antenna Azimuth Half-Power Beam Width (HPBW),°	7.8
TX Antenna Elevation HPBW,°	7.8
RX Antenna Azimuth HPBW,°	7.8
RX Antenna Elevation HPBW,°	7.8

After the path loss samples using the parameters provided in Table 1 have been collected, the path loss samples are then extracted into MATLAB software for path loss modelling. The modelling of path loss are based from the models described in Section 2 alongside with the parameters from the previous studies [4,6,7,10,12-14]. Thereafter, the

optimal parameters (parameters showing the closest plot to the path loss samples) from each path loss models are identified by observing the output plot from MATLAB. The predicted path loss values with their optimal parameters are compared with the path loss samples on the basis of Root Mean Square Error (RMSE) calculation. The calculation of RMSE are as below:

$$RMSE = \sqrt{\frac{\sum_{n=1}^N (PL_{\text{sampled},n} - PL_{\text{predicted},n})^2}{N}} \quad (5)$$

where  $PL_{\text{sampled}}$  is the path loss samples,  $PL_{\text{predicted}}$  is the predicted path loss obtained from the path loss models and  $N$  is number of samples obtained from the path loss samples. Based on equation (5), the path loss model with respect to the identified parameters that has the lowest RMSE indicates that this model has the closest path loss prediction. Thus, this model is chosen as the suitable model to be used for 5G networks in rural macrocell environment in Malaysia. Calculation on RMSE percentage degradation between identified model and the suitable model is also conducted. The reason of conducting this calculation is to see how much the RMSE of other identified models are degraded from the RMSE of the suitable model. The percentage degradation is depicted on equation (6) below.

$$RMSE \text{ Degradation (\%)} = \frac{|RMSE_{\text{IdentifiedModel}} - RMSE_{\text{SuitableModel}}|}{RMSE_{\text{SuitableModel}}} \times 100 \quad (6)$$

where  $RMSE_{\text{IdentifiedModel}}$  is the RMSE of the other identified models and  $RMSE_{\text{SuitableModel}}$  is the lowest RMSE identified from each models.

As a summary for this section, it is described in a form of research flow as shown in Fig. 2.

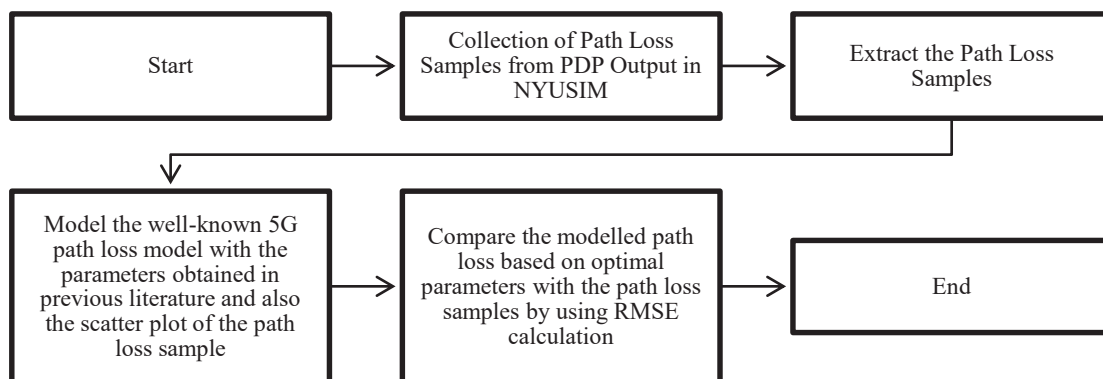


Fig. 2: Research flow for finding the accurate path loss model for 5G networks in rural macrocell environment in Malaysia.

#### 4. RESULTS AND DISCUSSION

This section contains results obtained via simulation being compared with the path loss samples obtained via measurement. The parameters of path loss models obtained from the previous studies that are closest to the path loss samples are identified and later analyse based on RMSE calculation so as to identify path loss model with the most



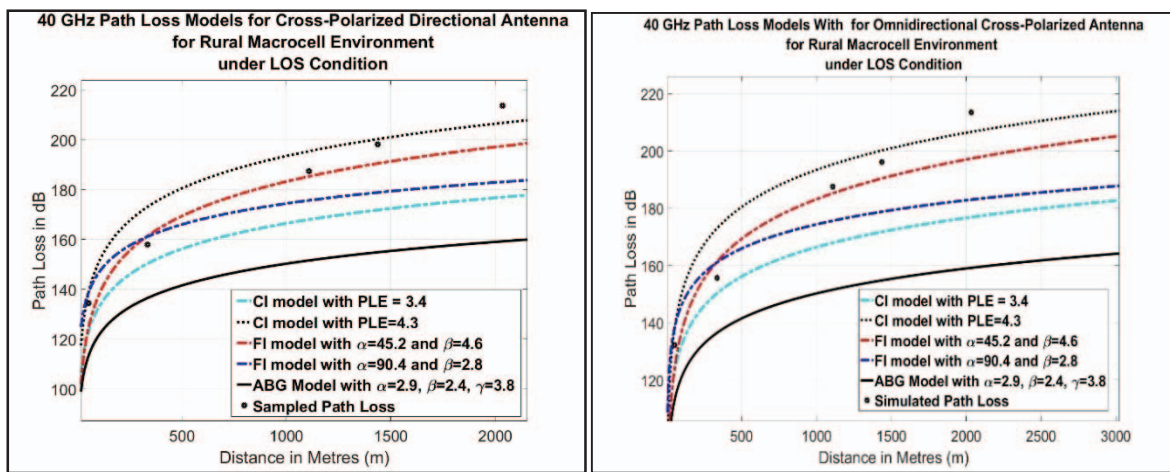
optimal parameter for different scenarios in rural macrocell environment in Malaysia. The scenarios studied include LOS or NLOS condition and cross-polarized antennas with respect to directional and omnidirectional patterns. Directional and omnidirectional patterns are considered because according to [13], directional antenna is used to cope with the feature of beamforming and beam combining techniques for implementing 5G networks, while omnidirectional antennas is studied because wireless user equipment (UE) uses this antenna pattern as UE needs to receive signal from all directions. Thus, showing that these two antenna patterns are required in the implementation of 5G networks.

The authors in [13] further defined the conditions where LOS is a condition where a clear propagation path occurred between transmitter and receiver while NLOS is a condition where transmitter and receiver are obstructed by blockage and there is no clear path of propagation between them. Thus, from the description of these two conditions, in real time, 5G users will always move from one location to another leading to changing condition of LOS or NLOS based on user's location.

Given the popularity of CI and ABG or FI models alongside with their parameters from [4,6,7,10-14], these basic path loss models are studied in this paper.

#### 4.1 Analysis of Path Loss Model for Rural Macrocell in Malaysia at LOS Condition

Simulation results of path loss models alongside with the scatter plot of the path loss samples for rural macrocell environment under LOS condition at 40 GHz is shown in Fig. 3. It was observed that there are four parameters that are closest to the path loss samples for cross-polarized antennas with different patterns. For CI model, the PLE parameters that are closest to the path loss samples are 3.4 and 4.3. FI model that have  $\alpha$  value of 45.2 dB with  $\beta$  value 4.6 and  $\alpha$  value of 90.4 dB with  $\beta$  value of 2.8 are observed to be the closest to the path loss samples. Meanwhile, the parameters of ABG model that are closest to the path loss samples have values of  $\alpha$ ,  $\beta$  and  $\gamma$  that equal to 2.9, 2.4 dB and 3.8 respectively. For CI and FI models, the values of the parameters were similar to [4] while for ABG model, the values obtained were similar to [12]. These two studies were conducted based on field measurement in Malaysia and probably have the same environmental condition set in the NYUSIM for this paper.



(a) Directional cross-polarized antenna under LOS condition.

(b) Omnidirectional cross-polarized antenna under LOS condition.

Fig. 3: 40 GHz rural macrocell simulated path loss model alongside scatter plot under LOS condition.

Thereafter the RMSE calculation was performed so as to find the most optimal parameters of path loss model for rural macrocell in Malaysia. Table 2 showed that different path loss models are suitable for cross-polarized antennas with different antenna patterns. The suitable path loss model for directional pattern is CI model with PLE of 4.3 while FI model with  $\alpha$  and  $\beta$  parameters of 45.2 dB and 4.6 is suitable for omnidirectional pattern. Referring to Table 2, for directional pattern, CI model with PLE of 4.3 has the lowest RMSE of 8.60 dB compared to other models with respect to different values of parameters. The reason why this model has the lowest RMSE probably because the PLE of 4.3 gives closer prediction of path loss when the separation distance are at 53.3 m, 1436.2 m and 2034.1 m as observed in Fig. 3(a). Compared to FI model with  $\alpha$  and  $\beta$  parameters of 45.2 dB and 4.6 which scores the second lowest of RMSE (i.e. 7.33% degradation as compared to the RMSE obtained by CI model with PLE of 4.3), the  $\beta$  parameter of this model can only give two predicted path loss values that are closest to the path loss samples which is when the location of the receiver are 1109.4 m and 1436.2 m away from the transmitter. Thus, showing that CI model with PLE of 4.3 is suitable due to the number simulated/predicted path loss that are closer (smaller value of RMSE) to the path loss samples. Furthermore, CI model with PLE of 4.3 which was proposed in [4] also can be adapted for path loss modelling for rural macrocell environment in Malaysia under LOS condition when using Cross-Polarized Directional antenna.

Referring back to Table 2, FI model with  $\alpha$  and  $\beta$  parameters of 45.2 dB and 4.6 have the lowest RMSE among the other models for omnidirectional pattern which is around 8.72 dB. Based on observation in Fig. 3(b), this model obtained the lowest RMSE probably because at distance of 1109.4 m, the  $\beta$  parameter of 4.6 obtained from this model provide closer predicted path loss values to the path loss samples where the difference between predicted path loss and path loss samples is around 2.22 dB. Compared to CI model with PLE of 4.3, where at 1109.4 m, larger difference value between the measured and predicted values of path loss was observed in which the difference is 7.85 dB. Hence, contributing to CI model with PLE of 4.3 to have slightly higher RMSE than FI model with  $\alpha$  and  $\beta$  parameters of 45.2 and 4.6. Furthermore, the findings achieved by [4] is suitable to be adapted in Cross-Polarized antenna for LOS rural macrocell environment by using CI model with 4.3 PLE for directional type and FI model with  $\alpha$  and  $\beta$  parameters of 45.2 dB and 4.6 for omnidirectional type.

Table 2: RMSE value for rural macrocell environment under LOS condition

Polarization	Antenna Pattern	RMSE [dB]				
		CI Model		FI Model		ABG Model
		PLE 3.4	PLE 4.3	$\alpha$ [dB]= 90.4 and $\beta$ = 2.8	$\alpha$ [dB]= 45.2 and $\beta$ = 4.6	$\alpha$ = 2.9, $\beta$ [dB]= 2.4 and $\gamma$ = 3.8
Cross-Polarized	Directional	22.80	8.60	17.24	9.23	37.45
	RMSE Degradation (%)	165.28	-	100.49	7.33	335.65
	Omnidirectional	21.99	9.83	17.05	8.72	36.47
	RMSE Degradation (%)	152.06	12.71	95.43	-	318.08

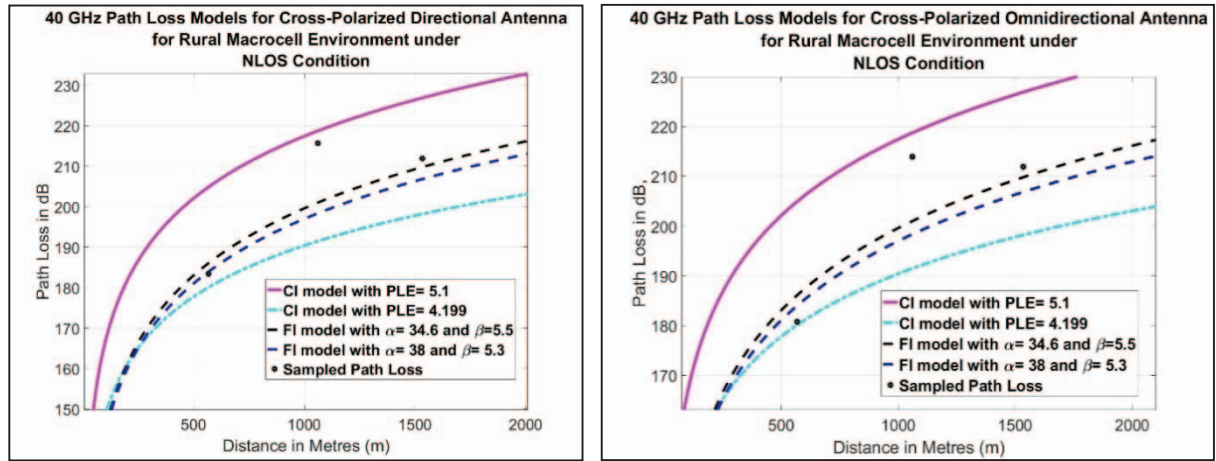
## 4.2 Analysis of Path Loss Model for Rural Macrocell in Malaysia at NLOS Condition

The results of path loss samples and the simulated path loss models with the best chosen parameters for rural macrocell environment in Malaysia under NLOS condition is shown in Fig. 4. It is observed in the figure that there are four parameters that have the closest prediction to the path loss samples. Parameters of CI model that are closest to path loss samples have PLE of 5.1 and 4.199 which were achieved in [4] and [7] respectively. Parameters  $\alpha$  equal to 34.6 dB with  $\beta$  equal to 5.5 and parameters  $\alpha$  of 38 dB with  $\beta$  of 5.3 of FI model are the closest to the path loss samples and the values of these parameters came from the research made in [13]. ABG model is excluded because most of parameters from this model of the previous studies give poor prediction of path loss under NLOS condition. Therefore, the only parameters that give closer prediction to the path loss samples obtained in this paper are the parameters  $\alpha$  equal to 34.6 dB with  $\beta$  equal to 5.5 and parameters  $\alpha$  of 38 dB with  $\beta$  of 5.3 of FI model and PLE of 5.1 and 4.199 of CI model.

However, to simplify the process of finding the suitable path loss model based on the identified optimal parameters for Malaysia's rural macrocell environment under NLOS condition, RMSE calculations were conducted which are shown in Table 3 respectively. FI model with parameters  $\alpha$  equal to 34.6 dB and  $\beta$  of 5.5 are suitable as it has the lowest RMSE around 8.70 and 8.14 for directional and omnidirectional respectively. The reason is because the parameter  $\beta$  of this model provide the smallest average of difference between the measured and predicted path loss for all distances measured (ADMPPL). This average is calculated as below.

$$ADMPPL = \frac{\sum_{i=1}^N |(PL_{Predicted})_i - (PL_{Sampled})_i|}{N} \text{ [dB]} \quad (7)$$

where  $PL_{Predicted}$  is the predicted path loss in dB,  $PL_{Sampled}$  is the sampled path loss, and  $N$  is the number of sampled path loss obtained in the NYUSIM simulator. The reason for utilizing Eq.(7) is because each identified path loss model has some predicted values that are close to the sampled path loss at certain distances. For instance and as tabulated in Table 5, using Cross-Polarized Omnidirectional antenna, CI model with PLE 4.199 gives closer prediction at 567.9 m where the difference between predicted path loss and path loss samples is around 0.71 dB, compared to FI model with  $\alpha$  equal to 34.6 dB and  $\beta$  equal to 5.5 where the difference is around 5.28 dB. However, the latter model gives closer prediction of path loss when the receiver is at 1533.9m where the difference between predicted path loss and the sampled path loss is around 2.08 dB compared to the former model where difference is 13.69 dB. These examples leads to the requirement of using Eq.(7) for better justifications on why FI model with  $\alpha$  equal to 34.6 dB and  $\beta$  equal to 5.5 has the lowest RMSE. Based on Table 6 and referring to omnidirectional type as an example, using equation (7), the average for this suitable model is 6.76 dB compared to the second lowest path loss which is FI model with  $\alpha$  equal to 38 dB and  $\beta$  equal to 5.3 where the average difference around 7.93 dB. Thus, this lowest ADMPPL gives the former model to have lowest RMSE and leads to this model to have the best fit of slope to the path loss samples. Further, the results obtained also agree with the statement made by [14] as path loss prediction made by the FI model with parameters  $\alpha$  equal to 34.6 dB and  $\beta$  of 5.5 give slight accuracy to the sampled path loss.



(a) Directional cross-polarized antenna under NLOS condition.

(b) Omnidirectional cross-polarized antenna under NLOS condition.

Fig. 4: 40 GHz rural macrocell simulated path loss model under NLOS condition.

Table 3: Sampled path loss and predicted path loss results for rural macrocell environment under NLOS condition

Polarization	Antenna	Distance [m]	Sampled Path Loss [dB]	Predicted Path Loss [dB]			
				CI Model		FI Model	
				PLE	PLE	$\alpha$ [dB]= 34.6 $\beta = 5.5$	$\alpha$ [dB] = 38 $\beta = 5.3$
Cross-Polarized	Directional	567.9	183.5	180.10	204.91	186.08	183.98
		1060.2	215.7	191.48	218.74	201.00	198.35
		1533.9	211.9	198.21	226.92	209.82	206.85
	Omni-directional	567.9	180.8	180.09	204.91	186.08	183.98
		1060.2	213.9	191.48	218.74	201.00	198.35
		1533.9	211.9	198.21	226.92	209.82	206.85

Table 4: RMSE value for rural macrocell environment under NLOS condition

Polarization	Antenna Pattern	RMSE [dB]			
		CI Model		FI Model	
		PLE 4.199	PLE 5.1	$\alpha$ [dB]= 34.6 $\beta = 5.5$	$\alpha$ [dB] = 38 $\beta = 5.3$
Cross-Polarized	Directional	16.18	15.20	8.70	10.44
	RMSE Degradation (%)	85.96	74.65	-	19.95
	Omni-directional	15.17	16.63	8.14	9.62
	RMSE Degradation (%)	86.40	104.36	-	18.17

Table 5: Difference of sampled path loss and predicted path loss results for rural macrocell environment under NLOS condition

Polarization	Antenna	Distance [m]	Sampled Path Loss - Predicted Path Loss   [dB]			
			CI Model		FI Model	
			PLE 4.199	PLE 5.1	$\alpha$ [dB]= 34.6 $\beta$ = 5.5	$\alpha$ [dB] = 38 $\beta$ = 5.3
Cross-Polarized	Directional	567.9	3.4	21.41	2.58	0.48
		1060.2	24.22	3.04	14.7	17.35
		1533.9	13.69	15.02	2.08	5.05
	Omnidirectional	567.9	0.71	24.11	5.28	3.18
		1060.2	22.42	4.84	12.9	15.55
		1533.9	13.69	15.02	2.08	5.05

Table 6: ADMPPPL calculation results as to find justification on why FI Model with parameters of  $\alpha$  equal to 34.6 dB and  $\beta = 5.5$  has the lowest RMSE for rural macrocell environment under NLOS condition

Polarization	Antenna Pattern	RMSE			
		CI Model		FI Model	
		PLE 4.199	PLE 5.1	$\alpha$ [dB]= 34.6 $\beta$ = 5.5	$\alpha$ [dB] = 38 $\beta$ = 5.3
Cross-Polarized	Directional	13.77	13.15	6.46	7.63
	Omnidirectional	12.27	14.65	6.76	7.93

### 4.3 Analysis of Suitable 40 GHz Path Loss Models for Rural Macrocell in Malaysia

After finding out the suitable parameters of path loss models for cross-polarized antenna under LOS and NLOS conditions for rural macrocell in Malaysia, a summary of these suitable models is tabulated in Table 7. The table shows the most effective model that provide good path loss prediction is FI model and only CI model is obtained in Cross-Polarized Directional Antenna under LOS condition. This is probably because the various  $\beta$  parameter values of FI model obtained in the previous studies give the best fit of slope to the scatter plot of the path loss samples for most antenna patterns polarizations. Therefore, the results shown in Table 7 validates the statement made by [14] that ABG or FI model offers slightly improved accuracy of the path loss samples.

Another finding is that most of the suitable path loss models have the same parameter values for the case of different antenna patterns under NLOS condition. This is probably due to the slight difference of path loss samples when directional and omnidirectional patterns are used. Thus, these findings are in line with the findings obtained in [7] when using Cross-Polarized antenna with different patterns under LOS condition whereas results from NLOS condition differ from this study.

Table 7: Summary of path loss models suitable for rural macrocell environment in Malaysia

Condition	Antenna Pattern	Model	Parameters
LOS	Directional	CI model	PLE 4.3
	Omnidirectional	FI model	$\alpha$ [dB]= 45.2 and $\beta$ = 4.6
NLOS	Directional	FI model	$\alpha$ [dB]= 34.6 and $\beta$ = 5.5
	Omnidirectional	FI model	$\alpha$ [dB]=34.6 and $\beta$ = 5.5

## 5. CONCLUSION AND FUTURE WORKS

This research aims to study the performance of 5G path loss models based on their optimal parameter values for cross-polarized antennas in Malaysia's rural macrocell environment. Results show that when tested in LOS and NLOS conditions with different antenna patterns, the FI model with their respective parameters is the most suitable model to be used for the majority of the scenarios of rural macrocell in Malaysia whereas CI model only can be used for Cross-Polarized Directional antenna under LOS scenario only. This is because the suitable models score the lowest RMSE compared to all models. Besides that, similar parameter values of FI model can be used for different antenna patterns under NLOS condition only as small difference of sampled path loss values were obtained for both Cross-Polarized Directional and Omnidirectional antennas. As a conclusion, the results obtained from this research can be recommended to be standardized for Malaysia's 5G implementation for rural macrocell areas when using cross polarized antennas as the parameter values of the basic path loss models are from the studies made from previous researches.

This research can be improved by using map-based simulator or field measurements as the total number of path loss samples taken is less than 10 samples and at inconsistent distance intervals. This due to NYUSIM placed the receivers at unknown and random locations and at distances that causes the sampled path loss value to exceed the threshold limit set by this simulator. Thus, new weakness on using NYUSIM is found based on this findings. Other than that, the results could also be better if more locations of rural macrocell areas in Malaysia are tested. This is to ensure that the path loss models that are suitable for other rural macrocell areas are similar to the suitable models obtained in this research. Therefore, the results obtained in this research can be more accurate if large number of path loss samples is obtained through known locations and consistent distance intervals and tested in various rural macrocell locations in Malaysia.

## ACKNOWLEDGEMENTS

We are very grateful to Ministry of Education Malaysia for supporting this research under the grant ID of FRGS/1/2019/TK04/UIAM/02/2.

## REFERENCES

- [1] Rappaport TS, Xing Y, MacCartney GR, Molisch AF, Mellios E, Zhang J. (2017) Overview of millimeter wave communications for Fifth-Generation (5G) wireless networks-with a focus on propagation models. *IEEE Transactions on Antennas and Propagation*, 65(12): 6213-6230.
- [2] Mitra RN, Agrawal DP. (2015) 5G mobile technology: A survey. *ICT Express*, 1(3): 132-137. <https://doi.org/10.1016/j.ict.2016.01.003>
- [3] Prabu RT, Benisha M, Bai VT, Yokesh V. (2016) Millimeter wave for 5G mobile communication application. In *Proceedings of 2016 2nd International Conference on Advances in Electrical, Electronics, Information, Communication and Bio-Informatics (AEEICB)*, 27-28 February 2016, Chennai, India; pp. 236-240.
- [4] Al-Samman AM, Hindia MN, Rahman TA. (2016) Path loss model in outdoor environment at 32 GHz for 5G system. In *Proceedings of 2016 IEEE 3rd International Symposium on Telecommunication Technologies (ISTT)*, 28-30 November 2016, Kuala Lumpur, Malaysia; pp. 9-13.
- [5] Andrews JG, Buzzi S, Choi W, Hanly S, Lozano A, Soong ACK, Zhang JC. (2014) What will 5G be? *IEEE Journal on Selected Areas in Communications*, 32(6):1065-1082.
- [6] Sun S, Rappaport TS, Rangan S, Thomas TA, Ghosh A, Kovacs IZ, Rodriguez I, Koymen O, Partyka A, Jarvelainen J. (2016) Propagation path loss models for 5G urban micro-and macro-cellular scenarios. In *Proceedings of 2016 IEEE 83rd Vehicular Technology Conference (VTC Spring)*, 15-18 May 2016, Nanjing, China; pp.1-6.
- [7] Zhao X, Li S, Wang Q, Wang M, Sun S, Hong W. (2017) Channel measurements, modeling, simulation and validation at 32 GHz in outdoor microcells for 5G radio systems, *IEEE Access*, 5:1062-1072.
- [8] Gupta A, Jha RK. (2015), A survey of 5G network: architecture and emerging technologies. *IEEE Access*, 3:1206-1232.
- [9] MacCartney GR, Rappaport TS. (2017) Study on 3GPP rural macrocell path loss models for millimeter wave wireless communications. In *Proceedings of IEEE International Conference on Communications, 2017*, 21-25 May 2017, Paris, France; pp. 3-9.
- [10] MacCartney GR, Rappaport TS. (2017) Rural macrocell path loss models for millimeter wave wireless communications. *IEEE Journal on Selected Areas in Communications*, 35(7): 1663-1677,
- [11] Rural Area. [<https://www.nationalgeographic.org/encyclopedia/rural-area/>].
- [12] Al-Samman AM, Rahman TA, Hindia MHDN, Daho A, and Hanafi E (2018) Path loss model for outdoor parking environments at 28 GHz and 38 GHz for 5G wireless networks. *Symmetry*, 10(12):1-15. doi: 10.3390/sym10120672.
- [13] Rappaport TS, MacCartney GR, Samimi MK, Sun S. (2015) Wideband millimeter-wave propagation measurements and channel models for future wireless communication system design. *IEEE Transactions on Communications*, 63(9): 3029-3056.
- [14] Sun S, Rappaport TS, Thomas TA, Ghosh A, Nguyen HC, Kovacs IZ, Rodriguez I, Koymen O, Partyka A. (2016) Investigation of prediction accuracy, sensitivity, and parameter stability of large-scale propagation path loss models for 5G wireless communications. *IEEE Transactions on Vehicular Technology*, 65(5): 2843-2860.
- [15] Sun S, MacCartney GR, Rappaport TS. (2017) A novel millimeter-wave channel simulator and applications for 5G wireless communications. In *Proceedings of IEEE International Conference on Communications, 21-25 May 2017, Paris, France*; pp.1-5 .
- [16] Reddy MMP. (2018), The effect of cross polarization and co polarization on channel modeling in 5G Communications. *International Journal for Science and Advance Research in Technology*, 4(3):53-58.  
Retrieved from <http://ijsart.com/Content/PDFDocuments/IJSARTV4I321194.pdf>
- [17] Budalal AA, Islam MR, Habaebi MH, Rahman TA. (2018) Millimeter wave channel modeling - present development and challenges in tropical areas. In *Proceedings of the 2018 7th International Conference on Computer and Communication Engineering (ICCC)*, 19-20 September 2018, Kuala Lumpur, Malaysia; pp.23-28.

- [18] Weather Forecast. Available: <https://www.worldweatheronline.com/>
- [19] Characteristics of Precipitation for Propagation Modelling P Series Radiowave Propagation.  
[[https://www.itu.int/dms\\_pubrec/itu-r/rec/p/R-REC-P.837-6-201202-S!!PDF-E.pdf](https://www.itu.int/dms_pubrec/itu-r/rec/p/R-REC-P.837-6-201202-S!!PDF-E.pdf)]
- [20] Advanced Antenna Systems for 5G Networks.  
[[https://www.ericsson.com/4a8a87/assets/local/reports-papers/white-papers/10201407\\_wp\\_advanced\\_antenna\\_system\\_nov18\\_181115.pdf](https://www.ericsson.com/4a8a87/assets/local/reports-papers/white-papers/10201407_wp_advanced_antenna_system_nov18_181115.pdf)]



# USING MODIFICATION OF PRIM'S ALGORITHM AND GNU OCTAVE AND TO SOLVE THE MULTIPERIODS INSTALLATION PROBLEM

WAMILIANA<sup>1\*</sup>, MUSTOFA USMAN<sup>1</sup>, WARSONO<sup>1</sup>, WARSITO<sup>2</sup>  
AND JAMAL IBRAHIM DAUD<sup>3</sup>

<sup>1</sup>Department of Mathematics, FMIPA Universitas Lampung, Bandar Lampung, Indonesia

<sup>2</sup>Department of Physics, FMIPA Universitas Lampung, Bandar Lampung, Indonesia

<sup>3</sup>Department of Science in Engineering, Faculty of Engineering,  
International Islamic University Malaysia,  
P.O. Box 10, 50728 Kuala Lumpur, Malaysia.

\*Corresponding author: [wamiliana.1963@fmipa.unila.ac.id](mailto:wamiliana.1963@fmipa.unila.ac.id)

(Received: 19<sup>th</sup> February 2019; Accepted: 28<sup>th</sup> November 2019; Published on-line: 20<sup>th</sup> January 2020)

**ABSTRACT:** The Minimum Spanning Tree (MST) is one of the famous problems that is used mostly as the backbone in many network design problems. Given a graph  $G(V,E)$ , where  $V$  is the set of vertices and  $E$  is the set of edges connecting vertices in  $V$ , and for every edge  $e_{ij}$  there is an associated weight  $c_{ij} \geq 0$ . The Multi Period Degree Constrained Minimum Spanning Tree (MPDCMST) is a problem of finding an MST while also considering the degree constrained on every vertex, and satisfying vertices installation requirement on every period. Two algorithms (WWM1 and WWM2) are proposed for solving this problem. GNU OCTAVE is used for coding and visualization. GNU is a recursive acronym for "GNU's Not Unix!", and that name is chosen because it is like Unix but differs from Unix because it is free and contains no Unix code. Those algorithms were implemented using 300 randomly generated problems. Moreover, we compare WWM1 and WWM2 algorithms using existing data from the literature and the results show that WWM2 is the best.

**ABSTRAK:** Minimum Spanning Tree (MST) merupakan salah satu masalah mahsyur yang banyak digunakan sebagai tulang belakang kepada masalah banyak rekaan jaringan. Menerusi graf  $G(V,E)$ , di mana  $V$  adalah himpunan titik dan  $E$  adalah himpunan garis yang menghubungkan titik-titik dalam  $V$ , dan bagi setiap garis  $e_{ij}$  terdapat berat berhubung  $c_{ij} \geq 0$ , Multi-period Degree Constrained Minimum Spanning Tree (MPDCMST) merupakan masalah dalam menentukan MST, pada masa sama turut menimbangkan kekangan pada setiap titik vertek, dan memenuhi syarat keperluan pemasangan pada setiap detik. Dua algoritma (WWM1 dan WWM2) dicadangkan bagi menyelesaikan masalah ini. GNU OCTAVE digunakan bagi pengaturcaraan dan visualisasi. GNU merupakan suatu singkatan kepada "GNU's Not Unix", dan nama tersebut dipilih kerana ianya seperti Unix, tetapi berbeza dari Unix kerana ia percuma dan tidak mempunyai kod Unix. Algoritma tersebut dilaksana dengan menggunakan 300 masalah terhasil secara rawak. Tambahan, algoritma WWM1 dan WWM2 dibandingkan dengan kajian terdahulu dan hasil kajian menunjukkan WWM2 adalah terbaik.

**KEYWORDS:** *multi-period; degree constrained; minimum spanning tree; Prims' algorithms; GNU OCTAVE*

## 1. INTRODUCTION

In most network design problems, The Minimum Spanning Tree (MST) is usually used as the backbone. If we add degree restriction on the vertices (can represent cities,

stations, etc.) of the graph (represents the network), the problem becomes a Degree Constrained Minimum Spanning Tree (DCMST) problem. Moreover, if we restrict and divide the stages or periods of the network's installation, the problem emerges as a Multi Period Degree Constrained Minimum Spanning Tree (MPDCMST) problem. The later constraint usually occurs because of the fund limitation for installing (connecting) the network. This problem arises when we want to design a network that requires that every vertex (node) restricts the number of connections/interfaces whilst also considering a set of vertices that have to be connected/ installed in a certain period due to the fund restriction (weather, etc.)

In this paper, we organize the discussion as follows: in Section, 2 we give the history of the problem; in Section 3, we discuss how to apply the algorithms developed using GNU Octave and implement them; in Section 4, we discuss the results; followed by a conclusion.

## 2. THE CONSTRAINED MINIMUM SPANNING TREE PROBLEM

It Because of its specific structure and use in many network design problems, the Minimum spanning tree problem has been studied extensively and a variety of fast algorithms have been developed. An efficient and fast minimum spanning tree algorithm that requires computational time nearly linear in the number of edges had been developed [1]. The MST problem is one of the classical problems where the objective is to construct a minimum cost/weight network. This problem usually arises in network design applications that must satisfy other graph parameters such as: degree, distance, diameter, connectivity, flow, etc. For instance, in a transportation network, a distance restriction on the flow commodities could represent the maximum distance allowed for delivery.

The Degree Constrained Minimum Spanning Tree (DCMST) problem is a Minimum Spanning Tree with a degree restriction on every vertex. This problem arises when designing networks where the degree restriction represents the number of allowable links on that vertex, i.e. the handling capacity of each of the vertices imposes a restriction on the number of edges (or wires/roads) that can be connected to a vertex. For example, the application of The DCMST is present in designing the road system, where the set of roads must connect a collection of suburbs/towns, but there is a restriction that no more than a certain number of roads (example: four roads) are allowed to meet at an intersection.

There are lots of investigations regarding the DCMST problem. This problem is considered to be an NP-Complete problem. An NP-complete problem is any of a class of computational problems for which no efficient solution algorithm has been found. Because of its NP-completeness [2], heuristic methods have dominated such as: the greedy algorithm based on Prim's and Kruskal's algorithm by [3], the Genetic Algorithm by Zhou and Gen[4], the Iterative Refinement by Deo and Kumar [5], the Simulated Annealing by Krishnamoorthy et al [6], the Modified Penalty by Wamiliana [7], and the Tabu Search by Caccetta and Wamiliana [8], Wamiliana and Caccetta [9-10].

In real situations, connecting all components in a network requires a certain time and process in order to be completed. The time of completion can vary depending on the need and priority of the network itself. The Multi Period Degree Constrained Minimum Spanning Tree (MPDCMST) problem was introduced in 2002 by Kawatra [11] and it proposed the hybrid of branch exchange and Lagrangean relaxation method to solve the problem on directed graph with vertex order ranging from 40 to 100. By modifying the problem in using the undirected graph, some algorithms based on Kruskal's and Prim's

algorithms were developed. WADR1 and WADR2 algorithms were developed by doing some modifications on Kruskal's algorithm [12], while WADR3 and WADR4 are the algorithms developed as variants of WADR1 and WADR2 [13]. Motivated by the connectivity property on the process of finding MST by Prim's algorithm, some algorithms were developed by Wamiliana et al. [14-16]. Wamiliana et al. [17] illustrated why the quality of the solution also depends on the number of vertices in  $HVT_i$  (the set of vertices that must be installed/connected in  $i^{\text{th}}$  period or before). The comparison of some algorithms developed and implemented on undirected graphs was given in Wamiliana et al [18] especially on the process of installation/connection of vertices in  $HVT_i$ .

### 3. GNU OCTAVE, MPDCMST AND IMPLEMENTATION

#### 3.1 GNU OCTAVE

GNU Octave is a free software that runs on GNU/Linux, macOS, BSD, and windows. This software originally was intended as a companion to a chemical reactor design course, but the one who first developed it is John W. Eaton [19]. Since this is free software, users are encouraged to modify and develop this software and are free to distribute it as well.

The difference in using GNU Octave as opposed to other language programming (such as Java), is that GNU Octave is more rigid. Certain rules must be followed (such as converting to matrix form or others). Java is more flexible to development of the program. For example, the data used for implementation represent the edges of the complete graph for certain vertex orders. For vertex order 10, the number of edges is 45, which is obtained from the formula  $n(E) = \frac{n(n-1)}{2}$ ,  $n=10$ . Before putting in GNU Octave, we have to modify this equation to be  $2n(E) = n^2 - n$ . This is a quadratic equation and to find  $n$ ,  $n = \frac{1+\sqrt{1+8n(E)}}{2}$  is used. Thus, to read the data, the source code for reading the data (vertex order) is as follows ( let  $n(E) = Un$ ):

```
function vertex = check_vertex(matrix)
bykedge=length(matrix);%bykedge=Un
c=2*bykedge;
n=(1+sqrt(1+(4*c)))/2;
vertex=n;
end
```

In GNU Octave, the graph was represented using a matrix, therefore a source code was designed so that when a problem is entered as a data problem, then the program would automatically detect the data and arrange it as two matrices, one as the matrix for original vertices (X) and the other for terminal vertices (Y). For example, if the data of a complete graph with order ten (consists of 45 edges) is entered, then the program automatically defines X and Y as follows:

X =	1	1	1	1	1	1	1	1	1
	2	2	2	2	2	2	2	2	3
	3	3	3	3	3	3	4	4	4
	4	4	4	5	5	5	5	5	6
	6	6	6	7	7	7	8	8	9
Y =	2	3	4	5	6	7	8	9	10
	3	4	5	6	7	8	9	10	4

5	6	7	8	9	10	5	6	7
8	9	10	6	7	8	9	10	7
8	9	10	8	9	10	9	10	10

After the X and Y are generated, the value of the weight will be put to connect X and Y in the form of a symmetrical matrix K, as follows (example for datafile 10.dat):

K =

0	115	74	42	955	712	660	697	450	806
115	0	391	504	597	537	452	709	452	784
74	391	0	939	472	372	272	250	644	354
42	504	939	0	212	515	132	248	603	642
955	597	472	212	0	935	70	715	328	24
712	537	372	515	935	0	426	987	72	227
660	452	272	132	70	426	0	144	814	82
697	709	250	248	715	987	144	0	740	703
450	452	644	603	328	72	814	740	0	886
806	784	354	642	24	227	82	703	886	0

For implementation, the same data used as in [12, 14, 16]. The data are generated randomly with the edge weight varying from 1 to 1000. For every vertex order, 30 problems were generated.

### 3.2 WWM1 and WWM2 Algorithms

We developed two algorithms to solve the MPDCMST based on Prim's algorithm and modified them to satisfy the given constraints. The reason for choosing Prim's algorithm was that Prim's maintains the connectivity property during the connection/installation process. In these algorithms, we used the terminologies  $HVT_i$  as the set of vertices that must be installed/connected on  $i^{th}$  period or before, and  $MAXVT_i$  as the maximum number of vertices that can be connected on the  $i^{th}$  period. The reason for using  $HVT_i$  was that in reality, it is possible to add some requirements that some components in the network be connected early due to public needs or other reasons. For example, in designing a fresh water pipe or electricity network, there is a requirement that some buildings (hospitals, police stations, government buildings, etc.) must be installed/connected within a certain period or earlier in the network.

#### 3.2.1 WWM1 Algorithm

The WWM1 algorithm starts by setting vertex 1 as the root and puts it in set V. V is the set of vertices in the network. Initially, V only contains vertex 1 as the central vertex,  $V = \{1\}$ , and no edges in T,  $T = \{\}$ . Then, the algorithm checks the nearest vertices in  $HVT_i$  to be connected/installed in V and the corresponding edges to the network (T). The algorithm will continue connecting/installing those vertices in  $HVT_i$  as long as the connection neither violates the degree restriction nor constitutes a cycle. If degree violation occurs, then edge exchange will be performed while also maintaining the connectivity of vertices in  $HVT_i$ . Next, the algorithm will check the  $MAXVT_i$ , and connect the edges with the smallest edge weight to T, as long as the connection neither violates the degree constraint nor constitutes a cycle. If the number of vertices connected on that period is already the same as  $MAXVT_i$ , the algorithm will continue to the next period, and the process is similar to the previous period until all vertices are connected/installed. To illustrate the WWM1 algorithm we used one problem with vertex

order 10 in the data (datafile.22.dat). The weight of the problem is given in Table 1. The data represents a complete graph of order 10, and the graph is illustrated in the Fig. 1. Moreover, we use the same set of  $HVT_i$  as in [12-17] as given in Table 2, and also use  $MaXVT_i$  as the floor function of  $\frac{n-1}{3}$ ,  $MaXVT_i = \left\lfloor \frac{n-1}{3} \right\rfloor$ .

Table 1: datafile.22.dat (graph with order 10)

Edge	e <sub>12</sub>	e <sub>13</sub>	e <sub>14</sub>	e <sub>15</sub>	e <sub>16</sub>	e <sub>17</sub>	e <sub>18</sub>	e <sub>19</sub>	e <sub>1,10</sub>	e <sub>23</sub>	e <sub>24</sub>	e <sub>25</sub>	e <sub>26</sub>	e <sub>27</sub>	e <sub>28</sub>
Weight	740	572	447	835	427	807	362	832	120	221	109	276	741	978	352
Edge	e <sub>29</sub>	e <sub>2,10</sub>	e <sub>34</sub>	e <sub>35</sub>	e <sub>36</sub>	e <sub>37</sub>	e <sub>38</sub>	e <sub>39</sub>	e <sub>3,10</sub>	e <sub>45</sub>	e <sub>46</sub>	e <sub>47</sub>	e <sub>48</sub>	e <sub>49</sub>	e <sub>4,10</sub>
Weight	368	403	505	921	757	884	369	886	545	639	253	750	251	187	857
Edge	e <sub>56</sub>	e <sub>57</sub>	e <sub>58</sub>	e <sub>59</sub>	e <sub>5,10</sub>	e <sub>67</sub>	e <sub>68</sub>	e <sub>69</sub>	e <sub>6,10</sub>	e <sub>78</sub>	e <sub>79</sub>	e <sub>7,10</sub>	e <sub>89</sub>	e <sub>8,10</sub>	e <sub>9,10</sub>
Weight	807	926	781	605	112	559	411	473	743	882	693	851	509	434	828

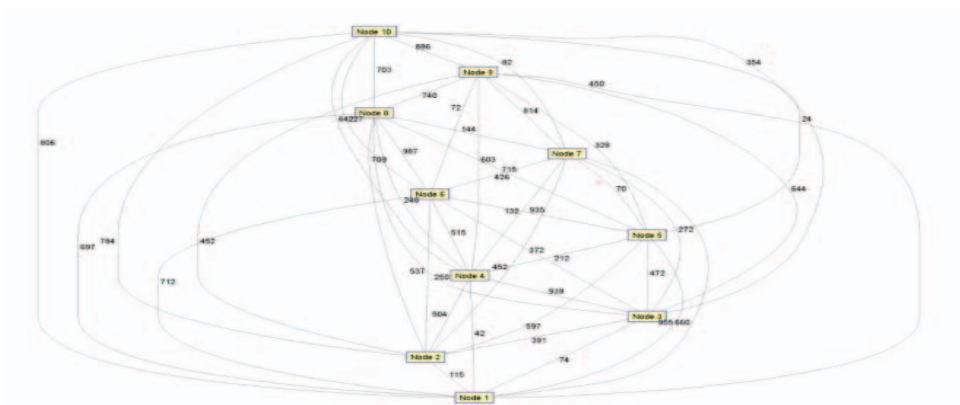


Fig. 1: The graph of datafile.22.dat.

Table 2: Element of  $HVT_i$  for every period

n	$HVT_1$	$HVT_2$	$HVT_3$
10	2	3	4
20	2	3	4
30	2,3	4,5	6,7
40	2,3,4	5,6,7	8,9,10
50	2,3,4,5	6,7,8,9	10,11,12,13
60	2,3,4,5,6	7,8,9,10,11	12,13,14,15
70	2,3,4,5,6,7	8,9,10,11,12,13	14,15,16,17,18,19
80	2,3,4,5,6,7,8	9,10,11,12,13,14,15	16,17,18,19,20,21,22
90	2,3,4,5,6,7,8	9,10,11,12,13,14,15	16,17,18,19,20,21,22
100	2,3,4,5,6,7,8,9	10,11,12,13,14,15,16,17	18,19,20,21,22,23,24,25

For the first period, the algorithm checks the vertices in  $HVT_1 = \{2\}$ . Vertex 2 is the only vertex in  $HVT_1$  then the algorithm connects vertex 2 to T using edge  $e_{12}$  with weight 740. V and T are updated to  $V = \{1,2\}$  and  $T = \{e_{1-2}\}$ . Next, the algorithm checks the difference of  $MAXVT_1 = \left\lfloor \frac{n-1}{3} \right\rfloor = 3$  and the number of vertices in  $HVT_1$ .  $|HVT_1|$  is the number of vertices in  $HVT_1$ ,  $|HVT_1| = 1$ . Since the difference of  $MAXVT_1$  and  $|HVT_1|$  is 2, then it is possible to add two more vertices. Therefore, the algorithm searches for the next smallest edge with the vertices in the network which is  $e_{2-4}$  with weight 109. Adding  $e_{2-4}$  to

T neither creates a cycle on T nor violates degree restriction on the vertices in V. Then,  $e_{2-4}$  is added to T and vertex 4 to V. V and T are again updated to  $V = \{1,2,4\}$  and  $T = \{e_{1-2}, e_{2-4}\}$ . Since vertex 4 was already added to V, then only one more vertex can be added, and  $e_{1-10}$  is the next smallest edge with weight 120. Adding  $e_{1-10}$  neither creates a cycle in T nor violates degree restriction on vertices in V. Therefore  $e_{1-10}$  was added to T and vertex 10 to V. V and T are updated to  $V = \{1,2,4,10\}$  and  $T = \{e_{1-2}, e_{2-4}, e_{1-10}\}$ . Since  $MAXVT_1$  is achieved, the first period is finished. The following figure shows the network after the first period is finished.

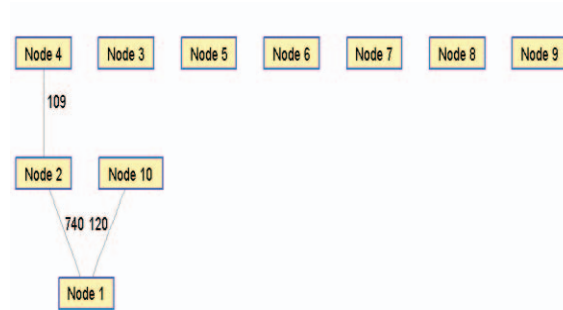


Fig. 2: The network after the first period of WWM1 algorithm is done.

On the second period,  $HVT_2 = \{3\}$ , therefore the algorithm connects vertex 3 to the network using the smallest edge of incidence with vertex 3; edge  $e_{2-3}$  is the smallest. Adding  $e_{2-3}$  to T neither violates the degree condition nor constitutes a cycle, therefore  $e_{2-3}$  is added to T and vertex 3 to V. V and T are updated to  $V = \{1,2,4,10,3\}$  and  $T = \{e_{1-2}, e_{2-4}, e_{1-10}, e_{2-3}\}$ . Then, the algorithm checks  $MAXVT_2 - |HVT_2|$  which is 2. Therefore, in this period, we can add two more edges to T and two more vertices in V. The next smallest edge of incidence with the vertices in V is  $e_{5-10}$  with a weight of 112. Adding  $e_{5-10}$  to T neither violates the degree condition nor constitutes a cycle, therefore  $e_{5-10}$  is added to T and vertex 5 to V. V and T are updated to  $V = \{1,2,4,10,3,5\}$  and  $T = \{e_{1-2}, e_{2-4}, e_{1-10}, e_{2-3}, e_{5-10}\}$ . Next, the algorithm searches the smallest edge of incidence with the vertices in V which is  $e_{4-9}$  with a weight of 187. Adding  $e_{4-9}$  to T neither violates the degree condition nor constitutes a cycle, therefore  $e_{4-9}$  is added to T and vertex 9 to V. V and T are updated to  $V = \{1,2,4,10,3,5,9\}$  and  $T = \{e_{1-2}, e_{2-4}, e_{1-10}, e_{2-3}, e_{5-10}, e_{4-9}\}$ . This is the end of the second period, and the network is illustrated in Fig. 3.

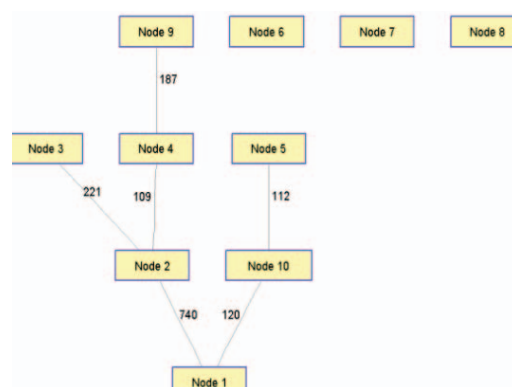


Fig. 3: The network after the second period of WWM1 algorithm is done.

Now, there are seven vertices already in the network, which are vertex 1, 2, 10, 4, 3, 5, and 9; and there are three more vertices that need to be connected. Those vertices are vertex 6, 7, and 8. Please note here that vertex 4 is already in the network (installed on the

first period). After the second period was done, vertex 3 (the member of vertices in  $HVT_2$ ) was in the network, as well as vertex 4 (an element in  $HVT_3$ ). Therefore, the algorithm is just searching for the smallest edges of incidence to the uninstalled vertices and to connect them to the network. Three edges that satisfy that condition and also neither create a cycle nor violate the degree condition (maximum degree is 3 for every vertex) are  $e_{4-8}$ ,  $e_{6-8}$ ,  $e_{6-7}$  with weight 251, 411, and 559 respectively.  $V$  and  $T$  are updated to  $V = \{1,2,4,10,3,5,9,8,6,7\}$  and  $T = \{e_{1-2}, e_{2-4}, e_{1-10}, e_{2-3}, e_{5-10}, e_{4-9}, e_{4-8}, e_{6-8}, e_{6-7}\}$ . All vertices are then in set  $V$ , so the algorithm stops. Figure 4 represents the network when the third period is finished.

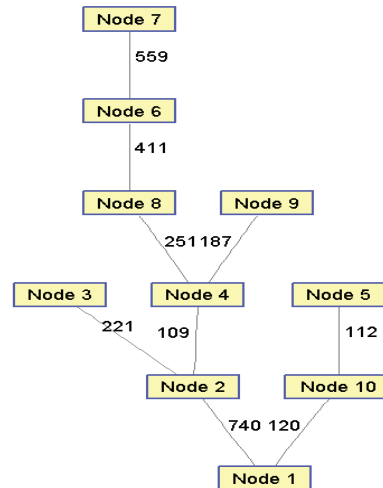


Fig. 4: The network when the third period is finished.

Table 3 gives the information about the period when the edges are installed/connected, the weight, and the total weight after the connection are done.

Table 3: The period when the vertices were connected in WWM1 algorithm

Period	From vertex	To vertex	Weight
1	1	2	740
1	1	10	120
1	2	4	109
2	2	3	221
2	10	5	112
2	4	9	187
3	4	8	251
3	8	6	411
3	6	7	559
<b>Total</b>			<b>2710</b>

### 3.2.2 WWM2 Algorithm

The WWM2 algorithm is similar with the WWM1 algorithm, except in the WWM2, the process of connecting the vertices in  $HVT_i$  is more flexible. Those vertices in  $HVT_i$

can be installed in the beginning of the period or at the end, as long as the installation/connection process is still within that period or before. In the first period of the WWM2 algorithm, vertex 2 is not installed first, but the algorithm searches for possible smallest edges among those in the data that connect to vertex 1. This is possible because  $MAXVT_1 = 3$  and the number of  $HVT_1 = |HVT_1| = 1$  (only consist of vertex 2). Therefore, it is possible to add two more vertices (but not vertex 2) in the network. Therefore vertex (node) 10 was connected first, followed by vertex 5, and finally, because vertex 2 must be installed/connected in the first period, then vertex 2 is installed. Figure 5 shows the network after the first period of the WWM2 algorithm is done.



Fig. 5: The network after the first period of WWM2 algorithm is done.

For the second period of the WWM2 Algorithm, the vertex in  $HVT_2$  is vertex 3. However, the algorithm first checks the difference between  $MAXVT_2$  and the number of  $HVT_2$ . Since  $MAXVT_2 - |HVT_2| = 2$ , then it is possible to add the other two vertices (besides vertex 3). However, if vertex 3's incidence with the smallest edge that connected with the vertices already in the network during the first period, then vertex 3 will be installed/connected first on the second period (of course, without violating the degree requirement on the vertices that are already in the network). Since the smallest edge on the second period is edge  $e_{24}$  then that edge is connected first on the second period, followed by edge  $e_{49}$ . After edge  $e_{49}$  was added in the network, then there are no more choices except adding the smallest edge of incidence with vertex 3, because vertex 3 must be installed/connected on the second period or before. Figure 6 shows the network after the second period of the WWM2 algorithm is done.

Similar with the WWM1 algorithm, on the third period of the WWM2 there are 7 vertices already in the network and there are three more vertices still uninstalled. Those vertices are vertex 6, 7, and 8. The difference between WWM1 and WWM2 is that vertex 4 in WWM1 is installed/connected on the first period, while in WWM2, vertex 4 is connected on the second period. The next three smallest are  $e_{48}$ ,  $e_{28}$ , and  $e_{210}$ . There are no degree restrictions and cycle occurrences by adding  $e_{48}$ , therefore vertex 8 is connected. However, there is a problem with adding  $e_{28}$ . The degree of vertex 2 is already 3, then adding  $e_{28}$  will violate the degree restriction, therefore  $e_{28}$  is omitted, and not connected. A different reason is applied to  $e_{210}$ . Adding  $e_{210}$  will create a cycle, therefore  $e_{210}$  is also omitted. Now, the algorithm is just searching for the next two smallest edges of incidence to the uninstalled vertices to connect them to the network (as long as the connection neither violates the degree restriction nor creates a cycle). The next two smallest are  $e_{68}$  and  $e_{67}$ . Figure 7 shows the network after the third period is finished.



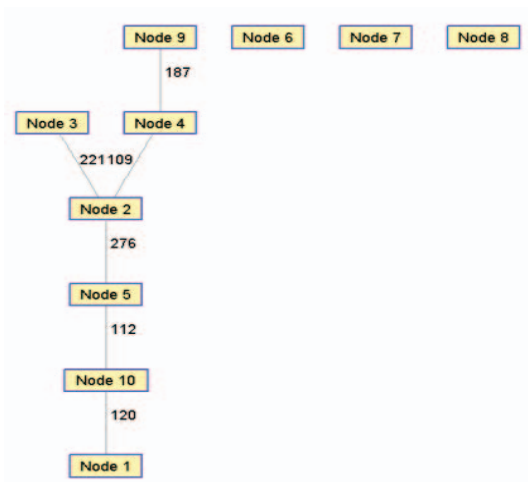


Fig. 6: The network after the second period of WWM2 algorithm is done.

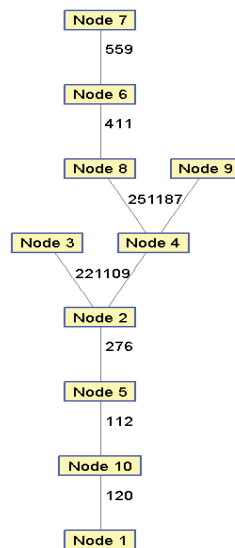


Fig. 7: The network after the second period of WWM2 algorithm is done.

Table 4: The period when the vertices were connected in the WWM2 algorithm

Period	From vertex	To Vertex	Weight
1	1	10	120
1	10	5	112
1	5	2	276
2	2	4	109
2	4	9	187
2	2	3	221
3	4	8	251
3	8	6	411
3	6	7	559
<b>Total</b>			<b>2246</b>

Table 4 gives the information about the period when the edges are installed/connected, the weight, and the total weight after the WWM2 Algorithm finishes the process.

#### 4. RESULTS AND DISCUSSION

The WWMI and WWM2 algorithms were compared against WADR5, WAC1 and WAC2 algorithms because those three algorithms are developed based on the same algorithm (Prim’s algorithm). Moreover, those algorithms were implemented using the same data, same set of  $HVT_i$ ,  $MAXVT_i$  and the number of periods. The data used for implementation was random problems generated using uniform distribution with weight ranging from 1 to 1000 (integer). For every vertex order, there are 30 problems generated and the vertex order used are 10 to 100 in increments of 10. Therefore, there are a total of 300 problems implemented. The solution taken is the average solution from 30 problems for every vertex order. The following table shows the result:

Table 5: The Comparative Solutions

Vertex order	MST	DCMST	WWM1	WWM2	WADR5	WAC1	WAC2
10	1129.43	1178.8	1498.6	1286.6	1341.93	1495.1	1359.93
20	1196.1	1299	1804.97	1428.57	1557.63	1790.37	1437.5
30	1177.43	1319.53	2039.97	1490.03	1755.40	2018.9	1516.43
40	1151.23	1286.3	2117.1	1440.03	1719.27	2079.73	1455.3
50	1223.43	1356.47	2427.27	1566.6	1844.10	2381	1603.7
60	1175.57	1320.73	2389.87	1573.57	1851.20	2364.4	1639.53
70	1242.1	1410.03	2558.5	1612.27	1963.83	2520.2	1671.9
80	1236.83	1410.23	2579.4	1675.2	1942.40	2547.8	1722.23
90	1248	1404.93	2618.43	1613.23	1941.33	2588.07	1649.33
100	1234.1	1370.8	2564.07	1567.53	1992.40	2535.2	1597.63
<b>Average</b>	<b>1201.42</b>	<b>1335.68</b>	<b>2259.82</b>	<b>1525.36</b>	<b>1790.95</b>	<b>2232.08</b>	<b>1565.35</b>

From Table 5 we can see the average solutions for MST, DCMST, WWM1, WWM2, WADR5, WAC1, and WAC2. For the algorithms developed for solving MPDCMST (WWM1, WWM2, WADR5, WAC1, and WAC2) the best performance is gained by the WWM2 algorithm, which is slightly close to the performance of WAC2, while the WWM1 and WAC1 are the two worse algorithms compared in this study. WWM1 and WAC1 are two algorithms developed based on the Modified Prim’s algorithm where the priority vertices in the set  $HVT_i$  must be installed/connected as soon as possible, while WWM2 is a modification of WWM1, and WAC2 is a modification of WAC1. The modification made for those two algorithms is the same: relaxing the process of connecting the priority vertices in  $HVT_i$  whilst also maintaining those vertices to be connected in the  $i^{th}$  period or before. WADR5 is an algorithm developed based on Modified Prim’s algorithm where the algorithm searches two smallest edges for being considered to be connected in the network, except the last one in the period. In this study, we compared the ratio of the algorithms (WWM1, WWM2, WADR5, WAC1, and WAC2) against their lower bound (DCMST). The ratio is  $\frac{H - LB}{LB}$ , where H is the heuristic (algorithm) and LB is the lower bound (DCMST). Table 6 below shows the ratio of  $\frac{H - LB}{LB}$ .

Table 6: The value of ratio  $\frac{H-LB}{LB}$  of the algorithms against the lower bound

Vertex order	MST	DCMST	WWM1	WWM2	WADR5	WAC1	WAC2	$\frac{WWM1 - DCMST}{DCMST}$	$\frac{WWM2 - DCMST}{DCMST}$	$\frac{WADR5 - DCMST}{DCMST}$	$\frac{WAC1 - DCMST}{DCMST}$	$\frac{WAC2 - DCMST}{DCMST}$
10	1129.43	1178.8	1498.6	1286.6	1341.93	1495.1	1359.93	27.129%	9.145%	13.839%	26.832%	15.366%
20	1196.1	1299	1804.97	1428.57	1557.63	1790.37	1437.5	38.950%	9.974%	19.910%	37.827%	10.662%
30	1177.43	1319.53	2039.97	1490.03	1755.40	2018.9	1516.43	54.598%	12.921%	33.032%	53.001%	14.922%
40	1151.23	1286.3	2117.1	1440.03	1719.27	2079.73	1455.3	64.588%	11.952%	33.660%	61.683%	13.138%
50	1223.43	1356.47	2427.27	1566.6	1844.10	2381	1603.7	78.940%	15.491%	35.949%	75.530%	18.226%
60	1175.57	1320.73	2389.87	1573.57	1851.20	2364.4	1639.53	80.950%	19.143%	40.165%	79.022%	24.138%
70	1242.1	1410.03	2558.5	1612.27	1963.83	2520.2	1671.9	81.450%	14.342%	39.276%	78.733%	18.572%
80	1236.83	1410.23	2579.4	1675.2	1942.40	2547.8	1722.23	82.906%	18.789%	37.736%	80.665%	22.124%
90	1248	1404.93	2618.43	1613.23	1941.33	2588.07	1649.33	86.374%	14.826%	38.180%	84.213%	17.396%
100	1234.1	1370.8	2564.07	1567.53	1992.40	2535.2	1597.63	87.049%	14.352%	45.346%	84.943%	16.548%
Average								68.293%	14.094%	33.709%	66.245%	17.109%

From Table 6 we see that average ratio of the WWM1 and WAC1 algorithms against the lower bound are above 50%. These values show that the performance of the algorithm is not good. The performance of WWM2 and WAC2 are below 20%, while the ratio of WADR5 is around 34%. The smaller the value of the ratio, the better the performance. The closer the solution of the algorithm to the solution of the DCMST, the better the algorithm. Figure 8 shows the performance of the algorithm.

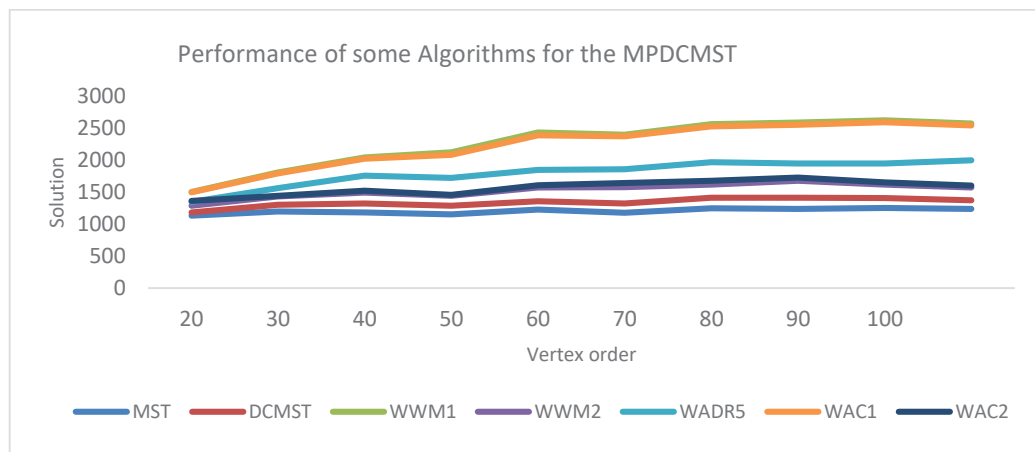


Fig. 8: Performance of WWM1, WWM2, WADR5, WAC1, and WAC2 algorithms.

## 5. CONCLUSIONS

From the results and discussion we can see that among WWM1, WWM2, WADR5, WAC1, and WAC2 algorithms, WWM2 performs the best, followed by WAC2 algorithm. These two algorithms have similar approaches: relaxing the time of installation for vertices in  $HVT_i$  or adding flexibility to the algorithm. Accepting flexibility in the process of connecting/installing the vertices without violating the rules gives a better solution rather than sticking with the schedule of connecting the vertices in a certain order.

## ACKNOWLEDGEMENT

This research work was supported by Research Grant No: 582/ UN26.21/KU/2017. The authors would also like to acknowledge the contributions and financial support from the Directorate General of Higher Education, Ministry of Research, Technology and Higher Education, Republic of Indonesia.

## REFERENCES

- [1] Gabow H.N and R.E. Tarjan.(1984) Efficient algorithms for a family of matroid intersection problems. *Journal of Algorithms*, 5:80-131.
- [2] Garey, M.R.,and Johnson, D.S.(1979) *Computers and Intractability, A Guide to the Theory of NP-Completeness*. Freeman, San Francisco.
- [3] Narula, S.C., and C. A.Ho.(1980) Degree-Constrained Minimum Spanning Tree. *Computer and Operation Research*, 7:239-249.
- [4] Krishnamoorthy, M.,A.T. Ernst and Y. M Sharaila.(2001) Comparison of Algorithms for the Degree Constrained Minimum Spanning Tree. *Journal of Heuristics*, 7(6): 587-611.
- [5] Deo N. and N. Kumar.(1997) *Computation of Constrained Spanning Trees: A Unified Approach*. Network Optimization ( Lecture Notes in Economics and Mathematical Systems. Editor : Panos M. Pardalos, et al. ,Springer-Verlag, Berlin, Germany: 194 – 220.
- [6] Zhou, G. and M Gen. (1997) A Note on Genetics Algorithms for Degree- Constrained Spanning Tree Problems. *Networks*, Vol. 30: 91 – 95.
- [7] Wamiliana. (2004) Solving the Degree Constrained Minimum Spanning Tree Using Tabu and Penalty Method. *Jurnal Teknik Industri*:1-9.
- [8] Caccetta L. and Wamiliana.(2001) Heuristics Algorithms for the Degree Constrained Minimum Spanning Tree Problems.Proceeding of the International Congress on Modelling and Simulation (MODSIM),Canberra, Editors: F. Ghassemi et.al:2161-2166.
- [9] Wamiliana and L. Caccetta. (2003)Tabu search Based Heuristics for the Degree Constrained Minimum Spanning Tree Problem.Proceeding of South East Asia Mathematical Society:133-140.
- [10] Wamiliana and L. Caccetta.(2012) The Modified CW1 Algorithm for The Degree Restricted Minimum Spanning Tree Problem, Proceeding of International Conference on Engineering and Technology Development, Bandarlampung 20-21 June:36-39.
- [11] Kawatra R. (2002)A multi period degree constrained Minimum Spanning Tree Problem, *European Journal of Operational Research*,143: 53 – 63.
- [12] [Wamiliana, D. Sakethi, and R. Yuniarti,(2010) Computational Aspect of WADR1 and WADR2 Algorithms for The Multi Period Degree Constrained Minimum Spanning Tree Problem. Proceeding SNMAP, Bandar lampung 8 – 9 December:208 – 214.
- [13] Wamiliana, Amanto, and M. Usman.(2013) Comparative Analysis for The Multi Period Degree Constrained Minimum Spanning Tree Problem. Proceeding The International Conference on Engineering and Technology Development (ICETD):39 – 43.
- [14] JWamiliana, F. A.M. Elfaki, M. Usman, and M. Azram. (2015) Some Greedy Based Algorithms for Multi Periods Degree Constrained Minimum Spanning Tree Problem. *ARPN Journal of Engineering and Applied Sciences*, 2015: 10 (21): 10147 – 10152.
- [15] Wamiliana, M. Usman, D. Sakethi, R. Yuniarti, and A. Cucus.(2015) The Hybrid of Depth First Search Technique and Kruskal's Algorithm for Solving The Multiperiod Degree Constrained Minimum Spanning Tree Problem. *The 4th International Conference on Interactive Digital Media (ICIDM)*. IEEE Explore, Dec 2015
- [16] Wamiliana, Asmiati, M. Usman, A. Hijriani, and W. C. Hastono. (2018) Comparative Analysis of Some Modified Prim's Algorithms to Solve the Multiperiod Degree Constrained Minimum Spanning Tree Problem. *Indian Journal of Science and Technology*,11(11):1-6.

- [17] Wamiliana, Warsono, Asmiati, A. Hijriani, and W. C. Hastono.(2018) Different Time Installation Effect on The Quality Of The Solution For The Multiperiod Installation Problem Using Modified Prim's Algorithm. Far East Journal of Electronics and Communications, 18(2): 291-300.
- [18] GNU Octave. Available: <https://www.gnu.org/software/octave>.

# OPTIMIZATION OF THE REGULARIZATION OF THE SOLUTION TO PLATE HEAT TRANSFER PROBLEMS

FARGANA AKTER<sup>1</sup>, ABDUMALIK RAKHIMOV<sup>2\*</sup>, AHSAN ALI KHAN<sup>1</sup>  
AND TORLA HJ HASSAN<sup>2</sup>

<sup>1</sup>*Department of Materials and Manufacturing Engineering,*

<sup>2</sup>*Department of Science in Engineering,*

*Faculty of Engineering, International Islamic University Malaysia,  
P.O. Box 10, 50728 Kuala Lumpur, Malaysia.*

*\*Corresponding author: [abdumalik@iium.edu.my](mailto:abdumalik@iium.edu.my)*

*(Received: 16<sup>th</sup> April 2019; Accepted: 14<sup>th</sup> October 2019; Published on-line: 20<sup>th</sup> January 2020)*

**ABSTRACT:** Optimization of the regularization of the Fourier series in the case of a steady state heat transfer plate and heat transfer insulated plate problems are investigated and the regularization of the series solutions at a fixed point on the plates are studied at initial time and critical index.

**ABSTRAK:** Pengoptimuman aturan siri Fourier telah dikaji pada keadaan tetap masalah plat pindah haba dan plat penebat pindah haba. Penyelesaian bersiri secara aturan pada titik tetap plat telah dikaji pada masa mula dan indeks penting.

**KEYWORDS:** *optimization; regularization; heat transfer; initial time; critical index*

## 1. INTRODUCTION

Heat transfer problems confront researchers in many branches of science and engineering. Many researchers use Fourier transforms to solve the heat problem in different kinds of engineering applications such as in [1], where the problem of a hydromagnetic hot two-dimensional laminar jet supplying quiescent fluid of a lower temperature is studied using the Fourier series method. Therefore, it is shown that the process which is based on the Fourier series is very efficient and appropriate to solve boundary layer equations applied to plane jet flows with high accuracy. A temperature Fourier series solution in a hollow sphere subjected to periodic boundary conditions is studied in [2]. In this case, the material of the sphere is presumed to be homogeneous and isotropic with time-independent thermal properties [2]. The main purpose of [3] is to identify the flow types and exhibit augmented heat transfer in dependence on a magnetic induction gradient using Fast Fourier Transform analysis. Fourier transform blackbody spectroscopy to measure the radiation from blackbody sources operated at a series of various temperatures is studied in [4]. In [5], the author used a three-dimensional Fourier series solution to discuss the thermal characterization of electronic packages. Here, a Fourier series solution is used for computing local temperature distributions, heat fluxes and thermal resistances. Optimization of the regularized Fourier series solution for a fixed point plate vibration problem is studied at initial time and critical index [6].

The solutions of all above mentioned problems are based on the application of the Fourier series and transformations. Therefore, a regular summation method is required in

the case of some singularities within the problem's input data. An example of this is when input data is expressed by singular distributions. In this paper, we will classify the singularity in terms of the Sobolev spaces and the Reisz method of summation will be considered as regularization of the Fourier series solutions to the problems.

## 2. PRELIMINARIES

Convergence or divergence of the Fourier series of an integrable function at a certain point depends only from the behaviour of the function in an arbitrary small neighbourhood of that point (localizations principles). When both expansions (Fourier series and integral) converge or diverge at the same time and same term, it is called equiconvergence. In the Liouville space  $L_2(T^N)$ , for any arbitrary self-adjoint elliptic operators, the sufficient condition for the localization of the Reisz means of order  $s$  of multiple Fourier series and integrals is [7]

$$l + s \geq \left\{ \frac{N-1}{2}, \frac{N-1}{p} \right\}, \quad 1 \leq p \leq \infty \quad (1)$$

But for any elliptic operator, a sufficient localization condition is  $l + s \geq \frac{N-1}{p}$  [7].

Moreover, the sufficient localization condition (1) can be weakened if summation of the multiple Fourier integrals occurs by the surface level of the elliptic operators from the class  $A_r$ ,

$$l + s \geq \frac{N-1}{p} - r \left\{ \frac{1}{p} - \frac{1}{2} \right\}, \quad 1 \leq p \leq \infty \quad (2)$$

In  $N$ -dimension, equiconvergence for both expansions (Fourier series and integral) is not valid for the rectangular partial sums. Equiconvergence in summation of the Fourier expansion of the linear continuous functional that is associated with an elliptic polynomial is discussed in [8]. Moreover, the general expanded expansions of the distributions are discussed in [9-19].

Let  $\mathcal{E}(T^N)$  be the space of an infinitely differentiable function  $\phi: T^N \rightarrow \mathbb{C}$ . The system of semi norm for any compact subset  $K$  of  $T^N = [-\pi, \pi]^N$  is defined by,

$$P_{k,\gamma}(\phi) = \sup_{x \in K} |D^\gamma \phi(x)| \quad (3)$$

where  $\gamma$  is a multi-index denoted by  $|\gamma| = (\gamma_1 + \gamma_2 + \dots + \gamma_N)$  and  $\gamma = (\gamma_1, \gamma_2, \dots, \gamma_N)$  is  $N$  dimensional vector with the non-negative integer components  $\gamma_j$  ( $j = 1, 2, \dots, N$ ). For instance,  $D^\gamma = D_1^{\gamma_1} D_2^{\gamma_2} \dots D_N^{\gamma_N}$ , where  $D_j = \frac{1}{i} \frac{\partial}{\partial x_j}$ ,  $j = 1, 2, \dots, N$ .

For any functional  $f \in \mathcal{E}'(T^N)$  (where  $\mathcal{E}'(T^N)$  is the conjugate space of the locally convex topological space  $\mathcal{E}(T^N)$ ), we can write

$$f = (2\pi)^{-N/2} \sum_{n \in \mathbb{Z}^N} f_n e^{inx}, \quad (4)$$

where  $z^N$  is the set of all vectors with integer components,  $f_n$  is the Fourier coefficient, which is defined as the value of  $f$  on the test function on  $(2\pi)^{-N/2} e^{-inx}$  and  $x \in T^N$ .

Consider the following elliptic polynomial:

$$A(n) = \left( \sum_{j=1}^{r+1} n_j^2 \right)^{m+1} + \left( \sum_{j=r+2}^N n_j^2 \right)^m \left( \sum_{j=1}^N n_j^2 \right)$$

where  $n = (n_1, n_2, \dots, n_N) \in Z^N$ .  $m$  is a positive integer number and  $r = 0, 1, 2, \dots, N-1$ . Polynomial  $A(n)$  is a homogeneous of degree  $2(m+1)$  and an elliptic ( $A(n) > 0$ ). Note that,  $A(n) \in A_r$  but  $A(n) \notin A_{r+1}$  [20].

For any non-negative real number  $s$ , the Riesz means of order  $s$  of the Fourier series in equation (1) is defined as,

$$\sigma_\lambda^s f(x) = (2\pi)^{\frac{N}{2}} \sum_{A(n) < \lambda} \left( 1 - \frac{A(n)}{\lambda} \right)^s f_n \exp(inx). \quad (5)$$

Now, we extend a distribution  $f$  from  $N$ -dimensional torus  $T^N$  to the whole space  $R^N$  by zero. Then the Bochner-Riesz means of order  $s$  of the Fourier integral of  $f$  is,

$$R_\lambda^s f(x) = (2\pi)^{\frac{N}{2}} \int_{A(\xi) < \lambda} \left( 1 - \frac{A(\xi)}{\lambda} \right)^s \hat{f}(y) \exp(i\xi x) d\xi, \quad (6)$$

where,  $\hat{f}(y) = \langle f, (2\pi)^{-N/2} \exp(-i\xi x) \rangle$  is the Fourier transformation of the extended functional  $f$  and it acts on,  $(2\pi)^{-N/2} \exp(-i\xi x)$  via  $x$ .

For any real number  $l$ , the Sobolev space of distributions  $L_2^l(T^N)$  is

$$L_2^l(T^N) = \{f \in \mathcal{E}' : \sum_{n \in Z^N} (1 + |n|^2)^l f_n^2 < \infty\} \quad (7)$$

Theorem 1

We have  $\mathcal{E}(T^N) \subset \bigcup_{l=-\infty}^{\infty} L_2^{-l}$ . The Dirac delta function  $\delta \in L_2^{-l}$  (where  $l > N/2$ ), and

$s > \max\left\{ \frac{(N-r-1)(1-1/2m)}{2} + \frac{r}{2}, \frac{N-1}{2} \right\} + l$ . Then for any  $f \in L_2^{-l}(T^N)$

$$\sigma_\lambda^s f(x) = R_\lambda^s f(x) + O(1) \|f\|_{-l} \quad (8)$$

where  $\|\cdot\|_{-l}$  is a norm in  $L_2^{-l}(T^N)$  :

$$\|f\|_{-l} = (2\pi)^{\frac{N}{2}} \sqrt{\sum_{n \in Z^N} (1 + |n|^2)^{-l} f_n^2} \quad [8] \quad (9)$$

In [21,22] mathematical models of thermo control processes in a rectangular plate are studied. In [21] it is considered that the temperature in a plate is controlled by heat exchange through one boundary while the other three are insulated. In these two papers, they study sufficient conditions for achieving the given projection by controlling the parameter on the boundary. Mathematical models of thermo control processes when control parameter is a vector function are studied in [23]. In [24] a control of the heat transfer was studied based on time/norm and it found sufficient and necessary conditions



for such a control. Equiconvergence of the spectral expansions associated with the operators with singular coefficients was studied in [25] and for the Sturm Liouville operator in [26]. The definition of the operator  $A(n)$  and application of the Poisson summation method is explained in [27].

In the next sections, for a steady-state heat transfer problem and insulated heat problems, we will verify this theorem numerically for different plates subjected to different boundary conditions. As mentioned, the Regular summation method will be used for excellent accuracy and convergence.

### 3. DESCRIPTION OF THE PROBLEM

Consider a thin square plate made of some thermally conductive material. Suppose the dimensions of the plate are  $X \times Y$ . The plate is heated in some way. For example, in a steady state heat transfer problem or heat transfer insulated (no heat escapes from this surface) plate problems. The plate is homogeneous, that is -its mass per unit volume is a constant.

Assume that,

$$v(x, y, t) = \text{temperature of the plate at position } (x, y) \text{ and time } t.$$

For a fixed  $t$ ,  $v(x, y, t)$  gives the temperature of the plate at position  $(x, y)$ .

For the thin plate in which the temperature  $v$  is a function of time  $t$  and position  $(x, y)$  satisfy the two-dimensional heat equation

$$v_t = h(v_{xx} + v_{yy}), \quad 0 < x < b, \quad 0 < y < c \quad (10)$$

where  $h$  is the heat conductivity coefficient and it is constant.

The solution of the heat equation (10) is subject to the boundary conditions and initial conditions.

The solution of the heat transfer problems in the two dimensional case has a form of a double Fourier series by eigenfunctions and these eigenfunctions depend on the boundary conditions. The coefficient of the Fourier series is found from the initial conditions. That is why convergence or divergence of the corresponding Fourier series depends on the smoothness or singularity of the initial conditions. If the initial conditions are given by very good functions then this series converges. In many engineering phenomena, the initial data may be not represented by good functions. Sometimes initial conditions may not even be functions. For example, initial conditions can be expressed as the Dirac delta function. In a one dimensional case, the Fourier series of the Dirac delta function diverges at a regular point. However, the arithmetic means of the Fourier series of the Dirac delta function converges. Thus, for the solutions of the corresponding heat problems some regularizations of the Fourier series solutions are required. Here, based on the singularity, we consider the Reisz method of summation as regularization of the Fourier series solutions of the heat problems. When we increase the order of the Reisz means, the solutions will converge but the numerical calculations will be increase. So, the regularized Fourier series solutions need optimization.

Optimization of the regularization of the solutions of the plate heat transfer problems is finding the solutions from the regularized Fourier series for minimum order of the Reisz means. The minimum order is  $s > (N - 1)/2 + l$ . Here,  $s$  is the order and  $N$  is dimension.

After optimization, we will calculate the numerical solutions. Here, we will find the optimization of the regularization of the series solutions at a fixed point on the plates at the initial time and critical index. Finally, we will verify if the solution is convergent or not.

### 3.1 Problem 1: Steady-State Heat Transfer Problem

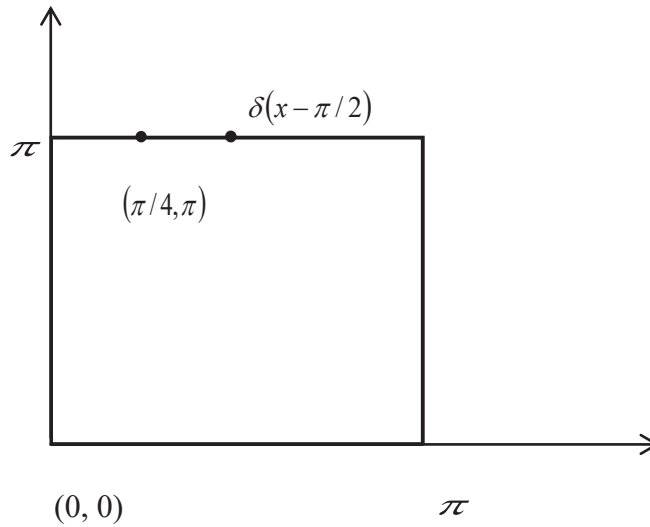


Fig. 1: A plate of dimensions  $\pi \times \pi$  in the  $xy$ -plane.

Consider an aluminium plate of dimensions  $\pi \times \pi$  in the  $xy$ -plane as shown on Fig. 1. The steady state equation subjected to the boundary conditions is

$$u_{xx} + u_{yy} = 0, \quad 0 < x < \pi, \quad 0 < y < \pi \quad (11)$$

$$u(0, y) = 0, \quad (12)$$

$$u(x, 0) = 0, \quad (13)$$

$$u(\pi, y) = 0, \quad (14)$$

$$u(x, \pi) = \delta\left(x - \frac{\pi}{2}\right), \quad (15)$$

where  $\delta$  is a Dirac delta function.

Solution of the steady state problem is,

$$u(x, y) = \sum_{n=1}^{\infty} A_n \text{Sin}h(ny) \text{Sin}(nx), \quad (16)$$

where,  $A_n$  is a constant coefficient. After putting the boundary condition in equation (16) we found the value of  $A_n$

$$A_n = \frac{\text{Sin} \frac{n\pi}{2}}{\text{Sin}h(n\pi)}, \quad (17)$$

Now, the solution of the steady state problem is,

$$u(x, y) = \sum_{n=1}^{\infty} \frac{\sin \frac{n\pi}{2}}{\sinh(n\pi)} \sinh(ny) \sin(nx), \quad (18)$$

The steady state solution at  $y = \pi$  is

$$u(x, \pi) = \sum_{n=1}^{\infty} \sin \frac{n\pi}{2} \sin(nx), \quad (19)$$

Therefore, to find the convergence of the series we have to choose a point. We know that in the point  $\left(\frac{\pi}{2}, \pi\right)$ , the value of the series is infinity. Now, take a point in  $x = \pi$  axis

except the Dirac delta function. Here we choose  $x = \frac{\pi}{4}$  and  $y = \pi$ .

It should not be convergent. Here, regularization is required in order to solve this series in a stable manner. The Riesz means of order  $s$  ( $s$  is non-negative real number) of the Fourier series in equation (19) is defined as

$$E_{\lambda}^s u(x, \pi) = \sum_{|n| < \lambda} \left(1 - \frac{|n|}{\lambda}\right)^s \sin \frac{n\pi}{2} \sin(nx) \quad (20)$$

### 3.1.1 Regularization of the Steady-State Heat Transfer Plate Problem at Initial Time

Here, we will test the regularization of the series in equation (20). We set order  $s = 0, 1$  and time  $t = 0$ . The series solution in equation (20) for different values of  $\lambda$  and at the point  $\left(\frac{\pi}{4}, \pi\right)$  is given below:

Table 1: Solution of the regularized series in equation (20) for different  $s$  ( $s = 0, s = 1$ ) and time  $t = 0$ .

$\lambda$	$E_{\lambda}^0(\pi/4, \pi, 0)$	$E_{\lambda}^1(\pi/4, \pi, 0)$
350	-0.707106781	0.002020305
450	0.707106781	0.001571348
550	-0.707106781	0.001285649
650	0.707106781	0.001087857
750	-0.707106781	0.000942809
850	0.707106781	0.000831891
950	-0.707106781	0.000744323
1050	0.707106781	0.000673435
1150	-0.707106781	0.000614875
1250	0.707106781	0.000565685
1350	-0.707106781	0.000523783
1450	0.707106781	0.000487663

From Table 1, it is clear that for  $s = 0$  the Fourier series diverges. After regularization, the Riesz means of order  $s = 1$  of the Fourier series is convergent. The solution of the series of the Riesz means of order  $s = 1$  is approximately very near to zero.

### 3.1.2 Regularization of the Steady-State Heat Transfer Plate Problem at Critical Index

From Table 1, it is clear that when  $s = 1$ , the series converges. We know that the series will converge when  $s > \frac{N-1}{2} + l$ . So  $s = 1/2$  is the critical point for the regularized series. Here, we choose a more complicated point, the critical point  $s = 0.5$ . To understand the difference between values below the critical point and values above the critical point, we take two more points:  $0.5 - \varepsilon$  and  $0.5 + \varepsilon$  ( $\varepsilon$  is very small number). Here, we choose  $\varepsilon = 0.1$ . Where all the other parameters are kept the same.

Table 2: Solution of the regularized series in equation (20) for different  $s$  ( $s = 0.4, s = 0.5, s = 0.6$ ).

$\lambda$	$E_{\lambda}^{0.4}(\pi/4, \pi, 0)$	$E_{\lambda}^{0.5}(\pi/4, \pi, 0)$	$E_{\lambda}^{0.6}(\pi/4, \pi, 0)$
650	0.041758111	0.019793588	0.009259818
700	0.020462554	0.013759143	0.008979066
850	0.037451159	0.017249285	0.007826599
1300	-0.015876433	0.009997791	0.006101631
1450	0.030173547	0.013132134	0.005611037
1900	0.013602391	0.008230995	0.004822541
3700	-0.010381654	0.005860529	0.003197979
4250	0.019565055	0.076112881	0.002889619
9500	0.007096985	0.003635011	0.001795733

From Table 2, it is clear that below the critical point, the series diverges and after the critical point, the series is converges. But, at the critical point, the answer of the regularized series is so near to zero but still diverges.

### 3.2 Problem 2: Heat Transfer Problem of the Insulated Plate (when the Lower Plate is Insulated)

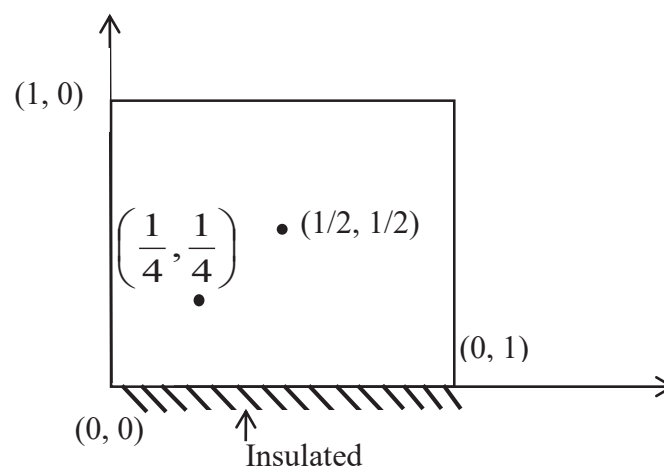


Fig. 2: An aluminium plate of dimensions  $1 \times 1$  in the  $xy$ -plane.

Consider a square aluminium plate of dimensions  $1 \times 1$  in the  $xy$ -plane as shown in Fig. 2. The plate is insulated in the  $x$ -axis. The heat transfer equation subjected to boundary conditions is

$$u_t = k(u_{xx} + u_{yy}), \quad 0 < x < 1, \quad 0 < y < 1 \quad (21)$$

$$u(0, y, t) = 0, \tag{22}$$

$$u_y(x, 0, t) = 0, \tag{23}$$

$$u(1, y, t) = 0, \tag{24}$$

$$u(x, 1, t) = 0, \tag{25}$$

$$u(x, y, 0) = \delta\left(x - \frac{1}{4}, y - \frac{1}{4}\right), \tag{26}$$

where  $\delta$  is a Dirac delta function.

Solution of the steady state problem is,

$$u(x, y, t) = \sum_{n=1}^{\infty} \sum_{m=0}^{\infty} U_{nm} e^{-k(n^2 + (\frac{2m+1}{2})^2)\pi^2 t} \text{Sin}(n\pi x) \text{Cos}\left(\frac{2m+1}{2}\right)\pi y, \tag{27}$$

where,  $U_{nm}$  is a constant coefficient. After putting the boundary condition in equation (27) we can find

$$U_{nm} = \text{Sin} \frac{n\pi}{4} \text{Cos}\left(\frac{2m+1}{8}\right)\pi, \tag{28}$$

Now, the solution of the heat transfer problem is,

$$u(x, y, t) = \sum_{n=1}^{\infty} \sum_{m=0}^{\infty} e^{-k(n^2 + (\frac{2m+1}{2})^2)\pi^2 t} \text{Sin} \frac{n\pi}{4} \text{Cos}\left(\frac{2m+1}{8}\right)\pi \text{Sin}(n\pi x) \text{Cos}\left(\frac{2m+1}{2}\right)\pi y \tag{29}$$

In this problem, we know that at the point  $\left(\frac{1}{4}, \frac{1}{4}\right)$ , the value of the series is infinity.

Now, choose a point in the plate except the Dirac delta function. Here, we take  $x = \frac{1}{2}$  and  $y = \frac{1}{2}$ .

In this case, the input data has some singularities. It should not be convergent. Here, regularization is required in order to solve this series in a stable manner. The Riesz means of order  $s$  ( $s$  is non-negative real number) of the Fourier series in equation (29) is defined as

$$E_{\lambda}^s u(x, y, t) = \sum_{\sqrt{n^2 + m^2} < \lambda} \left(1 - \frac{\sqrt{n^2 + m^2}}{\lambda}\right)^s e^{-k(n^2 + (\frac{2m+1}{2})^2)\pi^2 t} \text{Sin} \frac{n\pi}{4} \text{Cos}\left(\frac{2m+1}{8}\right)\pi \text{Sin}(n\pi x) \text{Cos}\left(\frac{2m+1}{2}\right)\pi y \tag{30}$$

### 3.2.1 Regularization of the Two Dimensional Heat Transfer Problem at Initial Time

Here, we will test the regularization of the series in equation (30). Therefore, we take order  $s = 0, 1, 2$  and time  $t = 0$ . The series solution in equation (30) for different value of  $\lambda$  and at the point  $\left(\frac{1}{2}, \frac{1}{2}\right)$  is given below:

Table 3: Solution of the regularized series in equation (30) for different  $s$  ( $s = 0, s = 1, s = 2$ ) and time  $t = 0$ .

$\lambda$	$E_{\lambda}^0(1/2, 1/2, 0)$	$E_{\lambda}^1(1/2, 1/2, 0)$	$E_{\lambda}^2(1/2, 1/2, 0)$
1700	-4.889995713	0.008050281	0.002943257
2500	-9.416538804	-0.003613664	0.001310513
5500	4.039739941	0.001821067	0.000226622
6500	11.13298168	-0.003669672	0.000153341
8500	-14.55226918	0.003217023	0.000077823
10500	17.22542063	-0.002024961	0.000047231
12500	-27.03824111	0.001093712	0.000040143
12700	30.23102475	-0.003398458	0.000039281
12900	9.304453421	0.001452938	0.000035381
13400	-15.70031947	-0.000344863	0.000030437

From Table 3, it is clear that for  $s = 0$  the Fourier series diverges. Although after regularization the value of the Riesz means of order  $s = 1$  of the Fourier series is approximately near to zero but the series is diverges. Finally, when the Reisz means of order  $s = 2$ , the series converges.

### 3.2.2 Regularization of the Square Plate Steady-State Heat Transfer Problem at Critical Index

From Table 3, it is clear that the series converges for  $s = 2$ . We know that the series converges when order  $s > \frac{N-1}{2} + l$ . So,  $s = 3/2$  is the critical point for the regularized series. Here, we choose the critical point  $s = 1.5$ . To understand the difference between below the critical point and above the critical point we take two more points  $1.5 - \varepsilon$  and  $1.5 + \varepsilon$  ( $\varepsilon$  is very small number). Here, we choose  $\varepsilon = 0.1$ . Where all the other parameters are kept the same.

Table 4: Solution of the regularized series in equation (30) for different  $s$  ( $s = 1.4, s = 1.5, s = 1.6$ ).

$\lambda$	$E_{\lambda}^{1.4}(1/2, 1/2, 0)$	$E_{\lambda}^{1.5}(1/2, 1/2, 0)$	$E_{\lambda}^{1.6}(1/2, 1/2, 0)$
500	0.005020001	0.006763001	0.009379112
6500	0.000085401	0.000119112	0.000134201
7500	0.000150021	0.000130211	0.000118011
10500	-0.000038311	0.000006641	0.000066401
10520	0.000114353	0.000069814	0.000050122
10550	-0.000003256	0.000024155	0.000024811
10650	0.000117794	0.000069664	0.000020271
10800	-0.000057245	-0.000002461	0.000011784
18500	0.000004991	0.000007342	0.000009682
33000	-0.000000511	0.000009821	0.000000756

From Table 4, we can conclude that below the critical point, the series diverges and after the critical point, the series converges. But, at the critical point, the answer of the regularized series is so near to zero but it diverges.

### 3.3 Problem 3: Heat Transfer Problem of the Insulated Plate (when the Upper Plate is Insulated)

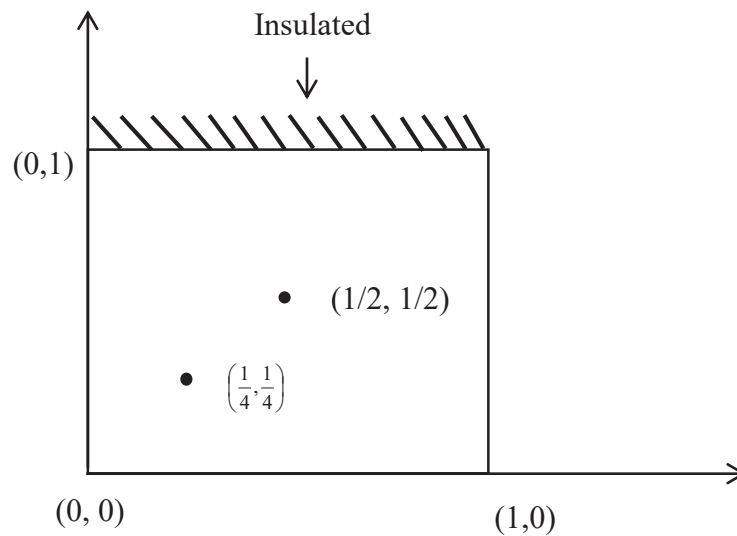


Fig. 3: A square plate of dimensions  $1 \times 1$  in the  $xy$ -plane.

Consider a square aluminium plate of dimensions  $1 \times 1$  in the  $xy$ -plane as shown on Fig. 3. The plate is insulated in the  $x = 1$  axis. The heat transfer equation subjected to boundary conditions is

$$u_t = k(u_{xx} + u_{yy}), \quad 0 < x < 1, \quad 0 < y < 1 \quad (31)$$

$$u(0, y, t) = 0, \quad (32)$$

$$u(x, 0, t) = 0, \quad (33)$$

$$u(1, y, t) = 0, \quad (34)$$

$$u_y(x, 1, t) = 0, \quad (35)$$

$$u(x, y, 0) = \delta\left(x - \frac{1}{4}, y - \frac{1}{4}\right), \quad (36)$$

where,  $\delta$  is a Dirac delta function. Solution of the heat transfer equation of the insulated plate subjected to the boundary condition is,

$$u(x, y, t) = \sum_{n=1}^{\infty} \sum_{m=0}^{\infty} V_{n_m} e^{-k(n^2 + (\frac{2m+1}{2})^2)\pi^2 t} \sin(n\pi x) \sin\left(\frac{2m+1}{2}\pi y\right), \quad (37)$$

where,  $V_{n_m}$  is a constant coefficient. From the Dirac delta function and the boundary condition, we found

$$V_{n_m} = \sin\frac{n\pi}{4} \sin\left(\frac{2m+1}{8}\pi\right), \quad (38)$$

Finally, the solution of the heat transfer problem is,

$$u(x, y, t) = \sum_{n=1}^{\infty} \sum_{m=0}^{\infty} e^{-k(n^2 + (\frac{2m+1}{2})^2)\pi^2 t} \sin\frac{n\pi}{4} \sin\left(\frac{2m+1}{8}\pi\right) \sin(n\pi x) \sin\left(\frac{2m+1}{2}\pi y\right) \quad (39)$$

In the point  $\left(\frac{1}{4}, \frac{1}{4}\right)$ , the temperature of the plate is infinity. Here, we choose another point in the plate except the Dirac delta function. Therefore, we take  $x = \frac{1}{2}$  and  $y = \frac{1}{2}$ . In the above series, the input data has some singularities. It should not be convergent. Here, regularization is required in order to solve this series in a stable manner. The Riesz means of order  $s$  ( $s$  is non-negative real number) of the Fourier series in equation (39) is defined as

$$E_{\lambda}^s u(x, y, t) = \sum_{\sqrt{n^2+m^2} < \lambda} \left(1 - \frac{\sqrt{n^2+m^2}}{\lambda}\right)^s e^{-k(n^2 + (\frac{2m+1}{2})^2)\pi^2 t} \text{Sin} \frac{n\pi}{4} \text{Sin} \left(\frac{2m+1}{8}\right)\pi \text{Sin} (n\pi x) \text{Sin} \left(\frac{2m+1}{2}\right)\pi y \quad (40)$$

### 3.3.1 Regularization of the Two Dimensional Heat Transfer Problem at Initial Time

Now, we will test the regularization of the heat transfer plate. Here, we take order  $s = 0, 1, 2$  and time  $t = 0$ . For different values of  $\lambda$  and a fixed point  $\left(\frac{1}{2}, \frac{1}{2}\right)$ , the series solution (40) is given below:

Table 5: Solution of the regularized series in equation (40) for different  $s$  ( $s = 0, s = 1, s = 2$ ) and time  $t = 0$ .

$\lambda$	$E_{\lambda}^0(1/2, 1/2, 0)$	$E_{\lambda}^1(1/2, 1/2, 0)$	$E_{\lambda}^2(1/2, 1/2, 0)$
500	2.75804036	0.01009106	0.01553744
1500	1.58279358	-0.00267634	0.00178935
1700	-2.56669864	0.00588032	0.00140549
2100	21.1892037	-0.00640545	0.00093207
2300	-12.4315789	0.00600931	0.00078491
2500	3.13509121	-0.00789911	0.00067197
3500	-19.2678209	0.00344795	0.00035346
5500	18.9915902	-0.00108365	0.00015099
8500	-24.9696107	0.00417739	0.00006941
10500	34.1948078	-0.00256344	0.00004952
13500	-13.6204239	0.00238150	0.00003851

From Table 5, we can summarize that for  $s = 0$ , the Fourier series diverges. Although, after regularization the value of the Riesz means of order  $s = 1$  of the Fourier series is approximately near to zero but the series diverges. Finally, for  $s = 2$ , the series converges.

### 3.3.2 Regularization of the Two Dimensional Heat Transfer Problem at Critical Index

From Table 5, it is clear that the series converges for  $s = 2$ . We know that the series converges when order  $s > \frac{N-1}{2} + l$ . So,  $s = 3/2$  is the critical point for the regularized series. Here, we choose the critical point  $s = 1.5$ . To understand the difference between below the critical point and above the critical point we take two more points  $1.5 - \varepsilon$  and  $1.5 + \varepsilon$  ( $\varepsilon$  is very small number). Here, we choose  $\varepsilon = 0.1$ . Where all the other parameters are kept the same.



Table 6: Solution of the regularized series in equation (40) for different  $s$  ( $s = 1.4, s = 1.5, s = 1.6$ ).

$\lambda$	$E_{\lambda}^{1.4}(1/2, 1/2, 0)$	$E_{\lambda}^{1.5}(1/2, 1/2, 0)$	$E_{\lambda}^{1.6}(1/2, 1/2, 0)$
4500	0.00020801	0.00017612	0.00017332
6500	-0.00000105	0.00005941	0.00008501
8500	0.00010912	0.00008002	0.00006922
10500	-0.00004652	0.00000438	0.00002671
10550	0.00002892	0.00003761	0.00004122
10750	-0.00002072	0.00001082	0.00002711
10900	0.00005763	0.00004984	0.00004572
11100	-0.00002301	0.00001051	0.00002701
14500	0.00002222	0.00002484	0.00002722

From Table 6, it is clear that below the critical point, the series diverges and after critical point, the series converges. But, at the critical point, the answer of the regularized series is so near to zero but it diverges.

#### 4. CONCLUSION

In this paper, we studied optimization of the regularization of the Fourier series of the plate problems such as the steady state heat transfer problem and insulated heat transfer problems. Here, we investigated the regularized Fourier series solution at a fixed point on the plate at the initial time and critical index. As it is expected, we achieved the good convergence after the critical point.

#### REFERENCES

- [1] Rosales-Vera M, Niño Y, Valencia A. (2012) On the Application of the Fourier Series Solution to the Hydromagnetic Buoyant Two-Dimensional Laminar Vertical Jet. *Mathematical Problems in Engineering*, 2012.
- [2] Atefi G, Moghimi M. (2006) A temperature Fourier series solution for a hollow sphere. *Journal of heat transfer*, 128(9): 963-968.
- [3] Pyrda L. (2014) Application of Fast Fourier Transform in thermo-magnetic convection analysis. In *Journal of Physics: Conference Series* (Vol. 530, No. 1, p. 012060). IOP Publishing.
- [4] Steele AG, Rowell NL. (2001) Fourier transform blackbody spectroscopy: toward thermodynamic temperature measurement. In *Thermosense XXIII* (Vol. 4360, pp. 455-464). International Society for Optics and Photonics.
- [5] Culham JR, Yovanovich MM, Lemczyk TF. (2000) Thermal characterization of electronic packages using a three-dimensional Fourier series solution. *Journal of Electronic Packaging*, 122(3): 233-239.
- [6] Fargana A, Rakhimov AA, Khan AA, Hassan TBH. (2018) Optimization of the Regularization of the Solution of the Plate Vibration Problem. *International Journal of Applied Engineering Research*, 13(8): 6364-6368.
- [7] Alimov ShA. (1974) On the localization of spectral decompositions. *Differ. Uravn.* 10(4), 744-746. English translation (1975). *Differ. Equations* 10, 576-578, Zbl. 284.35059.
- [8] Fargana A, Rakhimov AA, Khan AA, Hassan TBH. (2017) Equiconvergence in Summation Associated with Elliptic Polynomial. In *Journal of Physics: Conference Series* (Vol. 949, No. 1, p. 012001). IOP Publishing.

- [9] Rakhimov A, Ahmedov A, Zainuddin H. (2011) Localization Principle of the Spectral Expansions of Distributions Connected with Schrodinger Operator. Australian Journal of Basic and Applied Sciences, 5(5): 1-4.
- [10] Rakhimov AA, Zakaria K, Khan NIA. (2010) On the uniformly convergence spectral expansions connected with Schrödinger's operator of continuous functions in a closed domain. Nucleus, 47(4): 261-265.
- [11] Rakhimov AA. (2003) Localization of the spectral decompositions of distributions, connected with the Schrödinger operator. Modern problems of math. Physics and information technologies, Tashkent, 1: 167-172.
- [12] Alimov ShA, Rakhimov AA. (1996) Localization of Spectral Expansions of Distributions. Differential Equations. 32(6), 798-802.
- [13] Alimov ShA, Rakhimov AA. (1997) Localization of Spectral Expansions of Distributions in a Closed Domain. Difference Equations. 33: 80-82.
- [14] Rakhimov AA. (2000) On the Localization of Multiple Trigonometric Series of Distributions. Dokl. Math. 62(2): 163-165.
- [15] Rakhimov AA. (1996) Localization Conditions for Spectral Decompositions Related to Elliptic Operators from Class  $A_r$ . Mathematical Notes. 59(3): 298-302.
- [16] Rakhimov A, Ahmedov A, Zainuddin H. (2012) On the Spectral Expansions of Distributions Connected with Schrodinger Operator. Applied Mathematics Letters. 25: 921-924.
- [17] Rakhimov AA. (1996) Spectral Decompositions of Distributions from Negative Sobolev Classes. Difference Equations. 32, 1011-1013. <https://zbmath.org/?q=an:0890.47031>.
- [18] Rakhimov AA. (1987) On uniform convergence of spectral resolutions of a continuous function in a closed domain. Izvestiya Akademya Nauk UZSSR, 6: 17-22.
- [19] Rakhimov AA. (2017) On the uniform convergence of Fourier series on a closed domain. Eurasian Mathematical Journal 8 (3), 60-69.
- [20] Ashurov RR. (1983). Localization conditions of spectral expansions, corresponding to elliptic operators with constant coefficients. Mathematical Notes, 33(6): 434-439.
- [21] Fayziev YE. (2018). On the control of the heat conduction. IIUM Engineering Journal, 19(1): 168-177.
- [22] Fayziev YE, Khalilova N. (2016) On a control problem associated with the heat transfer process, J. Vestnik NUU, 2:1 49-54.
- [23] Alimov SA. (2010) On a control problem associated with the heat transfer process. Eurasian mathematical journal, 1(2): 17-30.
- [24] Fattorini HO. (2003) Time and norm optimal controls for linear parabolic equations: necessary and sufficient conditions. In Control and Estimation of Distributed Parameter Systems (pp. 151-168). Birkhäuser, Basel.
- [25] Denisov SA. (1998) Equiconvergence of a spectral expansion, corresponding to a Schrödinger operator with integrable potential, with the Fourier integral. Differentsial'nye Uravneniya, 34(8): 1043-1048.
- [26] Sadovnichaya IV. (2010) Equiconvergence of eigenfunction expansions for Sturm-Liouville operators with a distributional potential. Sbornik: Mathematics, 201(9): 1307.
- [27] Khavin VP, Nikol'skii NK. (1992) Commutative Harmonic Analysis. IV, Encyclopaedia of Mathematical Sciences, vol. 42.

## PARALLEL PROCESS DISCOVERY USING A NEW TIME-BASED ALPHA++ MINER

YUTIKA AMELIA EFFENDI<sup>1\*</sup> AND RIYANARTO SARNO<sup>2</sup>

<sup>1</sup>*Information Systems Study Program, Department of Engineering,  
Universitas Airlangga, Surabaya, Indonesia*

<sup>2</sup>*Department of Informatics, Institut Teknologi Sepuluh Nopember,  
Surabaya, Indonesia*

\*Corresponding author: [yutika.effendi@vokasi.unair.ac.id](mailto:yutika.effendi@vokasi.unair.ac.id)

(Received: 3<sup>rd</sup> June 2019; Accepted: 26<sup>th</sup> October 2019; Published on-line: 20<sup>th</sup> January 2020)

**ABSTRACT:** A lot of services in business processes lead information systems to build huge amounts of event logs that are difficult to observe. The event log will be analysed using a process discovery technique to mine the process model by implementing some well-known algorithms such as deterministic algorithms and heuristic algorithms. All of the algorithms have their own benefits and limitations in analysing and discovering the event log into process models. This research proposed a new Time-based Alpha++ Miner with an improvement of the Alpha++ Miner and Modified Time-based Alpha Miner algorithm. The proposed miner is able to consider noise traces, loop, and non-free choice when modelling a process model where both of original algorithms cannot override those issues. A new Time-based Alpha++ Miner utilizing Time Interval Pattern can mine the process model using new rules defined by the time interval pattern using a double-time stamp event log and define sequence and parallel (AND, OR, and XOR) relation. The original miners are only able to discover sequence and parallel (AND and XOR) relation. To know the differences between the original Alpha++ Miner and the new one including the process model and its relations, the evaluation using fitness and precision was done in this research. The results presented that the process model obtained by a new Time-based Alpha++ Miner was better than that of the original Alpha++ Miner algorithm in terms of parallel OR, handling noise, fitness value, and precision value.

**ABSTRAK:** Banyak sistem perniagaan perkhidmatan menghasilkan sejumlah besar log data maklumat yang payah dipantau. Log data ini akan dianalisis menggunakan teknik proses penemuan bagi memperoleh model proses dengan menerapkan beberapa algoritma terkenal, seperti algoritma deterministik dan algoritma heuristik. Semua algoritma ini memiliki kelebihan dan kekurangannya dalam menganalisis dan mencari log data ke dalam model proses. Kajian ini mencadangkan *Time-based Alpha++ Miner* baru yang merupakan pembaharuan dari algoritma *Alpha++ Miner* dan *Modified Time-based Alpha Miner*. Algoritma baru ini dapat mempertimbangkan kesan bunyi, pusingan, dan pilihan tidak bebas ketika memodelkan model proses di mana kedua algoritma asal tidak dapat menggantikan isu tersebut. *Time-based Alpha++ Miner* baru menggunakan pakai Pola Interval Waktu berjaya memperoleh model proses menggunakan peraturan baru berdasarkan Pola Interval Waktu menggunakan log peristiwa waktu-ganda dan menentukan jujukan dan hubungan selari (AND, OR, dan XOR). Dibandingkan algoritma asal, ia hanya dapat menemukan jujukan dan hubungan selari (AND dan XOR). Bagi membezakan Alpha++ Miner asal dan yang baru termasuk model proses dan kaitannya, penilaian menggunakan nilai padanan dan penelitian telah dijalankan dalam kajian ini. Hasil kajian model proses yang diperoleh oleh *Time-based Alpha++ Miner* baru, adalah lebih baik keputusannya berbanding menggunakan algoritma Alpha++

Miner asal, berdasarkan hubungan selari OR, bunyi kawalan, nilai padanan, dan nilai penelitian.

---

**KEYWORDS:** *Alpha++ miner; business process model; parallel process; process discovery; process mining; time interval pattern*

## 1. INTRODUCTION

Collections of activities that produce services for organizations or companies are called business processes [1]. A lot of services are available in the organization, which requires a means to handle all the services in an efficient way. Information systems were built to facilitate business processes and produce event logs as the documented business processes.

Due to the huge amount of event logs, they will be difficult to observe manually. Well-documented business processes are important because they act as navigator for organizations to operate and analyse their business processes. Obtaining the model of business processes from those event logs is becoming a concern in order to monitor and improve business processes easily and automatically. A process mining technique is a good choice to solve this issue [2].

Process mining consists of several tasks; one of them is process discovery. It is a method to automatically construct a current business process and record variations to the process that occurred within an organization. Because process discovery is a part of the process mining technique, the main goal becomes to discover the process models from an event log that describes the best behaviour of this business process implemented in an organization [3]. To carry out its duties properly, process discovery uses some well-known algorithms to help analyse the event log, such as the deterministic algorithm [4], consisting of Alpha Miner and its renewal versions; Alpha+ Miner, Alpha++ Miner, and Modified Time-based Alpha Miner [5], or the heuristic algorithm [4] i.e. Heuristics Miner and Fuzzy Miner. All of these algorithms have their own limitations and benefits in analysing the event log. In this research, the improvement of Alpha++ Miner and Modified Time-based Alpha Miner, which were the latest improvements on Alpha Miner related to parallel findings, are the main highlights.

This research proposes A New Time-based Alpha++ Miner algorithm to mine a process model along with its relations based on a Time Interval Pattern. The New Time-based Alpha++ Miner is an upgraded version of the Alpha++ Miner [6] and Modified Time-based Alpha Miner [5]. As a process discovery algorithm, the Alpha++ Miner algorithm can handle loop and non-free choice in a business process. This algorithm brings implicit dependencies out of a process model in a Petri Net form for showing non-free choice conditions. As an expansion of Alpha Miner, the steps to discover the model is exactly the same, with the Alpha Miner algorithm using a single-time stamp event log. However, the disadvantages of Alpha++ are that it cannot distinguish the differences between AND and OR in parallel relations and still use sequential relations between activities to obtain a business process. In other words, the Alpha++ algorithm can only determine whether the relations of business processes are sequential and parallel (AND, XOR) in a sequential way. On the other hand, a Modified Time-based Alpha Miner, usually known as a MTBAM algorithm, is the latest update from Alpha Miner which uses time-based information in discovering the process model using a double-time stamp event log. This algorithm can discover sequence and parallel AND, OR, XOR relation. However, this algorithm cannot mine length one loop (L1L), length two loop (L2L), and

non-free choice in the event log to be modelled in a business process. Loop and non-free choice are included in the issues of process discovery. Each issue of process discovery implies that the process discovery cannot present the overall information of an event log in a process model. The similarity between the two algorithms is that they do not consider the noise traces in the event log when obtaining a process model.

To cover the shortcomings of the Alpha++ Miner and MTBAM algorithm, an improvement of the Alpha++ Miner that utilizes Time Interval Pattern is proposed in order to be able to discover process models, including discovering loop, non-free choice, as well as their sequential and parallel relations (AND, OR, XOR) by determining new rules so that the business process cannot only be discovered in a sequential way. In addition, the new one can override noise traces when modelling a process model. To compare our method with the original Alpha++ Miner, fitness and precision will be presented as evaluation of the discovered process models in the experimental result.

The paper is arranged in structured way. Section II is for related work, while in Section III the authors will explain the proposed method; A New Time-based Alpha++ Miner with Time Interval Pattern. Discussion related to experimental results is put in Section IV and Section V will provide the conclusion to this paper.

## 2. LITERATURE REVIEW

### 2.1 Process Mining

Process mining is a study where data mining and machine learning are connected, then do analysis in business processes implemented in an organization. As a popular technique, process mining is always used to observe Standard Operating Procedure (SOP) based on event log run in the organization. The overview of process mining and its tasks is shown in Fig. 1. As shown in the figure, process mining consists of several tasks, namely *discovery*, *conformance*, and *enhancement* [4].

First task is called *process discovery*. It is a method to automatically construct a current business process and occurrences of variations to the process that happened in an organization. Because process discovery is a part of the process mining technique, discovering the process models from an event log that describes the best behaviour of the business process implemented in an organization becomes its main goal. A lot of *process discovery* techniques are suggested. Several of them are Alpha algorithm and Heuristics Miner algorithm. The goal of process discovery techniques is not only representing models that show the relations of activities. The other goal is discovering the social network between resources in business processes.

*Conformance checking* is the second task in process mining. It compares the behaviour captured in the process model and the behaviour captured in the event log. The value of conformance checking is higher if the process model captures more of the behaviour in the event log. It divides into four criteria: fitness, precision, simplicity, and generalization.

The last task of process mining is *enhancement*. An *enhancement* extends or improves the process model which contains the information of the event log. There are two types of *enhancement*. First one is repairing a process model and the second one is extending the process model which refers to the information described in event log, such as durations or allocations. Figure 2 shows the simple explanation of the three tasks in process mining.

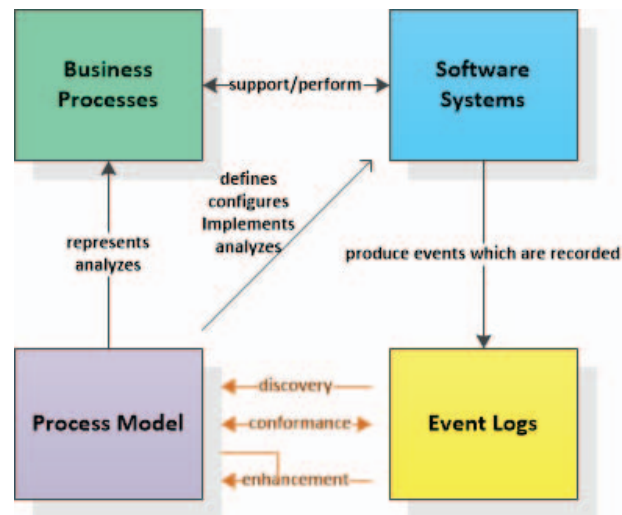


Fig. 1: Mind map of process mining.

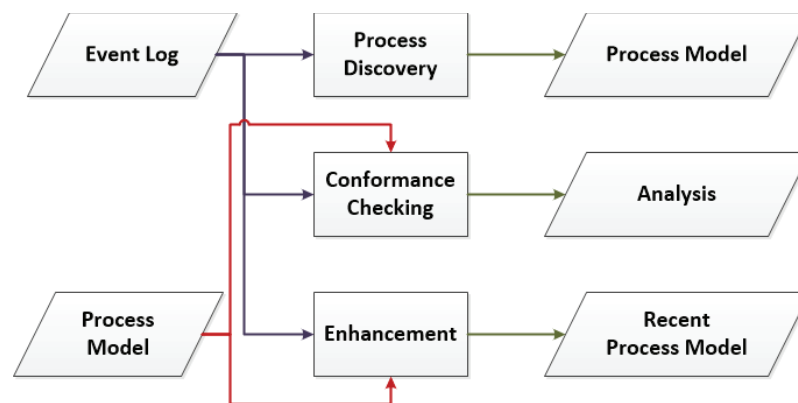


Fig. 2: The explanation of three tasks in process mining.

## 2.2 Event Log

In the process mining technique, the event log becomes the main input. All three tasks of process mining consider that information systems are capable of recording events. An event log contains several processes. Each process recorded in the event log is called a *case*. Usually, a *case* is symbolized by a number in the event log and consists of a series of ordered *events*.

The event log records several pieces of information about the event, such as *activity*, *time stamp*, and *resource*. *Activity* indicates the name of the ordered event. *Time stamp* indicates the time when the ordered event occurred. *Resource* indicates the person who is doing the event. Process mining might use those pieces of information to provide the best understanding of the real processes.

Table 1 shows a piece of the event log. This event log shows the selection acceptance of a journal. As shown, there are two types of processes. The first process is acceptance of a journal, which is displayed in *case 1*. The second process is rejection of a journal, which is displayed in *case 2*. In fact, not all event logs record only three types of information, like in Table 1. There are several event logs that record other information to describe the process clearly. Based on the time stamp, the event log can be divided into single-time stamp event log and double-time stamp event log.

Table 1: An example of event log

Case ID	Activity	Timestamp	Resource
1	Inviting Reviewers	3/8/2016 10:35	John
1	Getting Reviews from Judges	3/8/2016 10:38	Leo
1	Collecting Reviews	3/8/2016 10:41	Smith
1	Checking Reviews from Judges	3/8/2016 10:44	Carlote
1	Deciding Final Result of Journal based on Reviews	3/8/2016 10:47	Novi, Fiona, Helli
1	Determining The Final Result as Accepted Journal	3/8/2016 10:50	Novi, Fiona, Helli
1	Announcing the Final Result	3/8/2016 10:53	John
2	Inviting Reviewers	3/8/2016 10:56	John
2	Getting Reviews from Judges	3/8/2016 10:59	Dion
2	Collecting Reviews	3/8/2016 11:02	Smith
2	Checking Reviews from Judges	3/8/2016 11:05	Rayna
2	Deciding Final Result of Journal based on Reviews	3/8/2016 11:08	Novi, Fiona, Helli
2	Determining The Final Result as Rejected Journal	3/8/2016 11:11	Novi, Fiona, Helli
2	Announcing the Final Result	3/8/2016 11:14	John

### 2.2.1 Single-Time Stamp Event Log

Initially, the single-time stamp event log is a form of general event log. The characteristic of the single-time stamp is to only have one time stamp for each activity. The most common time stamp recorded in the event log is a finish time. Both Alpha algorithm [7] and Heuristics Miner algorithm [8] use single-time stamps to analyse the business processes. An example of the single-time stamp event log is shown in Table 1.

### 2.2.2 Double-Time Stamp Event Log

In some cases, using the single-time stamp event log makes the analysis of business processes difficult. It is because the single-time stamp only records the finish time of the activities, while sometimes the analysis needs to use both of the time stamps of activities to obtain a complete version of the process model. This matter is the reason that double-time stamp event logs appeared. Some algorithms use a double-time stamp event log to determine the model, such as Heuristics Miner with Interval Time [9] and Modified Time-based Alpha Miner [5]. The characteristic of the double-time stamp is to have a start time and a finish time. Because the two time stamps are recorded, they can help solving parallel processes in process mining. This research will use a double-time stamp event log to model the business process.

### 2.3 Existing Algorithm of Process Discovery

In process discovery, issues appeared during the implementation to discover the model. This becomes the main concern in process discovery. Many algorithms are proposed to handle the issues. The algorithms are divided into two principal categories, namely deterministic algorithms consisting of Alpha, Alpha+, Alpha++, and heuristic algorithms consisting of heuristics miner, heuristics miner with time interval, and fuzzy miner. All of these algorithms have their own limitations and excellences in analysing the event log to model the business processes. Therefore, process discovery in terms of modifying the algorithms becomes the most challenging task for researcher.

Deterministic algorithms define reproducible results [10]. A concept of deterministic algorithms is that behaviours of inputs become behaviours of results. It means that this algorithm delivers all behaviours of event log in the process model. Alpha algorithm is a

deterministic algorithm and it has several modifications, such as Alpha+ and Alpha++ algorithm.

### 2.3.1 Alpha Algorithm

Alpha algorithm is the first algorithm used in process discovery. It develops causality of activities based on the event log. The event log used in Alpha algorithm is a single time-stamped event log. The Alpha algorithm focuses on the workflow process and is displayed in the form of workflow-nets, which are also part of Petri Nets [7].

To build a process model using Alpha algorithm [4], the first step is to list all activities that are recorded in the event log. Next, a set of beginning activities and a set of last activities are created. A set of beginning activities contains activities that are recorded first for some cases. Meanwhile, a set of last activities consists of activities that occur as end activities of some cases. In the third step, several tuples are created. In the fourth step a set of tuples is obtained from the third step by taking the activities as well as the set inclusion [7]. The fifth step is listing places that connect activities in every tuple constructed, based on the fourth step. The last step is to connect places with their respective activities and a Petri Net is formed.

Alpha algorithm is a basic algorithm and easy to apply. However, Alpha algorithms have some disadvantages. Alpha algorithm cannot deal with short loop, long loop, invisible task, and non-free choice. Because Alpha algorithm cannot handle several issues, other deterministic algorithms appear to improve Alpha algorithm. Those algorithms are Alpha+ algorithm and Alpha++ algorithm.

### 2.3.2 Alpha+ Algorithm

Alpha+ algorithm is an advanced form of Alpha algorithm. Alpha+ focuses on dealing with short loop conditions [4,5,11]. Both Alpha and Alpha+ algorithms do not consider *noise* in the event log. This algorithm assumes that all information in the event log is correct in order to build an output model, usually presented in a Petri-Net form.

To obtain a Petri Net using Alpha+ algorithm, there are several steps that must be followed [11]. The first step is to list all of activities based on the event log. The second step is to list activities that have dependency relations with itself (have *one loop* condition). The third step is to create a set of activities that do not consist of *one loop* activities. The fourth step is to create a set of arcs that connect *one loop* activities. The fifth step is to discover a workflow net from a set of activities from the third step. The sixth step is combine the fifth step and the fourth step to build a Petri Net. It can be concluded that Alpha+ algorithm cannot deal with skip conditions. The other disadvantage of Alpha+ algorithm is that it cannot override noise traces when modelling a process.

### 2.3.3 Alpha++ Algorithm

Alpha++ algorithm is also an expansion of the Alpha algorithm. It offers a method for handling non-free choice. This algorithm also brings implicit dependencies out of the process model in a Petri Net form for showing non-free choice conditions. The Alpha++ algorithm states that this algorithm is able to discover explicit and implicit dependencies between tasks.

Alpha++ algorithm has several steps to mine non-free choice conditions [12]. An outline of the steps is determining possible implicit dependencies between activities and reducing the possible implicit dependencies by several steps. The obtained implicit dependencies will be added in a process model as the output of the Alpha++ algorithm. The Alpha++ algorithm has the same disadvantages as the Alpha+ algorithm. However,



the Alpha++ algorithm has an extra advantage. That is handling non-free choice conditions.

### 2.3.4 Modified Time-based Alpha Algorithm

Modified Time-based Alpha algorithm (MTBAM) is the latest update on the deterministic algorithm [5]. This algorithm uses time-based information from a double-time stamp event log to discover the model. Not only is it able to take advantage of the double-time stamp event log, but it is also able to define OR relationships in a process model. However, although this algorithm can overcome some of Alpha Miner’s weaknesses, it still cannot discover loops, non-free choices, and it also cannot override noise traces when modelling a process.

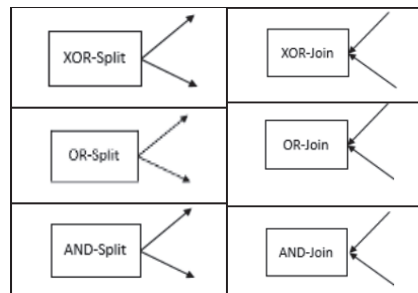
## 3. RESEARCH METHOD

This section presents the event log, temporal pattern and integrated discovery approach for discovering business processes in this research.

### 3.1 Differentiation of Parallel Relations of Activities

A process model has relations to connect all activities. Relations in the process model consist of a sequence and parallel relations. Sequence relation is a relation to connect one activity to another activity directly. Parallel relations are divided into AND, XOR, and OR. Each parallel relation will be presented in Petri Nets form as in Table 2.

Table 2: Parallel relations presented in Petri Nets



Almost all algorithms in process discovery can distinguish AND and XOR relations correctly, but not OR relations. OR relations have high possibilities of appearing in the process model, but a lot of algorithms have difficulty in classifying OR relations. Many algorithms will construe OR relations into XOR or AND whereas these two relations are very different from the function of the OR relation.

### 3.2 A New Time-based Alpha++ Miner with Time Interval Pattern

A new Time-based Alpha++ Miner algorithm will be introduced in this section. This algorithm is divided into three steps: defining the double-time stamp event log, determining the sequence relation, classifying the parallel relation, defining the loop condition and non-free choice, and the last, establishing the process model.

#### 3.2.1 Defining the Double-Time Stamp Event Log

The Double-time stamp event log will be used as an input in this research. However, if there is only a single-time stamp provided in an organization, using the technique explained in [5], a single-time stamp event log can be converted into a double-time stamp event log. After it is obtained, the next step is to determine the relations. In this step, we will pay attention to noise traces in the event log. The event log will be processed without

noise, with 10% noise, with 30% noise, and with 50% noise. We separate the discovery process based on noise traces because they will affect the obtained process model as well as the fitness and precision values.

### 3.2.2 Determining the Relations

As explained in Section 3.1, relations in process model consist of sequence and parallel AND, OR, XOR relations. However, besides those relations, there are conditions wherein the activities proceed to themselves again or return to the previous activity rather than advance to the next activity. This is known as a loop condition [13].

Other than that, non-free choice is also an issue to be solved. The inability to identify a non-free choice process is one of the issues in discovering process models. This is because several processes implement non-free choice. For example, consider the selection of provinces and cities in software systems. Usually, the choice of cities appears appropriate to the selected province. The city cannot be chosen if it is not a part of the selected province. It means that the selection of provinces and cities is a non-free choice process.

This research proposes definitions to determine the sequence and parallel relations from an event log considering noise traces by utilizing a time interval pattern. The definitions in the proposed algorithm are:

**Definition 3.1** There are *event log* ( $EL$ ) and *trace* ( $\sigma$ ) wherein  $\sigma \in EL$ . The types of time interval pattern between activity  $X$  and activity  $Y$ ;  $X (X_s, X_f)$  and  $Y (Y_s, Y_f)$ , according to which  $X, Y \in EL$  can be classified into *before*, *meet*, *is-started-by*, *is-completed-with*, *overlap*, *contain*, and *equal*.

**Definition 3.2** Based on *event log* ( $EL$ ), *trace* ( $\sigma$ ) and activities  $X, Y \in EL$ , the relations of process models both sequential and parallel can be distinguished as follows:

*NotRelated*,  $X \# Y$  iff  $XOY \wedge YOX$

*Sequence*,  $X \rightarrow Y$  iff  $X > Y \wedge YOX$

*Parallel*,  $X \parallel Y$  iff  $X > Y \wedge Y > X \vee \{XOY \vee X @ Y \vee X_f Y \vee X \approx Y \vee X_p Y\}$

*AND*,  $X \bullet Y$  iff  $X \parallel Y$  and there is no  $X \otimes Y$  in  $\sigma$  in  $EL$

*OR*,  $X \oplus Y$  iff  $X \parallel Y$  and there is  $X \otimes Y$  in  $\sigma$  in  $EL$

*XOR*,  $X \otimes Y$  iff  $X \parallel Y$  if there is only  $X$  or  $Y$  in  $\sigma$  in  $EL$

### 3.2.3 Establishing a Process Model

This research proposed how to discover process models using a new Time-based  $\alpha++$  Miner algorithm. There are 10 steps in this proposed algorithm to obtain the process model.

**Step I.** A double-time stamp event log is an input

**Step II.** Define Place (before and after), Start Activities, End Activities, Loop, Non-free Choice, Relations, and Rule Numbers in Time Interval Pattern

**II.1** Steps to determine the loop:

$$LL = \{t \in T_L \mid \exists \sigma = t1t2 \dots tn \in W; i \in \{1, 2, \dots, n\} [t = ti - 1 \wedge t = ti]\} \quad (1)$$

where:

$LL$  : loop

$t$  : activity

$T_L$  : transition between activities

$W$  : workflow of process model

## II.2 Steps to set the rules in the time interval pattern

The model of time interval pattern is based on a double-time stamp to mine the process model. [14] introduced the use of time-based process mining algorithms. In her research, the definition of a time-based process mining algorithm consists of *before and meets, overlaps, contains, is-finished-by, equals, and starts*. In this research, we specify and categorize an improvement of time interval pattern between activities in business processes. We divide the sequence relations into *before* and *meet*, whereas parallel relations become *is-started-by, is-completed-with, overlap, contain* and *equal*. Table 3 presents the rules and the relations proposed in this research.

Table 3: Rules of Determining Activity Relations by Algorithm with HMM

Number	Rules	Relations
1	<b>before</b> : wherein $X > Y$ iff $X_f \leq Y_s$	Sequence
2	<b>meet</b> : wherein $X > Y$ iff $X_f \leq Y_s$	Sequence
3	<b>is-started-by</b> : wherein $X_f Y$ iff $X_f = Y_f \wedge X_s < Y_s \wedge Y_s < X_f$	Parallel
4	<b>is-completed-with</b> : wherein $X \rho Y$ iff $X_s = Y_s \wedge X_f = Y_f$	Parallel
5	<b>overlap</b> : wherein $X O Y$ iff $X_f > Y_s \wedge X_f < Y_f$	Parallel
6	<b>contain</b> : wherein $X @ Y$ iff $X_s < Y_s \wedge Y_f > X_s \wedge X_f > Y_f$	Parallel
7	<b>equal</b> : wherein $X \approx Y$ iff $X_s = Y_s \wedge X_f = Y_f$	Parallel

## II.3 Steps to specify the parallel relations:

XOR relation

$$\text{If Avg PPM} \leq \text{Min ASR in EL, then XOR} \quad (2)$$

OR relation

$$\text{If Min ASR} \leq \text{Avg PPM} \leq \text{Avg ASR in EL, then OR} \quad (3)$$

AND relation

$$\text{If Avg ASR} \leq \text{Avg PPM in EL, then AND} \quad (4)$$

where:

*Min ASR* : minimum value of all sequential relations in EL

*Avg ASR* : average of all sequential relations in EL

*Avg PPM* : average of parallel relations with the same parent activity in process model (the frequency of each activity is both directly and indirectly followed by another activity)

**Step III.** Generate process models by following these steps:

**III.1** Generate set of transition  $T_L = \{t \in T \mid \exists_{\sigma \in L} t \in \sigma\}$  (5)

**III.2** Generate set of input  $T_I = \{t \in T \mid \exists_{\sigma \in L} t = first(\sigma)\}$  (6)

**III.3** Generate set of output  $T_o = \{t \in T \mid \exists_{\sigma \in L} t = last(\sigma)\}$  (7)

**III.4** Generate the places  $P_L = \{p_{(A,B)} \mid (A,B) \in Y_L\} \cup \{I_L, O_L\}$  (8)

**Step IV.** Display the final result of business process in Petri Net [15]

$$\alpha(L) = (P_L, T_L, F_L) \quad (9)$$

where:

$\alpha$  : A business process in Petri Net form

$P$  : place

In the business process, it is symbolized by circle shape and named as p1, p2, p3, etc.

$T$  : transition

In the business process, it shows the activities with square shape

$F$  : function

In the business process, function means an arc.

$F = \{P \times T\}$  means the arc connects the place ( $P$ ) and transition ( $T$ )

**Step V.** Evaluation of the process model using Fitness and Precision [16,17].

## 4. RESULTS AND DISCUSSION

The experimental results will present the process model to prove that our new approach can mine business processes using a new Time-based Alpha++ Miner algorithm utilizing a time interval pattern.

### 4.1 Case Study and Event Log

#### a) Case Study

The experiment data are business processes in a textile industry where the event log is generated from PT. XYZ, a yarn production company in Jakarta, Indonesia. The business processes of PT. XYZ consist of 11 activities as described in Table 4. The pieces of the event log from PT. XYZ are shown in Table 5. The process model will be presented in a Petri Net form [15,18].

#### b) Data Set

The case study uses a double-time stamp event log that has information including case id, activities, start time, and finish time.

This event log contains 50 cases in four conditions. These conditions are event log without noise, event log with 10% noise, event log with 30% noise, and event log with 50% noise. The event log after being processed using the proposed method explained in Section 3 in this experiment is presented in Table 6.

Table 4: Lists of Activities

Activities	Activity code used in this experiment
<i>Getting-good-receive</i>	A
<i>Opening-blending-bale</i>	B
<i>Opposing-spike</i>	C
<i>Blowing-air</i>	D
<i>Striking-cotton</i>	E
<i>Carding</i>	F
<i>Framing-drawing</i>	G
<i>Framing-roving</i>	H
<i>Combing</i>	I
<i>Framing-ring</i>	J
<i>Winding-cone</i>	K

Table 5: Part of Event Log

PP1	A	6/20/2014 10:32	6/20/2014 13:42	PP48	A	9/1/2014 0:15	9/1/2014 16:30
PP1	B	6/20/2014 13:42	6/20/2014 16:52	PP48	B	9/1/2014 16:30	9/2/2014 8:45
PP1	C	6/20/2014 16:52	6/20/2014 20:02	PP48	D	9/2/2014 8:45	9/3/2014 1:00
PP1	D	6/20/2014 17:49	6/20/2014 20:59	PP48	C	9/2/2014 16:52	9/4/2014 1:22
PP1	E	6/20/2014 20:59	6/21/2014 0:09	PP48	E	9/4/2014 1:22	9/4/2014 17:37
PP1	F	6/21/2014 0:09	6/21/2014 3:19	PP48	F	9/4/2014 17:37	9/5/2014 9:52
PP1	G	6/21/2014 3:19	6/21/2014 6:29	PP48	H	9/5/2014 9:52	9/6/2014 2:07
PP1	H	6/21/2014 5:13	6/21/2014 8:23	PP48	G	9/5/2014 18:00	9/7/2014 2:30
PP1	I	6/21/2014 8:23	6/21/2014 11:33	PP48	I	9/7/2014 2:30	9/8/2014 11:00
PP1	J	6/21/2014 11:33	6/21/2014 14:43	PP48	J	9/8/2014 11:00	9/9/2014 19:30
PP1	K	6/21/2014 14:43	6/21/2014 17:53	PP48	K	9/9/2014 19:30	9/11/2014 4:00

Table 6: Event log after being processed using proposed method

Place (Before)	Place (After)	Start Activities	Finish Activities	Relation	Rule Number
PP1	PP2	A	B	Sequence	2
PP2	PP3	B	C,D	Parallel	5
PP3	PP4	C,D	E	Parallel	5
PP4	PP5	E	F	Sequence	1
PP5	PP6	F	G,H	Parallel	6
PP6	PP7	G,H	I	Parallel	7
PP7	PP8	I	J	Sequence	1
PP8	PP8	J	J	Sequence	2
PP8	PP9	J	K	Sequence	1
PP9	PP10	K	<i>e</i>	-	1

## 4.2 Experimental Results

Based on the event log in Table 5, there are sequence and parallel activities in the business processes of PT. XYZ. All activities are in sequence relations except for: *opposing-spike*, *blowing-air*, *framing-roving*, and *framing-drawing*. Activities of *Opposing-spike* and *Blowing-air* are parallel following rule number 5 according to section

3, meanwhile activities *Framing-drawing* and *Framing-roving* follow rule number 6 (contain) and 7 (equal) respectively. Therefore, four of them are parallel relations.

By implementing a new Time-based Alpha++ algorithm for parallel processes utilizing a Time Interval Pattern as explained in Section 3 and by following all steps, the final process model is described in Fig. 3. The type of parallel relations in the process model after (2), (3), and (4) are applied, are also shown in Table 7.

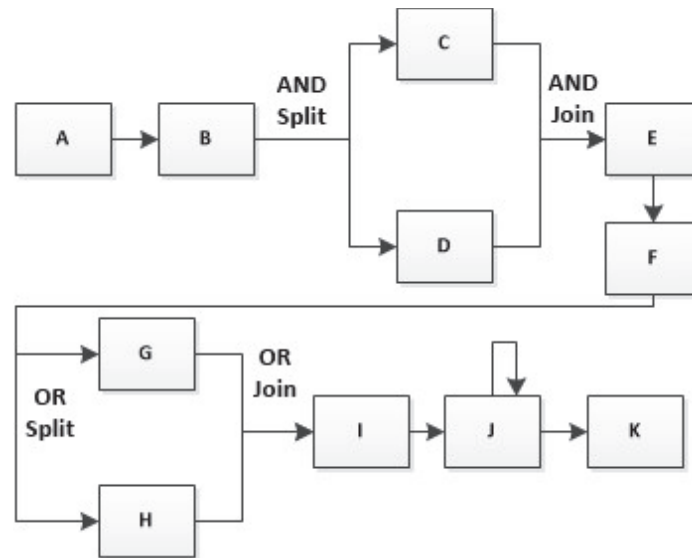


Fig. 3: Process model obtained by using proposed algorithm.

Table 7: Relations of process model generated by proposed algorithm

Place (Before)	Place (After)	Start Activities	Finish Activities	Relation
PP1	PP2	A	B	Sequence
PP2	PP3	B	C,D	Parallel AND
PP3	PP4	C,D	E	Parallel AND
PP4	PP5	E	F	Sequence
PP5	PP6	F	G,H	Parallel OR
PP6	PP7	G,H	I	Parallel OR
PP7	PP8	I	J	Sequence
PP8	PP8	J	J	Sequence
PP8	PP9	J	K	Sequence
PP9	PP10	K	e	-

The evaluation by the proposed algorithm was also tried out in event logs that contain 10% noise, 30% noise, and 50% noise. The percentage of noise shows the total of cases that are noise in the event log. For example, 10% noise means that 10% of all cases restored in the event log are noise. Based on the experiments, the process models from those event logs are the same as the process model displayed in Fig. 3.

This research also presents the results of the same case study and event log processed by the original Alpha++ algorithm in order to compare and prove that our proposed algorithm can discover the process model better than that of the original Alpha++ Miner. The process model of the Alpha++ Miner will be obtained using ProM [19,20], a process mining tool to accelerate the process discovery. Fig.4 shows the resulting process model and Table 8 presents the result of its relations.

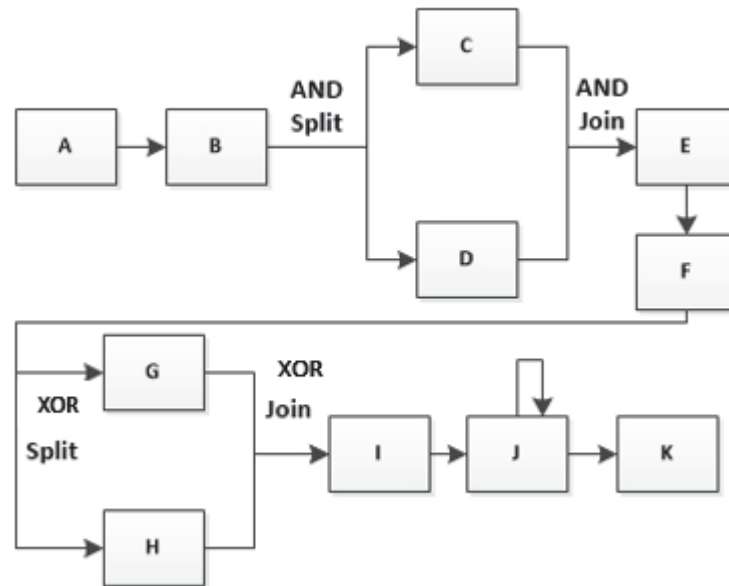


Fig. 4: Process model obtained by applying Alpha++ Miner.

Table 8: Relations of process model generated by original algorithm

Start Activities	Finish Activities	Relation
A	B	Sequence
B	C,D	Parallel AND
C,D	E	Parallel AND
E	F	Sequence
F	G,H	Parallel XOR
G,H	I	Parallel XOR
I	J	Sequence
J	J	Sequence
J	K	Sequence
K	<i>e</i>	-

The results presented in Fig. 4 and Table 8 show that Alpha++ Miner cannot define an OR relation in a process model and considers it as an XOR relation. The reason for this is that the original Alpha++ Miner has difficulties in interpreting the OR relation and is only able to define either AND or XOR relations, so it automatically construes OR relations into XOR or AND if there is an OR relation in the process model, whereas these two relations are very different from the function of OR relation.

### 4.3 Evaluation of the Business Processes

The quality of an algorithm can be measured from the results of that algorithm. In the data mining context, especially clustering and classification, the proposed algorithm is measured based on the obtained classes of respective data. The accuracy, recall, and precision are mostly used criteria to measure the quality of data mining algorithms.

Process mining also has several criteria to measure the quality of algorithms [4,16]. There are fitness, precision, generalization, and simplicity. Our proposed algorithm for parallel processes utilizing time interval pattern is evaluated by measuring fitness and precision value.

The definition of fitness is the total number of cases in the event log displayed in the process model. Fitness is measured using the formula explained in [15]. [15] reviewed that there are two ways to calculate the fitness of an obtained process model. The first way measures the fitness by calculating the percentage of activities that can be generated in the process model. The second way is by calculating the percentage of traces that can be represented in the process model. This evaluation uses the second way to calculate fitness. The equation of the second way is shown in (10).

$$\text{Fitness} = \frac{n_{ct}}{n_t} \quad (10)$$

Table 9: The details of fitness and precision of the proposed algorithm

Process Model of Event Log	Fitness			Precision		
	$n_{ct}$	$n_t$	Result	$n_{ctm}$	$n_{tm}$	Result
Event Log without noise	50	50	1	16	16	1
Event Log with 10% noise	45	50	0,9	16	16	1
Event Log with 30% noise	35	50	0,7	16	16	1
Event Log with 50% noise	25	50	0,5	16	16	1

The precision measures how many traces in process model occur in the event log. The precision can be calculated from the total of correct traces divided by the total of all traces that are generated from process model. The correct traces are combination traces that are generated from the process model and occur in the event log. The equation of precision is shown in (11).

$$\text{Precision} = \frac{n_{ctm}}{n_{tm}} \quad (11)$$

This evaluation measures the quality of the proposed algorithm based on the process models, as shown in Fig. 3. The calculation details of fitness using (10) and precision by applied (11) of the proposed algorithm are presented in Table 9. The final fitness and precision of the proposed algorithm as well as the original algorithm for parallel processes are shown in Table 10.

Based on Table 10, the proposed algorithm for parallel processes has relatively high fitness and high precision to produce a process model from the event log without noise or with noise of 10%, 30%, and 50% compared with the original Alpha++ Miner itself.

Table 10: The Comparison of fitness and precision from both proposed and original algorithm

Algorithm	Fitness	Precision
A New Time-based Alpha++ Miner	0.7	1
Original Alpha++ Miner	0.6	0.83



## 5. CONCLUSIONS

The conclusions for this paper are as follows:

- This research paper focused on introducing a new approach to mine parallel business processes using a time interval pattern that was implemented in Alpha++ Miner algorithm. The proposed method defined seven types of time interval patterns which included both sequence and parallel relations and grouped them into rules.
- A New Time-based Alpha++ algorithm was an upgraded version of Alpha++ Miner algorithm. Compared to original Alpha++ Miner algorithm, the improved algorithm could detect sequence and parallel time stamp using time interval pattern and identifies them as sequence and parallel processes, discovered loop, determined non-free choice, and also distinguished AND, OR, XOR relations in a correct way. Meanwhile, Alpha++ Miner algorithm was not able to define the differences between OR and XOR in parallel relations according to the results of the experiment.
- The experimental results proved that our new process discovery approach could mine the business processes with parallel AND and OR relations, which could not be obtained by the original Alpha++ Miner algorithm. In addition, the results of fitness and precision also clearly stated that a new Time-based Alpha++ also gave better results rather than that of the original Alpha++ Miner algorithm.

## REFERENCES

- [1] Sienou A, Karduck AP, Lamine E, Pingaud H. (2018) Business Process and Risk Models Enrichment: Considerations for Business Intelligence. IEEE International Conference on e-Business Engineering. DOI: 10.1109/ICEBE.2008.123
- [2] Peña MR, Bayona-Oré S. (2018) Process Mining and Automatic Process Discovery. 7th International Conference On Software Process Improvement (CIMPS). DOI: 10.1109/CIMPS.2018.8625621
- [3] Saylam R, Sahingoz OK. (2013) Process mining in business process management: Concepts and challenges. International Conference on Electronics, Computer and Computation (ICECCO). DOI: 10.1109/ICECCO.2013.6718246
- [4] Van der Aalst WMP. (2011) Process mining: discovery, conformance and enhancement of business processes. Springer Science and Business Media. <http://dx.doi.org/10.1007/978-3-642-19345-3>
- [5] Effendi YA, Sarno R. (2018) Modeling Parallel Business Process Using Modified Time-based Alpha Miner. International Journal of Innovative Computing, Information and Control, 14(5). DOI: 10.24507/ijicic.14.05.1565
- [6] Wen L, Van der Aalst WMP, Wang J, Sun J. (2007) Mining Process Models with Non-Free-Choice Constructs. Data Mining and Knowledge Discovery, 15(2):145-180.
- [7] Van der Aalst WMP, Weijters T, Maruster L. (2004) Workflow mining: Discovering process models from event logs. IEEE Transactions on Knowledge and Data Engineering, 16(9):1128-1142.
- [8] Weijters AJMM, Van der Aalst WMP, Alves de Medeiros AK. (2006) Process Mining with the Heuristic-miner algorithm. Technische Universiteit Eindhoven, Tech. Rep. WP, 166:1-34.
- [9] Burattin A, Sperduti A. (2010) Heuristics Miner for Time Intervals. European Symposium on Artificial Neural Networks - Computational Intelligence and Machine Learning, d-side publi., ISBN 2-930307-10-2.
- [10] Gehrke N, Werner M. (2013) Process mining. Das Wirtschaftswachstum, 42(7):934-943.

- [11] Alves de Medeiros AK. (2004) Process mining: Extending the  $\alpha$ -algorithm to mine short loops. Eindhoven, Netherland: BETA working paper series, WP 113, Eindhoven University of Technology, Eindhoven.
- [12] Wen L, Van der Aalst WMP, Wang J, Sun J. (2007) Mining Process Models with Non-Free-Choice Constructs. *Data Mining and Knowledge Discovery*, 15(2):145-180.
- [13] Sarno R, Effendi YA, Haryadita F. (2016) Modified Time-Based Heuristics Miner for Parallel Business Processes. *International Review on Computers and Software (IRECOS)*, 11 (3):249-260. <http://doi.org/10.15866/irecos.v11i3.8717>
- [14] Sutrisnowati RA, Bae H, Dongha L, Minsoo K. (2014) Process Model Discovery based on Activity Lifespan. *International Conference on Technology Innovation and Industrial Management*, pp.137-156. <http://dx.doi.org/10.1016/j.eswa.2014.05.055>
- [15] Effendi YA, Sarno R. (2018) Implementation of the Semantic Web in Business Process Modeling Using Petri Nets,” *International Conference on Information and Communications Technology (ICOIACT)*. DOI: 10.1109/ICOIACT.2018.8350724
- [16] Effendi YA, Sarno R. (2018) Conformance Checking Evaluation of Process Discovery Using Modified Alpha++ Miner Algorithm. *International Seminar on Application for Technology of Information and Communication*, pp. 435 – 440. DOI: 10.1109/ISEMANTIC.2018.8549770.
- [17] Burattin A, Maggi FM, Sperduti A. (2016) Conformance checking based on multi-perspective declarative process models. *Expert Systems with Applications*, 65:194-211. DOI: 10.1016/j.eswa.2016.08.040
- [18] Ishihara K, Hiraishi K. (2001) The completeness of linear logic for Petri net models. *Logic Journal of the IGPL*, 9(4):549 - 567. DOI: 10.1093/jigpal/9.4.549
- [19] De Cnudde S, Claes J, Poels G. (2014) Improving the Quality of the Heuristics Miner in Prom 6.2. *Expert System with Application*, 41:7678-7690.
- [20] Van Dongen BF, Verbeek HMW, Van der Aalst WMP, De Medeiros AKA, Weijters AJMM. (2005) The ProM Framework: A New Era in Process Mining Tool Support. *26th International Conference Applications and Theory of Petri Nets (ICATPN)*. DOI: 10.1007/11494744\_25

## SOFTWARE, ALGORITHMS AND METHODS OF DATA ENCRYPTION BASED ON NATIONAL STANDARDS

RAKHMATILLO DJURAEVICH ALOEV<sup>1</sup>, MIRKHON MUKHAMMADOVICH NURULLAEV<sup>2\*</sup>

<sup>1</sup>*Department of Computational Mathematics and Information Systems, National University of Uzbekistan named after M. Ulugbek, Tashkent, Uzbekistan*

<sup>2</sup>*Department of Information Communication Technology, Bukhara Engineering Technological Institute, Bukhara, Uzbekistan*

*\*Corresponding author: mirxon@mail.ru*

*(Received: 13<sup>th</sup> June 2019; Accepted: 30<sup>th</sup> September 2019; Published on-line: 20<sup>th</sup> January 2020)*

**ABSTRACT:** The article provides a brief description of the cryptography service provider software developed by the authors of this article, which is designed to create encryption keys, create private and public keys of electronic digital signature, create and confirm authenticity of digital signatures, hashing, encrypting, and simulating data using the algorithms described in the State Standards of Uzbekistan. It can be used in telecommunications networks, public information systems, and government corporate information systems by embedding into applications that store, process, and transmit information that does not contain information related to state secrets, as well as in the exchange of information, and ensuring the legal significance of electronic documents. The cryptography service provider includes the following functional components: a dynamically loadable library that implements a biophysical random number sensor; a dynamic library that implements cryptographic algorithms in accordance with the State Standards of Uzbekistan; a module supporting work with external devices; an installation module that provides the installation of a cryptography service provider in the appropriate environment of operation (environment).

**ABSTRAK:** Artikel ini memberikan penerangan ringkas tentang perisian penyedia perkhidmatan kriptografi yang dibangunkan oleh pengarang artikel ini, yang direka untuk membuat kunci penyulitan, kunci persendirian dan awam tandatangan digital elektronik, membuat dan mengesahkan kesahihan tandatangan digital, hashing, penyulitan dan simulasi data menggunakan algoritma yang dinyatakan dalam Standard Negeri Uzbekistan. Ia boleh digunakan dalam rangkaian telekomunikasi, sistem maklumat awam, sistem maklumat korporat kerajaan dengan memasukkan aplikasi aplikasi yang menyimpan, memproses dan menghantar maklumat yang tidak mengandungi maklumat yang berkaitan dengan rahsia negara, serta pertukaran maklumat dan memastikan undang-undang kepentingan dokumen elektronik.

Penyedia perkhidmatan kriptografi termasuk komponen berfungsi sebagai berikut: perpustakaan dinamik yang boleh dimuatkan yang melaksanakan sensor nombor rawak biofisika; perpustakaan dinamik yang melaksanakan algoritma kriptografi mengikut Standard Negeri Uzbekistan; modul menyokong kerja dengan peranti luaran; modul pemasangan yang menyediakan pemasangan penyedia perkhidmatan kriptografi dalam persekitaran operasi yang sesuai (persekitaran).

**KEY WORDS:** *Tools of cryptographic protection of information, Data encryption algorithm, Cryptographic provider, Hash function, Encryption key.*

## 1. INTRODUCTION

The cryptography service provider (CSP) provides the creation of private and public electronic digital signature keys and encryption keys; creation and confirmation of authenticity of electronic digital signature according to the algorithms described in [2, 7]; the formation of derived encryption keys used by data encryption algorithms described in [4, 5]; work with key information stored on external media; hashing of memory areas and other data according to the algorithms described in [3, 6]; and encryption of memory areas and other data in accordance with the data encryption algorithms described in [4, 5].

The cryptography service provider provides support for identifiers of algorithms and parameters for compatibility with third-party crypto-providers in terms of the ability to work with public-key certificates issued by third-party registration centers, provided they use the cryptographic algorithms described in [2, 3, 4, 5, 6, and 7]. The cryptography service provider provides the ability to work with digital certificates of public keys, which are structured in binary ASN.1 format, conforming to the ITU-T X.509 v.3 standard and IETF RFC 5280 and RFC 3739 recommendations. The cryptography service provider provides work with external key carriers such as USB-flash, and eToken Aladdin (eToken PRO 72K (JAVA)). As part of CIPF<sup>1</sup> – CSP, modules are provided that provide for calling cryptographic functions through the Microsoft CryptoAPI 2.0 interface when running under Microsoft operating systems.

In accordance with the functional purpose of a cryptography service provider, it generates public and private electronic digital signature keys, hash keys, functional keys and encryption keys for use, respectively, in the algorithms described in [2, 3, 4, 5, 6, and 7]. In applications where the cryptography service provider will be integrated, an appropriate key manufacturing and distribution system is provided, which will be based on the key generation functions of the cryptography service provider. The cryptography service provider allows the use of a multi-level key protection model using random and derivative keys of key protection. Protection of keys is carried out on the basis of cryptographic transformations in accordance with the PKCS #5 standard [9] using the State Standards of Uzbekistan [3], [4] or the interstate standard [5]. A cryptography service provider provides storage of key information on a hard magnetic disk drive (HDD) and/or external key storage devices, such as USB-flash or eToken Aladdin (eToken PRO 72K (JAVA)). A cryptography service provider provides work with key containers of signature keys, encryption keys, and additional information necessary to ensure the cryptographic protection of keys and ensure control of their integrity. To protect key information from substitution and/or distortion during its storage on HDD and external key carriers, as well as during distribution, key information is supplied with a checksum. In order to ensure the safe use of the cryptography service provider installed on a PC, organizational measures are provided, as well as software and hardware methods and means of protecting information are used to ensure the secrecy of secret keys located in the PC's memory during the operation of the cryptography service provider, as well as the service cryptography service provider parameters stored on the hard disk. The cryptography service provider contains a component that allows you to verify the operability of the cryptographic algorithms implemented in it. Functioning is carried out on the basis of test examples. To ensure the safe use of an application with a built-in ICS-CSP, mechanisms are provided to control the integrity of the cryptography service provider libraries. In the cryptography service provider, a biophysical sensor of random numbers is used to generate random binary

---

<sup>1</sup> CIPF - Cryptographic Information Protection Facility

sequences, which implements the mechanism for generating secret digital signature keys, encryption keys, initialization vectors using various algorithms.

The paper briefly describes the software necessary for the operation of the tools of cryptographic protection of information (TCPI) - data encryption cryptography service provider which is developed by the authors based on national standards. Furthermore, the purpose, capabilities of the TCPI - CSP software and its main characteristics, and the limitation of the using area of this software are given here.

One of the following operating systems is necessary in order to perform the TCPI - CSP: Microsoft Windows XP (32 bit) Professional SP3; Microsoft Windows Vista (32 bit) Ultimate SP2; Microsoft Windows 7 (32 bit) Ultimate; Microsoft Windows Server 2003 (32 bit) Enterprise Edition R2 SP2; Microsoft Windows Server 2008 (32 bit) Enterprise Edition SP2.

The original programming languages for the TCPI - CSP are C and C++.

TCPI - CSP performs the following main functions:

- generation of encryption keys for the data encryption algorithm O`z DSt<sup>2</sup> 1105: 2009 [1] and the algorithm GOST<sup>3</sup> 28147-89 [6];
- encryption of RAM<sup>4</sup> areas and other data in accordance with the data encryption algorithm O`z DSt 1105: 2009 [1] and the algorithm GOST 28147-89 [6];
- generation of keys for implementing and verifying the electronic digital signature (EDS) using algorithms 1 and 2 of O`z DSt 1092: 2009 [3] and the algorithm of GOST R 34.10-2001 [8];
- hashing of memory areas and other data according to algorithm 1 with the parameter  $p = 256$  O`z DSt 1106: 2009 [2] and the algorithm GOST 34.11-94 [7];
- formation and verification of the EDS result in accordance with O`z DSt 1092: 2009 [3] algorithms 1 and 2 and GOST R 34.10-2001 [8];

work with key information stored on external media.

TCPI - CSP can be used as a default crypto-provider for the Windows operating system. TCPI - CSP supports the cryptographic algorithms of the Republic of Uzbekistan and Russia as well as some of the common cryptographic algorithms used in Windows OS, such as RSA, 3DES, SHA-1 etc.

## 2. FUNCTIONS OF WORKING WITH KEY INFORMATION

TCPI - CSP product works with key information in a key container - storage (Key Container).

Since TCPI - CSP is built in accordance with Microsoft technology, the container contains the following keys:

- **AT\_KEYEXCHANGE** key used to encrypt and exchange session keys;
- **AT\_SIGNATURE** - keys used to create and verify a digital signature.

---

<sup>2</sup> O`z DSt - State standard of Uzbekistan

<sup>3</sup> GOST - Interstate standard

<sup>4</sup> RAM - Random Access Memory

*Note:* Private keys (encryption keys and secret signature keys) contained in the container are protected using a security key, which is derived from the value of the user's PIN-code of the token.

Cryptographic procedures are invoked in TCPI - CSP using the PKCS #11 interface.

The underlying concepts of the PKCS #11 interface are slot and token. The token is a repository of some personal information (various keys, certificates, private data, etc.), and the slot acts as a link between a computer and a token that allows different tokens to be connected at different times.

For both *AT\_KEYEXCHANGE* and *AT\_SIGNATURE*, the same and different PKCS #11 slots can be used.

TCPI - CSP supports work with containers located both on the hard disk of the computer and on removable media such as Flash Memory and Smart Card.

Each container has a unique name consisting of a prefix or several prefixes and the name itself. Prefixes in the container name are separated from each other by the “\” symbol. The container name can contain from zero to three prefixes:

$$\text{Container Name} = [\text{pref1} \setminus] [\text{pref2} \setminus] [\text{pref3} \setminus] \text{Name}$$

The location of the media is determined by the first prefix in the container name, depending on the presence of the *CRYPT\_MACHINE\_KEYSET* flag in the *CPAcquireContext* function.

In the container name, the second prefix is a reference to the slot for *AT\_KEYEXCHANGE*, and the third is for *AT\_SIGNATURE*. If the third prefix is absent, then *AT\_KEYEXCHANGE* and *AT\_SIGNATURE* are stored in the same slot.

Protection of token's private objects is carried out using the PKCS #5 cryptographic interface. This algorithm solves two problems at once: encrypting private data and protecting it from accidental or intentional distortion.

### 3. ENCRYPTION FUNCTION

The encryption function is a cryptographic algorithm, which is a bijective mapping from a finite set of plaintext to a finite set of encrypted texts, in which the mapping function depends on a secret parameter called a key. The encryption function is used to encrypt and decrypt information. The encryption function in accordance with [1] can use cryptographic keys of length **256** or **512 bits** for encrypting and decrypting data blocks of length **256 bits**. The encryption function is used for cryptographic protection of data storing and transmitting in computer networks, telecommunications, in separate computing systems or in computers of enterprises, organizations, and institutions.

In symmetric cryptosystems, data exchange takes place in three stages:

- 1) the sender of the message sends the encryption key (or/and functional key) to the recipient via a secure channel that is known only to them;
- 2) the sender, using the encryption key and the function key, converts the original data into encrypted data and sends them to the recipient via the communication channel;

- 3) the recipient, having received the encrypted data, decrypts it with the help of an encryption key and a function key. Both sides may use these keys several times.

In addition to data protection, the encryption function can be used to protect the symmetric keys themselves as they are transmitted over unprotected communication channels. In this case, the transmitted symmetric key is encrypted with some other key, called the security key.

The encryption function [1] contains two modes:

- electronic codebook mode (ECM);
- block chaining mode (BCM).

**The electronic codebook mode** is an encryption mode in which all plaintext blocks are encrypted independently of one another on the same key, in accordance with the data encryption algorithm.

ECM mode is usually used when encrypting symmetric keys.

**The block chaining mode** of encryption is a mode in which each encrypted (decrypted) depends on the previous block of an encrypted (decrypted) block. For the first block, the initialization vector is used as the previous block. If the last block of text is not complete, it is supplemented to the required length. This procedure is called padding. BCM mode is usually used when encrypting data.

The purpose of these functions and functionality of operation algorithms are presented in the document “O`z DSt 1105: 2009. State Standard of Uzbekistan. Information technology. CRYPTOGRAPHIC PROTECTION OF INFORMATION. Data encryption algorithm.”

#### 4. HASH FUNCTION

The hash function is designed to implement a unidirectional compressing mapping  $f$  from set  $A$  to set  $B$ , the input of which is a message of arbitrary length  $M$ , and the output is a string of fixed length  $h(M)$ . Using a hashing transform allows you to reduce the input text redundancy.

The hashing function is used in cryptographic methods for processing and protecting information, including for the implementation of electronic digital signature procedures (herein after referred to as EDS<sup>5</sup>) when transferring, processing and storing information in automated systems.

The following are the basic requirements for a hash function:

- the input of the function must be a message of any length;
- at the output of the function, a message of fixed length is obtained;
- the hash function is simply calculated for any message;
- hash function - unidirectional function;
- knowing the message  $M$ , it is almost impossible to find another message  $M'$  for which  $h(M) = h(M')$ .

In the TCPI - CSP hash function, the output sequence and the hash key have fixed lengths of **256 bits**.

---

<sup>5</sup> EDS - electronic digital signature

The composition and purpose of this function, functionality, and functioning algorithm are presented in the document “O`z DSt 1106: 2009. State Standard of Uzbekistan. Information technology. CRYPTOGRAPHIC PROTECTION OF INFORMATION. A hash function”.

## 5. SIGNATURE FUNCTION

The electronic digital signature function is used to generate and confirm the authenticity of an electronic digital signature (EDS) under a given message (electronic document) transmitted over unprotected public telecommunications channels. Upon receipt of the message, the recipient can verify the integrity of the message transmitted by the sender and verify the authenticity of the sender's authorship. EDS is an electronic analog of a written signature and therefore an EDS can be used by the recipient or a third party to verify that the message was actually signed by the sender. To describe the formation and confirmation of the authenticity of a digital signature, two algorithms are used (Algorithm 1, Algorithm 2)<sup>6</sup>. Algorithm 1 is considered in two basic modes:

- without session key<sup>7</sup>;
- with a session key.

Algorithm 2 is used in the classical (without session key) mode. Algorithm 1 provides a backup path for detecting a fake digital signature by introducing a session key procedure used in the process of authenticating the authenticity of a digital signature to the EDS generation process.

The composition and purpose of this function, functionality, and functioning algorithm are presented in the document “O`z DSt 1092: 2009. State Standard of Uzbekistan. Information technology. CRYPTOGRAPHIC PROTECTION OF INFORMATION. Processes of formation and verification of electronic digital signature”.

### Functional restrictions on the use of TCPI – CSP

The cryptographic interface TCPI - CSP is implemented in accordance with the CSP standard, which is applicable only in the Windows operating system and is not applicable in other operating systems such as Linux, Mac, Unix, etc.

Since cryptographic algorithms of the Republic of Uzbekistan are implemented in TCPI - CSP, which are not recognized by standard Windows tools, embedding TCPI in typical Windows applications (MS Outlook, Internet Explorer, VPN, etc.) requires changes to the standard OS software (advapi32.dll, cryptsp.dll, crypt32.dll, inetcomm.dll, schannel.dll, secur32.dll, mailcomm.dll, etc.). Making such changes to Windows can be done in various ways.

## 6. DESCRIPTION OF THE LOGICAL STRUCTURE

### 6.1. The algorithms and methods used

When implementing cryptographic algorithms of the Republic of Uzbekistan, including the implementation of operations with big numbers, the source texts of programs from the

---

<sup>6</sup> Algorithm 1, Algorithm 2 - A description of these algorithms is given in the document “O`z DSt 1092: 2009. State standard of Uzbekistan. Information technology CRYPTOGRAPHIC PROTECTION OF INFORMATION. Processes of formation and verification of electronic digital signature”.

<sup>7</sup> a session key is a single-use symmetric key used for encrypting all messages in one communication session.



OpenSSL<sup>8</sup> the software package was used. When implementing cryptographic algorithms of the Republic of Uzbekistan, all simple numbers that are part of the parameters of the algorithms are checked for simplicity using the standard procedures contained in the OpenSSL package.

## 6.2. Data Encryption Algorithm

Data encryption in TCPI - CSP supports both cryptographic algorithms of the Republic of Uzbekistan [1] and cryptographic standards of the Russian Federation (GOST 28147-89) [6].

### Data encryption

Cryptographic provider TCPI - CSP supports various algorithms for symmetric data encryption (SDE) [10], including the data encryption algorithm of the Republic of Uzbekistan [1]. According to section 6.4 [1], an SDE in TCPI - CSP is implemented in three different ways:

- DEA<sup>9</sup> with key 256-bit;
- DEA with key 512-bit;
- DEA with the function key update.

Here is the implementation of all three of these methods using the TCPI - CSP.

#### 6.2.1. DEA with key 256-bit

To implement a DEA with a key of 256 bits, you need to:

- 1) get the key for the algorithm *CALG\_SYMM*<sup>10</sup>. This key can be obtained in the following ways, in which *AlgId = CALG\_SYMM*:
  - CryptGenKey,
  - CryptDeriveKey,Either through CryptImportKey from *SIMPLEBLOB*<sup>11</sup> or *SYMMETRICWRAPKEYBLOB*<sup>12</sup>, created previously via CryptExportKey;
- 2) call function CryptEncrypt or CryptDecrypt depending on the operation performed.

#### 6.2.2. DEA with key 512-bit

To implement a DEA with a key of 512 bits, you need to:

- 1) get the key of the DEA algorithm with the key 256 (in accordance with paragraph 1 of the DEA with the key of 256 bits);
- 2) perform a function CryptSetKeyParam with parameter *KP\_FUNC\_KEY* (#define KP\_FUNC\_KEY 200). The value *pbData* will be the value of the function key that can be generated, in particular, using the function CryptGenRandom or by other means;
- 3) perform a function CryptEncrypt or CryptDecrypt depending on the operation performed.

---

<sup>8</sup> **OpenSSL** - OpenSSL is a robust, commercial-grade, and full-featured toolkit for the Transport Layer Security (TLS) and Secure Sockets Layer (SSL) protocols. It is also a general-purpose cryptography library.

<sup>9</sup> **DEA** - Data Encryption Algorithm

<sup>10</sup> **CALG\_SYMM** - The description of this parameter is given in the document [1]

<sup>11</sup> **SIMPLEBLOB** - The description of this parameter is given in the document [1]

<sup>12</sup> **SYMMETRICWRAPKEYBLOB** - The description of this parameter is given in the document [1]

### 6.2.3. DEA with the function key update

To implement a DEA with a function key update, you need to:

- 1) get the key of the DEA algorithm with the key 256 (in accordance with paragraph 1 of the DEA with the key of 256 bits);
- 2) if necessary, install a function key (see p. 2 of the DEA with a key of 512 bits);
- 3) perform a function `CryptSetKeyParam` with parameter `KP_OID` (#define `KP_OID` 102). As a value for `pbData` fed to the input value of the function `szOID_SYMM_B`<sup>13</sup>;
- 4) call function `CryptEncrypt` or `CryptDecrypt` depending on the performed operation.

In the encryption function, the lengths of the input and output blocks, as well as the length of the elements of the array *Holat*<sup>14</sup> are equal **256 bit**. The length of the encryption key and the function key are also equal **256 bit**. The number of steps for the encryption feature is set to  **$e = 8$** .

In both the encryption mode and the decryption mode, the algorithm uses a one-time conversion - forming an array of the session key and the next four bytes - oriented and one bit - oriented conversion at each stage. These transformations include:

- forming arrays of step keys;
- mixing data based on the session key array;
- cyclic shifts of rows and columns of the array *Holat* for various values of displacement;
- byte-wise replacement of bytes of the *Holat* array based on linear array arrays;
- addition operation modulo 2 *Holat* arrays and an array of the stage key  $K_e$ ;
- cyclic shifts of a linear array of a session-stage key by the same value of bits at each stage.

When encrypting a cryptographic module is initialized, the encryption key  $k$  and functional key  $k_f$ , number of stages  $e$  and also initialization vector  $IV$  for mode  $m=ShBil$  is first loaded into the cryptographic module. Also, when encrypting a cryptographic module into the *Holat* array, the plaintext is loaded; when decrypted, the ciphertext is loaded. At the beginning of the encryption procedure, *ShaklSeansKalitBayt(k, k<sub>f</sub>)*<sup>15</sup>, *ShaklSeansKalit(K<sub>st</sub>)*<sup>16</sup> and *ShaklBosqichKalit(k<sub>se</sub>)* crypto-transformations are initialized. At the outputs of crypto transformations *ShaklSeansKalitBayt(k, k<sub>f</sub>)*, *ShaklSeansKalit(K<sub>st</sub>)*, byte-level arrays of substitutions and a session key consisting of diamatrix parts are formed at the byte level. These arrays are used in the following sessions as long as  $k$ ,  $k_f$  remain constant. At the output of the crypto-transformation *ShaklBosqichKalit(k<sub>se</sub>)* the initial key and the set of stage keys formed for each stage are formed.

## 7. CRYPTOGRAPHIC TRANSFORMATIONS

*Aralash()* – is a function that is a cryptographic transformation and is performed on diamatrix parts during encryption and decryption.

---

<sup>13</sup> *szOID\_SYMM\_B* - The description of this parameter is given in the document [1]

<sup>14</sup> *Holat* - array containing one block of information

<sup>15</sup> *ShaklSeansKalitBayt(k, k<sub>f</sub>)* - is a function that is used to generate the key for each session and to perform the BaytAlmash() conversion when encrypting and decrypting.

<sup>16</sup> *ShaklSeansKalit(K<sub>st</sub>)* - is a function that is used to generate the key for each session and to perform the Aralash() transformation when encrypting and decrypting.

---

When encrypting, the input data are the diamatrix parts of the *Holat* array, the  $K_1$  and  $K_2$  arrays, the output is the *Holat* array.

The *Aralash* (*Holat*,  $K_s$ ) transformation involves performing the following operations:

- if  $m=sh$ , then:
  - 1) is accepted  $K_1 = K_{1t}, K_2 = K_2$ ;
  - 2) is calculated  $H_1 \otimes_2 K_1 \pmod p, H_2 \otimes_2 K_2 \pmod p$ ;
  - 3) the result is written to arrays  $H_1, H_2$ ;
  - 4) copy the result to an array *Holat*;
- if  $m=dsh$ , then:
  - 5) is accepted  $K_1 = K_1, K_2 = K_{2t}$ ;
  - 6) is calculated  $H_1 \otimes_2 K_1 \pmod p, H_2 \otimes_2 K_2 \pmod p$ ;
  - 7) the result is written to arrays  $H_1, H_2$ ;
  - 8) copy the result to an array *Holat*.

The operation of diamatrix multiplication  $\otimes_2$  is performed on the basis of the following expressions, here the index used in the expressions takes the values  $s \in \{1, 2\}$ .

Expressions for  $i = j \in \{0, 1, 2, 3\}$ :

$$h'_s[0, 0] = h_s[0, 0](k_s[0, 0] + k_s[1, 0] + k_s[2, 0] + k_s[3, 0]) - h_s[1, 1]k_s[1, 0] - h_s[2, 2]k_s[2, 0] - h_s[3, 3]k_s[3, 0] \pmod p,$$

$$h'_s[1, 1] = h_s[1, 1](k_s[0, 1] + k_s[1, 1] + k_s[2, 1] + k_s[3, 1]) - h_s[0, 0]k_s[0, 1] - h_s[2, 2]k_s[2, 1] - h_s[3, 3]k_s[3, 1] \pmod p,$$

$$h'_s[2, 2] = h_s[2, 2](k_s[0, 2] + k_s[1, 2] + k_s[2, 2] + k_s[3, 2]) - h_s[0, 0]k_s[0, 2] - h_s[1, 1]k_s[1, 2] - h_s[3, 3]k_s[3, 2] \pmod p,$$

$$h'_s[3, 3] = h_s[3, 3](k_s[0, 3] + k_s[1, 3] + k_s[2, 3] + k_s[3, 3]) - h_s[0, 0]k_s[0, 3] - h_s[1, 1]k_s[1, 3] - h_s[2, 2]k_s[2, 3] \pmod p,$$

Expressions for  $i \neq j \in \{0, 1, 2, 3\}$ :

$$h'_s[0, 1] = h_s[0, 1](k_s[0, 1] + k_s[1, 1] + k_s[2, 1] + k_s[3, 1]) + (h_s[0, 0] + h_s[1, 0] + h_s[2, 0] + h_s[3, 0])k_s[0, 1] - h_s[0, 2]k_s[2, 1] - h_s[0, 3]k_s[3, 1] \pmod p,$$

$$h'_s[0, 2] = h_s[0, 2](k_s[0, 2] + k_s[1, 2] + k_s[2, 2] + k_s[3, 2]) + (h_s[0, 0] + h_s[1, 0] + h_s[2, 0] + h_s[3, 0])k_s[0, 2] - h_s[0, 1]k_s[1, 2] - h_s[0, 3]k_s[3, 2] \pmod p,$$

$$h'_s[0, 3] = h_s[0, 3](k_s[0, 3] + k_s[1, 3] + k_s[2, 3] + k_s[3, 3]) + (h_s[0, 0] + h_s[1, 0] + h_s[2, 0] + h_s[3, 0])k_s[0, 3] - h_s[0, 1]k_s[1, 3] - h_s[0, 2]k_s[2, 3] \pmod p,$$

$$h'_s[1, 0] = h_s[1, 0](k_s[0, 0] + k_s[1, 0] + k_s[2, 0] + k_s[3, 0]) + (h_s[0, 1] + h_s[1, 1] + h_s[2, 1] + h_s[3, 1])k_s[1, 0] - h_s[1, 2]k_s[2, 0] - h_s[1, 3]k_s[3, 0] \pmod p,$$

$$h'_s[1, 2] = h_s[1, 2](k_s[0, 2] + k_s[1, 2] + k_s[2, 2] + k_s[3, 2]) + (h_s[0, 1] + h_s[1, 1] + h_s[2, 1] + h_s[3, 1])k_s[1, 2] - h_s[1, 0]k_s[0, 2] - h_s[1, 3]k_s[3, 2] \pmod p,$$

$$h'_s[1, 3] = h_s[1, 3](k_s[0, 3] + k_s[1, 3] + k_s[2, 3] + k_s[3, 3]) + (h_s[0, 1] + h_s[1, 1] + h_s[2, 1] + h_s[3, 1])k_s[1, 3] - h_s[1, 0]k_s[0, 3] - h_s[1, 2]k_s[2, 3] \pmod p,$$

$$h'_s[2, 0] = h_s[2, 0](k_s[0, 0] + k_s[1, 0] + k_s[2, 0] + k_s[3, 0]) + (h_s[0, 2] + h_s[1, 2] + h_s[2, 2] + h_s[3, 2])k_s[2, 0] - h_s[2, 1]k_s[1, 0] - h_s[2, 3]k_s[3, 0] \pmod p,$$

$$h'_s[2, 1] = h_s[2, 1](k_s[0, 1] + k_s[1, 1] + k_s[2, 1] + k_s[3, 1]) + (h_s[0, 2] + h_s[1, 2] + h_s[2, 2] + h_s[3, 2])k_s[2, 1] - h_s[2, 0]k_s[0, 1] - h_s[2, 3]k_s[3, 1] \pmod{p},$$

$$h'_s[2, 3] = h_s[2, 3](k_s[0, 3] + k_s[1, 3] + k_s[2, 3] + k_s[3, 3]) + (h_s[0, 2] + h_s[1, 2] + h_s[2, 2] + h_s[3, 2])k_s[2, 3] - h_s[2, 0]k_s[0, 3] - h_s[2, 1]k_s[1, 3] \pmod{p},$$

$$h'_s[3, 0] = h_s[3, 0](k_s[0, 0] + k_s[1, 0] + k_s[2, 0] + k_s[3, 0]) + (h_s[0, 3] + h_s[1, 3] + h_s[2, 3] + h_s[3, 3])k_s[3, 0] - h_s[3, 1]k_s[1, 0] - h_s[3, 2]k_s[2, 0] \pmod{p},$$

$$h'_s[3, 1] = h_s[3, 1](k_s[0, 1] + k_s[1, 1] + k_s[2, 1] + k_s[3, 1]) + (h_s[0, 3] + h_s[1, 3] + h_s[2, 3] + h_s[3, 3])k_s[3, 1] - h_s[3, 0]k_s[0, 1] - h_s[3, 2]k_s[2, 1] \pmod{p},$$

$$h'_s[3, 2] = h_s[3, 2](k_s[0, 2] + k_s[1, 2] + k_s[2, 2] + k_s[3, 2]) + (h_s[0, 3] + h_s[1, 3] + h_s[2, 3] + h_s[3, 3])k_s[3, 2] - h_s[3, 0]k_s[0, 2] - h_s[3, 1]k_s[1, 2] \pmod{p},$$

This transformation is more efficient compared to the matrix transformation. Here, when changing one element in the *Holat* source array, depending on the address of the changed element, 6 or 7 elements change.

**BaytAlmash()** – a function that is a cryptographic transformation and is used to replace elements of the *Holat* array with elements of the replacement array at the byte level.

The input data of this crypto-transform is *Holat* array, linear array of  $B_{sA}[256]$  or  $B_{sAD}[256]$  replacements at the byte level, output data is *Holat* array at the byte level.

**BaytAlmash(Holat,  $B_a$ )** conversion involves performing the following operations:

- 1) renaming the *Holat*[8,4] array, specified at the byte level, as *Holatb*[8, 4] at the byte level;
- 2) if  $m=sh$ , then accepted  $B_a[256] = B_{sA}[256]$ ; each element of the *Holatb*[8, 4] is replaced with an element of the  $B_a$  array located at an address equal to the value of the *Holatb*[8,4] array element; the resulting *Holatb*[8, 4] array is assigned to the *Holat*[8, 4] array specified by the byte level;
- 3) if  $m=dsh$ , then accepted  $B_a[256] = B_{sAD}[256]$ ; replaces each element of the array *Holatb*[8,4] element of the array  $B_a$  located at the address equal to the value of the element of the array *Holatb*[8, 4]; the resulting *Holatb* [8,4] array is assigned to the *Holat* [8,4] array specified by the byte level, here  $s \in \{1, 2\}$ .

**Sur()** – a function that is used when encrypting and decrypting to thoroughly mix the elements of the *Holat* array.

The input data of this transformation is the *Holat* array, while the output data is encrypted: *Holat* array with columns cyclically shifted downwards and rows cyclically shifted to the right; when decrypted, the output is a *Holat* array with columns cyclically shifted upwards and rows cyclically shifted to the left.

The **Sur (Holat)** conversion is to perform the following operations:

- if  $m = sh$ , then first cyclically shift the  $j$ -column of the *Holat* array to  $(j + 1) \pmod{8}$  bytes down, then shift the  $i$ -string of the resulting array to  $(i + 1) \pmod{4}$  bytes right;
- if  $m=dsh$ , then first cycle the  $i$  - string of the *Holat* array by  $(i + 1) \pmod{4}$  bytes left, then shift the  $j$ -column of the resulting array by  $(j + 1) \pmod{8}$  bytes up. Here,  $0 \leq i \leq 4, 0 \leq j \leq 8$ .  $\rightarrow \downarrow \leftarrow$

## 8. KEY GENERATION

*ShaklSeansKalitBayt()* – a function that is used to generate a key for each session and to perform the *BaytAlmash()* transformation when encrypting and decrypting. In this transformation, the input data is the encryption key  $\mathbf{k}$  and the function key  $\mathbf{k}_f$ , the output is arrays  $\mathbf{B}_{sA}[256]$  or  $\mathbf{B}_{sAD}[256]$  byte level. The *ShaklSeansKalitBayt(k, k<sub>f</sub>)* transformation is to perform the following operations:

- 1) Calculation  $\mathbf{k}_{se} = \mathbf{k} + \mathbf{k}' * (\mathbf{1} + \mathbf{k}_f * \mathbf{k})$  and the remaining **672 bits** on the left, here  $\mathbf{k}$  – is **192 bits**  $\mathbf{k}_f$  on the right.

**Note.** When generating an encryption key, a set of functional keys that are updated using an encryption key, and forming a  $\mathbf{k}_{se}$  key based on them, they must be checked based on randomness criteria and **672 bits** are allocated from the left side of the resultant  $\mathbf{k}_{se}$ ;

- 2) selection from the right side of  $\mathbf{k}_{se}$  **256+64 bits**, from the left 256-bit part of the formation of a linear array of  $\mathbf{K}_{st} = [\mathbf{0}, \mathbf{1}, \mathbf{2}, \mathbf{3}, \dots, \mathbf{31}]$ , consisting of byte elements, from the remaining 64-bit part, the formation of a linear array  $\mathbf{B} = [\mathbf{0}, \mathbf{1}, \mathbf{2}, \mathbf{3}, \mathbf{4}, \mathbf{5}, \mathbf{6}, \mathbf{7}]$ , consisting of elements at the byte level;
- 3) formation of a pair of arrays  $\mathbf{B}$  from the elements of the linear array  $\mathbf{B}_1 = [\mathbf{0}, \mathbf{1}, \mathbf{2}, \mathbf{3}]$  and  $\mathbf{B}_2 = [\mathbf{4}, \mathbf{5}, \mathbf{6}, \mathbf{7}]$  and the formation of the three parameters  $(\mathbf{d}_1, \mathbf{R}_1, \mathbf{L}_1)$  and  $(\mathbf{d}_2, \mathbf{R}_2, \mathbf{L}_2)$  based on the following rules:
  - for  $\mathbf{j} = \mathbf{0}$ , if  $\mathbf{b}[\mathbf{j}] < \mathbf{3}$ , is accepted  $\mathbf{d}_1 = \mathbf{3}$ , otherwise –  $\mathbf{d}_1 = \mathbf{b}[\mathbf{0}]$ ;
  - for  $\mathbf{j} = \mathbf{4}$ , if  $\mathbf{b}[\mathbf{j}] < \mathbf{3}$ , is accepted  $\mathbf{d}_2 = \mathbf{3}$ , otherwise –  $\mathbf{d}_2 = \mathbf{b}[\mathbf{4}]$ ;
  - for  $\mathbf{j} = \mathbf{1}$ , if  $\mathbf{b}[\mathbf{j}] = \mathbf{0}$ , is accepted  $\mathbf{R}_1 = \mathbf{1}$ , otherwise –  $\mathbf{R}_1 = \mathbf{b}[\mathbf{1}]$ ;
  - for  $\mathbf{j} = \mathbf{5}$ , if  $\mathbf{b}[\mathbf{j}] = \mathbf{0}$ , is accepted  $\mathbf{R}_2 = \mathbf{1}$ , otherwise –  $\mathbf{R}_2 = \mathbf{b}[\mathbf{5}]$ ;
  - for  $\mathbf{j} = \mathbf{2}$ , if  $\mathbf{b}[\mathbf{j}] = \mathbf{0}$ , is accepted  $\mathbf{L}_1 = \mathbf{1}$ , otherwise –  $\mathbf{L}_2 = \mathbf{b}[\mathbf{2}]$ ;
  - for  $\mathbf{j} = \mathbf{6}$ , if  $\mathbf{b}[\mathbf{j}] = \mathbf{0}$ , is accepted  $\mathbf{L}_2 = \mathbf{1}$ , otherwise –  $\mathbf{L}_2 = \mathbf{b}[\mathbf{6}]$ ;
  - for  $\mathbf{d}_s(\bmod \mathbf{2}) = \mathbf{0}$ , if  $\mathbf{d}_s(\bmod \mathbf{4}) = \mathbf{0}$ , is accepted  $\mathbf{d}_s = \mathbf{d}_s - \mathbf{1}$ , otherwise –  $\mathbf{d}_s = \mathbf{d}_s + \mathbf{1}$ , here  $\mathbf{s} \in \{\mathbf{1}, \mathbf{2}\}$ ;
  - for  $\mathbf{d}_s(\bmod \mathbf{2}) = \mathbf{1}$ , if  $\mathbf{d}_s - \mathbf{1}(\bmod \mathbf{4}) = \mathbf{0}$ , then is accepted  $\mathbf{d}_s = \mathbf{d}_s - \mathbf{2}$ ;
  - for  $\mathbf{j} = \mathbf{3}$ , if  $\mathbf{b}[\mathbf{j}] = \mathbf{0}$ , is accepted  $\mathbf{b}[\mathbf{j}] = \mathbf{1}$ ;
  - for  $\mathbf{j} = \mathbf{7}$ , if  $\mathbf{b}[\mathbf{j}] = \mathbf{0}$ , is accepted  $\mathbf{b}[\mathbf{j}] = \mathbf{1}$ ;
- 4) formation of a pair of arrays  $(\mathbf{B}_{1A}[256], \mathbf{B}_{2A}[256])$  to perform transformations at the byte level and get the encrypted text;
- 5) raising to the power  $\mathbf{d}_s$  with the parameter  $\mathbf{R}_s$  modulo **257** value  $((\mathbf{i} + \mathbf{L}_z) \bmod \mathbf{256}) + \mathbf{1}$ , corresponding to each address  $\mathbf{i} \in \{\mathbf{0}, \mathbf{1}, \mathbf{2}, \dots, \mathbf{255}\}$ , the result is given modulo **256** and in each step the current value compared with the value of the previous step and  $\mathbf{i}$ . If the values are equal or if the current value is close  $(|\mathbf{b}_{sA}[\mathbf{i} - \mathbf{1}] - \mathbf{b}_{sA}[\mathbf{i}]| \geq \mathbf{8})$  to the previous value, then the current value is replaced with  $(\mathbf{i} - \mathbf{b}[\mathbf{3}])$  with  $\mathbf{s} = \mathbf{1}$  and on  $(\mathbf{i} - \mathbf{b}[\mathbf{7}])$  with  $\mathbf{s} = \mathbf{2}$ . Here,  $\mathbf{s} \in \{\mathbf{1}, \mathbf{2}\}$ .

**Note.** In the pseudo-code, in the odd-numbered stages, the  $\mathbf{B}_{1A}[256]$  is used, and in the even-numbered stages, the  $\mathbf{B}_{2A}[256]$  is used.

The algorithm of calculations includes the following operations:

- 1) calculation  $\mathbf{bsA}[\mathbf{i}] \equiv (((\mathbf{i} + \mathbf{L}) \bmod \mathbf{256}) + \mathbf{1}) \bmod \mathbf{256} \bmod \mathbf{257} \bmod \mathbf{256}$

for  $i = 0 \dots 255$ ;

- 2) condition check  $i - \mathbf{bsA}[i] \neq 0$  and  $|\mathbf{bsA}[i - 1] - \mathbf{bsA}[i]| \geq 8$ , at every step since  $i = 1$ . If both conditions are met, then the value is accepted. Otherwise, when  $s = 1$ , swap  $\mathbf{bsA}[i]$  and the element located at  $(i - \mathbf{b}[3]) \pmod{256}$ , or when  $s = 2$  the position  $\mathbf{bsA}[i]$  and the element located at  $(i - \mathbf{b}[7]) \pmod{256}$ . Then accepted  $(\mathbf{b}[3] = \mathbf{b}[3] - 5 \pmod{256})$  for  $s = 1$  or  $\mathbf{b}[7] = \mathbf{b}[7] - 5 \pmod{256}$  for  $s = 2$ ;
- 3) formation of a pair of linear arrays  $(\mathbf{B}_{1A}[256], \mathbf{B}_{2A}[256])$  of the elements  $\mathbf{b}_{sA}[i, i = 0, 1, 2, \dots, 255]$ . It is necessary to get the cipher text at the byte level, i.e. for use in *sh* mode;
- 4) formation of a pair of linear arrays  $(\mathbf{B}_{1AD}[256], \mathbf{B}_{2AD}[256])$  for decryption at the byte level, i.e. for use in *dsh* mode;
- 5) replacing each element  $\mathbf{b}_{sA}[i]$  with a value in the linear array  $\mathbf{B}_{sA}[256]$  with an index equal to its value and positioning the elements of the formed array in increasing order of the address. It is necessary to get the cipher text (*dsh*) at the byte level. Here,  $s \in \{1, 2\}$ .

*Note.* In the pseudo-code in the odd-numbered stages, the  $\mathbf{B}_{2AD}[256]$  array is used, in the even-numbered stages, the  $\mathbf{B}_{1AD}[256]$  array is used;

*ShaklSeansKalit()* – is a function that is used to generate a key for each session and to perform the *Aralash()* conversion when encrypting and decrypting. The input to this transformation is the  $\mathbf{K}_{st} = [32]$  array at the byte level; the output is a pair of arrays  $(\mathbf{K}_{1t}, \mathbf{K}_{2t})$  or  $(\mathbf{K}_1, \mathbf{K}_{2t})$ , consisting of diamatrix of a special structure.

The *ShaklSeansKalit* ( $\mathbf{K}_{st}$ ) transformation is to perform the following operations:

- 1) the formation of a linear array  $\mathbf{K}_{ss} = [0, 1, 2, \dots, 19]$ , consisting of 20 byte elements from the left of the linear array  $\mathbf{K}_{st} = [0, 1, 2, \dots, 31]$ , consisting of byte elements;
  - if  $\mathbf{k}_{ss}[i] = 0$  for  $i = 0 \dots 9$ , to replace  $\mathbf{k}_{ss}[i]$  on  $\mathbf{k}_{ss}[i] - 1 \pmod{p}$ ;
  - if  $\mathbf{k}_{ss}[6] \pmod{2} = 0$ , to replace  $\mathbf{k}_{ss}[6]$  on  $\mathbf{k}_{ss}[6] - 1 \pmod{p}$ ;
  - if  $\mathbf{k}_{ss}[16] \pmod{2} = 0$ , to replace  $\mathbf{k}_{ss}[16]$  on  $\mathbf{k}_{ss}[16] - 1 \pmod{p}$ ;
  - if  $\mathbf{k}_{ss}[6] + \mathbf{k}_{ss}[0] + \mathbf{k}_{ss}[8] + \mathbf{k}_{ss}[3] + \mathbf{k}_{ss}[5] \pmod{2} = 0$ , to replace  $\mathbf{k}_{ss}[8]$  on  $\mathbf{k}_{ss}[8] - 1 \pmod{p}$ ;
  - if  $\mathbf{k}_{ss}[16] + \mathbf{k}_{ss}[10] + \mathbf{k}_{ss}[18] + \mathbf{k}_{ss}[13] + \mathbf{k}_{ss}[15] \pmod{2} = 0$ , to replace  $\mathbf{k}_{ss}[18]$  on  $\mathbf{k}_{ss}[18] - 1 \pmod{p}$ ;
  - if  $\mathbf{k}_{ss}[6] + \mathbf{k}_{ss}[1] + \mathbf{k}_{ss}[3] + \mathbf{k}_{ss}[9] + \mathbf{k}_{ss}[4] \pmod{2} = 0$ , to replace  $\mathbf{k}_{ss}[9]$  on  $\mathbf{k}_{ss}[9] - 1 \pmod{p}$ ;
  - if  $\mathbf{k}_{ss}[16] + \mathbf{k}_{ss}[11] + \mathbf{k}_{ss}[13] + \mathbf{k}_{ss}[19] + \mathbf{k}_{ss}[14] \pmod{2} = 0$ , to replace  $\mathbf{k}_{ss}[19]$  on  $\mathbf{k}_{ss}[19] - 1 \pmod{p}$ ;
  - if  $\mathbf{k}_{ss}[6] + \mathbf{k}_{ss}[2] + \mathbf{k}_{ss}[3] + \mathbf{k}_{ss}[4] + \mathbf{k}_{ss}[7] \pmod{2} = 0$ , to replace  $\mathbf{k}_{ss}[7]$  on  $\mathbf{k}_{ss}[7] - 1 \pmod{p}$ ;
  - if  $\mathbf{k}_{ss}[16] + \mathbf{k}_{ss}[12] + \mathbf{k}_{ss}[13] + \mathbf{k}_{ss}[14] + \mathbf{k}_{ss}[17] \pmod{2} = 0$ , to replace  $\mathbf{k}_{ss}[17]$  on  $\mathbf{k}_{ss}[17] - 1 \pmod{p}$ .
- 2) formation of two-dimensional arrays  $\mathbf{K}_1[4, 4]$  and  $\mathbf{K}_2[4, 4]$  from the elements of the linear array  $\mathbf{K}_{ss}$  in the following order:

division of the linear array  $K_{ss} = [0, 1, 2, \dots, 19]$  into two linear arrays  $K_{ss1} = [0, 1, 2, \dots, 9]$  and  $K_{ss2} = [10, 11, 12, \dots, 19]$ . Each of them is uniquely displayed in an ordered set  $\{k_{s1}[0, 1], k_{s1}[0, 2], k_{s1}[0, 3], k_{s1}[1, 0], k_{s1}[2, 0], k_{s1}[2, 1], k_{s1}[2, 2], k_{s1}[3, 0], k_{s1}[3, 1], k_{s1}[3, 2]\}$  and

$\{k_{s2}[0, 1], k_{s2}[0, 2], k_{s2}[0, 3], k_{s2}[1, 0], k_{s2}[2, 0], k_{s2}[2, 1], k_{s2}[2, 2], k_{s2}[3, 0], k_{s2}[3, 1], k_{s2}[3, 2]\}$ .

The formation of the elements  $k_1[i, j], k_2[i, j]$  of arrays  $K_1[4, 4]$  and  $K_2[4, 4]$ ;

the formation of the remaining elements of the array  $K_s[4, 4]$ ,  $s \in \{1, 2\}$  based on the following rule:

- for  $j \in \{0, 1, 2, 3\}$ , if  $i = j$ , then the corresponding elements are equal in value  $k_s[2, 2]$ ;
  - for  $i = 1, j = 0, 2, 3$  corresponding elements are equal in value  $k_s[1, 0]$ ;
  - for  $i = 2, j = 0, 3$  corresponding elements are equal in value  $k_s[2, 0]$ ;
- 3) as a result, for use in encryption mode as  $K_s[8, 4]$  a pair of diamatrix of a special structure is formed  $K_1[4, 4]$  and  $K_2[4, 4]$ ;

Array  $K_1$

$k_{ss}[6]$	$k_{ss}[0]$	$k_{ss}[1]$	$k_{ss}[2]$
$k_{ss}[3]$	$k_{ss}[6]$	$k_{ss}[3]$	$k_{ss}[3]$
$k_{ss}[4]$	$k_{ss}[5]$	$k_{ss}[6]$	$k_{ss}[4]$
$k_{ss}[7]$	$k_{ss}[8]$	$k_{ss}[9]$	$k_{ss}[6]$

$k_1[0, 0]$	$k_1[0, 1]$	$k_1[0, 2]$	$k_1[0, 3]$
$k_1[1, 0]$	$k_1[1, 1]$	$k_1[1, 2]$	$k_1[1, 3]$
$k_1[2, 0]$	$k_1[2, 1]$	$k_1[2, 2]$	$k_1[2, 3]$
$k_1[3, 0]$	$k_1[3, 1]$	$k_1[3, 2]$	$k_1[3, 3]$

Array  $K_2$

$k_{ss}[16]$	$k_{ss}[10]$	$k_{ss}[11]$	$k_{ss}[12]$
$k_{ss}[13]$	$k_{ss}[16]$	$k_{ss}[13]$	$k_{ss}[13]$
$k_{ss}[14]$	$k_{ss}[15]$	$k_{ss}[16]$	$k_{ss}[14]$
$k_{ss}[17]$	$k_{ss}[18]$	$k_{ss}[19]$	$k_{ss}[16]$

$k_2[0, 0]$	$k_2[0, 1]$	$k_2[0, 2]$	$k_2[0, 3]$
-------------	-------------	-------------	-------------

$$\begin{array}{cccc} k_2[1, 0] & k_2[1, 1] & k_2[1, 2] & k_2[1, 3] \\ k_2[2, 0] & k_2[2, 1] & k_2[2, 2] & k_2[2, 3] \\ k_2[3, 0] & k_2[3, 1] & k_2[3, 2] & k_2[3, 3] \end{array}$$

- 4) calculation of the inverse matrix of a special structure  $K_{1t}[4, 4]$  for the matrix of the special structure  $K_1[4, 4]$  for use in *sh* mode;
- 5) calculation of the inverse matrix of the special structure  $K_{2t}[4, 4]$  for the matrix of the special structure  $K_2[4, 4]$  for use in *dsh* mode;
- 6) obtaining an inverse matrix for the diamatrix of a special structure  $K_{1i}[4, 4]$  (here  $i = \{1, 2\}$ ), in which the diadeterminant is not zero, consists in calculating the inverse matrix for the matrix obtained as a result of performing a diagonal transformation over it and the result of performing a transform over the obtained inverse matrix;
- 7) as a result of the inversion of the diamatrices of the special structure  $K_1[4, 4]$  and  $K_2[4, 4]$  the diamatrices of the special structure  $K_{1t}[4, 4]$  and  $K_{2t}[4, 4]$ , are formed, having the following form ( $K_{1t}$  and  $K_{2t}$ ).

Array  $K_{1t}$

$$\begin{array}{cccc} k_{1t}[0, 0] & k_{1t}[0, 1] & k_{1t}[0, 2] & k_{1t}[0, 3] \\ k_{1t}[1, 0] & k_{1t}[1, 1] & k_{1t}[1, 2] & k_{1t}[1, 3] \\ k_{1t}[2, 0] & k_{1t}[2, 1] & k_{1t}[2, 2] & k_{1t}[2, 3] \\ k_{1t}[3, 0] & k_{1t}[3, 1] & k_{1t}[3, 2] & k_{1t}[3, 3] \end{array}$$

Array  $K_{2t}$

$$\begin{array}{cccc} k_{2t}[0, 0] & k_{2t}[0, 1] & k_{2t}[0, 2] & k_{2t}[0, 3] \\ k_{2t}[1, 0] & k_{2t}[1, 1] & k_{2t}[1, 2] & k_{2t}[1, 3] \\ k_{2t}[2, 0] & k_{2t}[2, 1] & k_{2t}[2, 2] & k_{2t}[2, 3] \\ k_{2t}[3, 0] & k_{2t}[3, 1] & k_{2t}[3, 2] & k_{2t}[3, 3] \end{array}$$

In *sh* mode, a pair consisting of  $(K_{1t}, K_{2t})$ , is fed to the input; in *dsh* mode, a pair consisting of  $(K_1, K_{2t})$  is fed to the input.

*ShaklBosqichKalit()* – is a function that is used to form a stage key from a session-stage key and to perform the *Qo'shBosqichKalit()* transformation when encrypting and decrypting.

The input data of this transformation is the linear array of the session-stage key  $k_{se}$ , the output data is the two-dimensional array specified by the byte level  $K_e[8, 4]$ ;



The *ShaklBosqichKalit* ( $k_{se}$ ) transformation (generation of a linear session-stage key) occurs as follows:

- 1) if  $bosqich=1$  and  $m=sh$ , then the  $k_{se}$  array of the linear session-stage key is left unchanged, if  $bosqich=1$  and  $m=dsh$ , then the  $k_{se}$  array is shifted by  $672-(e \times 83) \bmod 672$  bits to the right;
- 2) the left **256 bit** part of the linear session-stage key array is separated and the  $K_e[8, 4]$  array is formed from it at the byte level. This conversion is performed for all stages prior to the start of the encryption procedure;
- 3) if  $bosqich > 1$  and  $m=sh$ , then the  $k_{se}$  array cyclically shifts **83 bits** to the left, if  $bosqich > 1$  and  $m=dsh$ , then the  $k_{se}$  array cyclically shifts **83 bits** to the right;
- 4) the left **256 bit** part of the linear session-stage key array is separated and an array is formed from it at the byte level  $K_e[8, 4]$ . This conversion is performed for all stages prior to the start of the decryption procedure.

## 9. SIMPLE CRYPTO-TRANSFORMATION

*Qo'shBosqichKalit()* – is a function that is simple crypto-transform and consists of performing an exclusive “or” (bitwise addition modulo 2) when encrypting and decrypting *Holat* arrays and an array of the step-key  $K_e$ . The input data of this transformation are the *Holat* and  $K_e$  arrays at the byte level, the output data is the *Holat* array at the byte level. The *Qo'shBosqichKalit (Holat, K<sub>e</sub>)* transformation consists of performing an exclusive “or” operation (bitwise modulo-2 addition) on elements of the same name at the byte level of *Holat* and  $K_e[8, 4]$  arrays.

For  $0 \leq c < 8$ :

$$[h'[c, 0], h'[c, 1], h'[c, 2], h'[c, 3]] = [h[c, 0], h[c, 1], h[c, 2], h[c, 3]] \oplus [k_e[c, 0], k_e[c, 1], k_e[c, 2], k_e[c, 3]].$$

The result must be copied to the *Holat* array.

*Qo'shHolat()* – is a function that is a simple crypto-transform and is performed on blocks of encrypted blocks using the *XOR* operation when encrypting and decrypting in all modes except the electronic codebook mode.

In the *Qo'shHolat(Holatn, Holat)* transformation, each byte of the *Holatn* array is added bitwise using the *XOR* addition operation (modulo 2 addition operation) the same byte of the *Holat* array. *Holatn* array consists of eight words. When these words are in the range of  $0 \leq s < 8$ , the elements of the *Holat* array that are in the columns are added separately as follows:

$$[h'[s, 0], h'[s, 1], h'[s, 2], h'[s, 3]] = [h[s, 0], h[s, 1], h[s, 2], h[s, 3]] \oplus [hn[s, 0], hn[s, 1], hn[s, 2], hn[s, 3]],$$

here: *hn* - array elements *Holatn*, *h'* – elements of the resulting array.

The result of the conversion is copied to the *Holat* array.

### 9.1. Encryption of symmetric keys using symmetric keys

To encrypt symmetric keys using symmetric keys, a DEA is used in ECM mode. To produce imitation protection, a hash function from cryptographic standards of Uzbekistan in

256 bit mode is used. The first 4 bytes of the key's hash function is the simulated prefix for the encrypted key.

## 9.2. Encryption of symmetric keys using asymmetric keys

When encrypting symmetric keys using asymmetric keys, the following algorithm is used. Using the Diffie-Hellman method, a common key of the form  $a^{xy}$  is formed, where  $x$ ,  $y$  are private keys, the common key size is 256 and 64 bytes for algorithms 1 and 2, respectively. This shared key is used instead of a password to generate a shared symmetric key and initialization vector in accordance with PKCS #5. The original symmetric key is encrypted in BCM mode using a common symmetric key and an initialization vector. The size of the encrypted key is 64 bytes. Imitation protection provides padding size of 32 bytes.

## 9.3. An algorithm of generation and verification of EDS

Processes of formation and verification of electronic digital signatures in TCPI - CSP supports both cryptographic algorithms of the Republic of Uzbekistan [3] and the cryptographic standard of the Russian Federation (GOST R 34.10-2001) [8]. The function of EDS (formation and verification) is designed to ensure the reliability of the transmitted and received information and confirm its authorship.

## 9.4. Development and verification of EDS

The following parameters are used for the signature function:

- $(x, u)$  – pair of integers - private key of EDS;
- $(y, z)$  – pair of integers – public key EDS;
- $(r, s)$  – pair of integers – electronic digital signature under the message  $M$ ;
- $(R_1, y_1)$  – pair of integers – fake detection key EDS, which is a pair of control and session public key;
- $(R, g, k_h)$  – special private key of the authorized subject.

The generally accepted digital signature model spans three processes:

- generation of EDS keys;
- formation of EDS;
- verification (authentication) EDS.

### 9.4.1. Algorithm 1

Algorithm 1 uses the following parameters:

- $p$  – is a module, a prime number. The upper limit of this number should be determined by the specific implementation of the electronic digital signature algorithm, depending on the type of cryptographic module;
- $p > 2^{1023}$  for software, hybrid and hardware types and  $p > 2^{255}$  for special hardware type;
- $q$ - is a prime number, which is a factor (simple factor)  $p - 1$ , where  $2^{25} < q < 2^{256}$ ;
- $R$  – is the parameter - a positive integer satisfying the condition  $R < q$ ;  $R$  can be an open, shared private key for a limited group of users or a component of a special private key of an authorized entity;
- $m = H(M)$  – is a hash function that displays the message  $M$  in a string of length 256 bits; In software, hybrid and hardware types of a cryptographic module, a hash function without a key is used, and in a special hardware type, a key hash function.

To implement EDS processes (i.e., EDS key generation, EDS generation, and EDS authentication), each user must have a private EDS key  $(x, u)$ , where:  $x, u$  are private keys, randomly or pseudo-randomly generated integers satisfying the condition  $1 < x, u < q$ ; the  $g$  parameter is a private or public parameter representing an integer that is calculated:  $g \equiv h^{(p-1)/q} \pmod{p}$ , the public key of the digital signature  $(y, z)$ . Where:  $(y, z)$  are public keys calculated by the formula  $y \equiv g^x \pmod{p}$  and  $z \equiv g^u \pmod{p}$ ; if the open parameter (base)  $g$  is used, then  $u = 1$  and  $z = g$ ; and the EDS fake detection key  $(R_1, y_1)$ , where:  $R_1$  is the control key (open or closed), selected from the range  $1..q - 1$ ; if  $R_1$  is closed, then  $R_1$  must be a joint secret key for the signer and the verifier;

- $y_1$  – is a session (public) key calculated for each electronic digital signature as a result of exponentiation with the parameter.

### Formation of electronic digital signature and session key

To create a digital signature and session key under the message  $M$  for **Algorithm 1**, the following actions are performed:

- 1) the hash function of the message is calculated:  $m = H(M)$ . Moreover,  $c = x$ ;
- 2)  $k = H(m + (1 + mR)c)$  is calculated. If  $k = 0$ , then  $c = c + 2$  is assumed and it is necessary to return to step 2;
- 3) calculate  $T \equiv g^{-k} \pmod{p}$  with the parameter  $R$ ;
- 4) calculate  $r \equiv m + (1 + mR)T \pmod{p}$ . If  $r \pmod{q} = 0$ , then  $k \equiv k + 1 \pmod{p}$  is assumed and it is necessary to return to step 3.
- 5)  $s_1 \equiv k - rx \pmod{q}$  is calculated. If  $s_1 = 0$ , then  $k \equiv k + 1 \pmod{p}$  is assumed and it is necessary to return to step 3;
- 6) compute  $s \equiv s_1 u^{-1} \pmod{q}$ . If  $\mu = 0$ , then  $r, s$  is output and calculations stop;
- 7) calculate  $r_1 \equiv R_1 + (1 + RR_1)r \pmod{q}$ . If  $r_1 = 0$ , then  $k \equiv k + 1 \pmod{p}$  is assumed and it is necessary to return to step 3;
- 8)  $x_1 \equiv (k - suR_1)r_1^{-1} \pmod{q}$  is calculated. If  $x_1 = 0$ , then  $k \equiv k + 1 \pmod{p}$  is assumed and it is necessary to return to step 3;
- 9)  $y_1 \equiv (gR_1^{-1})^{x_1} \pmod{p}$  with the parameter  $RR_1$  is calculated and output  $r, s, y_1$ .

Further, the signed message (message and addition) is transmitted to the receiving side.

Also, the session key is transmitted to the receiving side if the session key mode is used.

### Digital Signature Authentication

To confirm the authenticity of EDS under the received message,  $M$ , the following actions are performed:

- 1) hash function  $m = H(M)$  is calculated;
- 2) if  $L(s) \leq L(q)$  AND  $L(r) \leq L(p)$  then go to the next step, otherwise the “signature is not authentic” is accepted;
- 3)  $z_0 \equiv z^s \pmod{p}$  is calculated with the parameter  $R$ ;
- 4)  $r' \equiv r \pmod{q}$  is calculated;
- 5)  $y_2 \equiv y^{r'} \pmod{p}$  is calculated with the parameter  $R$ ;
- 6)  $z_1 \equiv z_0 + (1 + z_0R)y_2 \pmod{p}$  is calculated;
- 7)  $y_3 \equiv z_1 + (1 + z_1R)r \pmod{p}$  is calculated;

- 8) if  $\mu = \mathbf{0}$  and  $\mathbf{m} = \mathbf{y}_3$ , then the output is “signature authentic”;  
 if  $\mu = \mathbf{1}$  and  $\mathbf{m} = \mathbf{y}_3$ , then go to the next step;  
 if  $\mathbf{m} \neq \mathbf{y}_3$ , then the “signature is not authentic” is accepted;
- 9)  $\mathbf{g}_3 \equiv \mathbf{z}_1 \mathbf{R}_1^{-1}(\bmod p)$  is calculated;
- 10)  $\mathbf{s}_1 \equiv \mathbf{s} \mathbf{R}_1(\bmod q)$  is calculated;
- 11)  $\mathbf{r}_1 \equiv \mathbf{R}_1 + (\mathbf{1} + \mathbf{R} \mathbf{R}_1) \mathbf{r}'(\bmod q)$  is calculated;
- 12)  $\mathbf{z}_2 \equiv \mathbf{z} \mathbf{R}_1^{-1}(\bmod p)$  is calculated;
- 13)  $\mathbf{y}_4 \equiv \mathbf{y}_1$ ;
- 14)  $\mathbf{z}_3 \equiv \mathbf{z}_2^{s_1}(\bmod p)$  is calculated with the parameter  $\mathbf{R} \mathbf{R}_1$ ;
- 15)  $\mathbf{y}_5 \equiv \mathbf{y}_4^{r_1}(\bmod p)$  is calculated with the parameter  $\mathbf{R} \mathbf{R}_1$ ;
- 16)  $\mathbf{g}_4 \equiv \mathbf{z}_3 + (\mathbf{1} + \mathbf{z}_3 \mathbf{R} \mathbf{R}_1) \mathbf{y}_5(\bmod p)$  is calculated;
- 17) if  $\mathbf{g}_3 \equiv \mathbf{g}_4$ , then “signature is authentic” is accepted, otherwise “signature is not authentic” is accepted.

Algorithm 1 uses a **one-way function** in a group with a parameter, calculations for which are carried out easily at the same level of labor intensity as in the exponentiation operations, and inverting (inversion) of a function requires no less computational time and effort than in solving a discrete problem logarithm. The main operations of multiplication, exponentiation, and treatment in a group with a parameter are called multiplication, exponentiation, and treatment of the parameter. The one-sided exponentiation function is a special case of this one-way function.

#### 9.4.2. Algorithm 2

For Algorithm 2, the following parameters are used:

- elliptic curve  $\mathbf{E}$ , given by its invariant  $\mathbf{J}(\mathbf{E})$  or by coefficients  $\mathbf{a}, \mathbf{b} \in \mathbf{F}_p$ ;
- integer  $\mathbf{w}$  is the order of a group of points of an elliptic curve  $\mathbf{E}$ ;
- prime  $\mathbf{t}$  is the order of a cyclic subgroup of a group of points of an elliptic curve  $\mathbf{E}$  for which the following conditions are satisfied:

$$\begin{cases} \mathbf{w} = \mathbf{lt}, \mathbf{l} \in \mathbf{Z}, \mathbf{l} \geq \mathbf{1} \\ 2^{254} < \mathbf{t} < 2^{256} \end{cases}$$

- point  $\mathbf{N} \neq \mathbf{0}$  of an elliptic curve  $\mathbf{E}$ , with coordinates  $(\mathbf{x}_p, \mathbf{y}_p)$ , satisfying the equality  $[\mathbf{t}]\mathbf{N} = \mathbf{0}$ ;
- hash function  $\mathbf{m} = \mathbf{H}(\mathbf{M})$ , displaying the message  $\mathbf{M}$ , in a string of length **256 bits**.

For the listed parameters of EDS the following requirements are met:

- 1)  $\mathbf{p}^i \neq \mathbf{1}(\bmod \mathbf{t})$  for all integers  $\mathbf{i} = \mathbf{1}, \mathbf{2}, \dots, \mathbf{B}$ , where  $\mathbf{B}$  satisfies the inequality  $\mathbf{B} \geq \mathbf{31}$ ;
- 2)  $\mathbf{w} \neq \mathbf{p}$ ;
- 3) the invariant of the curve satisfies the condition  $\mathbf{J}(\mathbf{E}) \neq \mathbf{0}$  or **1728**.

To implement EDS processes (i.e., EDS key generation, EDS generation and EDS authentication), each user must have an EDS private key, an integer  $\mathbf{d}$ , satisfying  $\mathbf{0} < \mathbf{d} < \mathbf{t}$

and the public EDS key is a point of an elliptic curve  $T$  with coordinates  $(x_t, y_t)$ , satisfying the equality  $[d]N = T T(x_t, y_t)$ .

### Formation of electronic digital signature

To obtain a digital signature under the message,  $M$ , the following actions are performed:

- 1) calculate the hash function of message:  $m = H(M)$ ;
- 2) calculate  $e \equiv m(\bmod t)$ . If  $e = 0$ , then define  $e = 1$ ;
- 3) a random (pseudo-random) integer  $k$  is generated, satisfying the inequality  $0 < k < t$ ;
- 4) the point of the elliptic curve  $C = [k]N$  is calculated and  $r = x_c(\bmod t)$ , is determined, where  $x_c$  is the  $x$  coordinate of point  $C$ . If  $r = 0$ , then it is necessary to return to step 3;
- 5) compute the value of  $s \equiv (rd + ke)(\bmod t)$ . If  $s = 0$ , then you need to return to step 3;
- 6) issue to the output of  $r$  and  $s$  as a digital signature.

### Digital Signature Authentication

To confirm the authenticity of EDS under the received message,  $M$ , the following actions are performed:

- 1) if  $0 < r < t, 0 < s < t$ , then go to the next step, otherwise the “signature is not authentic” is accepted;
- 2) calculate the message hash function:  $m = H(M)$ ;
- 3) compute by  $e \equiv m(\bmod t)$ . If  $e = 0$ , then define  $e = 1$ ;
- 4) calculate the value of  $v \equiv e^{-1}(\bmod t)$ ;
- 5)  $z_1 \equiv sv(\bmod t)$ ,  $z_2 \equiv -rv(\bmod t)$  values are calculated;
- 6) the point of the elliptic curve  $C = [z_1]N + [z_2]T$  is calculated and  $R \equiv x_c(\bmod t)$  is defined, where  $x_c$  – is the  $x$  coordinate of point  $C$ ;
- 7) if the equality  $R = r$  holds, then the “signature is authentic” is accepted, otherwise “the signature is not authentic”.

### Algorithm of generation and verification of EDS using the algorithm of the Russian Federation

For the algorithm of the Russian Federation, the following parameters of the digital signature scheme are used:

- a prime number  $p$  - is a module of an elliptic curve such that  $p > 2^{255}$ ;
- the elliptic curve  $E$  is defined by its invariant  $J(E)$  or the coefficients  $a, b \in F_p$ , where  $F_p$  is a finite field of  $p$  elements.  $J(E)$  is related to the coefficients  $a$  and  $b$  as follows  
$$J(E) = 1728 * \left(\frac{4a^3}{4a^3 + 27b^2}\right)(\bmod p)$$
, and  $4a^3 + 27b^2 \neq 0 (\bmod p)$ ;
- integer  $m$  - is the order of a group of points of an elliptic curve,  $m$  must be different from  $p$ ;
- a prime number  $q$ , the order of a cyclic subgroup of a group of points of an elliptic curve, that is,  $m = n * q$ ; for some  $n \in N$ . Also  $q$  lies within  $2^{254} < q < 2^{256}$ ;

- the point  $P = (x_p, y_p)$  of the elliptic curve  $E$ , which is the generator of a subgroup of order  $q$ , that is,  $q * P = O$  and  $k * P \neq O$  for all  $k = 1, 2, \dots, q - 1$ , where  $O$  is a neutral element groups of points of an elliptic curve  $E$ ;
- $h(M)$  - hash function (GOST R 34.11-94) [7], which displays message  $M$  in binary vector length of 256 bits.

Every digital signature user has private keys:

- encryption key  $d$  – integer number within  $0 < d < q$ ;
- decryption key  $Q = (x_Q, y_Q)$ , calculated as  $Q = d * P$ .

Additional requirements:

- $p^t \neq 1 \pmod{q}$ , any  $t = 1..B$ , where  $B \geq 31$ ;
- $J(E) \neq 1728$ .

### Digital Signature Generation

To obtain a digital signature under the message  $M$ , the following actions are performed:

- 1) calculation of the hash function from the message  $M$ :  $\check{h} = h(M)$ ;
- 2) calculation of  $e = z \pmod{q}$ , and if  $e = 0$ , set  $e = 1$ . Where  $z$  is an integer corresponding to  $\check{h}$ ;
- 3) generation of a random number  $k$  such that  $0 < k < q$ ;
- 4) calculation of the point of the elliptic curve  $C = k * P$ , and finding  $r = xc \pmod{q}$  where  $xc$  is the  $x$  coordinate of the point  $C$ . If  $r = 0$ , we return to the previous step;
- 5) verification of  $s = (r * d + k * e) \pmod{q}$ . If  $s = 0$ , go back to step 3;
- 6) digital signature generation  $\xi = (\check{r}|\hat{s})$ , where  $\check{r}$  and  $\hat{s}$  are vectors corresponding to  $r$  and  $s$ .

### Verifying Digital Signatures.

To confirm the authenticity of EDS under the received message  $M$ , the following actions are performed:

- 1) calculation by digital signature  $\xi$  of numbers  $r$  and  $s$ , taking into account that  $\xi = (\check{r}|\hat{s})$ , where  $r$  and  $s$  are numbers corresponding to vectors  $\check{r}$  and  $\hat{s}$ . If at least one of the inequalities  $r < q$  and  $s < q$  is incorrect, then wrong signature;
- 2) calculation of the hash function from the message  $M$ :  $\check{h} = h(M)$ ;
- 3) calculation of  $e = z \pmod{q}$ , and if  $e = 0$ , set  $e = 1$ . Where  $z$  is an integer corresponding to  $\check{h}$ ;
- 4) calculation of  $\vartheta = e - 1 \pmod{q}$ ;
- 5) calculation of  $z_1 = s * \vartheta \pmod{q}$  and  $z_2 = -r * \vartheta \pmod{q}$ ;
- 6) calculation of the point of the elliptic curve  $C = z_1 * P + z_2 * Q$ ;
- 7) definition  $R = xc \pmod{q}$ , where  $xc$  is the  $x$  coordinate of the curve  $C$  definition  $R = xc \pmod{q}$ , where  $xc$  – is the  $x$  coordinate of the curve  $C$ ;
- 8) in the case of equality  $R = r$  the signature is correct, otherwise - is incorrect.

## Program structure

This subsection presents the general structure of the TCPI - CSP, as well as a description of the functions of each module of the system.

## 10. GENERAL STRUCTURE

TCPI - CSP is implemented in the form of the following dynamic libraries:

- **CSP.DLL** - loading the CSP interface using the Crypto API;
- **CSPFUNC.DLL** - loading the CSP interface directly;
- **PKCS11.DLL** - loading the PKCS #11<sup>17</sup> interface (PKCS #11 interface for TCPI - CSP, hereinafter PKCS #11);
- **SCTOKEN.DLL** - functions for working with a smart card through the interface PKCS #11;
- **VTOKEN.DLL** - functions for working with virtual slots and tokens through the interface PKCS #11;
- **CRYPTOSP.DLL** - a library of cryptographic procedures.

The above libraries are located in the WINDOWS \ SYSTEM32 folder. Also, the following modules are included in the scope of delivery of TCPI - CSP:

- **GUI.DLL** - interface for entering the password to the key, random number generation using the electronic roulette mechanism;
- **CSP\_INTEGRAL\_TEST.EXE** integral test for TCPI - CSP;
- **PKCS11INI.EXE** initialization of virtual slots and tokens for the PKCS #11 interface;
- **CRYPTOTEST.EXE** - tests of cryptographic algorithms;
- **KEYMANAGER.EXE** - test program for obtaining and viewing certificates;
- **KM.DLL** - dynamic library for supporting the work of the test program **KEYMANAGER.EXE**;
- **CSPCON.DLL** is a dynamic library for supporting the import and export of private keys in the PFX format.

Note. The **KEYMANAGER.EXE** program and two dynamic libraries supporting it are intended only for testing the operation of CSP with certificates and private keys.

## 11. CSP INTERFACE

The TCPI - CSP interface consists of two dynamic libraries **CSP.DLL**, **CSPFUNC.DLL**, as well as an auxiliary test program **CSP\_INTEGRAL\_TEST.EXE**.

The cryptographic interface TCPI - CSP was created in accordance with the requirements of the Microsoft Cryptography Service Provider (CSP) standard. A description of the CSP standard (with a detailed description of all functions) can be found on the Microsoft website ([http://msdn.microsoft.com/en-us/library/aa380245\(v=VS.85\).aspx](http://msdn.microsoft.com/en-us/library/aa380245(v=VS.85).aspx)). The TCPI - CSP

---

<sup>17</sup> PKCS #11 - is one of the standards of the Public-Key Cryptography Standards (PKCS) family. It defines a platform-independent software interface for accessing cryptographic devices (smartcards, tokens, cryptographic accelerators, key servers and other means of cryptographic information protection).

interface was developed for the implementation of cryptographic algorithms of the Republic of Uzbekistan [1], [2], [3], Russian encryption algorithms and electronic signatures [6, 7, 8] using PKCS #11 [5] interface.

When developing the software implementation of the cryptographic interface of TCPI - CSP, the source texts of programs from the world - famous and freely distributed software package OpenSSL were widely used.

Using TCPI - CSP can be done directly, by loading the **CSPFUNC.DLL** library using the LoadLibrary mechanism and obtaining addresses of cryptographic functions using the GetProcAddress<sup>18</sup> command, or via the CryptoAPI<sup>19</sup> interface.

### **Input and output data**

The cryptographic interface of TCPI-CSP was created in accordance with the requirements of the Microsoft Cryptography Service Provider (CSP). A description of the CSP standard can be found on the Microsoft website. A description of the input and output data for the CSP standard can also be found on the Microsoft website at the links below.

CSP connection functions:

#### **Function & Description**

**CPAcquireContext** – Associates a key container with a CSP pointer.

**CPGetProvParam** – Displays CSP parameters.

**CPReleaseContext** – Frees pointer received by **CPAcquireContext**.

**CPSetProvParam** – Sets specific CSP parameters.

Key generation and CSP key exchange functions:

#### **Function & Description**

**CPDeriveKey** – Creates a key from a password.

**CPDestroyKey** – Removes a key from memory.

**CPDuplicateKey** – Creates a copy of the key.

**CPExportKey** – Export key.

**CPGenKey** – Generates a random key.

**CPGenRandom** – Generates random numbers.

**CPGetKeyParam** – Gets key parameters.

**CPGetUserKey** – Gets a user key pointer.

---

<sup>18</sup> GetProcAddress - The GetProcAddress function retrieves the address of the exported function or variable from the specified dynamic link library (DLL).

<sup>19</sup> CryptoAPI - CryptoAPI is an application programming interface that provides Windows developers with a standard set of functions for working with a cryptographic provider. Included in the Microsoft operating systems. Most CryptoAPI features are supported starting from Windows 2000. CryptoAPI supports asymmetric and symmetric keys, that is, allows you to encrypt and decrypt data, as well as work with electronic certificates. The set of supported cryptographic algorithms depends on the specific cryptographic provider.



**CPImportKey** – Imports key.

**CPSetKeyParam** – Sets key parameters.

Encryption and decryption functions:

#### **Function & Description**

**CPDecrypt** – Decrypts encrypted text with a key for encryption.

**CPEncrypt** – Encrypts plaintext with an encryption key.

Hashing and EDS functions:

#### **Function & Description**

**CPCreateHash** – Creates a hash pointer.

**CPDestroyHash** – Deletes a hash pointer.

**CPDuplicateHash** – Creates a copy of the hash function.

**CPGetHashParam** – Gets the properties of the hash function.

**CPHashData** – Hashes data

**CPHashSessionKey** – Hashes session key.

**CPSetHashParam** – Sets hash options.

**CPSignHash** – Sets signature hash function.

**CPVerifySignature** – Sets signature verification hash function.

## **12. CONCLUSION REMARKS**

This work is devoted to a brief description of the CSP software, which is designed to create encryption keys, private and public keys of an electronic digital signature, creating and authenticating EDS, hashing, encrypting and simulating data using the algorithms described in the State Standards of Uzbekistan. It can be used in telecommunications networks, public information systems, government corporate information systems by embedding into applications that store, process and transmit information that does not contain information related to state secrets, as well as in the exchange of information and ensuring the legal significance of electronic documents [11].

CSP includes the following functional components: a dynamically loadable library that implements a biophysical sensor of random numbers; dynamic library that implements cryptographic algorithms in accordance with the State Standards of Uzbekistan; module supporting the work with external devices; installation module that provides the installation of CSP in the appropriate environment of operation (environment).

CSP provides the creation of private and public EDS keys and encryption keys; creation and confirmation of authenticity of EDS according to the algorithms described in [2, 7]; the formation of derived encryption keys used by data encryption algorithms described in [4, 5]; work with key information stored on external media; hashing of memory areas and other data according to the algorithms described in [3, 6]; encryption of memory areas and other data in accordance with the data encryption algorithms described in [4, 5].

CSP provides support for identifiers of algorithms and parameters for the implementation of compatibility with third-party cryptographic providers in terms of the ability to work with

public-key certificates issued by third-party registration centers, provided they use the cryptographic algorithms described in [2, 3, 4, 5, 6, and 7]. The cryptography service provider provides the ability to work with digital certificates of public keys, which are structured binary in ASN.1 format, conforming to ITU-T X.509 v.3 standard and IETF RFC 5280, RFC 3739 Recommendations. CSP provides work with external key carriers such as USB-flash, eToken Aladdin (eToken PRO 72K (JAVA)). As part of CSP, modules are provided that provide for calling cryptographic functions through the Microsoft CryptoAPI 2.0 interface when running under Microsoft operating systems.

In accordance with the functional purpose, CSP provides the generation of public and private EDS keys, hashing keys, functional keys and encryption keys for use, respectively, in the algorithms described in [2, 3, 4, 5, 6, and 7]. In the application where the CSP will be integrated, an appropriate system for the manufacture and distribution of keys will be provided, which will be based on the functions of generation of CSP keys. CSP allows the use of a multi-level key protection model using random and derivative keys of key protection. Protection of keys is carried out on the basis of cryptographic transformations in accordance with the PKCS #5 standard [9] using the State Standards of Uzbekistan [3], [4] or the interstate standard [5]. CSP provides storage of key information on a hard disk drive (HDD) and/or external key storage devices, such as USB-flash, eToken Aladdin (eToken PRO 72K (JAVA)). CSP provides work with key containers containing: signature keys, encryption keys and additional information necessary to ensure the cryptographic protection of keys and ensure control of their integrity. To protect key information from substitution and/or distortion during its storage on HDD and external key carriers, as well as during distribution, key information is supplied with a checksum. In order to ensure the safe use of the CSP installed on the PC, organizational measures are provided, as well as software and hardware methods and means of protecting information are used to ensure that secret keys stored in the PC's memory during operation of the CSP are kept secret, as well as the CSP service parameters stored on the hard drive. CSP contains a component that allows you to verify the operation of cryptographic algorithms implemented in it. Functioning is carried out on the basis of test examples. To ensure the safe use of an application with a built-in CSP, mechanisms are provided to control the integrity of the CSP libraries. In CSP, a biophysical random number sensor is used to generate random binary sequences that implement the mechanism for generating secret digital signature keys, encryption keys, initialization vectors using various algorithms.

## REFERENCES

- [1] O`z DSt 1105: 2009. State standard of Uzbekistan. Information technology CRYPTOGRAPHIC PROTECTION OF INFORMATION. Data encryption algorithm.
- [2] O`z DSt 1106: 2009. State standard of Uzbekistan. Information technology CRYPTOGRAPHIC PROTECTION OF INFORMATION. A Hash function.
- [3] O`z DSt 1092: 2009. State standard of Uzbekistan. Information technology CRYPTOGRAPHIC PROTECTION OF INFORMATION. Processes of formation and verification of electronic digital signature.
- [4] PKCS #5 v2.0: Password-Based Cryptography Standard. RSA Laboratories. March 25, 1999. [Electronic resource]. - Access mode: <https://tools.ietf.org/html/rfc2898>.
- [5] Expansion of PKCS #11 for the use of Russian cryptographic algorithms. Moscow, 2008.
- [6] GOST 28147-89 - Information processing systems. Cryptographic protection. An algorithm of cryptographic transformation.
- [7] GOST R 34.11-94 - Information technology. Cryptographic protection of information. A Hash function.

- [8] GOST R 34.10-2001 - Information technology. Cryptographic protection of information. Processes of formation and verification of electronic digital signature.
- [9] RFC 4357 Additional Cryptographic Algorithms for Use with GOST 28147-89, GOST R 34.10-94, GOST R 34.10-2001, and GOST R 34.11-94 Algorithms.
- [10] Aloev R.D., Nurullaev M.M. (2019) Cryptography Service Provider - Data Encryption. In Proceedings of the 10 th International Multi-Conference on Complexity, Informatics and Cybernetics: 12-15 March 2019; Orlando, Florida, USA. Edited by Nagib Gallaos, Hsing-Wie Chu, Jeremy Horne, Suzanne K. Lunsford, Belkis Sánchez, Michael Savoie; pp 127-131.
- [11] Aripov M.M., Alaev R.H. (2019) Research of the application of the new cryptographic algorithms: applying the cipher algorithm O'zDSt1105:2009 for MS office document encryption. In Proceedings of the 5th International Conference on Engineering and MIS (ICEMIS '19): 06-08 June 2019; Astana, Kazakhstan. ACM, New York, NY, USA. <https://doi.org/10.1145/3330431.3330434>.

# NUMERICAL ALGORITHM FOR FINDING OPTIMAL INITIAL CONCENTRATIONS OF CHEMICAL REACTIONS

SVETLANA MUSTAFINA<sup>1\*</sup>, ANDREY ANTIPIN<sup>1</sup>, EVGENIA ANTIPINA<sup>1</sup>,  
ELENA ODINOKOVA<sup>2</sup>, LARISA TUCHKINA<sup>2</sup>, KONSTANTIN KOLYAZOV<sup>2</sup>,  
AND SOFIA MUSTAFINA<sup>1</sup>

<sup>1</sup>Dept. Mathematics and Information Technology, Bashkir State University, Ufa, Russia

<sup>2</sup>Dept. Information Technology and Management Systems, Moscow State University of Technologies and Management, Moscow, Russia.

\*Corresponding author: Mustafina\_SA@mail.ru

(Received: 16<sup>th</sup> June 2019; Accepted: 19<sup>th</sup> October 2019; Published on-line: 20<sup>th</sup> January 2020)

**ABSTRACT:** This article is devoted to the problem of developing methods for mathematical modelling in the sphere of optimal planning in a chemical experiment. In the article, the problem of finding the optimal ratio for initial concentrations of substances is formulated in general terms and an algorithm for solving this problem is constructed basing on the method of artificial immune systems. The developed algorithm for finding the optimal initial concentrations of substances allows solving the problem of experiment planning in chemistry at the computational experiment stage. In this case, the solution of the optimization problem found with its help does not depend on the choice of the initial approximation. The algorithm was tested for the industrially meaningful process of benzilidenebenzilamine synthesis for which the optimum values of the initial concentrations were calculated in order to obtain maximum yield of the reaction product.

**ABSTRAK:** Artikel ini ditujukan untuk masalah mengembangkan kaedah pemodelan matematik dalam bidang perancangan optimum dalam percubaan kimia. Dalam artikel itu, masalah mencari nisbah optimum untuk konsentrasi awal bahan digubal secara umum dan algoritma untuk menyelesaikan masalah ini dibina berdasarkan kaedah sistem imun buatan. Algoritma yang dibangunkan untuk mencari kandungan konsentrasi awal yang optimum membolehkan menyelesaikan masalah perancangan percubaan dalam kimia pada peringkat percubaan pengkomputeran. Dalam kes ini, penyelesaian masalah pengoptimuman yang didapati dengan bantuannya tidak bergantung pada pilihan permulaan awal. Algoritma ini telah diuji untuk proses sintesis benzilidenebenzilamin yang bermakna industri yang mana nilai-nilai optimum kepekatan awal dikira untuk mendapatkan hasil maksimum produk reaksi.

**KEYWORDS:** chemical kinetics; artificial immune systems; initial concentration

## 1. INTRODUCTION

The solution to many problems in chemistry and chemical technology is associated with complex and expensive experiments. In the study of the chemical process at the computational experiment stage, it is advisable to identify its main regularities because of the complexity of the initial raw materials' compositions and the low content of valuable components in them. In this regard, the actual task is to develop methods for optimal planning of the experiment, which allow saving time and material resources for conducting a full-scale experiment.

The development of computer technology and information technology allows the use of mathematical methods in the planning of the chemical experiments. The methods of mathematical modelling allow the determination of optimal concentrations of reagents to obtain the best yield of the final product and significantly reduce the cost of substance synthesis.

The calculation of the initial concentrations of the reactants in a chemical reaction is made by searching for an extremum of the function for calculating the dynamics of the substance concentrations during the chemical experiment. The significant drawbacks of most numerical methods for finding the extremum of functions are the difficulties in achieving convergence of the process, which depends on the choice of the initial approximation.

Currently, metaheuristic optimization methods are widely used, which make it possible to efficiently find a global optimum in a reasonable time [1-3]. Their important feature is the ability to overcome the local extremum point of the target function in the search process. Therefore, they allow finding better solutions in comparison with classical heuristics [4-7].

Among the metaheuristic algorithms, the method of artificial immune systems is distinguished. Its advantage is the presence of a memory mechanism. The memory mechanism makes it possible to use information about previously found best solutions, thereby increasing the efficiency of global search. An important feature of the method of artificial immune systems is the independence of the optimization problem solution from the initial approximation [8-10].

## 2. FORMULATION OF THE PROBLEM

Let us formulate in general terms the problem of finding the optimal ratio for initial concentrations of substances. A mathematical model for the dynamics of substance concentrations is a system of ordinary differential equations

$$\frac{dx}{dt} = f(t, x(t), T), \quad (1)$$

with initial conditions

$$x_i(0) = x_i^0, \quad i = \overline{1, n}, \quad (2)$$

where  $x(t) = (x_1(t), x_2(t), \dots)$  is the vector of the concentrations of the reacting substances,  $f(t, x(t), T)$  is continuous together with their partial derivatives of the function,  $t \in [0, t_2]$  is the time of reaction, and  $T$  is the reaction temperature [11].

At the initial moment of time, substances are interconnected by some ratio:

$$x_1(0) : \dots : \dots \quad (3)$$

It is required to find the ratio for initial concentrations of substances, which ensures the extremum of optimality criterion

$$Q(x) = \sum_{i=1}^n \lambda_i x_i(t_2) \rightarrow \text{extr}. \quad (4)$$

The optimality criterion expresses the maximum yield of the target products or the minimum impurity content depending on the coefficients  $\lambda_i$  (positive or negative). You

can also specify some economic criterion, then the coefficients  $\lambda_i$  are the cost coefficients of the reagents.

### 3. THE ALGORITHM FOR THE METHOD OF ARTIFICIAL IMMUNE SYSTEMS TO CALCULATE OPTIMAL INITIAL CONCENTRATIONS OF SUBSTANCES

The method of artificial immune systems simulates the functioning of a living organism immune system, designed to destroy foreign bodies and improve the fight against them. Consider the main concepts of the method.

An antigen is an alien substance from which the body tries to protect itself with antibodies. An antibody is a substance that recognizes and destroys an antigen [12]. A memory cell is an immune cell that accumulates data about new antibodies that can recognize an antigen. The target function of the optimization problem is called the fitness function [13,14].

As a function of fitness, we used the maximum yield of the target reaction product at the final moment of the reaction. This required the solution of a direct kinetic problem with a given ratio for the initial concentrations of the initial substances, that is, the solution of a system of differential equations (Eq. (1)) with initial conditions (Eq. (2)).

We modified the algorithm to solve the problem of finding the optimal initial concentrations of the components in the reacting mixture. As a population of immune cells, we introduced sets of initial concentrations of substances  $x^j(0) = (x_1^j(0), x_2^j(0), \dots)$ ,  $j = \overline{1, k}$ , where  $k$  is the number of immune cells in the population.

To calculate the value of the fitness function  $Q(x)$ , it is necessary to know the concentration of reagents at the final point in time. To do this, we introduced a block for solving a direct kinetic problem into the algorithm.

The problem of finding the minimum of the target function  $Q(x)$  was reduced to the problem of finding the maximum by replacing the sign in front of the function with the opposite one:  $Q(x^*) = \min Q(x) = \max [-Q(x)]$ . If  $Q(x)$  was positive then  $Q(x^*) < 0$ .

We formulated this algorithm.

Step 1. *The creation of an initial population for the starting substance concentrations.*

Set the number of immune cells in the population  $k$ , the number of parental cells for the selection  $r\_sel$ , the number of cells in the population with the worst value of the fitness function  $n\_bad$ , the maximum number of iterations  $i\_max$ , the clone operator parameter  $n\_cl$ , the mutation parameter  $m$ , the iteration counter  $num = 0$ .

Randomly set the values of  $k$  cells of the initial population  $x^j(0)$ ,  $j = \overline{1, k}$ ,  $0 \leq x^j(0) < 1$ .

Step 2. *Calculation of fitness function values.*

For sets  $x^j(0)$  calculate the value of fitness function  $Q(x^j)$ , by solving a direct kinetic problem for each immune cell. That is, at this step it is necessary to find a numerical solution to the system of differential equations (Eq. (1)) with the initial

conditions (Eq. (2)) by an explicit or implicit method. The initial conditions of the system (Eq. (2)) are the immune cell.

Step 3. Cloning.

Select  $r\_sel$  parent cells from the population (a set of antibodies), which correspond to the best values of fitness function  $Q(x)$ . Generate  $n\_cl$  clones for each cell.

Step 4. Mutation.

For each parent cell generate random numbers  $l \in [0,1]$ ,  $h_1 \in [0,1-x_i^j(0)]$ ,  $h_2 \in [0,x_i^j(0)]$ ,  $i = \overline{1,n}$ . Perform a mutation of its clones by the rule: if  $l > 0,5$ , then  $x_i^s(0) := x_i^s(0) + h_1 \cdot m$ , else  $x_i^s(0) := x_i^s(0) - h_2 \cdot m$ , where  $s = \overline{1,n\_cl}$ ,  $m$  – mutation parameter.

Step 5. Calculation of fitness function values.

For each mutant clone calculate the value of the fitness function by Eq. (4).

Step 6. Selection and transition to a new population.

For each parent cell, find the mutant clone with the lowest value of the fitness function. Compare its value with the value of the fitness function of the parent cell. In the new population, leave the parent cell or replace it with a mutant clone with the best fitness function value.

Step 7. Renewal of a population.

In the population, find  $n\_bad$  cells with the lowest value of fitness function  $Q(x)$ . Replace these cells with new ones, randomly generated in the interval  $[0,1)$ , and calculate the value of the fitness function  $Q(x)$  for them.

Increase the iteration counter:  $num = num + 1$ .

Step 8. Checking the conditions for the end of search.

If  $num < i\_max$ , then go to step 3, else finish the search and go to step 9.

Step 9. Selection of optimal concentrations of substances from the population.

As a solution to the problem of finding the optimal concentrations of substances, select the cell with the highest fitness function value from the last population.

The developed algorithm was implemented as a software tool in the visual programming environment Delphi.

## 4. COMPUTATIONAL EXPERIMENT

Based on the formulated algorithm, we calculated the optimal ratio of the initial concentrations for the reaction of the benzylidenebenzylamine synthesis in order to obtain the maximum yield of the reaction product. The mechanism of the chemical reaction for the synthesis of benzylidenebenzylamine in the presence of a catalyst  $FeCl_3 \cdot 6H_2O$  is represented by a set of stages [15]:



where  $X_1$  – benzylamine ( $C_7H_9N$ ),  $X_2$  – carbon tetrachloride ( $CCl_4$ ),  $X_3$  – chlorobenzylamine ( $C_7H_8NCl$ ),  $X_4$  – chloroform ( $CHCl_3$ ),  $X_5$  – 1-phenylmethanimine ( $C_7H_7N$ ),  $X_6$  – hydrogen chloride ( $HCl$ ),  $X_7$  – benzylidenebenzylamine ( $C_{14}H_{13}N$ ),  $X_8$  – ammonium ( $NH_3$ ),  $X_9$  – ammonium chloride ( $NH_4Cl$ ).

The speed of each stage is determined according to the law of mass action:

$$\begin{aligned}
 \omega_1 &= k_1 x_1 x_2, \\
 \omega_2 &= k_2 x_3, \\
 \omega_3 &= k_3 x_5 x_1, \\
 \omega_4 &= k_4 x_8 x_6,
 \end{aligned}
 \tag{6}$$

where  $x_i$  is the concentration of the  $i$ -th substance ( $i = \overline{1,9}$ ) (mole fraction),  $k_j$  is the rate constant of the  $j$ -th reaction stage ( $j = \overline{1,4}$ ), calculated according to the Arrhenius equation

$$k_j(T) = k_{0j} \cdot \exp\left(-\frac{E_j}{RT}\right),$$

where  $E_j$  is the energy of activation of the  $j$ -th stage (kJ/mol),  $T$  is the reaction temperature (K), and  $R$  is the universal gas constant (8,31 J/(mol·K)).

The matrix of stoichiometric coefficients of substances ( $\gamma_{ij}$ ) ( $i = \overline{1,4}$ ,  $j = \overline{1,9}$ ) is given in Table 1.

Table 1: Matrix of stoichiometric coefficients of the reaction of synthesis of benzylidenebenzylamine

	$\omega_1$	$\omega_2$	$\omega_3$	$\omega_4$
$X_1$	-1	0	-1	0
$X_2$	-1	0	0	0
$X_3$	1	-1	0	0
$X_4$	1	0	0	0
$X_5$	0	1	-1	0
$X_6$	0	1	0	-1
$X_7$	0	0	1	0
$X_8$	0	0	1	-1
$X_9$	0	0	0	1
$\delta$	0	1	0	-1

Since there are nonzero elements among the elements of the last line  $\delta$ , the reaction proceeds with a change in the reaction volume [16, 17]. Then the kinetic model of the reaction is a system of differential equations:



$$\begin{cases} \frac{dx_i}{dt} = \frac{F_i(x, T) - x_i \cdot F_n(x, T)}{N}, & i = \overline{1, 9}, \\ \frac{dN}{dt} = F_n(x, T), \end{cases} \quad (7)$$

with initial conditions:

$$x_i(0) = x_i^0, \quad i = \overline{1, 9}, \quad N(0) = 1, \quad (8)$$

where  $N$  is the variable reaction volume,  $F_i = \sum_{j=1}^4 \gamma_{ij} W_j$ ,  $i = \overline{1, 9}$ ,  $F_n = \sum_{j=1}^4 W_j \sum_{i=1}^9 \gamma_{ij}$ ,

$W_j = \frac{\omega_j}{C_0}$  is the values of rate of reaction stages ( $j = \overline{1, 4}$ ) ( $\text{h}^{-1}$ ), and  $C_0$  is the initial total concentration of substances (mol/l).

The functions  $F_n(x, T)$ ,  $F_i(x, T)$  ( $i = \overline{1, 9}$ ) have the form:

$$\begin{aligned} F_1(x, T) &= -W_1(x, T) - W_3(x, T), \\ F_2(x, T) &= -W_1(x, T), \\ F_3(x, T) &= W_1(x, T) - W_2(x, T), \\ F_4(x, T) &= W_1(x, T), \\ F_5(x, T) &= W_2(x, T) - W_3(x, T), \\ F_6(x, T) &= W_2(x, T) - W_4(x, T), \\ F_7(x, T) &= W_3(x, T), \\ F_8(x, T) &= W_3(x, T) - W_4(x, T), \\ F_9(x, T) &= W_4(x, T), \\ F_n(x, T) &= W_2(x, T) - W_4(x, T). \end{aligned} \quad (9)$$

The initial substances of the reaction are benzylamine ( $X_1$ ) and carbon tetrachloride ( $X_2$ ), the concentrations of which are related by the ratio:  $x_1(0) + x_2(0) = 1$ .

For other substances  $x_i(0) = 0$ ,  $i = \overline{3, 9}$ .

Since the target substance of the reaction scheme is benzylideneaniline ( $X_7$ ), the optimization problem is formulated as follows: find the ratio for the initial concentrations  $x_1(0) : x_2(0)$  of the source substances  $X_1$  and  $X_2$ , at which at the final time of the reaction the maximum yield of benzylidenebenzylamine  $X_7$  is reached, i.e.  $Q(x) = x_7(t_2) \rightarrow \max$ .

The solution of this problem was obtained at the temperature  $T = 23^\circ \text{C}$  and the time of the reaction was  $t_2 = 4$  h. The solution of the system (Eq. (7)) with initial conditions (Eq. (8)) was obtained by the implicit Euler method.

The result of the calculation obtained the optimal ratio for the initial concentrations of the source substances was:

$$x_1(0) : x_2(0) = 0,51 : 0,49. \quad (10)$$

The maximum yield of the reaction (benzylideneaniline) was 0,013 mole fractions.

Figure 1 shows the dynamics of the benzylidenebenzylamine concentration at optimal initial concentrations.

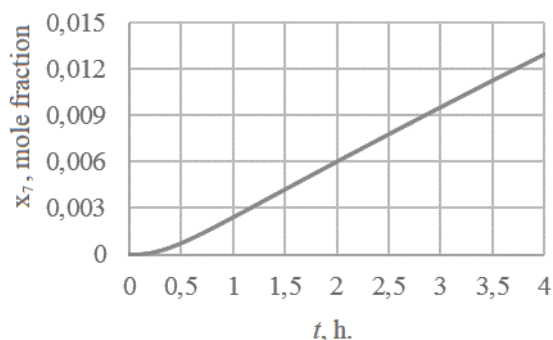


Fig. 1: Dynamics of the optimal concentration of benzylidenebenzylamine.

## 5. CONCLUSIONS

Consider the solution of a direct kinetic problem for the reaction scheme (Eq. (5)) with arbitrary sets for initial concentrations of substances.

According to Table 2, the maximum concentration of benzylidenebenzylamine is observed at a specific ratio of the source substances (Eq. (10)). This confirms the correct operation of the algorithm.

Table 2: Dependence of the concentration of benzylidenebenzylamine  $X_7$  from the ratio of source substances  $X_1$  and  $X_2$

$x_1$ , mole fraction	$x_2$ , mole fraction	$x_7$ , mole fraction
0.1	0.9	0.004
0.2	0.8	0.008
0.3	0.7	0.010
0.4	0.6	0.012
0.51	0.49	0.013
0.7	0.3	0.011
0.8	0.2	0.009
0.9	0.1	0.005

Thus, the developed algorithm for finding the optimal initial concentrations of the initial substances makes it possible to solve the problem of planning an experiment in chemistry at the stage of a computational experiment. The solution of the optimization problem will be found for any set of values of the initial concentrations of substances, since the work of the artificial immune systems method does not depend on the initial approximation.

## ACKNOWLEDGEMENT

The reported study was funded by RFBR according to the research project No 17-47-020068 and project No. 13.5143.2017 / 8.9.

## REFERENCES

- [1] Goldberg D. (1989) Genetic Algorithms in Search, Optimization and Machine Learning. Addison-Wesley, USA.
- [2] Holland JN. (1975) Adaptation in Natural and Artificial Systems. Ann Arbor, Michigan: Univ. of Michigan Press.
- [3] Stepashina EV. (2014) Optimization the financial performance of enterprise on neural network model. Information Systems and Technologies, 5: 34-42.
- [4] Igel C, Hansen N, Roth St. (2007) Covariance matrix adaptation for multi-objective optimization. Evolutionary Computation, 15(1): 1-28.
- [5] Mahdavi M. (2007) An improved harmony search algorithm for solving optimization problems. Applied Mathematics and Computation, 188(2): 1567-1579.
- [6] Herrera F, Lozano M, Verdegay JL. (1998) Tackling real-coded genetic algorithms: operators and tools for the behavior analysis. Artificial Intelligence Review, 12(4): 265-319.
- [7] Lee KS, Geem ZW. (2005) A new meta-heuristic algorithm for continuous engineering optimization: harmony search theory and practice. Computer Methods in Applied Mechanics and Engineering, 194: 3902-3933.
- [8] Ishida Y, Hirayama H, Fujita H, Ishiguro A, Mori K. (1998) Immunity-Based Systems-Intelligent Systems by Artificial Immune Systems. Corona Pub. Co., Japan.
- [9] Sedova NA, Sedov VA, Bazhenov RI. (2018) Analysis of emergency level at sea using fuzzy logic approaches. Advances in Intelligent Systems and Computing, 658: 314-322.
- [10] Antipin AF. (2013) A computer-aided system for designing multidimensional logic controllers with variables representing a set of binary logic arguments. Automation and Remote Control, 74(9): 1573-1581.
- [11] Mustafina SA, Vaytiev VA, Stepashina EV. (2014) Search the kinetic parameters of the reduced scheme of A-methylstyrene dimerization reaction. ARPN Journal of Engineering and Applied Sciences, 9(7): 1118-1120.
- [12] de Castro L, Timmis J. (2002) An Artificial Immune Network for Multimodal Function Optimization. Proceedings of IEEE Congress on Evolutionary Computation, 1: 669-674.
- [13] Pantelev AV, Metlitskaya DV. (2012) Applying of the method of the synthetic immune systems in a problems of searching conditional extremum of the function. Civil Aviation High Technologies, 184: 54-61.
- [14] Antipin AF. (2015) Improving response time of real time control systems based on multidimensional interval-logical controllers. Automation and Remote Control, 76(3): 480-486.
- [15] Stepashina EV, Baitimerova AI, Mustafina SA. (2011) The software package for the computer aided procedure of qualified mechanism of chemical reactions based on DRGEP method. Bashkir chemical journal, 18(3): 112-115.
- [16] Vaytiev VA, Stepashina EV, Mustafina SA. (2013) Identification of a mathematical model of the reduced scheme of  $\alpha$ -methylstyrene dimerization reaction. European Journal of Natural History, 6: 30-32.
- [17] Sedov VA, Sedova NA. (2014) Modelling collision avoidance actions in closest approach zones by means of neural networks. Asia-Pacific Journal of Marine Science & Education, 4(2): 104-111.

## DIABETES CLASSIFICATION BASED ON KNN

AMEER ALI<sup>1\*</sup>, MOHAMMED ALRUBEI<sup>2</sup>, LAITH FALAH MOHAMMED HASSAN<sup>1</sup>,  
MOHANNAD AL-JA'AFARI<sup>1</sup> AND SAIF ABDULWAHED<sup>2</sup>

<sup>1</sup>Najaf Technical Institute, Al-Furat Al-Awsat Technical University, 31001 Al-Najaf, Iraq.

<sup>2</sup>Al-Furat Al-Awsat Technical University, 31001 Al-Najaf, Iraq,

<sup>3</sup>Al-Furat Al-Awsat Technical University, 31001 Al-Najaf, Iraq.

\*Corresponding author: inj.ame7@atu.edu.iq

(Received: 26<sup>th</sup> July 2019; Accepted: 7<sup>th</sup> December 2019; Published on-line: 20<sup>th</sup> January 2020)

**ABSTRACT:** Diabetes is a life-threatening syndrome occurring around the world; it can have huge complications and is documented by large amounts of medical data. Therefore, attempts at early detection of this disease took a large area of research and many methods were used to deal with diabetes. In this paper, different types of KNN algorithm have been used to classify diabetes disease using Matlab. The dataset was generated by the criteria of the American diabetes association. For the training stage, 4900 samples have been used by the classifier learner tool to observe the results. Then, 100 of the data samples were used for the test. The results show that the KNN types (Fine, Weighted, Medium and Cubic) give high accuracy over the Coarse and the Cosine methods. Fine KNN is considered the most suitable according to its accuracy of classified samples.

**ABSTRAK:** Penyakit kencing manis adalah sindrom penyakit ancaman nyawa yang berlaku di seluruh dunia dan ia mempunyai data perubatan yang besar serta komplikasi tinggi. Oleh itu, cubaan dalam mengesan awal penyakit ini mempunyai potensi luas dalam kajian dan banyak kaedah telah digunakan bagi mengkaji penyakit kencing manis. Dalam kajian ini, pelbagai jenis algoritma KNN telah digunakan bagi mengelas penyakit kencing manis menggunakan Matlab. Setdata dihasilkan berdasarkan kriteria Kesatuan Kencing Manis Amerika. Pada peringkat latihan, sebanyak 4900 sampel telah digunakan oleh pelatih alat pengelasan bagi memantau dapatan kajian. Kemudian, 100 daripada sampel data telah digunakan bagi ujian. Keputusan menunjukkan jenis KNN (Halus, Berat, Sederhana dan Kubik) lebih tepat berbanding kaedah Kasar dan Kosinus. KNN Halus di dapati lebih sesuai berdasarkan ketepatan sampel pengelasan.

**KEYWORDS:** diabetes; KNN; classification machine learning

### 1. INTRODUCTION

Diabetes disease is chronic and widespread in the world. It occurs by disorder in insulin secretion that causes an irregular increase in glucose level. Spread of this disease has been observed in due to unhealthy diets [1]. Generally, a higher probability of diabetes infection correlates to various factors such as female gender, age over 35, and persons with unhealthy weight [2]. Many methods have been produced for diagnosis of different types of diseases, which used intelligent algorithms to classify, cluster, and diagnose these diseases. Support Vector Machine (SVM) used as a classifier to diagnose diabetes based on a medical dataset [3,4,5]. Bayes theorem used to classify prediction accuracy in diabetes data with a data set delivered from Diabetes 130-US hospitals [6]. Decision Tree and Naïve Bayes algorithms presented to analyse and classify the patterns in order to

diagnose the diabetes disease [7]. Coupling methods: likelihood ratio test, joint clustering, and classification based data presented from Boston Medical Center, in order to diagnose diabetes [8]. Fasting plasma glucose used to predict and diagnose type 2 diabetes based on two machine-learning algorithms: logistic regression and naive Bayes classifier [9]. Fuzzy logic also presented system to diagnose diabetes based on five layers [10]. Convolution neural network used to diagnose many diseases belonging to the diabetes family using [11]. In this paper, six types of KNN algorithms have been used to investigate its ability to classify glucose levels.

The organization of this paper is arranged as follows: the description of KNN algorithms and their distance equations are presented in section two. Section three presents the dataset criteria for diabetes. The discussion of results for KNN algorithms has been explained in section four to identify which type of KNN is more suitable. Finally, the conclusion of this experiment has been introduced in section five.

## 2. K-NEAREST NEIGHBOURS (KNN)

The classification is a type of supervised machine learning. The KNN is one of the classification techniques that is commonly used to classify data input into pre-defined classes (k) [12]. It was proposed by Cover and Hart in 1968. The straightforward mechanism of the KNN algorithm is to compute the Euclidean distance function between pre-defined classes and each varying sample. After that, the KNN algorithm chooses the minimum nearest neighbours according to each category. The samples are assigned to their category based on the nearest k neighbours. There are many versions of distance function between the samples. In this paper, the most commonly used is the Euclidean distance, expressed in Eq. (1) [13].

$$d = \sqrt{\sum_{k=1}^n (X_{1k} - X_{2k})^2} \quad (1)$$

Where  $k$  is the number of values in each sample vector, and  $X_1, X_2$  are input samples.

Six types of KNN have been chosen to classify the dataset. Their details are described as follows [14]:

Fine KNN takes one neighbour to distinguish the sample data, while the Medium KNN takes more neighbours than Fine KNN for distinction. This type will cause a low distinction feature to the algorithm. The Coarse KNN takes more neighbours than Medium KNN, which leads to the lowest distinction feature amongst the three types.

The Cosine KNN uses a Cosine distance metric as in Eq(2). The Cubic KNN uses a cubic distance metric as in Eq(3). The weight KNN uses a distance weight as in Eq(4). The last three types have the same number of neighbours as Medium KNN [15].

$$d = \left( 1 - \frac{x_1 x_2'}{\sqrt{(x_1 x_1')(x_2 x_2')}} \right) \quad (2)$$

$$d = \sqrt[3]{\sum_{k=1}^n |x_{1k} - x_{2k}|^3} \quad (3)$$

$$d = \sqrt{\sum_{k=1}^n w_i (x_{1k} - x_{2k})^2} \quad (4)$$

When the numbers of neighbours are decreased, the accuracy of the classifier increases. This will increase the complexity of the classifier model, but does not guarantee that the out-of-samples will be classified correctly [16].

### 3. DIABETES CRITERIA

The dataset presents amounts for each of the variables based on the criteria, such as glucose before food and glucose after food of an object. Each value or amount is called as a datum. The criteria used in this research are summarized in Table 1. The objective of these criteria is to generate a dataset to diagnose diabetes in humans. Based on a personal dataset, such as (HB A1C test, Fasting test, and Random test), it tries to decide if a human subject has diabetes, based on whether its values are normal or not. Diabetes criteria are already in public domain, thanks to the American diabetes association standards [17].

Table 1: Diabetes criteria [17]

<b>HB A1C</b>	<b>Fasting (FPG)</b>	<b>Random (PG)</b>	<b>Response</b>
<b>A</b>	<b>B</b>	<b>C</b>	<b>Y</b>
5-5.9	90-119	140-199	Normal
A0	B0	C0	(0)
6-6.5	120-140	200-250	Neuropath
A1	B1	C1	(0.25)
6.6-7	141-180	251-300	Retinopathy
A2	B2	C2	(0.5)
7.1-7.5	181-250	301-350	Nephropathy
A3	B3	C3	(0.75)
7.6-8	251-600	351-500	Heart disease
A4	B4	C4	(1)

The diagnosis of diabetes is based on glucose and plasma; either the 2-h Plasma Glucose (2-h PG) value after a 75-g oral glucose tolerance test or the Fasting Plasma Glucose (FPG). A1C (threshold  $\geq 6.5\%$ ) is added as a third option in the diagnosis. The A1C test uses a Diabetes Control that is certified by the National Glycohemoglobin Standardization Program.

The relationship between the A1C and the risk of retinopathy, as with FPG and 2-h PG, were shown in epidemiological data. The compatibility between the 2-h PG tests with FPG and between A1C with glucose-based tests are  $<100\%$ . The A1C and oral glucose tolerance have several benefits to the FPG, including greater convenience and less daily disturbances during stress and sickness [17,18].

### 4. RESULTS

In this experiment, we will train the classifier using the sample data generated from Table 1. Each training sample has four values. The first three values are input samples that indicate HB A1C, Fasting (FPG), and Random (PG). The fourth one is the response. Then the classifier was tested using out-of-sample data to calculate the accuracy of the distinction. Table (2) summarizes the parameters of the experiment.

Table 3 shows the accuracy prediction speed and training time for all KNN types using 4900 input samples. For the accuracy, Fine KNN, Weighted KNN, Medium KNN, Cubic KNN, Cosine KNN, and Coarse KNN have been arranged according to their performance. In addition, according to the mathematical computation distance, the maximum training time was taken by the Cosine KNN while the Medium KNN takes the least training time. Thus, the prediction speed (observation/second) is maximum for Fine KNN and minimum for Cosine KNN.

Table 2: Simulation parameters

No.	Coefficient	Description
1	Fine KNN	K=1
2	Medium KNN	K=10
3	Coarse KNN	K=100
4	Cosine KNN	K=10
5	Cubic KNN	K=10
6	Weighted KNN	K=10
7	Number of training samples	4900
8	Number of testing samples	100
9	Training tool	Classification learner using Matlab

Table 3: Experiment outcome information

Preset	Accuracy	Training time	Prediction speed
Fine KNN	99.9%	0.54411 sec	200000 obs/sec
Medium KNN	98.4%	0.26525 sec	100000 obs/sec
Coarse KNN	74.3%	0.46863 sec	43000 obs/sec
Cosine KNN	85.6%	0.69376 sec	25000 obs/sec
Cubic KNN	98.2%	0.47105 sec	52000 obs/sec
Weighted KNN	99.8%	0.27984 sec	110000 obs/sec

The pre-trained classifier tested 100 random out-of-sample data to check the distinction capability, which it is enough to cover the reliability of the classifier over all classes. As expected, the numbers of classification errors are 0, 0, 19, 16, 2, and 0 for Fine KNN, Medium KNN, Coarse KNN, Cosine KNN, Cubic KNN, and Weighted KNN, respectively.

Figure 1 shows the confusion matrix for each of the KNN types. In each model in Fig. 1, the diagonal of green squares represents the correct prediction ratio of the predict classes over true classes while the red squares give the incorrect class ratio. The ratio of each square is associated with the disparity of the colours. The white squares are empty for samples from the training stage.

The results show the magnitude of decision ratio between the true value and the prediction value. Fine, Medium, Cubic, and Weighted give the best decision while Coarse and Cosine give high failure ratios. Figure 1 shows that the Fine KNN classifier is the most preferable because it gives 100% accuracy for Normal, Neuropath, and Retinopathy classes and <1% for Nephropathy and Heart disease.

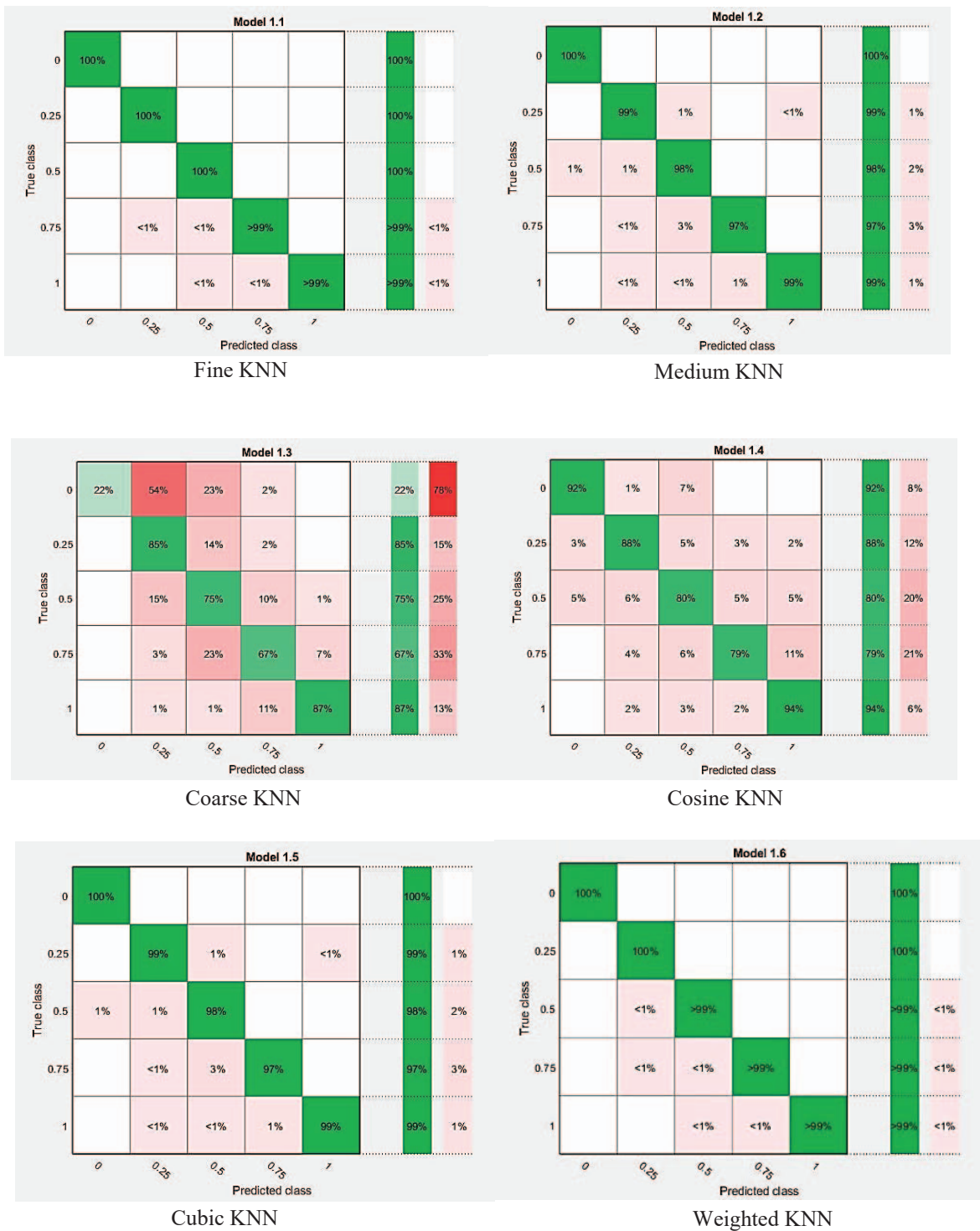


Fig. 1: The confusion matrix for different types of KNN.

## 5. CONCLUSION

The dataset of diabetes has been classified using different types of KNN algorithms. The simulation results show that Fine, Medium, Cubic, and Weighted KNN types have a superior performance over Coarse and Cosine. The classifier model of all KNN types required less than 0.7 sec to predict the target. In addition, it can be said that the Fine KNN



algorithm is suitable to solve the diabetes classification problem with higher accuracy than other types.

## REFERENCES

- [1] T.Karthikeyan, K.Vembandadsamy. (2015). An Analytical Study on Early Diagnosis and Classification of Diabetes Mellitus. *International Journal of Computer Application*,7:2250-1797.
- [2] Catherine C. Cowie, Keith F. Rust, Danita D. Byrd-Holt, Edward W. Gregg, Earl S. Ford, Linda S. Geiss, Kathleen E. Bainbridge, Judith E. Fradkin. (2010). Prevalence of diabetes and high risk for diabetes using A1C criteria in the US population in 1988–2006. *Diabetes care*, 33: 562-568.
- [3] V. Anuja Kumari, R.Chitra. (2013). Classification Of Diabetes Disease Using Support Vector Machine. *International Journal of Engineering Research and Applications*,3:1797-1801.
- [4] Longfei Han, Beijing, Senlin Luo, Jianmin Yu, Limin Pan, Songjing Chen. (2013) Rule Extraction from Support Vector Machines Using Ensemble Learning Approach: An Application for Diagnosis of Diabetes. *IEEE*,19:2168-2194.
- [5] Nahla H. Barakat, Andrew P. Bradley, Mohamed Nabil H. Barakat (2010). Intelligent Support Vector Machines for Diagnosis of Diabetes Mellitus. *IEEE*,40:2168-2194.
- [6] Subhankar Manna, Malathi G. (2017). Performance Analysis Of Classification Algorithm On Diabetes Healthcare Dataset. *International Journal of Research - Granthaalayah*,5:260-266.
- [7] Aiswarya Iyer, S. Jeyalatha, Ronak Sumbaly (2015). Diagnosis Of Diabetes Using Classification Mining Techniques. *International Journal of Data Mining & Knowledge Management Process (IJDKP)*,5:1-14.
- [8] Theodora S. Brisimi, Tingting Xu, Taiyao Wang, Wuyang Dai, William G. Adams , Ioannis Ch. Paschalidis(2018). Predicting Chronic Disease Hospitalizations from Electronic Health Records: An Interpretable Classification Approach. *IEEE*,106:1-18.
- [9] Bum Ju Lee, Boncho Ku, Jiho Nam, Duong Duc Pham, Jong Yeol Kim (2014). Prediction of Fasting Plasma Glucose Status Using Anthropometric Measures for Diagnosing Type 2 Diabetes. *IEEE*,18:555-561.
- [10] Chang-Shing Lee, Senior Member, Mei-Hui Wang (2011) A Fuzzy Expert System for Diabetes Decision Support Application. *IEEE*,41:139-153.
- [11] Yuliang Liu, Quan Zhang, Geng Zhao, Zhigang Qu, Guohua Liu, Zhiang Liu, Yang An (2018). Detecting Diseases by Human-Physiological- Parameter-Based Deep Learning. *IEEE*,7: 2169-3536
- [12] Shichao Zhang, Xuelong Li, Ming Zong, Xiaofeng Zhu, Ruili Wang (2017). Efficient kNN Classification With Different Numbers of Nearest Neighbors. *IEEE*,29:1-12.
- [13] Mehdi Zekriyapanah gashti (2018). A Modified Model Based on Flower Pollination Algorithm and K-Nearest Neighbor for Diagnosing Diseases. *IIUM Engineering Journal*, 19:144-157.
- [14] Jenifer Mariam Johnson and Anamika Yadav(2016). Fault detection and classification technique for HVDC transmission lines using KNN, Second International Conference on ICT for Sustainable Development, Goa, 1-2 July 2016.
- [15] Jaime Vitola , Francesc Pozo, Diego A. Tibaduiza, Maribel Anaya (2017). A Sensor Data Fusion System Based on k-Nearest Neighbor Pattern Classification for Structural Health Monitoring Applications. *Sensors*, 17.
- [16] Asad Hussain, Sajjad Ahmed Ghauri, M. Farhan Sohail, Sheraz A. Khan, Ijaz Mansoor Qureshi. (2016). KNN BASED CLASSIFICATION OF DIGITAL MODULATED SIGNALS. *IIUM Engineering Journal*, 17: 71-82.

[17] American Diabetes Association (2014). Standards of Medical Care in Diabetes 2014 ,Diabetes Care 37: S14-S80.

# ADAPTIVE SYSTEM OF FUZZY-LOGICAL REGULATION BY TEMPERATURE MODE OF A DRUM BOILER

SIDDIKOV ISAMIDDIN XAKIMOVICH<sup>1</sup>, UMURZAKOVA DILNOZA MAXAMADJONOVNA<sup>\*1</sup>  
AND BAKHRIEVA HURSHIDA ASKARXODJAEVNA<sup>2</sup>

<sup>1</sup>*Department of Information Processing Systems and Management,  
Tashkent State Technical University, 100097 Tashkent, Uzbekistan*

<sup>2</sup>*Department of Multimedia Technology, Tashkent University of Information Technologies,  
100200 Tashkent, Uzbekistan*

*\*Corresponding author: [umurzakovadilnoz@gmail.com](mailto:umurzakovadilnoz@gmail.com)*

*(Received: 13<sup>th</sup> August 2019; Accepted: 14<sup>th</sup> October 2019; Published on-line: 20<sup>th</sup> January 2020)*

**ABSTRACT:** The article discusses the creation of an adaptive system for managing dynamic objects based on neuro-fuzzy technology. This technology is used to actively identify and create temperature control algorithms for the superheated steam of a drum boiler in the presence of disturbances associated with a change in load. To solve this problem, the use of a fuzzy-logical controller is proposed. The rule base of this regulator is defined. A technique is proposed for determining the optimal number of neurons and the number of hidden layers. The neuro-fuzzy model of the controller is presented in the form of a multilayer neural network without feedback, which is characterized by a simple implementation in practice. The use of a fuzzy-logical controller gives the automatic control system the ability to maintain technological parameters at a given level in the presence of external disturbing influences, and also makes it possible to efficiently control the process.

**ABSTRAK:** Artikel ini membicarakan rekaan sistem penyesuaian bagi mengurus objek dinamik berdasarkan teknologi neura-kabur. Teknologi ini digunakan bagi mengenal pasti secara aktif dan mencipta algoritma kawalan suhu bagi stim melampau panas dalam drum dandang dengan kehadiran gangguan berkaitan perubahan beban. Bagi menyelesaikan masalah ini, penggunaan pengawal logik-kabur telah dicadangkan. Asas peraturan bagi pengaturan ini ditentukan. Satu teknik dicadangkan bagi mendapat bilangan optima neuron dan bilangan lapisan tersembunyi. Model neura-kabur pengawal ini dikemukakan dalam bentuk rangkaian neural berlapis tanpa suap balik, bercirikan praktik pelaksanaan mudah. Penggunaan pengawal logik-kabur memberi sistem kawalan automatik kebolehan mengekalkan parameter teknologi pada tahap tertentu dengan kehadiran pengaruh gangguan luar, dan juga memberi kebolehan proses kawalan yang cekap.

**KEYWORDS:** *fuzzy model; PID-controller; neural networks; drum boiler; controller; adaptive system; temperature; heat power industry*

## 1. INTRODUCTION

Currently, in most industrial facilities, including heat and power facilities for process control, PID controllers have found wide application. About 90-95 % of the regulators currently in operation use the PID algorithm. The reasons for such popularity are their

simplicity of construction, clarity of operation, suitability for most practical tasks, and low costs.

In existing thermal power facilities, a typical cascade system for superheated steam temperature control is used, which includes the control circuit of the proportional-integral (PI) regulator and the additional measurement loop of the auxiliary controlled variable formed in the signal conditioning unit.

Analysis of the operating characteristics of the superheater shows that the control object has a variable transport lag, its dynamic properties substantially depend on the oxygen content in the outgoing gases, contamination of heating surfaces, and regime factors - load, type, and grade of fuel burned, condition of heating surfaces, excess air, etc. [2]. In addition, obtaining a mathematical model of superheated steam temperature is usually associated with approximation of acceleration curves obtained experimentally, as a result of which the mathematical description becomes a priori inaccurate.

The study of scientific publications in the field of adaptive ARS (Automatic Control Systems) in dynamic systems [1,2] led to the conclusion that traditional methods of active identification and associated algorithms for calculating optimal settings for PI and PID controllers that analyse the complex frequency response of objects or the self-oscillation mode are widely used. It should be noted that for the considered ACS of the temperature of the steam, the self-oscillation process is unacceptable due to the requirements of the technological regulations, since a deviation of the steam temperature from the norm can lead to premature wear of the turbine equipment. Thus, the scientific problem arises of finding the optimal methods for identifying an object in cases of changes in its load and algorithms for calculating PI controller settings to ensure the expected transition process (by overshoot  $G < 30\%$ , attenuation degree, with minimum control time  $T_r$ ) [1,2].

The use of PID-law in power engineering leads to an increase in the quality of regulation. With regard to the ACS of the steam temperature, the use of the PID-law of regulation allows maintaining temperature fluctuations more accurately in the whole steam output range of the boiler unit, which is a top priority. The use of the PID algorithm is limited by the complexity of its setup. This is due to the peculiarity of ACS operation with PID controllers: high sensitivity to deviation of their optimum settings and the impossibility of applying the step method for obtaining the type of transient process.

A disadvantage of the known methods of setting the parameters of the PID controller is the incomplete information about the system stability margin and robustness. Safety margin and robustness determines the reliability of the regulator. To consider these factors, an analysis is needed to change the dynamics of the control object and, in this case, obtain a transient response of the control object, model the control object taking into account the range of changes in dynamic characteristics, and go to settings that are close to optimal and do not need significant additional tuning.

The algorithms of operation of automated control systems developed at the design stage, as a rule, differ significantly from the optimal values of the parameters of traditional regulators. This is due to the imperfection of mathematical models of objects. It is known that obtaining mathematical models of experimental control systems for operating complex objects is a difficult task. These difficulties are associated with the influence of external and parametric perturbations, some of which are non-stationary in nature and are not subject to control [3].

In this regard, it is necessary to use adaptive intelligent control systems for complex multi-mode dynamic objects, which include drum boilers, using neuro-fuzzy technology

and the necessary measure to improve the efficiency of production management in general.

## 2. RESEARCH METHODS

Currently, scientific approaches associated with the use of intelligent systems [5, 6], based on the hybrid application of neural regulators and neural networks, have become widely popular in the theory of adaptive control, which prompted the emergence of a new scientific direction - hybrid, or neuro-fuzzy networks (HN, NFN) [4]. Consideration of this technology in relation to the identification and adaptation of the ACS of the temperature of superheated steam is an important scientific task.

The control parameters of the fuzzy PID controller include fuzzy parameters, fuzzy inference rules, and the resolution of the parameters of the fuzzy PID controller. Based on the setup input and the feedback signal, the computer calculates the deviation and the current change in the deviation of the actual position and the theoretical position. It then processes the fuzzy reasoning according to a fuzzy rule. Finally, the fuzzy parameters were processed by a fuzzy solution and output a proportional (P), integral (I), and differential (D) coefficients of the PID controller.

As an object of regulation, we consider the automatic control system (ACS) of the temperature of the superheated steam of a drum boiler [1, 2]. The task of controlling the superheater was to provide a predetermined temperature in the steam path of the boiler. The steam temperature is changed by increasing or decreasing the amount of water injected into the superheater to stabilize the set value of the steam temperature at the superheater outlet.

To solve this problem, we will use intelligent control methods, in particular, the fuzzy logic method. This allows synthesis of process control systems in the class of neural network systems.

The task is then to stabilize the controlled variable with a given quality of the transition process with incomplete information about the control object and to obtain invariance properties to external disturbing influences of the automatic control system.

To solve the problem, it is necessary to [3]:

1. Describe the control object and define its input and output parameters and disturbing influences.
2. Choose the fuzzy inference algorithm that most fully determines the decisions made under the given conditions of the process.
3. Synthesise a fuzzy controller, which is an integral part of an intelligent controller and provides the required qualitative and quantitative indicators of temperature control in the presence of disturbing influences.
4. Investigate the obtained response surfaces of a fuzzy regulator under the conditions of the presence of disturbing influences and a pure delay characterizing the technological process.

As a control object (Fig. 1), we consider a superheater with a thermocouple. The transfer function obtained as a result of processing a family of acceleration curves [6], we write in explicit form as follows:

$$W_{FM}(s) = \frac{y(s)}{v(s)} = \frac{K \cdot e^{-s\tau}}{a_3 \cdot s^3 + a_2 \cdot s^2 + a_1 \cdot s + 1} \cdot \frac{m_{ChCT}}{T_{ChCT} \cdot + 1} \quad (1)$$

where  $s$  is a complex variable;  $y(s)$  and  $v(s)$  - images of scalar functions of output and input of an object;  $K$  - injection ratio;  $\tau$  - transport delay;  $a_1, a_2, a_3$  - parameters of the characteristic equation of the function;  $W_{FM}(s)$ ;  $T_{ChCT} = const$  and  $m_{ChCT} = const$  - time constant and static coefficient of a chromel-copel thermocouple.

Based on the technological regulations for a particular superheater, the interval of change of parameters is represented by the following relations:

$$\begin{aligned} 2.8 = K^{(-)} \leq K \leq K^{(+)} = 4.6, \quad 45 = \tau^{(-)} \leq \tau \leq \tau^{(+)} = 141, \\ 15 = T_{ChCT}^{(-)} \leq T_{ChCT} \leq T_{ChCT}^{(+)} = 20, \quad 244 = a_1^{(-)} \leq a_1 \leq a_1^{(+)} = 393, \\ 20160 = a_2^{(-)} \leq a_2 \leq a_2^{(+)} = 61920, \quad 345600 = a_3^{(-)} \leq a_3 \leq a_3^{(+)} = 3909600 \\ \xi = col(K, h, T_{ChCT}, a_1, a_2, a_3) \in \Xi, \end{aligned} \quad (2)$$

where the superscripts  $(-)$  and  $(+)$  - are the values of the boundaries of the coefficients that determine the known set  $\Xi$ ;  $\xi \in \Xi$  - vector of unknown parameters.

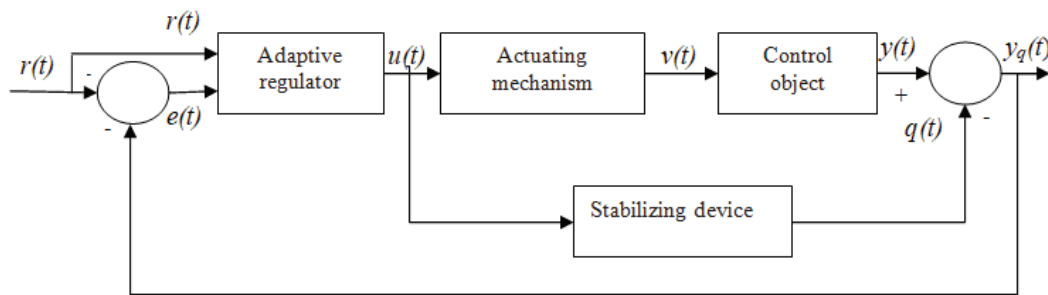


Fig. 1: The main circuit control temperature superheater.

The transfer function of the actuator (which moves the regulating body of the control object - the valve), taking into account its inertia with respect to the object, will be described as

$$W_{CA}(s) = \frac{v(s)}{u(s)} = \frac{1}{T_{CA} \cdot s}, \quad (3)$$

where  $T_{CA} = const$  is the time constant of the actuator.

The structure of the adaptive controller, taking into account the neuron, is given in the form

$$u(s) = \frac{K_2 \cdot s}{T_0 \cdot s + 1} \cdot g(s); \quad (4)$$

$$g(t) = \wp(t) \cdot r(t); \quad (5)$$

$$\wp(t) = f(e(t), r^*) = \frac{1}{1 + e^{\alpha \cdot (w \cdot e(t) + w_0)}};$$

$$r(t) = r^* = \text{const}; \tag{6}$$

$$e(t) = r^* - y_q(t) = r^* - y(t) - q(t),$$

where  $K_2$  and  $T_0$  - the transmission coefficient and the time constant of the linear part of the adaptive controller;  $u(s)$  - control action;  $g(t)$  - the output of the nonlinear part of the adaptive controller represented by a single neuron with a sigmoid activation function  $\wp(t)$  and weighting coefficients  $w$  and  $w_0$ . The input of the neuron is a generalized regulation error  $e(t)$ ;  $r(t)$  - setting effect equal to the value  $r^*$  in the stabilization mode;  $y_q(t)$  - generalized output control system of the form  $y_q(t) = y(t) + q(t)$ .

The proposed system differs in that, in the control circuit, there is a single fuzzy-logic controller (FLC) with two inputs and one output. The fuzzy controller is assigned the task of generating a control action in the range of variation of the dynamic regulation error and it is integral with respect to its threshold values. Therefore, when synthesizing a fuzzy controller, we use the Mamdani output algorithm [4] as the simplest one. Although the Mamdani algorithm is recommended for use in other areas (expert systems and decision-making systems), it can work effectively in the development of fuzzy process control systems.

As you know, a fuzzy controller consists of three main blocks: the fuzzification block, the fuzzy output block and the defuzzification block. In the first block, it is necessary to fuzz the input signals, i.e. translate well-defined signals into fuzzy form. To do this, we first determine the number of fuzzy statements for each input signal, which will be operated by the FLC knowledge base and is a meaningful component of the fuzzy output block. To fill an initially empty knowledge base, you must define a management goal.

In this case, the goal of control is to maintain the technological parameter in a given range of deviations from the desired value in the event of controlled and uncontrolled disturbances. In this case, the more the deviation of the technological parameter from the threshold value increases, the greater should be the increment that changes the coefficient of transfer of the regulator.

FLC has two input signals:

$$e_1 = (\text{"error"}, A_{e1}, [e_1^{\min}; e_1^{\max}]);$$

$$e_2 = (\text{"integral error"}, A_{e2}, [e_2^{\min}; e_2^{\max}]).$$

For the  $e_1$  signal, we write the following statements:

' $NB_{e1}$ ' - «Deviation of steam temperature is negatively large»;

' $NM_{e1}$ ' - «Deviation of steam temperature is negatively average»;

' $NS_{e1}$ ' - «Deviation of steam temperature is negatively small»;

' $ZE_{e1}$ ' - «Deviation of steam temperature near zero»;

' $PS_{e1}$ ' - «The deviation of the temperature of the steam is positively small»;

' $PM_{e1}$ ' - «Temperature deviation of steam is positively average»;

' $PB_{e1}$ ' – «Deviation of steam temperature is positively large.»;

Then the term - sets of the linguistic variable “Error” can be defined as:

$$A_{e1} = \{NB_{e1}, NM_{e1}, NS_{e1}, ZE_{e1}, PS_{e1}, PM_{e1}, PB_{e1}\}.$$

In the same way we will define a term - a set of the linguistic variable “Integral. Error” as:

$$A_{e2} = \{NB_{e2}, NM_{e2}, NS_{e2}, ZE_{e2}, PS_{e2}, PM_{e2}, PB_{e2}\}.$$

If we consider that FLC has an output signal  $u = Fuzzy(e_1, e_2)$ , then its output linguistic variable can be represented as:

$$u = ("Control", A_u, [u^{\min}; u^{\max}]),$$

where  $A_u = \{NB_u, NM_u, NS_u, ZE_u, PS_u, PM_u, PB_u\}$ ;

' $NB_u$ ' – «Water consumption is negatively large»;

' $NM_u$ ' – «Water consumption is negative average»;

' $NS_u$ ' – «Negatively low water consumption»;

' $ZE_u$ ' – «Water flow around zero»;

' $PS_u$ ' – «Positively low water flow»;

' $PM_u$ ' – «Water consumption is positively average»;

' $PB_u$ ' – «Positively large water flow».

Operating with the received input and linguistic variables, the goal of management will build a knowledge base for the fuzzy logic controller (Table 1).

Choosing linguistic variables and making up the knowledge base of FLC, you can proceed to the phase of fuzzification, the purpose of which is to establish the correspondence between the specific values of individual input and output variables of the fuzzy logic controller and the values of the membership functions of the corresponding thermal linguistic variables. At the end of this stage, the specific values of the membership functions for each of the linguistic terms should be defined. Table 1 applies to all linguistic variables.

Table 1: Values of membership functions for all linguistic variables

$e_1$	$e_2$								
	$NB_{e1}$	$NM_{e1}$	$NS_{e1}$	$ZE_{e1}$	$PS_{e1}$	$PM_{e1}$	$PB_{e1}$	$NB_{e1}$	$NM_{e1}$
$NB_{e1}$	$NB_u$	$NB_u$	$NB_u$	$NB_u$	$NM_u$	$NS_u$	$ZE_u$	$NB_u$	$NB_u$
$NM_{e1}$	$NB_u$	$NB_u$	$NB_u$	$NM_u$	$NS_u$	$ZE_u$	$PS_u$	$NB_u$	$NB_u$
$NS_{e1}$	$NB_u$	$NB_u$	$NM_u$	$NS_u$	$ZE_u$	$PS_u$	$PM_u$	$NB_u$	$NB_u$
$ZE_{e1}$	$NB_u$	$NM_u$	$NS_u$	$ZE_u$	$PS_u$	$PM_u$	$PB_u$	$NB_u$	$NM_u$
$PS_{e1}$	$NM_u$	$NS_u$	$ZE_u$	$PS_u$	$PM_u$	$PB_u$	$PB_u$	$NM_u$	$NS_u$
$PM_{e1}$	$NS_u$	$ZE_u$	$PS_u$	$PM_u$	$PB_u$	$PB_u$	$PB_u$	$NS_u$	$ZE_u$





$$u = \left[ \int_{\min}^{\max} \tilde{u} \mu(\tilde{u}) d\tilde{u} \right] / \left[ \int_{\min}^{\max} \mu(\tilde{u}) d\tilde{u} \right]. \quad (11)$$

To determine the tuning values of the neuron weighting coefficients, we perform the following procedure, let's set the mode of the system stabilization process described by the equations:

$$y_{q^*} = K_2 \cdot K \cdot m_{ChCT} \cdot T_{CA}^{-1} \cdot g^*, \quad (12)$$

$$g^* = \wp_0 \cdot r^*, \quad (13)$$

$$\wp_0 = f(e^*, r^*, \infty), \quad q^* = 0, \quad e^* = r^* - y_{q^*} = r^* - y^* = 0, \quad (14)$$

Where index \* is the designation of the steady-state values of the corresponding variables. Equations (12) - (14) can be combined and represented identically as an expression

$$y_{q^*} = K_2 \cdot K \cdot m_{ChCT} \cdot T_{CA}^{-1} \cdot \wp_0 \cdot r^*, \quad (15)$$

Which is often called the implicit reference model equation. In particular, from (15) it follows, taking into account the equality  $y_{q^*} = r^*$ , that the value  $\wp_0 = const$  always exists and is determined by the expression

$$\wp_0 = \frac{T_{CA}}{K_2 \cdot K \cdot m_{ChCT}}. \quad (16)$$

The adaptive fuzzy-logic controller is configured using the weighting coefficients of artificial neural networks, using the back-propagation error algorithm.

In this case, the output signal  $\wp(\tau)$  of the neuron  $\tau$ -th time is defined as ( $\tau = 1, 2, \dots$ )

$$\wp(\tau) = f(\sigma(\tau)) = \frac{1}{1 + e^{-\alpha\sigma(\tau)}}, \quad (17)$$

where

$$\sigma(\tau) = w_0 + w(\tau) \cdot e(\tau). \quad (18)$$

Thus we get a lot of output signals

$$\wp_1(\tau_1), \dots, \wp_i(\tau_i), \dots, \wp_n(\tau_n), \quad (19)$$

$$E(\tau) = \frac{1}{2} [\varepsilon(\tau)]^2 = \frac{1}{2} [\wp_0 - \wp(\tau)]^2. \quad (20)$$

which is subject to the condition  $\lim_{t \rightarrow \infty} y(t) = y^* = r^* = const$ , corresponds to the reference value of the output signal  $\wp_0 = const$ , i.e.  $\lim_{n \rightarrow \infty} \wp_n(\tau_n) = \wp_0 = const$ .

In our case, the reference output will be (16), and the reference input will be  $e^* = 0$ .

We formulate a measure of error, based on a comparison of signals (16) and (19), we define the half-sum of the squares of the differences

For the correction of the weighting coefficient  $w$ , we will use the method of fastest descent, which is the most simple to implement.

$$w(\tau + 1) = w(\tau) + y \frac{dE(\tau)}{dw(\tau)}, \quad (21)$$

where  $y > 0$  determines the size of the correction step. Here, it is necessary to take into account that

$$\frac{dE(\tau)}{dw(\tau)} = \frac{dE(\tau)d\sigma(\tau)}{d\sigma(\tau)dw(\tau)} = \frac{dE(\tau)}{d\sigma(\tau)} e(\tau). \quad (22)$$

Enter the designation

$$\delta(\tau) = \frac{dE(\tau)}{d\sigma(\tau)}, \quad (23)$$

get the algorithm for calculating the correction weights in the form

$$w(\tau + 1) = w(\tau) + y\delta(\tau)e(\tau). \quad (24)$$

Here  $\delta(\tau)$  is calculated by the formula:

$$\begin{aligned} \delta(\tau) &= \frac{dE(\tau)}{d\sigma(\tau)} = \frac{1}{2} \frac{d}{d\sigma(\tau)} ([\varepsilon(\tau)]^2) = \frac{1}{2} \frac{d}{d\sigma(\tau)} ([\varphi_0 - \varphi(\tau)]^2) = \\ &= -(\varphi_0 - \varphi(\tau)) f'_\sigma(\sigma(\tau)) = -(\varphi_0 - \varphi(\tau))(1 - \varphi(\tau))\varphi(\tau). \end{aligned} \quad (25)$$

Taking into account (25), the algorithm for setting the weights of the neurons is as follows:

$$w_0(\tau + 1) = w(\tau) - y(\varphi_0 - \varphi(\tau))(1 - \varphi(\tau))\varphi(\tau)e(\tau) \quad (26)$$

$$w_0(\tau + 1) = w_0(\tau) - y(\varphi_0 - \varphi(\tau))(1 - \varphi(\tau))\varphi(\tau). \quad (27)$$

Finally, taking into account (16), we obtain:

$$w(\tau + 1) = w(\tau) - y \left( \frac{T_{CA}}{K_2 \cdot K \cdot m_{chCT}} - \varphi(\tau) \right) (1 - \varphi(\tau))\varphi(\tau)e(\tau), \quad (28)$$

$$w_0(\tau + 1) = w_0(\tau) - y \left( \frac{T_{CA}}{K_2 \cdot K \cdot m_{chCT}} - \varphi(\tau) \right) (1 - \varphi(\tau))\varphi(\tau). \quad (29)$$

On the basis of the developed regulatory system, a simulation model was formalized and a computational experiment was performed in Matlab [4,7].

### 3. RESULTS AND DISCUSSION

Analysis of transients (Fig. 1) showed that with the influence of a parametric perturbation, the hybrid system has a shorter regulation time ( $T_{r1} = 138$  s) compared to traditional adaptive ACS ( $T_{r2} = 163$  s), as well as overshoot hybrid ACS  $G_{tr} = 28\%$  traditional  $G_{tr} = 50\%$ , the degree of attenuation of the hybrid  $\psi^{Tr} = 0,91$ , traditional  $\psi^{Tp} = 0,68$ , i.e. the proposed hybrid ACS is optimal and energy efficient.

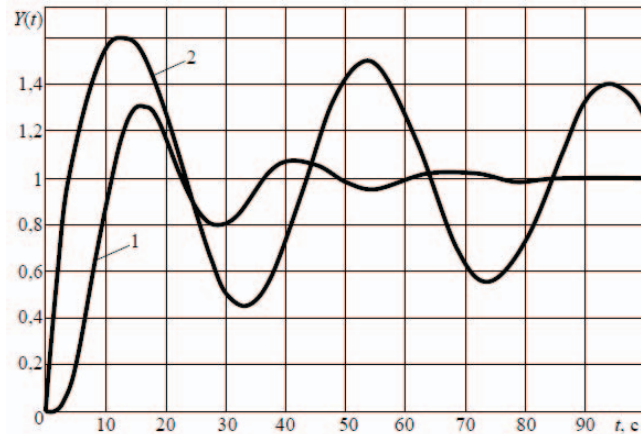


Fig. 2: Transient processes along the control channel: 1-neuro-fuzzy ACS (at nominal load), 2 - neuro-transparent ACS (when the load changes).

#### 4. CONCLUSION

Based on the obtained results, it can be concluded that the proposed intelligent adaptive ACS temperature of superheated steam has the following advantages:

- the speed of the process of finding the optimal settings of the PI controller of the cascade ACS with the possibility of approximation and extrapolation;
- smaller first deviation and time of the transition process regulation;
- the possibility of optimal functioning of the cascade ACS in all modes of the steam drum boiler;
- the use of adaptive fuzzy-logic allows you to provide a fairly good quality control of the temperature of superheated steam.
- the possibility of using adaptation of various ACS of TP, ACS with PD, and PID regulators in the heat supply in the processes of adaptation.

The results of the study showed that during the control of the temperature regime of the boiler unit, a developed adaptive system of fuzzy PID regulators has a faster response, higher regulatory accuracy, and the best functioning in stationary mode. It should be noted that when using an adaptive fuzzy PID regulator, the reconstitution is reduced by 20%, the control time of 35 seconds, degree attentiveness increased by 0.23, and the control regulation decreased by 15%, the dynamic characteristic of the adaptive control system with a fuzzy PID controller is improved.

The performance of the control system of adaptive fuzzy system with PID by a regulator is much better than the digital PID controller and more energy-efficient.

#### REFERENCES

- [1] O'Dwyer A. (2009) Handbook of PI and PID Controller Tuning Rules. 3rd Edition. Dublin: Institute of Technology; Ireland, Imperial College Press. 529 p.
- [2] Astrom KJ. (2006) Advanced PID control/ K. J. Astrom, T. Hagglund – ISA (The instrumentation, Systems, and Automation Society), - 460 p.
- [3] Demchenko VA. (2001) Automation and modeling of technological processes at nuclear power plants and thermal power plants / V. A. Demchenko. - Odessa: Astroprint. - 308 p.

- 
- [4] Kim T, Maruta I, Sugie T. (2008) Robust PID controller tuning based on the constrained particle swarm optimization, *Automatica*, 44(4): 1104-1110.
  - [5] Lu C, Hsu C, Juang C. (2013) Coordinated control of flexible AC transmission system devices using an evolutionary fuzzy lead-lag controller with advanced continuous ant colony optimization, *IEEE Transactions on Power Systems*, 28(1): 385-392.
  - [6] Pelusi D. (2012) PID and intelligent controllers for optimal timing performances of industrial actuators, *International Journal of Simulation: Systems, Science and Technology*, 13(2): 65-71.
  - [7] Pelusi D, Mascella R. (2013) Optimal control algorithms for second order systems, *Journal of Computer Science*, 9(2): 183-197.
  - [8] Pletnev GP. (2007) *Automation of Technological Processes and Productions in Heat and Power Engineering*. 4th Edition. Moscow: Publishing House Moscow Power Engineering Institute. -352 p.
  - [9] Rotach VY. (2008) *The Theory of Automatic Control*. Moscow: Publishing House Moscow Power Engineering Institute. - 396 p.
  - [10] Siddikov IX, Iskandarov Z. (2018) Synthesis of adaptive-fuzzy control system of dynamic in conditions of uncertainty of information // *International Journal of Advanced Research in Science, Engineering and Technology*, 5(1): 5089-5093.
  - [11] Siddikov IX, Umurzakova DM. (2019) Features of automatic control of technological parameters of water level in the drum steam boilers, *Journal of Southwest Jiaotong University*, 54(3): 1-10. DOI: 10.35741/issn.0258-2724.54.3.1.
  - [12] Siddikov IX, Umurzakova DM. (2019) Mathematical Modeling of Transient Processes of the Automatic Control System of Water Level in the Steam Generator, *Universal Journal of Mechanical Engineering*, 7(4): 139-146. DOI: 10.13189/ujme.2019.070401.
  - [13] Sidikov IX, Umurzakova DM. (2019) Adaptive neuro-fuzzy regulating system of the temperature mode of the drum boiler // *International Journal of Advanced Research in Science, Engineering and Technology*, 6(1): 7869-7872.
  - [14] Soroko EM, Golden Sections. (2006) *Processes of Self-Organizing and Evolution in Systems: Introduction into the General Theory of System Harmonizing*. Moscow: KomKniga. -264 p.

## MECHANICAL PROPERTIES, MORPHOLOGY, AND HYDROLYTIC DEGRADATION BEHAVIOR OF POLYLACTIC ACID / THERMOPLASTIC POLYURETHANE BLENDS

YOSE FACHMI BUYS<sup>1,2\*</sup>, MIMI SYAKINA AHMAD<sup>1</sup>, HAZLEEN ANUAR<sup>1</sup>, MUDRIKAH  
SOFIA MAHMUD<sup>1</sup>, NUR AIMI MOHD NASIR<sup>1</sup>

<sup>1</sup>Department of Manufacturing and Materials Engineering, International Islamic University  
Malaysia, Kuala Lumpur, Malaysia

<sup>2</sup>Department of Mechanical Engineering, University of Malaya, Kuala Lumpur, Malaysia

\*Corresponding author: yose@um.edu.my

(Received: 30<sup>th</sup> December 2018; Accepted: 28<sup>th</sup> August 2019; Published on-line: 20<sup>th</sup> January 2020)

**ABSTRACT:** Polylactic acid (PLA) has attracted tremendous interest to be utilized as the replacement for petroleum-based polymers as it possesses good biodegradability, can be derived from renewable sources, and shows high mechanical strength. However, its inherent brittleness and low toughness has limited its usage in broader applications. In this work, PLA was melt blended with tough thermoplastic polyurethanes (TPU) in order to produce eco-friendly polymeric materials with balanced mechanical properties. Moreover, the miscibility and the hydrolytic degradation behaviour of PLA/TPU blends were also investigated as it is important to control material degradation behaviour in some applications. Five compositions of specimens, i.e. neat PLA, PLA/TPU 75/25 vol%, PLA/TPU 50/50 vol%, PLA/TPU 25/75 vol%, and neat TPU, were prepared by melt blending PLA with TPU using an internal mixer, followed by compression moulding. Tensile and impact tests were performed to evaluate the mechanical properties. From the tests, it was apparent that the elongation-at-break and impact strength of the blends increased as the TPU content increased. Dynamic Mechanical Analysis (DMA) and Scanning Electron Microscopy (SEM) observation were conducted to evaluate the miscibility of PLA/TPU blends. DMA results of the blends revealed two tangent delta peaks, indicating that the blends were immiscible, and the SEM micrographs supported this trend. Finally, hydrolytic degradation behaviour of PLA, TPU and PLA/TPU blends was investigated by measuring the weight loss after immersion of the specimens in alkaline solution at a predetermined time, i.e. every 24 hours for up to 8 days. It was found that the degradation behaviour is affected by blend composition, where PLA/TPU 50/50 vol% showed the fastest degradation rate. This result might be ascribed to the co-continuous morphology shown in the PLA/TPU blend 50/50 vol%.

**ABSTRAK:** Polilaktik asid (PLA) telah menarik banyak minat untuk digunakan sebagai pengganti polimer berasaskan petroleum, kerana ia mempunyai biodegradabiliti yang baik, boleh diperolehi daripada sumber yang boleh diperbaharui, dan mempunyai kekuatan mekanikal yang tinggi. Walau bagaimanapun, kerapuhan dan ketiutannya yang rendah telah menghadkan penggunaannya dalam aplikasi yang lebih luas. Dalam kajian ini, leburan PLA dicampurkan dengan poliuretan termoplastik (TPU) bagi menghasilkan bahan polimer yang mesra alam beserta dengan sifat-sifat mekanikal yang seimbang. Selain itu, daya kebolehcampuran dan degradasi hidrolitik daripada campuran PLA/ TPU juga telah dikaji kerana bagi sesetengah aplikasi, faktor degradasi adalah sangat penting. Bagi menghasilkan lima komposisi sampel, iaitu PLA tulen, PLA/TPU 75/25 vol%, PLA/TPU 50/50 vol%,

PLA/TPU 25/75 vol%, dan TPU tulen, PLA dan TPU telah dicairkan dan diadun menggunakan mesin pencampur internal, diikuti dengan kaedah pengacuan kompresi. Untuk mengkaji sifat-sifat mekanikal, ujian regangan dan impak telah dijalankan. Hasil ujian tersebut menunjukkan peningkatan nilai pemanjangan pada titik putus dan kekuatan impak, seiring dengan peningkatan komposisi TPU. Manakala, penilaian daya kebolehcampuran diantara PLA dan TPU dijalankan menggunakan analisis mekanikal dinamik (DMA) dan mikroskop pengimbas elektron (SEM). Keputusan DMA, hasil daripada campuran tersebut mendedahkan dua puncak tangen delta, menunjukkan bahawa dua campuran tersebut tidak memiliki daya bolehcampur yang baik. Kesimpulan ini disokong pula oleh gambar mikro dari hasil ujian SEM. Akhir sekali, degradasi hidrolitik PLA, TPU dan campuran PLA/TPU dikaji melalui pengukuran berat sampel setelah direndam di dalam larutan alkali pada masa yang ditetapkan, iaitu setiap 24 jam sehingga 8 hari. Hasil daripada ujian tersebut mendapati degradasi hidrolitik dipengaruhi oleh komposisi campuran. Campuran PLA/TPU dengan komposisi 50/50 vol% menunjukkan kadar penurunan berat yang paling cepat. Hasil ujian ini mungkin boleh dikaitkan dengan sifat morfologi co-continuous yang ditunjukkan dalam campuran PLA/TPU 50/50 vol%.

**KEY WORDS:** *Polylactic Acid, Thermoplastic Polyurethane, Polymer Blends, Mechanical Properties, and Hydrolytic Degradation.*

## 1. INTRODUCTION

The interest in using degradable polymeric materials derived from renewable resources has been increasing day by day due to intensified environmental awareness from society and concerns about the depletion of petrochemical based plastics. Among other alternatives, polylactic acid (PLA), seems to be a polymer of choice due to its numerous advantages, such as biodegradability, compostability, recyclability, ability to be produced from renewable resources, as well as possessing good mechanical strength and stiffness. However, PLA's inherent brittleness, indicated by low values of elongation at break and impact strength, has limited its usage in broader applications [1-2], such as the applications that need plastic deformation at higher stress levels (e.g., screws and fracture fixation plates) [3]. One of the techniques to overcome the brittleness of PLA is by blending with other elastomeric polymers, such as thermoplastic polyurethane (TPU). Several recent reports have highlighted the mechanical properties of PLA/TPU blends, where it has been reported that TPU addition into PLA increased the elongation at break of the blends, hence improving the brittle nature of PLA [4-9].

On the other hand, in real applications, in addition to mechanical properties it is also important to investigate the degradation behaviour of materials. Polymer-based products are required to degrade in a controlled manner [10]. There are instances where materials in the products need to degrade in relatively short time after being used [11], such as food and toiletries packaging materials in composting environments [10]. There are also cases where materials must have low and controllable degradation rates, especially in biomaterials applications, such as in bone implants or drug release applications [11]. From the previous reports highlighting properties of PLA/TPU blends [4-9, 12-13], only a few focused on degradation behaviour of the blends [12-13], and to the best of our knowledge, there have been no reports to date discussing hydrolytic degradation behaviour of the blends. Therefore, in this work, PLA/TPU blends were produced, and the mechanical properties, miscibility, as well as hydrolytic degradation behaviour of the blends were investigated.

## **2. EXPERIMENTAL**

### **2.1. Materials**

PLA used in this work was 3051D from NatureWorks LLC, with density of 1.25 g/cm<sup>3</sup> and melt flow index of 10-25 g/10 min. While the TPU used was Desmopan 8785A from Bayer Material Science with density of 1.20 g/cm<sup>3</sup>.

### **2.2. Sample Preparation**

Prior to mixing, PLA and TPU were dried in an oven at 60°C for at least 10 h, in order to remove moisture. PLA was melt blended with TPU using a Haake internal mixer with a 50 cm<sup>3</sup> cell at 200°C, mixing speed of 50 rpm for 15 min. The blend ratios of PLA/TPU were 75/25, 50/50, and 25/75 vol%. For further characterization, the blends were then compression moulded using an XH-406B Tablet Press machine at 200°C with 5 min preheating time and 5 min pressing time under 15 MPa pressure. Neat PLA and TPU specimens were also produced by directly pressing the respective pellets.

### **2.3. Mechanical Properties Characterization**

A tensile strength test was conducted to determine the Young's modulus, tensile strength, and elongation at break of the specimens. It was performed according to ASTM D638 standard, using a universal testing machine model AGS-X (Shimadzu Corp.) with 5 mm/min strain rate. Meanwhile, the impact strength of the specimens was evaluated using a notched Charpy method, according to ASTM D256 standard. The test was carried out by Dynisco Polymer Test Advance Pendulum Impact, using a 7.5 J hammer.

### **2.4. Miscibility and Morphology Evaluation**

Dynamic Mechanical Analysis (DMA) measurement was performed to study the miscibility of the PLA/TPU blend. The measurement was carried out using a Pyris Diamond DMA (Perkin Elmer) with single cantilever using 3-points bending mode over the temperature range of -100 to 160°C at a heating rate of 5°C/min and a frequency of 1Hz. Meanwhile, in order to investigate the phase morphology of PLA/TPU blend, Scanning Electron Microscopy (SEM) observation was performed at room temperature using an InTouch Scope JSM-IT100 (Jeol) on the fractured surface of the specimen. Before being inserted into the observation chamber, the sample was coated with palladium in order to make the surface conductive.

### **2.5. Hydrolytic Degradation Test**

Alkaline hydrolytic degradation test was performed by immersing the specimens with 10 mm × 10 mm × 1 mm dimension in 10 ml of 1 M NaOH aqueous solution of pH 12 at 30°C for a predetermined period of time. To obtain the initial weight of samples before degradation, all the specimens were dried in an oven with 50°C for 6 hours. After hydrolyses, specimens were washed in distilled water at room temperature, followed by a few hours drying at room temperature, before being dried in the oven at 50°C for 2 days. The final weight after drying was measured to determine the weight loss. Similar procedures were conducted by other researchers in previous papers [14-16]. During the degradation test, a digital camera was also used to record the physical change of specimens after a predetermined period of degradation time.



### 3. RESULTS AND DISCUSSION

#### 3.1. Mechanical Properties

Fig. 1 shows the stress vs. strain graph of the PLA, TPU and PLA/TPU blends, and the values of Young's modulus, tensile strength, and elongation at break is tabulated in Table 1. From Fig. 1 and Table 1, it is apparent that neat PLA is a brittle material with only less than 3% elongation at break, similar with the works had been reported by others [3, 6]. It is also obvious that addition of TPU to PLA brought the blends into more flexible materials, indicated by the increase of elongation at break. Significant increase in elongation at break was observed in PLA/TPU 25/75 specimen that elongated more than 240% before break. However, addition of TPU also brought on a decrease of Young's modulus and tensile strength. Similar trends of increase in elongation at break and decrease in Young's modulus and tensile strength of PLA/TPU blends as the amount of TPU increased had also been reported in other works [4-9]. Therefore, by adjusting the blend composition, one may obtain PLA/TPU based materials with desirable mechanical properties.

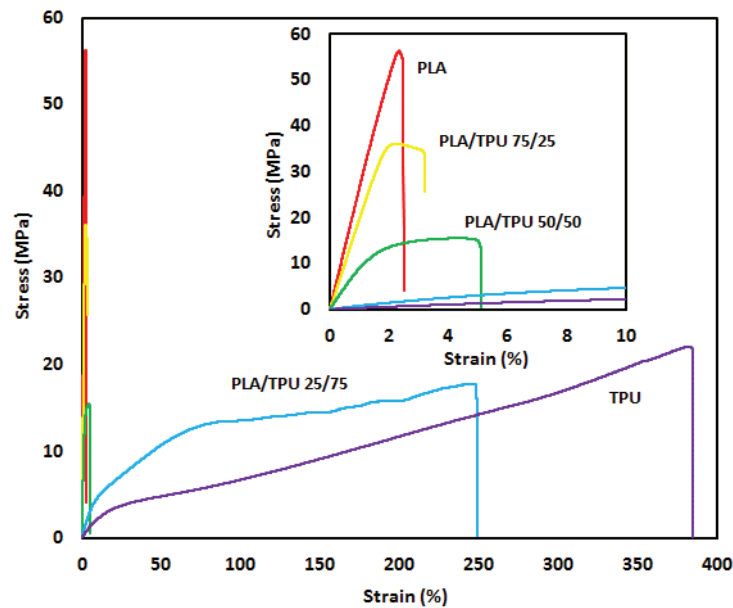


Fig. 1. Stress vs strain curves of PLA, TPU and PLA/TPU blends

Table 1: Young's modulus, tensile strength and elongation at break values of PLA, TPU and PLA/TPU blend

Samples	Young's Modulus (MPa)	Tensile Strength (MPa)	Elongation at break (%)
PLA	2749.52	56.30	2.49
PLA/TPU 75/25	1871.64	36.13	3.21
PLA/TPU 50/50	989.07	22.47	5.11
PLA/TPU 25/75	69.93	17.74	248.62
TPU	24.873	22.03	384.63

Impact strength of PLA, TPU and PLA/TPU blends is shown in Fig. 2. From this figure, it is clear that the addition of TPU increased the toughness of PLA. The elastomeric nature of TPU improved the crack propagation resistance of PLA/TPU blends. It is also interesting to note that drastic increase in impact strength was observed starting from the addition of 50% TPU. It is believed that this drastic change of impact strength correlates with the morphology development of the blends, which is described in the next section.

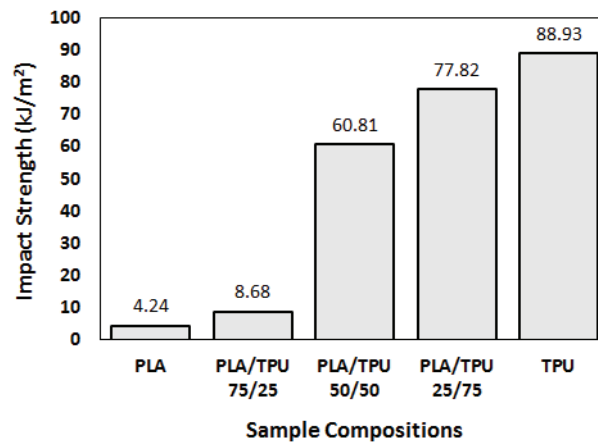


Fig. 2. Impact strength of PLA, TPU and PLA/TPU blends

### 3.2. Miscibility and Morphology

DMA is an excellent tool to characterize the miscibility of polymer blends, due to its sensitivity to detect the glass transition temperature ( $T_g$ ) of the specimens. Fig. 3 shows the tangent delta curves of PLA, TPU and PLA/TPU blends obtained from DMA measurement. The peak of tangent delta in DMA represents the  $T_g$  of the specimens. It is apparent that the neat PLA and the neat TPU used in this work showed the  $T_g$  around 62°C and -25°C, respectively. While it is interesting to note that all PLA/TPU blends showed two tangent delta peaks, i.e. the peaks in the region of -40°C until -25°C, which correlated to the glass transition temperature ( $T_g$ ) of TPU part in the blends, and those in the region of 60°C until 65°C, which correlated to the  $T_g$  of PLA part in the blends. The existence of two  $T_g$ s indicates the immiscibility of PLA and TPU in PLA/TPU blends.

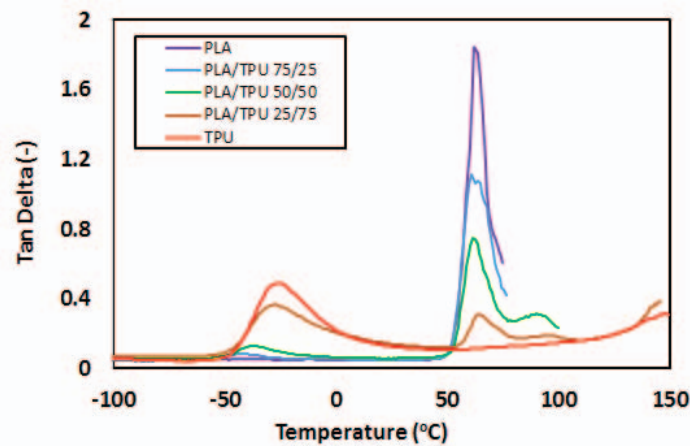


Fig. 3. Tangent delta of PLA, TPU, and PLA/TPU blends

SEM micrographs of neat PLA, PLA/TPU blends, and neat TPU are shown in Fig. 4. While a single phase is observed in the micrographs of pristine PLA as well as in that of pristine TPU, two different phases are observed in the micrographs of PLA/TPU blends, supporting the immiscibility trend of the blends, as indicated by the DMA result. The micrographs of PLA/TPU 75/25 and PLA/TPU 25/75 show many “droplet like” phases, suggesting these two compositions exhibited “sea-island” morphology. Considering the amount of the droplets were less than the main phase, it is reasonable to deduce that the droplets, or the “island” phase in PLA/TPU 75/25 was the TPU, and droplets or the island phase in PLA/TPU 25/75 was the PLA. Meanwhile, co-continuous morphology was observed in the PLA/TPU 50/50 specimen. Correlating these morphology observations with the impact strength results exhibited in Fig. 2, it is sensible to conclude that the continuity of TPU phase in the blend plays a significant role in increasing the impact strength of PLA/TPU blends.

It is known that morphology of polymer blends affects the mechanical and properties of the materials [4, 8]. Here, it is believed that the drastic increase of impact strength of PLA/TPU 50/50 specimen has positive correlation with continuity of the TPU phase in the sample.

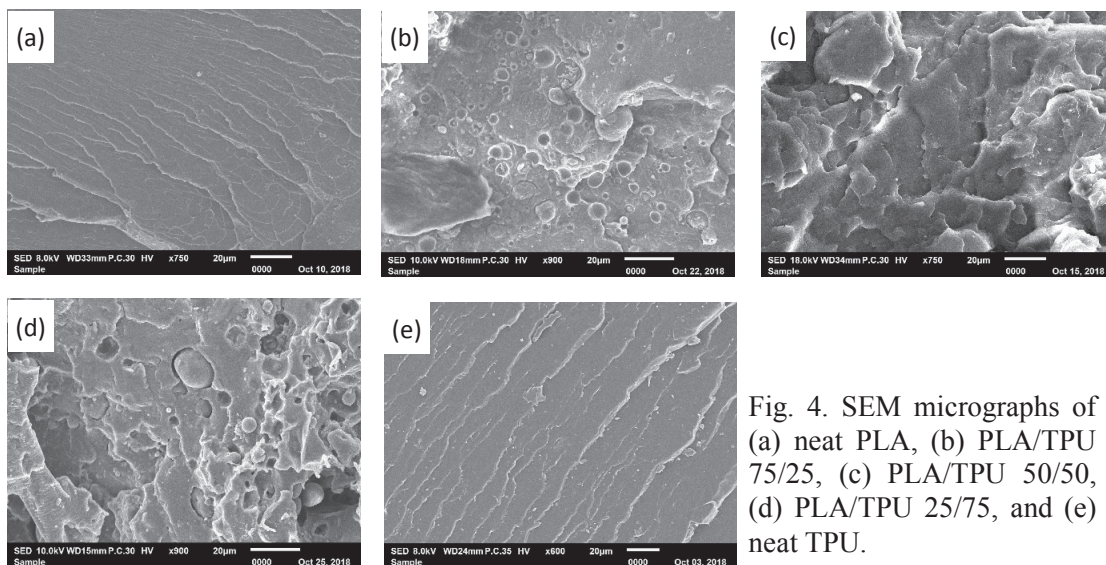


Fig. 4. SEM micrographs of (a) neat PLA, (b) PLA/TPU 75/25, (c) PLA/TPU 50/50, (d) PLA/TPU 25/75, and (e) neat TPU.

### 3.3. Hydrolytic Degradation Behavior

Fig. 5 shows the weight changes of PLA, TPU, and PLA/TPU blends after a predetermined time of immersion in alkaline solution while the physical changes of the specimens is shown in Fig. 6. From Fig. 5, it can be seen that TPU shows the slowest hydrolytic degradation rate with around 80% of the weight still remaining after 8 days (192 hours) of immersion. Meanwhile, neat PLA completely degraded after 8 days, confirming its good degradability. However, it is interesting to note that the relationship between blend composition and hydrolytic degradation behaviour is not linear. PLA/TPU 50/50 became the fastest blend to degrade, followed by PLA/TPU 75/25. While the degradation curve of PLA/TPU 25/75 lied between those of neat PLA and neat TPU.

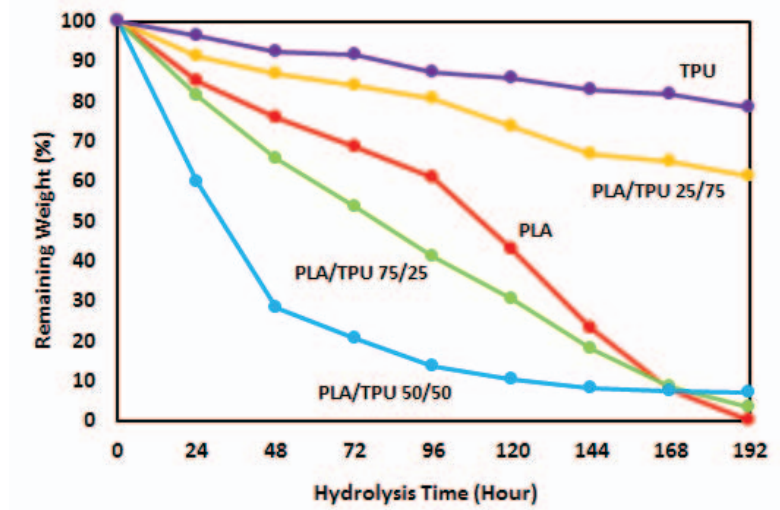


Fig. 5 Weight remaining of PLA, TPU and PLA/TPU blends after hydrolysis test



Fig. 6. Physical change of specimens after predetermined time of immersion in alkaline solution for (a) neat PLA, (b) PLA/TPU 75/25, (c) PLA/TPU 50/50, (d) PLA/TPU 25/75, and (e) neat TPU.

Several papers also reported that degradation behaviour of PLA blends is affected by blend composition [17] and that the relationship is sometimes not linear [15]. In this work, it is believed that the hydrolytic degradation behaviour is related to the sequence of alkaline

solution attacking the ester bond in the specimens, as well as the composition and morphology of the blends. It is thought that the degradation in the alkaline solution started from the surface, and PLA degraded faster compared with TPU. The PLA/TPU 75/25 degraded faster than the neat PLA might be due to the relative amount of PLA in the blend being less than in the neat one. PLA in PLA/TPU 75/25 blend acts as the sea phase where TPU acts as the island phase. Therefore, when the ester bond in the PLA phase was attacked by the alkaline solution, the dimension stability of the specimen collapsed, causing faster weight loss. Similar reasoning was applied to PLA/TPU 50/50 which has a lower PLA portion, so that the specimen dimension stability collapsed faster compared to PLA/TPU 75/25 and the neat PLA. This situation was confirmed with the fastest collapsing shape of PLA/TPU 50/50 blend as depicted in Fig. 6.

Meanwhile, PLA/TPU 25/75 degraded slower than neat PLA. This is because in this blend, the PLA no longer became a continuous phase, and the morphology of the blend was thought to be sea-island structure, with TPU becoming the sea phase and PLA becoming the island phase. Therefore, the surface of the specimens was thought to be dominated by TPU, causing slower degradation rate compared to the neat PLA. Here, Fig. 6 also confirmed the dimension stability of the PLA/TPU 25/75 and the neat TPU after up to 8 days of exposure in alkaline solution.

#### 4. CONCLUSION

PLA/TPU blends were successfully fabricated by melt blending process. From the mechanical properties evaluation, it is clear that the brittleness and the low toughness of PLA was improved as the TPU content increased. DMA measurement of PLA/TPU blends showed the appearance of two  $T_g$ 's, indicating that the blends were immiscible. The immiscibility of the PLA/TPU blend has also been supported by SEM micrographs. It has also been confirmed that blend composition affects the morphology of the blends. Finally the hydrolytic degradation behaviour of PLA, TPU and PLA/TPU blends showed some interesting behaviour, where PLA/TPU 50/50 showed the fastest degradation rate, followed by PLA/TPU 75/25, and the neat PLA. This degradation behaviour is believed to be strongly related with the morphology of the specimens.

#### ACKNOWLEDGEMENT

This work was supported by Research Initiative Grant Scheme RIGS16-085-0249 and RPDF18-010-0010, both from International Islamic University Malaysia.

#### REFERENCES

- [1] Imre B, Bedő D, Domján A, Schön P, Vancso GJ, Pukánszky B. (2013) Structure, properties and interfacial interactions in poly (lactic acid)/polyurethane blends prepared by reactive processing. *European Polymer Journal*, 49(10):3104-3113.
- [2] Wang M, Wu Y, Li YD, Zeng JB. (2017) Progress in toughening poly (lactic acid) with renewable polymers. *Polymer Reviews*, 57(4):557-93.
- [3] Rasal RM, Janorkar AV, Hirt DE. (2010) Poly (lactic acid) modifications. *Progress in Polymer Science*, 35(3):338-56.
- [4] Feng F, Ye L. (2011) Morphologies and mechanical properties of polylactide/thermoplastic polyurethane elastomer blends. *Journal of Applied Polymer Science*, 119(5):2778-2783.
- [5] Han JJ, Huang HX. (2011) Preparation and characterization of biodegradable polylactide/thermoplastic polyurethane elastomer blends. *Journal of Applied Polymer Science*, 120(6):3217-23.

- [6] Mi HY, Salick MR, Jing X, Jacques BR, Crone WC, Peng XF, Turng LS. (2013) Characterization of thermoplastic polyurethane/poly(lactic acid) (TPU/PLA) tissue engineering scaffolds fabricated by microcellular injection molding. *Materials Science and Engineering C*, 33(8):4767-4776.
- [7] Jašo V, Cvetinov M, Rakić S, Petrović ZS. (2014) Bio-plastics and elastomers from poly(lactic acid)/thermoplastic polyurethane blends. *Journal of Applied Polymer Science*, 131(22):41104.
- [8] Jing X, Mi HY, Peng XF, Turng LS. (2015) The morphology, properties, and shape memory behavior of poly(lactic acid)/thermoplastic polyurethane blends. *Polymer Engineering and Science*, 55(1):70-80.
- [9] Oliaei E, Kaffashi B, Davoodi S. (2016) Investigation of structure and mechanical properties of toughened poly (l-lactide)/thermoplastic poly (ester urethane) blends. *Journal of Applied Polymer Science*, 133(15):43104.
- [10] Siracusa V, Rocculi P, Romani S, Dalla Rosa M. (2008) Biodegradable polymers for food packaging: a review. *Trends in Food Science and Technology*, 19(12):634-43.
- [11] Elsayy MA, Kim KH, Park JW, Deep A. (2017) Hydrolytic degradation of poly(lactic acid) (PLA) and its composites. *Renewable and Sustainable Energy Reviews*, 79:1346-52.
- [12] Jašo V, Glenn G, Klameczynski A, Petrović ZS. (2015) Biodegradability study of poly(lactic acid)/thermoplastic polyurethane blends. *Polymer Testing*, 47:1-3.
- [13] Dogan SK, Boyacioglu S, Kodal M, Gokce O, Ozkoc G. (2017) Thermally induced shape memory behavior, enzymatic degradation and biocompatibility of PLA/TPU blends: "Effects of compatibilization". *Journal of the Mechanical Behavior of Biomedical Materials*, 71:349-61.
- [14] Li MX, Kim SH, Choi SW, Goda K, Lee WI. (2016) Effect of reinforcing particles on hydrolytic degradation behavior of poly (lactic acid) composites. *Composites Part B: Engineering*, 96:248-54.
- [15] Shirahase T, Komatsu Y, Tominaga Y, Asai S, Sumita M. (2006) Miscibility and hydrolytic degradation in alkaline solution of poly (L-lactide) and poly (methyl methacrylate) blends. *Polymer*, 47(13):4839-4844.
- [16] Gu X, Raghavan D, Nguyen T, VanLandingham MR, Yebassa D. (2001) Characterization of polyester degradation using tapping mode atomic force microscopy: exposure to alkaline solution at room temperature. *Polymer Degradation and Stability*, 74(1):139-49.
- [17] Yang S, Madbouly SA, Schrader JA, Srinivasan G, Grewell D, McCabe KG, Kessler MR, Graves WR. (2015) Characterization and biodegradation behavior of bio-based poly (lactic acid) and soy protein blends for sustainable horticultural applications. *Green Chemistry*, 17(1):380-393.

## STUDY OF PRODUCTIVITY IMPROVEMENT OF MANUAL OPERATIONS IN SOYA SAUCE FACTORY

ZAHARAH WAHID<sup>1\*</sup>, MOHD RADZI CHE DAUD<sup>2</sup> AND KARTINI AHMAD<sup>1</sup>

<sup>1</sup>Department of Science in Engineering,

<sup>2</sup>Department of Manufacturing and Materials Engineering,  
Faculty of Engineering, International Islamic University Malaysia,  
P.O. Box 10, 50728 Kuala Lumpur, Malaysia.

\*Corresponding author: zaharahwahid@iium.edu.my

(Received: 27<sup>th</sup> September 2019; Accepted: 28<sup>th</sup> October 2019; Published on-line: 20<sup>th</sup> January 2020)

**ABSTRACT:** Today with a rapidly changing world and markets, SMEs are facing a critical challenge to remain competitive in the business market. In this paper, a case study of the SMEs food industry is presented. Work study methodology was embedded in the strategy to improve the productivity of the soya sauce enterprise. The sample size required for the study was calculated and random observations were determined through a work sampling technique to achieve a 95% confidence level. The result from this study reveals that work sampling data can be used as a reliable estimation for identification of any potential bottleneck as well as idle time in the factory. The process flowchart at the filling and capping terminal were examined and the travelling distance was optimized to 12.5 feet from original distance of 17 feet. The modified plant layout significantly improves the people flow, production material handling, work safety, space utilization, and better working conditions. The survival of SMEs is critical as this sector contributes 38.3% to Malaysian's gross domestic productivity (GDP). Thus, these findings demonstrated that enhancing the productivity of SME food industries is effective through a work study. However, the successful adoption of this approach is mostly because of top administrative involvement and the participation of all staff members.

**ABSTRAK:** Pada hari ini, dengan perubahan pesat dunia dan pasaran, SMEs berhadapan cabaran getir bagi terus tetap berdaya saing dalam pasaran perniagaan. Kajian ini membincangkan berkaitan kes kajian SMEs dalam industri makanan. Kaedah kajian kerja telah diguna pakai dalam strategi bagi meningkatkan pengeluaran sos soya. Saiz sampel yang diperlukan bagi kajian ini dikira dan pemerhatian rawak diperoleh melalui teknik persampelan bagi memperolehi 95% tahap yakin diri. Hasil keputusan kajian menunjukkan data persampelan boleh digunakan sebagai anggaran boleh percaya bagi mengklasifikasi kemungkinan kesesakan dan juga masa terbiar dalam kilang. Proses carta alir pada terminal isian dan penutup telah diperiksa dan jarak perjalanan dioptimumkan pada 12.5 kaki dari jarak asal iaitu 17 kaki. Ubah suai susun atur kilang dapat memperbaiki dengan ketara aturan pekerja, pengendalian bahan pengeluaran, keselamatan kerja, penggunaan ruang tempat kerja dan persekitaran tempat kerja yang lebih bagus. Kemandirian SMEs adalah sangat kritikal kerana sektor ini menyumbang 38.3% kepada Keluaran Malaysia Dalam Negara Kasar (KDNK). Oleh itu, hasil kajian menunjukkan peningkatan produktiviti industri makanan SMEs adalah berkesan menerusi kajian ini. Walau bagaimanapun, keberhasilan kaedah ini berpunca daripada keterlibatan pentadbiran dan seluruh anggota pekerja.

**KEYWORDS:** food industry; work study; sustainability; time study; productivity

## 1. INTRODUCTION

Small and medium enterprises (SMEs) in Malaysia are regarded as the growth engine that drives the local economy as this sector contributed 38.3% to the gross domestic product (GDP) of this country. To completely realise their potential, the government has given high importance to supporting the development of SMEs. However, as per the statistics released by the Malaysian Productivity Centre (MPC) 2014/2015, even though the government has put efforts to increase productivity, SMEs' productivity growth (3.5%) has only slightly improved in Malaysia, [1]. Currently, with the establishment of the Trans-Pacific Partnership Agreement (TPPA), SMEs in Malaysia are expected to face higher competition due to free trade. To stay competitive, the SMEs have to be a lot more effective and thus yield a higher productivity. It is therefore of great importance not only to the individual enterprises but also for the country's economic sustainability as a whole. Deploying work study is a key strategy to boost SMEs' growth and enhance productivity. Managers often fail to recognise early the need to change their management practices and execution of production operations. They lack knowledge and professionalism. They are hampered by high production costs. Because of capital shortage, these firms are weak in market niche researches and R&D activities. Hence, there is an urgent need to respond to the challenges facing the SMEs. To alleviate this problem, deploying work studies is key strategy to achieving high yields and efficiency. This project will assist the entrepreneur to implement work study techniques through training and consultation efforts.

In Japan, soya sauce production occurs on a small scale. Since 1950, the manufacturing process has been studied and modernized using modern production control methods such as using microorganisms in the fermentation process [2]. However, in Malaysia, most soya sauce factories operate on a small scale partly due to the factors mentioned earlier.

This work study is comprised of method study and work measurement. The former involves minimisation of the work content and setting a single best way to execute a job. It is implemented to decrease manufacturing costs by saving on cycle time pertaining to the operation [3-6]. The latter deals mostly with investigation of ineffective time associated with a job, and setting time standards to execute an operation by conforming to the standard method [7]. This also results in a systematic investigation pertaining to all factors that can impact the production efficiency and economy pertaining to the case being studied, which effectively allows achieving productivity gains [8].

Productivity enhancement can be achieved by getting rid of inefficient methods, decreasing work content as well as effectively making use of manpower, machines, and materials. Also, it can be realised in multiple ways, such as by decreasing the production unit cost or decreasing the production work content, by increasing the products' value-added content [8-14], by line balancing with respect to the production line, or via combination of all of these [9-10,15]. Enhancement of productivity can be defined as a continuous improvement process that is applicable to many kinds of activities [7-8,11,16-17]. When harnessing more profit via the same types of resources, increasing productivity is regarded as a key issue [18]. Enhancing productivity also results in customer satisfaction, time and cost reduction, as well as delivery of products [19]. Productivity involves an effective relationship in order to determine method output, product prices, method utilisation, work in process, on-time delivery, and inventory levels [4]. Vergeer [5] regarded productivity as a driver for profit.

Assessing the entire process allows for the establishment of further best practices as well as optimum productivity, which also helps to decrease the cycle time. Since the



bottom line is affected by cycle time, assessing the process and determining consistency in best practices will aid in enhancing the overall business operations [9]. As per [6-10], decrease in cycle time has a cascading impact on the value as well as worth. With decrease in cycle times, there is equally an increase in output. It has been shown that there is considerable enhancement in production throughput with decrease in order-to-delivery cycle time. Seemingly, long cycle times result in higher cost, high inventory as well as poor customer service. Because of these facts, this study focuses on manpower utilisation and production cycle time. These days, a key element to successful management is reduction in cycle time [10].

The work study has been extensively employed in the manufacturing industry and in various other fields [11,14,18-19]. As per the literature, work study's application is not limited to manufacturing industries and can also be used in service sectors such as the hospitality sector [20-21]. Some recent works have considered new areas pertaining to improvement in productivity and layout planning with regards to SMEs food industry as well as the hospitality sector [20-24].

This study recommends a work study approach that can be used to devise an efficient strategy to attain sustainability in SMEs, which in turn can function as a means to improve both process efficiency and product quality, thereby enhancing productivity.

The factory setup comprises a manual assembly system, in which the work in progress (WIP) item undergoes manual transportation through its processes. The scope of the research includes the general factory layout at the filling area and the manual operation line of the 630 ml soya sauce bottle. The problems that the enterprise runs into include the unbalanced operation at each workstation that impacts the smooth functioning of the production line. The objectives of the study are to (a) assess the work performance of the existing operations with regards to manpower utilisation and production cycle time; (b) recommend a new operational layout design; and (c) analyse and compare the performance of the new and current operations.

## 2. METHOD

In this research, the work study technique was employed at the soya sauce 630 ml bottle operation line where the problems occurred. Cycle time reduction, manpower utilization, and plant layout were the main focus in this study as they impact the bottom line of the company.

### 2.1 Analysis method

This section outlines a systematic approach for recording, observing, and critically analysing the existing linked problems and processes. The approach also serves as a means for improving productivity, as shown in Table 1. Process charts were created after identification and selection of the operations or activities. A process chart provides an outline of the process and records the key events in a sequence, as well as captures all aspects of the job. Every operator's movement was recorded against time measured. This approach helps to identify the best pattern of movements for an operator that leads to minimum effort and optimum time consumption. It also enables finding the most economical route of movement.

Table 1: Analysis method

Item	How	Analysis
Line balance	Time study	Time analysis
Method study	Work improved	Work sampling
No proper Layout	Process flow and material flow	Routing analysis

In order to balance the work team, the line balancing approach was implemented, so that the idle time on the filling machine and workers could be detected. This in turn resulted in the optimisation of work distribution between machines and workers. To improve the performance at the 630 ml bottle operation line, the layout was also redesigned.

Figure 1 shows the process flow of the soya sauce 630 ml bottle operation line. Table 2 presents the breakdown of the operators based on the operation. In this assembly line, the total number of operators engaged was seventeen.

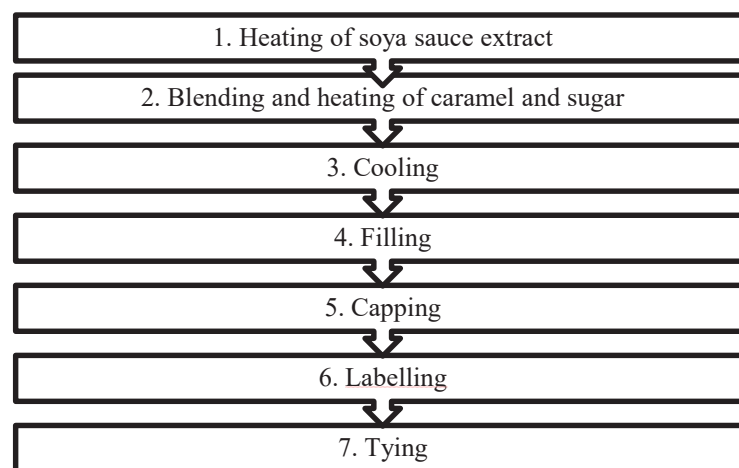


Fig. 1: Flow process chart of soya sauce 630 ml bottle line.

Figure 2 presents the flow diagram of the existing manual operation line. Trolleys were used for transportation between workstations. The workstations were about six feet apart. At the filling workstation, there were three filling barrels with one trolley between the filling barrels on which to place the filled bottle. Once the trolley was filled, it would be transported to the capping workstation. The capped bottle was placed back on the trolley on completion of the capping operation. Thereafter, it goes through a manual labelling operation.

Table 2: Breakdown of the operator based on the operation

Workstation	Number of Operator
Filling	6
Capping	2
Labelling	6
Tying	3
Total	17

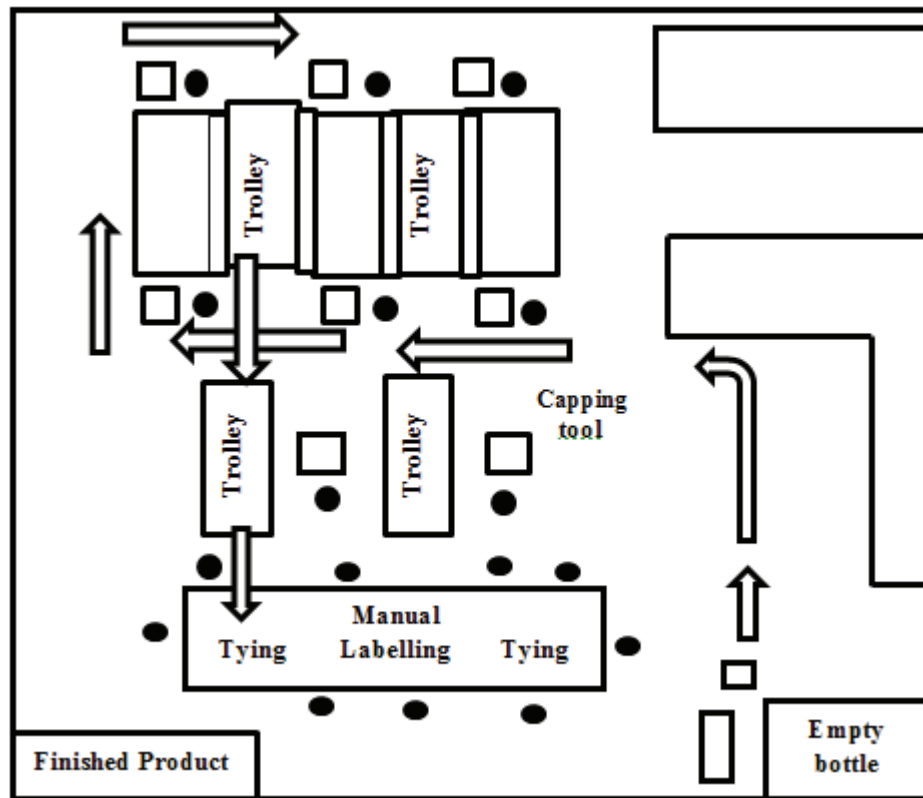


Fig.2: Flowchart of soya sauce 630 ml bottle line.

### 3. DATA COLLECTION AND ANALYSIS

Work sampling is one of the work measurement techniques employed in this study to find the percentage occurrence of a certain activity by statistical sampling and random observations. An established standard procedure was adopted before the study was performed. Various authors [24-26] recommended that the use of the sampling method is an effective way to detect idle time or unproductive work. According to [20] now more than 40,000 mainly industrial engineers are trained in work sampling due to its effectiveness and accuracy.

#### 3.1 Estimation of Number of Observations Required

The method of work sampling was employed at the filling terminal to determine the ineffective time/idle time of the operator. A pilot study was performed with 80 observations to measure the idle time of the operators and processes. From the result of this primary examination, it was found that 7.5% of the time was idle time, 92% of the time was filling time and 0.5% of the time was for other work. Determining the number of observations entailed assigning a limit of precision of  $\pm 5\%$  at 95% confidence level to the percentage of operation idle time. The following formula was employed.

$$N = [4P (100-P)] / L = [4 \times 7.5 (92.0)] / 25 = 111$$

Where,

$$P (\% \text{ of idle time}) = 7.5; \quad L (\text{limits of accuracy}) = 25;$$

111 actual observations were made and the following results were obtained.

Filling = 66.66%

$$\begin{aligned}\text{Idle time} &= 16.27\% \\ \text{Other work} &= 17.12\% \\ N &= [4 \times 16.27 (66.66)] / 25 = 385\end{aligned}$$

Therefore, required observations needed are 385 to achieve the desired level of accuracy. One of the basic foundations of statistical sampling theory is the concept that the larger the sample size, the results will be more accurate [20, 26-27]. [28] reported that work sampling as a method improves plant efficiency and increase productivity.

$$\begin{aligned}\text{Filling} &= 68.57\% \\ \text{Idle time} &= 23.38\% \\ \text{Other work} &= 8.05\%\end{aligned}$$

Hence the % of idle time was  $23.4 \pm 5$ .

Work sampling technique was also used at the capping workstation to determine the operator idle time. Causes of idle time at the capping workstation are waiting for the bottle, transfer of trolleys, transfer of bottles, talking/looking, and not at working place.

The preliminary results are as following:

$$\begin{aligned}\text{Observation, N} &= 27 \\ \text{Capping} &= 55.56\% \\ \text{Idle time} &= 37.01\% \\ \text{Other work} &= 7.41\%\end{aligned}$$

To determine the number of observations required to give a limit of accuracy of  $\pm 5\%$  at 95% confidence level in the percentage of operation idle time.

$$\begin{aligned}N &= [4 \times 37.03 (63)] / 25 = 373 \\ \text{Actual observation of N} &= 373 \\ \text{Capping} &= 65.19\% \\ \text{Idle time} &= 29.35\% \\ \text{Other work} &= 5.46\%\end{aligned}$$

Hence the % of idle time at the capping workstation was  $29.35 \pm 5$ .

#### 4. RESULTS AND DISCUSSION

The work sampling approach was employed at both the filling and capping workstations to determine the productive and non-productive element or idle time in the operation. It is basically a statistical technique where large numbers of observations are made. The purpose of this analysis is to take action to eliminate the problem. At the filling workstation, a sample size of 385 total observations was made to achieve 95% accuracy. The result of the examination indicated that the idle time of the operator was 23.4% with bounds of accuracy of 5%. Similarly, 29.35% idle time of the operator was found at the capping workstation based on a sample size of 373 observations made as discussed in section 3.1. This study discovered that the root causes were mostly attributed to the general factory layout at the filling area and the manual operation line of the 630 ml soya sauce bottle and it results in wasted time and unnecessary movements such as transferring the

trolleys from one workstation to another, which cause a delay or slow down the production line. The manual operations demand intensive engagement of manpower however, the extent of manpower engagement and utilisation is still low. In addition, documentation of any standard operating procedure was not in existence and as a result, the operators perform work based on their individual styles, which results in added work content that were not value added activities. Hence, the productivity could potentially be increased by an enormous amount based on the above factors. A study by [18, 25, 27-28] revealed that the use of work sampling enhanced the production capacity. A study by [26] also showed that it is simple and inexpensive to perform.

Based on the data collected, the idle time is higher at the capping workstation as compared to the filling workstation. The cycle time of these processes were measured and calculated. These analyses automatically confirmed where the bottlenecks or capacity constraints are in the process line. This bottleneck causes delay or slows down the operation system so it needs to be solved urgently. This is a major obstacle faced by this enterprise as most of the jobs are performed manually. According to [12] a bottleneck is one of the significant problems encountered by most SMEs. Subsequently the improvement action has been established and implemented using a semi-automatic filling machine having 6 nozzles, which is essential. Only a single worker was needed to work at this workstation compared to the existing operational conditions. The bottleneck is eliminated by the installation of the semi-automatic filling machine. Thus, the time of one processing cycle was decreased, which in turn increases the efficiency of the whole system and improves the earnings. The small investment for this semi-automatic filling machine was recuperated in 3 months.

The quantity of sauce loaded in the bottle was more consistent and easy to control and monitor. This improvement leads to better product quality and quantity. Underutilisation of the human resources was reduced. Using a semi-automatic process will benefit the firm with respect to productivity and will also solve the issue of manpower employment since the labour turnover is fairly high. Hence, the imbalance between the capping and the filling workstations was eliminated. This result was parallel with the result obtained by [11,19,29].

The existing process flowchart was critically studied. The layout was rearranged by minimising the transit time between each workstation. Using systematic layout planning a modified process flowchart was presented and the travel distance was reduced to 12.5 feet which was originally 17 feet. The cycle time for each operation is very much related to the transit times from one workstation to the next workstation. The number of trolleys involved was reduced from 5 to 3. Figure 3 displays the proposed new process flowchart of the soya sauce (630 ml) operation line. [18,24,28,] reported that increasing productivity by reducing cycle time in the assembly lines of the automotive industry.

The modified design layout and simplified process flowchart minimised the unnecessary movements of the operators, as shown in Fig. 3. It also improved the safety and the flow of the material on the workstation floor. Similar findings were also revealed by [8,18]. [29] reported that systematic layout planning and design layout is an influential factor in a company's performance to support the streamlined process of production. Furthermore, it provides better working conditions for the operators. These workstations are now connected to each other through a conveyor belt. The work elements at both workstations were reduced. Thus, time required to complete the final product was substantially reduced in comparison to the time taken in the current operational conditions. Thus, there was an increase in the output in less time and the results of this study support the findings of [26].

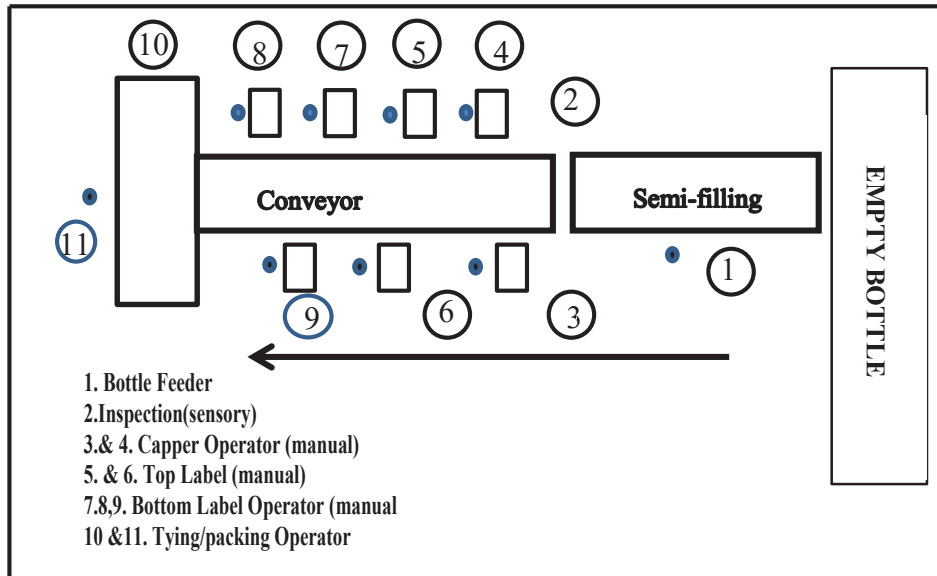


Fig. 3: Proposed improvement flow diagram of soya sauce (630 ml) operation line.

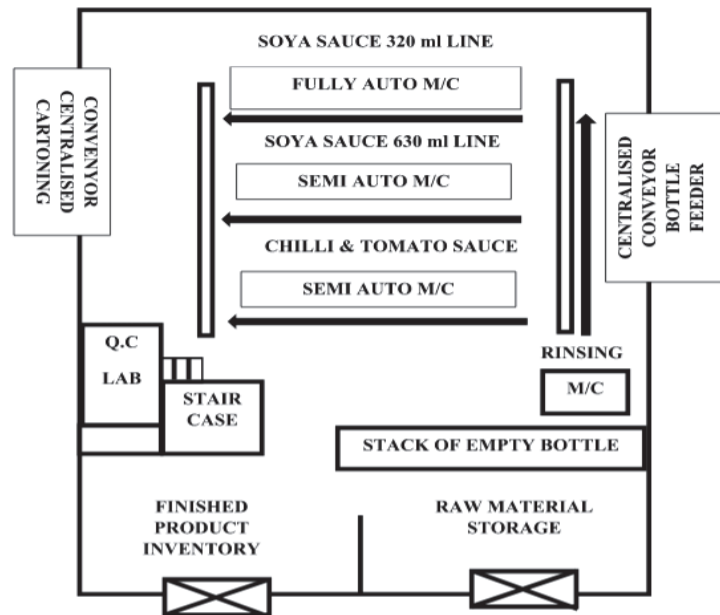


Fig. 4: The overall factory layout at the filling area.

Figure 4 presents the overall factory layout at the filling area which was quite congested due to the limitation of floor area. An improved layout was proposed so that a centralized bottle rinsing workstation could be achieved. As compared to the existing layout, the workstations were all over the factory. The improved layout design allowed feeding of the bottle to be centralized. [16, 18, 22, 27,29] also showed that the optimization of production layout was achieved and improve product flow and plant layout efficiency.

## 5. CONCLUSION

The deployment of the system proposed in the study at the capping and filling workstations have a significant impact on the productivity of the soya sauce factory. The

layout of the factory was optimised, the bottleneck was eliminated, the production capacity was improved, and the return on investment (ROI) was 3 months. Moreover, even the transportation was decreased from 5 to 3 trolleys with no delay in the assembly line. The standard operating process was well established by using the new proposed outline. New policies and observation schedules were introduced to keep up the improvement in the process. Thus, this study demonstrated that work study techniques are suitable tools to be implemented for productivity improvements. However, the successful adoption of this approach is mostly because of the top administration involvement and the participation of all the members of the staff.

## REFERENCES

- [1] Malaysian, Productivity Corporation. (2017) MPC Productivity Report 2016/2017.
- [2] Desmond KO'T. (2019) Role of microorganism in soya sauce production. *Advances in Applied Microbiology*, 108: 45-113.
- [3] Lakwinder PS. (2016) *Work Study and Ergonomics*. Cambridge University Press.
- [4] Baines A. (1997) *Productivity Improvement. Work Study*. MCB University Press 46: 49-51.
- [5] Vergeer R, Kleinknecht A. (2014) Do labour market performs reduce labour productivity growth? A Panel Data Analysis of 20 OECD Countries (1960-2004). *International Labor Review* (153):365-593.
- [6] Hiten Patel SCS. (2014) Review on cycle time reduction in industries. *Journal of Emerging Technologies and Innovative Research*, 1(7):955-956.
- [7] kansel M, Yagmahan B, Emel E. (2017). Determination of standard times for process improvement: A case Study. *Global Journal of Business, Economics and Manag.*, 7(1):62-68.
- [8] Hezekiah OA, Olasunkanmi A, Ayoola AB. (2018) Review of method study approach to productivity gain: A multi-case study of portable water producing factory. *ResearchGate* 3(2):1-6.
- [9] Macías-Jiménez MA, Romero-Conrado AR, Acosta-Fontalvo LC, Coronado-Hernández JR. (2019) Application of work study to process improvement: Fruit nectar case. In *proceedings of the 18<sup>th</sup> International Conference on Computer Information Systems and Industrial Management: 19-21 September 2019; Belgrade, Serbia*. Edited by Khalid S, Ritupama C, Valentina J. Springer International; pp 1-43.
- [10] Moktadir MA, Ahmed S, Zohra FT, Sultana R. (2017) Productivity improvement by work study technique: A case on leather products industry of Bangladesh. *Ind. Eng Manag. J.*, (6):207.
- [11] Chisosa, D.F., Chipambwa, W.(2018) An exploration of how work study techniques can optimize production in Zimbabwe's clothing industry. *J. Text. Apparel Technol. Manag.*, 10: 1-11.
- [12] Jaffrey V, Mohamed NMZN, Rose ANM. (2017) Improvement of productivity in low volume production industry layout by Using Witness Simulation software. *Material Science and Engineering*, vol.257.
- [13] Singh MP. (2016) Improvement in process industries by using work study methods: A case study. *IJMET*426-436.
- [14] Ozor PA, Olua C, (2015) Productivity improvement of small and medium scale enterprises using lean concept: Case study of bread factory. *European Journal of Business and Management* (7): 73-84.
- [15] Ojaghi, Y., et al. ( 2015) Production layout optimization for small and medium scale food industry. *Procedia CIRP*, (26): 247-251.
- [16] Ali Naqvi SA, et al. (2016) Productivity improvement of a manufacturing facility using systematic layout planning. *Cogent Engineering*, 3(1): 1207296.
- [17] Wanniarachchi WNC, Gopura RC, Punchihewa H. (2016) Development of a layout model suitable for the food processing industry. *Journal of Industrial Engineering*. 2:1-8.

- [18] Malashree P, Kulkarni, VN, Gaitonde VN, Sahebagowda M. (2018) An experimental study on productivity improvement using work study and ergonomics. *International J. of Darshan Inst. on Engineering Research and Emerging Technologies*, 7(1):31-36.
- [19] Shravan S R, Nilesh P, Ujjainwala F, Amit P. (2018) Productivity improvement through work sampling in a ceramic tiles manufacturing industry: A case study. *International J. for Science Research & Development*, 6(8): 662-670.
- [20] Martinec T, Skec S, Savsek T, Perisic MM.(2017) Work sampling for the production development: A Case Study of a supplier in European automotive industry. *Advances in Production Engineering & Manag.*, 12(4): 375-387.
- [21] Gaurav G, Verma DS.(2019) Optimization of plant layout in manufacturing industry. *IJRTE* 8(2): 41-47.
- [22] Buchmeister B, Palcic,I. (2017) Implementation of correlation analysis to work sampling results. In *Proceedings of the 28<sup>th</sup> DAAAM, International Symposium,0029-0034, Vienna, Austria*; pp.29-34.
- [23] Sidharth SR. (2019) Study and analysis of performance evaluation of the low level employees in tourism and hospitality: Case of five star hotel in Mussoorie, Uttarakhand. *International Journal of Research and Analytical Review* 6(1): 359-270.
- [24] Kunica Z. (2018). Optimization of the plant layout in the production of the special transformers: Case Study. *FME Transactions*, 46: 285-290.
- [25] Dhanashree R, Madhuri K, Pranjali C, Raichurkar PP. (2018) Enhancing efficiency and productivity of garment industry by using different techniques. *International Journal on Textile Engineering and Processes*. 4(1): 5-8.
- [26] Bogert A, Edwards W, Jalali F, Aqlan F. (2018) Process improvement and layout optimization in a forging company. *Proceedings of the International Conference on Industrial Engineering and Operations Management*, 1162-1170
- [27] Suhardi B, Juwita E, Astuti RB. (2019) Facility layout improvement in sewing department with systematic layout planning and ergonomics approach. *Cogent Engineering*, 6(1): Retrieved from <https://doi.org/10.1080/23311916.2019.1597412>.
- [28] Srijit Krisnan A., Sarang Dev, Rahul Suresh, A. Sumesh and Ramesh Kumar, K. (2018) Bottleneck identification in a tyre manufacturing plant using simulation analysis and productivity improvement. 5(11)3:24720-24730.
- [29] Wilson RN, Charles M. (2017) Process mapping and optimization of the process flows of a furniture manufacturing company in Zimbabwe using machine distance matrices. *Procedia Manufacturing* 8:447-454.



## THE EFFECTS OF SUPERCRITICAL CARBON DIOXIDE ON THE DEGRADATION AND ANTIMICROBIAL PROPERTIES OF PLA BIOCOMPOSITE

HAZLEEN ANUAR<sup>1</sup>, SITI NUR E'ZZATI MOHD APANDI<sup>1</sup>, SITI MUNIRAH SALIMAH ABD RASHID<sup>1</sup>, FATHILAH ALI<sup>2</sup>, YOSE FACHMI BUYS<sup>3</sup>, MOHD ROMAINOR MANSHOR<sup>4</sup>, SABU THOMAS<sup>5</sup>, NUR AIMI MOHD NASIR<sup>1</sup>

<sup>1</sup>Department of Manufacturing and Materials Engineering, Kulliyah of Engineering, International Islamic University Malaysia, Jalan Gombak, 53100, Kuala Lumpur, Malaysia

<sup>2</sup>Department of Biotechnology Engineering, Kulliyah of Engineering, International Islamic University Malaysia, Jalan Gombak, 53100, Kuala Lumpur, Malaysia

<sup>3</sup>Department of Mechanical Engineering, Faculty of Engineering, University of Malaya, 50603 Kuala Lumpur, Malaysia

<sup>4</sup>Food Technology Research Centre, Malaysian Agriculture Research And Development Institute (Mardi), 43400 Serdang, Selangor, Malaysia

<sup>5</sup>International and Inter University Centre for Nanoscience and Nanotechnology, Mahatma Gandhi University, Priyadarshini Hills, Kottayam 686560, Kerala, India

*\*Corresponding Author: hazleen@iium.edu.my*

*(Received: 12<sup>th</sup> April 2019; Accepted: 24<sup>th</sup> December 2019; Published on-line: 20<sup>th</sup> January 2020)*

**ABSTRACT:** Biopolymer products that is biodegradable presently attracting an attention from researchers and industry. The biodegradable packaging based on polylactic acid (PLA), durian skin fibre (DSF), epoxidized palm oil (EPO) and incorporated with cinnamon essential oil (CEO) as antimicrobial agent have been developed and showed to be a promising field of research. This paper reported the effects of supercritical carbon dioxide on the degradation and antimicrobial properties of PLA biocomposite films produced via solvent casting. The biocomposites underwent supercritical carbon dioxide (SCCO<sub>2</sub>) treatment at two different conditions under 40 °C temperature and at 100 bar and 200 bar pressure. Water absorption test showed that the untreated PLA biocomposite absorbed most water as compared to treated PLA biocomposite with SCCO<sub>2</sub> at 5.1%. This is due to the hydrophilic nature of the fibre that absorbed water molecules. Soil burial test showed that the treated PLA biocomposite possessed the highest value of weight losses after 80 days with 97.8%. Biocomposite with the presence of CEO demonstrated antimicrobial activity against both gram-positive and gram-negative bacteria. This showed that SCCO<sub>2</sub> significantly improved the properties of PLA biocomposite films. The supercritical fluid treatment of PLA biocomposite could be an alternative for active packaging industries to ensure that the packaging product meets the requirement by consumers as well as being an eco-friendly product.

**ABSTRAK:** Produk biopolimer yang biodegradasi pada masa ini menarik perhatian dari penyelidik dan industri. Pembungkusan biodegradasi berasaskan polilaktik asid (PLA), serat kulit durian (DSF), minyak kelapa sawit terepoksi (EPO) dan ditambah dengan

---

minyak pati kayu manis (CEO) sebagai agen antimikrobal telah dibangun dan menjadi bidang penyelidikan. Artikel ini melaporkan kesan karbon dioksida superkritikal terhadap sifat-sifat degradasi dan antimikrobik dari filem biokomposit PLA yang dihasilkan melalui pemutus pelarut. Biokomposit telah menjalani rawatan superkritikal karbon dioksida (SCCO<sub>2</sub>) pada dua keadaan yang berbeza di bawah suhu 40 °C pada 100 bar dan 200 tekanan bar. Ujian penyerapan air menunjukkan bahawa biocomposite PLA yang tidak dirawat menyerap kebanyakan air berbanding komposisi lain dengan 5.1%. Ini disebabkan sifat hidrofilik serat yang menyerap molekul air. Ujian penanaman dalam tanah menunjukkan bahawa biocomposite PLA yang dirawat mempunyai nilai kehilangan berat tertinggi setelah 80 hari dengan 97.8%. Biokomposit dengan kehadiran CEO menunjukkan aktiviti antimikrobal terhadap bakteria gram-positif dan gram-negatif. Ini menunjukkan bahawa SCCO<sub>2</sub> meningkatkan sifat-sifat filem biocomposite PLA. Rawatan cecair superkritikal PLA biocomposite boleh menjadi alternatif bagi industri pembungkusan untuk memastikan produk pembungkusan memenuhi keperluan pengguna serta menjadi produk mesra alam.

---

**KEY WORDS:** *Polylactic acid, Durian Skin Fibre, Supercritical carbon dioxide, Degradation properties, and Antimicrobial activity.*

## 1. INTRODUCTION

Food packaging is a packaging that provides food for carriage, distribution, packing, trade and end-user to fulfil the consumer expectations. Consumer requirements for secure, environment-friendly and high-quality packaging materials have been increased, and therefore the garbage disposal problems are being resolved [1]. Plastics, papers, metals and glasses are some of the main packaging materials; however plastic packaging is typically used in food packaging. Synthetic plastic packaging is crucial to be disposed and can be wasteful due to its compositions and elemental contents [2]. This waste material ends-up being discarded to landfills and the declining availability of land for this purpose [3]. Realizing this situation, many food packaging manufacturer tried to reduce the reliance on synthetic plastics as well as maintain the quality of food. Researchers have found a solution by developed biopolymers that easily degrade within a definite period, compared to non-degradable plastics.

Due to renewability, biodegradability and commercial viability, development of biodegradable materials is interesting in the food packaging sector, since it provides a replacement to the usage of synthetic products [4]. Other than that, production of biopolymer products can be an initiative income in the agriculture industry. PLA is one of the most promising candidates among the renewable source-based products, due to its availability, biocompatibility, excellent tensile strength, good process ability and biodegradability, which are a significant benefit from an environmental perspective. Biodegradable films produced from starch crops are defined as odor-free, flavourless, and neutral as well as non-toxicity [5]. Despite the benefit features, mechanical properties of PLA are unsatisfactory for packaging applications due to brittleness. The reinforced PLA matrix with natural fibre is believed to improve its mechanical performance [6]. Compared to petroleum-based fibre, natural fibres are more environmentally friendly and potentially decrease the environmental problems due to the biodegradable properties. In order to produce biocomposites while preserving the green features, biopolymers must be reinforced with natural fibre [7]. Natural fibres are also composed of low toxicity and cheap resources.

Durian skin fibre (DSF) has excellent features as reinforcement or filler in PLA biopolymer [4, 8, 9]. Durian or, its scientific name, *Durio zibethinus Murray* can be found

---

in Southeast Asian countries such as Malaysia, Thailand, Indonesia and Philippines. It is also recognised as the 'king of fruits'. About 45-55 wt% of durian can be considered as waste including skin and seed because only 55-65 wt% of durian is flesh [9]. To preserve the green environment, the durian skin waste can be used to produce durian skin fibre (DSF). This attempt could help in reducing the environmental pollution by decreasing the number of organic wastes. Besides, the processability of films can be increased with plasticizers that contribute to decreasing the glass transition temperature ( $T_g$ ) and enhance the polymer chain flexibility [10]. This plasticizer also might overcome specimen's brittleness created by high intermolecular forces. Some researchers acknowledge that the natural plasticizers are better, which can be found naturally extracted from animals, vegetable fats and plants oil [11, 12]. Among the natural plasticizer, epoxidized palm oil (EPO) is a favourable plant oil due to its characteristics like inexpensive, non-toxicity and availability as a renewable agriculture resource.

Nowadays, the safety issues of food are utterly worrisome in the world. Handling food packaging safety is just significant at the consumer level because many of them have contaminated food if not keep properly [13]. Hence, research in active food packaging could play a primary role in food security guarantee, comprehensively permitted with the industrial sector, farmers, producers, wholesalers, retailers, and government as well as consumer groups. Due to the problems highlighted, there is a necessity to produce food packaging with an anti-microbial agent and preventing food contamination. Bacteria and fungi are examples of active microorganisms which may have migrated through direct interaction between food and packaging material or via moisture from inside packaging layer to the food surface [14]. The movement activity of these compounds might interrupt the lifespan and quality of the product. Active packaging materials in the presence of antimicrobial agents like essential oil may be considered as the contemporary advancement of functional packaging. This antimicrobial agent in biocomposite films can avoid almost all bacteria activities that affect the food contamination [15].

The production of essential oil can be exploited as a natural antimicrobials agent and can be used as one of the additives for food [1]. Different types of essential oils show different significance functional group with own antimicrobial properties. The incorporation of essential oil in biocomposite material as secure antimicrobials is expected to be non-harmful for food product and human consumption. Cinnamon has been used as a spice since long time ago. The major component of essential oil extraction is cinnamaldehyde group, a well-known functional group because of its strong antioxidant and antibacterial activities [16, 17]. The combination of essential oils into viscous biocomposite solvents via solvent casting has some disadvantages mostly due to hydrophobic oil behaviour by EPO and cinnamon essential oil (CEO) which make it difficult to become a homogeneous film. Therefore, supercritical carbon dioxide (SCCO<sub>2</sub>) treatment is introduced in this study as the dispersion agent to employ PLA biocomposite films.

The SCCO<sub>2</sub> process can present an effective and beneficial medium for polymer processing. The major benefits of polymer treatment with SCCO<sub>2</sub> include processing at low temperatures, allowing a large amount of carbon dioxide (CO<sub>2</sub>) into different kinds of a polymer including synthetic and biopolymer and rapidly complete solvent elimination from the final product [13]. Besides its greener characteristics, SCCO<sub>2</sub> is chemically inert, inexpensive, easily purchased, non-flammable and highly pure. CO<sub>2</sub> gas is a suitable solvent for non-polar constituents and dissolves in most polymer compounds [18]. In short, SCCO<sub>2</sub> offers regulated product quality and safety as well as efficient time and energy management. To the best of the author's knowledge, the study of supercritical carbon dioxide (SCCO<sub>2</sub>)

treatment on antimicrobial biodegradable food packaging material has not been investigated. Therefore, in this study, PLA biocomposite was produced through solvent casting. This paper also discusses the effects of SCCO<sub>2</sub> on the anti-microbial, water absorption and soil degradation of PLA/DSF biocomposite films.

## 2. EXPERIMENTAL

### 2.1. Materials

PLA in a pallet form was purchased from NatureWorks®, China. The grade of PLA used was 4043D with a density of 0.998 g/cm<sup>3</sup> and glass transition between range 57-61 °C. Chloroform used as a reagent to dissolve the PLA pallet was supplied by Merck, Malaysia. Durian skin waste crops were obtained from a local market at Sri Gombak, Kuala Lumpur, Malaysia. The dried skins were ground using blender and mill crusher before sieving over 100 to 250 µm to obtain durian skin fibre (DSF). Epoxidized palm oil (EPO) was obtained from the Advanced Oleochemical Technology Division of the Malaysia Palm Oil Board (MPOB), Bangi. Cinnamon essential oil (CEO) was bought from IT Tech Research (M) Sdn. Bhd. Luria-Bertani agar (LBA) and Luria-Bertani broth (LHB) were purchased from a local supplier and *Escherichia coli* strains were collected from the International Islamic University Malaysia (IIUM) under Biotechnology Laboratory. Stock cultures of the studied bacteria were grown in LHB at 30 °C for 24 h prior to testing.

### 2.2. Biocomposite Preparation

PLA biocomposite film was produced via solution casting method. Before beginning the experiment, all materials used were kept in an oven with temperature 40 °C for 24 h to avoid moisture absorption. Then, 50 ml of chloroform liquid was measured and added into the mixture where the ratio between the PLA mixture and chloroform was 1:10 to obtain 0.05 mm of film sheet thickness. Fig. 1 (a) shows the mixture of PLA and chloroform in the covered beaker. The detailed amount of composition for each sample was shown in Table 1. The mixture was then mechanically stirred on a hot plate by using a magnetic stirrer until it reached the homogeneous phase. Total weight of each sample was 5.1 g. The solution mixture is poured into the flat surface of a mould in Fig. 1 (b). Samples were dried after left at room temperature for 1 day as in Fig. 1 (c). Dried films were peeled off from the casting surface and stored inside desiccators at 25 ± 1 °C until further evaluation.

### 2.3. Supercritical Carbon Dioxide (SCCO<sub>2</sub>)

The PLA biocomposite film underwent supercritical carbon dioxide (SCCO<sub>2</sub>) method for 2 h at temperature 40 °C with different pressure at 100 bar (condition 1) and 200 bar (condition 2). The samples were impregnated with CO<sub>2</sub> through a supercritical carbon dioxide machine model Waters (TAP SFE Biobotanical system, IPM) at International Institute for Halal Research and Training (INHART), International Islamic University Malaysia. The SCCO<sub>2</sub> treatment was carried out into a vessel containing spores in suspensions or film. The CO<sub>2</sub> was impregnated into the PLA biocomposite until the desired pressure was obtained. Next, the CO<sub>2</sub> vent valve was immediately unlocked to stop extra reactions in the container. The depressurize time depends on the pressure at that condition.

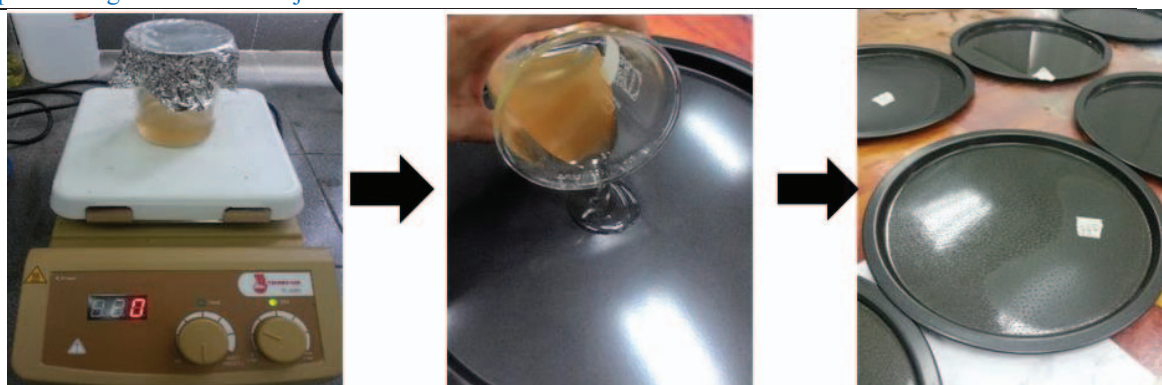


Fig. 1. The PLA biocomposite film preparation via solution casting method a) the mixture was mechanically stirred on a hot plate, b) poured the sample in mould and c) samples were dried for 24 h before peel-off.

Table 1: The composition for each sample

Sample	PLA (g)	DSF (g)	EPO (ml)	CEO (ml)	Chloroform (ml)
PLA	100 wt% (5.10)	-	-	-	51.00
PLA-DSF	97 wt% (4.94)	3 wt% (0.15)	-	-	51.00
PLA-DSF-EPO	93 wt% (4.68)	3 wt% (0.15)	5 wt% (0.26)	-	51.00
PLA-DSF-EPO-CEO	92 wt% (4.68)	3 wt% (0.15)	5 wt% (0.26)	1 wt% (0.05)	51.00

## 2.4. Testing Method

### 2.4.1. Water Absorption Analysis

Water absorption of the films was carried out as per ASTM D570. Before immersed in water, the specimens were dried in an oven for 1 day, placed in a desiccator to get constant weight and subsequently weighted. Each sample was immersed in the distilled water at room temperature until saturated weight was obtained. The weight of the samples was recorded every day for the first 14 days and once a week until the values are equilibrium. The water absorption (%) was calculated from the difference in weight and stated as the percentage increase of the initial weight as in Eq. (1) [19].

$$\text{Water absorption (\%)} = \left( \frac{W_i - W_o}{W_o} \right) \times 100 \quad (1)$$

where  $W_i$  is a weight of the sample after immersion (g) and  $W_o$  is the initial weight of the sample (g). All data were collected from averaged of five samples tested. Impregnated film at difference condition and non-impregnated specimens were also tested for comparison.

### 2.4.2. Soil Burial Degradation Analysis

Soil burial degradation analysis of PLA biocomposite was measured according to ASTM D5988. The dried thin film specimen of size 5 cm x 5 cm was prepared. The initial

mass of each sample was weighted before buried in soil at a 5 cm from the soil surface. At these depths, aerobic degradation (action of microorganism) condition could be achieved. The experiment is conducted in an outside laboratory that was exposed to the environment and end for 80 days. The specimens were removed, washed with water, dried in an oven and weighed. The weight losses of the biocomposite sample were studied and recorded based on Eq. (2).

$$\text{Weight loss (\%)} = \left( \frac{W_f - W_i}{W_i} \right) \times 100 \quad (2)$$

where  $W_i$  is initial weight of specimen (g) and  $W_f$  is the final weight of specimen (g). All samples were observed under scanning electron microscope (SEM) before and after soil burial test.

#### 2.4.3. Antimicrobial Test

Antimicrobial test used in this project was an inhibition zone test through the agar diffusion method. The sample films prepared beforehand were cut by using sterilized scissors. For this test, the films were cut into 6 mm diameter and were placed into micro-centrifuged tubes. Before place the film into an agar medium, the agar medium was inoculated with 100  $\mu$ L of tested bacteria, *S. aureus* (positive gram) and *E. coli* (negative gram). Biocomposite films were then placed on the cultured agar with bacteria. After 24 h to 36 h, the inhibition zone was remarked upon and measured at three different points by using a ruler to get precise average value.

#### 2.4.4. Gas Chromatography

Gas chromatography (GC-TOF/MS) was used to determine the presence of essential oil composition. The interface temperature for GC-MS is 220 °C. The temperature of the ion source is 200 °C and ionization energy is 70 V. The total ion monitoring (TIC) will be used to detect composition in cinnamon essential oil. Three replicates per each sample were analyzed.

### 3. RESULTS AND DISCUSSION

#### 3.1. Water Absorption Analysis

The water absorption test is important in food packaging since water or moisture contributes towards the deterioration of food products. The water absorption curves, which demonstrated the percentage of water uptake of the PLA biocomposites in 30 days, are shown in Fig. 2. Water affected the specimen films, based on the components present in the biocomposite films. It could be observed that the specimens underwent SCCO<sub>2</sub> presented lower water absorption in comparison to the untreated specimens. The results showed that the percentage of water absorption slowly increased over the time. Based on Fig. 2, the water uptake for all the specimens slowly increased during the initial days of the experiment and then levelled-off when it reached the equilibrium state. A similar behaviour was reported for the isolated soy protein (SPI) and PLA films, whereby the samples started to sharply swollen in the first minute and then began to slowly shrink due to solubilisation of the samples during the experiment [20]. The films achieved saturated after 18 days, as shown in Fig. 2.

In this present work, the PLA-DSF blend without SCCO<sub>2</sub> treatment absorbed the most water (5.1%) compared to the other compositions. The water absorption rate increased in the PLA blend when DSF was added. DSF is hydrophilic because it comprises an abundance of hydroxyl groups that tend to attract water molecules [9]. In contrast, PLA is a

hydrophobic polymer. The results for the impregnated PLA-DSF sample for conditions 1 and 2 were 4.90% and 4.83%, respectively. These values corresponded to the formation of micro-porosities observed under SEM in Fig. 4 due to the release of SCCO<sub>2</sub> from the polymer. The pressure applied during the SCCO<sub>2</sub> treatment significantly influenced the water absorption. Therefore, as the SCCO<sub>2</sub> pressure increased, the water uptake decreased. The treated biocomposites under condition 2 at a higher pressure presented lower water absorption for all the samples compared to the biocomposites under condition 1. This behaviour is in agreement with the findings studied by Souza et al. [21] where the cassava starch biocomposite films was impregnated by SCCO<sub>2</sub>.

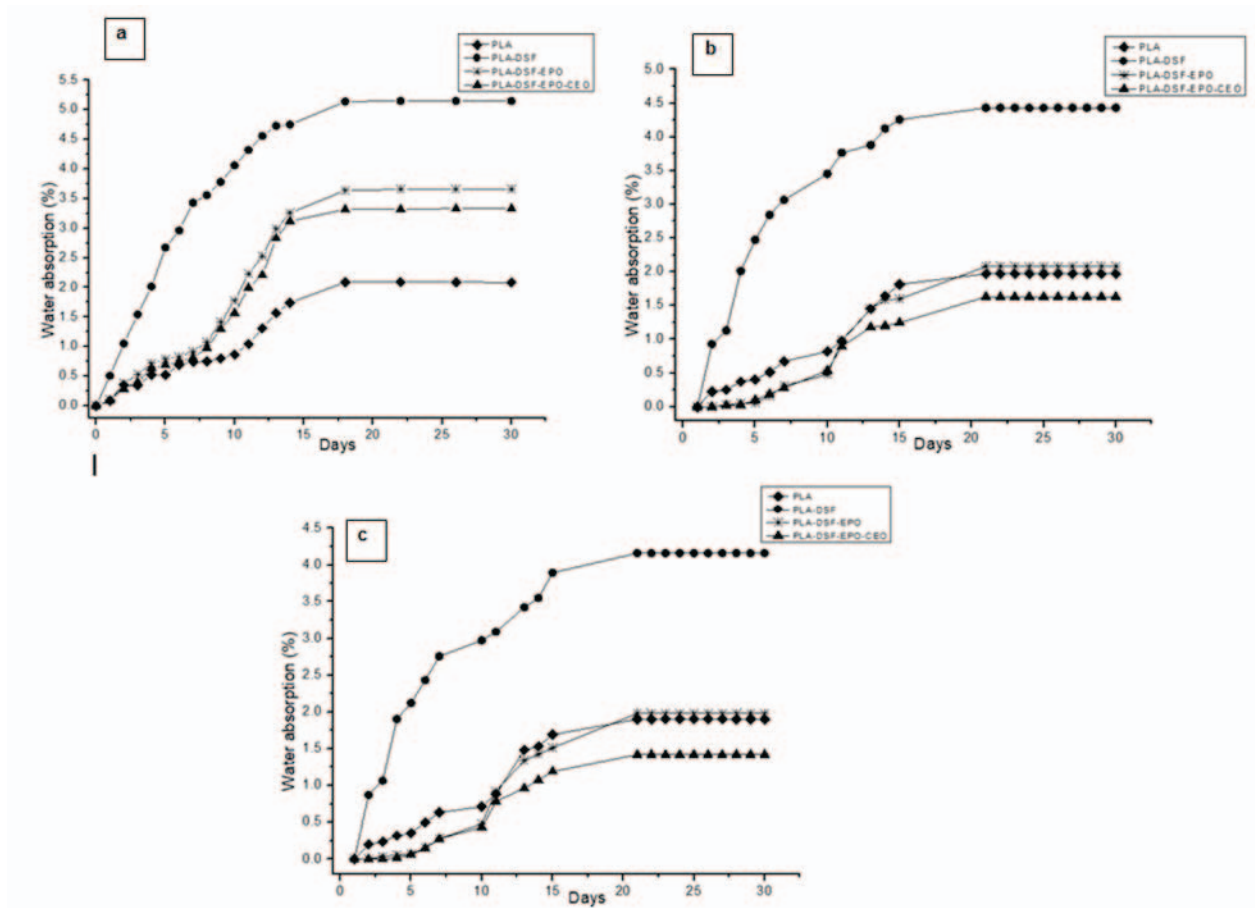


Fig. 2. Water absorption of PLA biocomposite for a) untreated SCCO<sub>2</sub>, b) treated SCCO<sub>2</sub> at condition 1 (100 bar) and c) treated SCCO<sub>2</sub> at condition 2 (200 bar).

The addition of hydrophilic fibre into the hydrophobic polymer causing swelling of the matrix [6]. Swelling affects the bonding between the matrix and fibre, thereby, indirectly decreasing the mechanical properties of a biocomposite. The water uptake in the untreated biocomposite after 30 days was 2.09%, while for the treated sample it was 1.96% (condition 1) and 1.83% (condition 2). These findings could be due to the hydrophobic nature of the polymer [22]. PLA also possesses good barrier properties against water absorption [20]. Other than that, the presence of EPO in the PLA biocomposite reduced the amount of water absorbed compared to the PLA biocomposite. It was shown that EPO slightly affected the water uptake because EPO functions as a plasticizer and exhibits a hydrophobic nature [23]. Hence, the addition of EPO resulted in a hydrophobic behaviour that tended to resist water molecules. The triglyceride oil compound present in palm oil enables samples to be insoluble in water as reported by Seniha et al. [24].

The effect of CEO on water absorption can be observed in Fig. 2. A significant difference was detected in the sample impregnated with CEO, which presented a lower water uptake. After 30 days, an increase of about 3.15% in the total water uptake of the impregnated film under condition 2 was noted, as depicted in Fig. 2(c), whereas for the film impregnated under condition 1, it was 3.47%, as shown in Fig. 2(b). These results could be correlated to the SCCO<sub>2</sub> treatment conditions. As shown in Fig. 2(a), the PLA-DSF-EPO-CEO biocomposite without SCCO<sub>2</sub> treatment exhibited a 3.66% increase, where the water absorption decreased with the addition of CEO. This showed that the presence of CEO in the biocomposite increased its hydrophobicity and subsequently, reduced its ability to absorb water molecules, which is an important improvement for packaging applications.

Nevertheless, the water absorption of the untreated and treated biocomposites varied insignificantly. The water uptake decreased slightly for the sample in the presence of cinnamaldehyde, a compound extracted from pure CEO, as evident in the GC analysis presented in Fig. 7. The water barrier is a property that dominates potential applications of these plastics in the food industry. Materials with a low ability to absorb water are required to protect food products against contact with water [20, 22].

### 3.2. Soil Burial Degradation Analysis

A soil burial degradation test was used to monitor weight loss of PLA biocomposite sample. Through the soil burial degradation test, the effects of an ordinary and real composting environment on the specimens without any enzymatic and composting resources could be studied. The biodegradability was tested using normal soil to mimic a real environment. The physical appearance was also observed to identify changes in the shape and size of the samples. After 60 days, the samples were observed under SEM. The percentage of weight loss was evaluated using Eq. (2). The weight loss of the untreated and SCCO<sub>2</sub>-treated PLA biocomposites with different element contents after 80 days of composting are presented in Fig. 3. The weight loss was affected by the absorption of moisture from the soil and the actions of microorganisms [25].

Fig. 3 shows the weight loss of the PLA biocomposite film after 80 days. The results revealed that the percentage of degradation for all the specimens increased with the time interval. The treated PLA biocomposite under condition 2 (200 bar) shows higher degradability with a weight loss of 96.58%, while for the treated PLA biocomposite under condition 1 (100 bar) and the untreated biocomposite the weight loss was 95.17% and 93.23%, respectively. The treated sample under condition 2 consisted of a more porous structure, which contributed to the increase in the degradation rate of the film. A similar trend had been reported in which the weight loss of the PLA biocomposite increased with the existence of more pores within the blends [3]. Porosity aids bacteria and microorganisms to move through the film as shown in the SEM micrograph in Fig. 5. Additionally, the presence of natural fibre is believed to speed up the degradation of specimens due to poor adhesion between the matrix and reinforcement [6]. Natural fibre is also more compatible with the surrounding environment, which leads to the degradation process. The high cellulose content in the fibre causes high water absorption, which has a synergistic effect on residual loss and improves the degradation rate of composites [5].

The lowest residual loss was exhibited by the unreinforced PLA (65.37%), while the weight loss of the treated PLA under condition 1 and condition 2 was 67.01% and 68.56%, respectively. These circumstances occurred due to the hydrophobic behaviour of the PLA, which resulted in a lower water uptake, leading to a reduction in the degradation rate [7]. As such, in the soil burial test, the lower composition of PLA resulted in an increase in the weight loss. However, PLA decomposes better than petroleum-based matrices because of



its biodegradability [5]. Biodegradable plastics will eventually degrade in landfills as they are made from natural resources [26]. Other than that, EPO reduced the percentage of weight loss of the PLA biocomposite. Based on Fig. 3, the weight loss for the untreated sample with the added of EPO was 76.72%. In addition, as compared to the untreated biocomposite, the treated biocomposite had an increment of about 2.87% and 3.56% in the degradation rate for condition 1 and 2, respectively. EPO acts as a plasticizer to improve the flexibility of PLA biocomposites. Therefore, the porosity of the treated sample increased its degradation rate [10, 23].

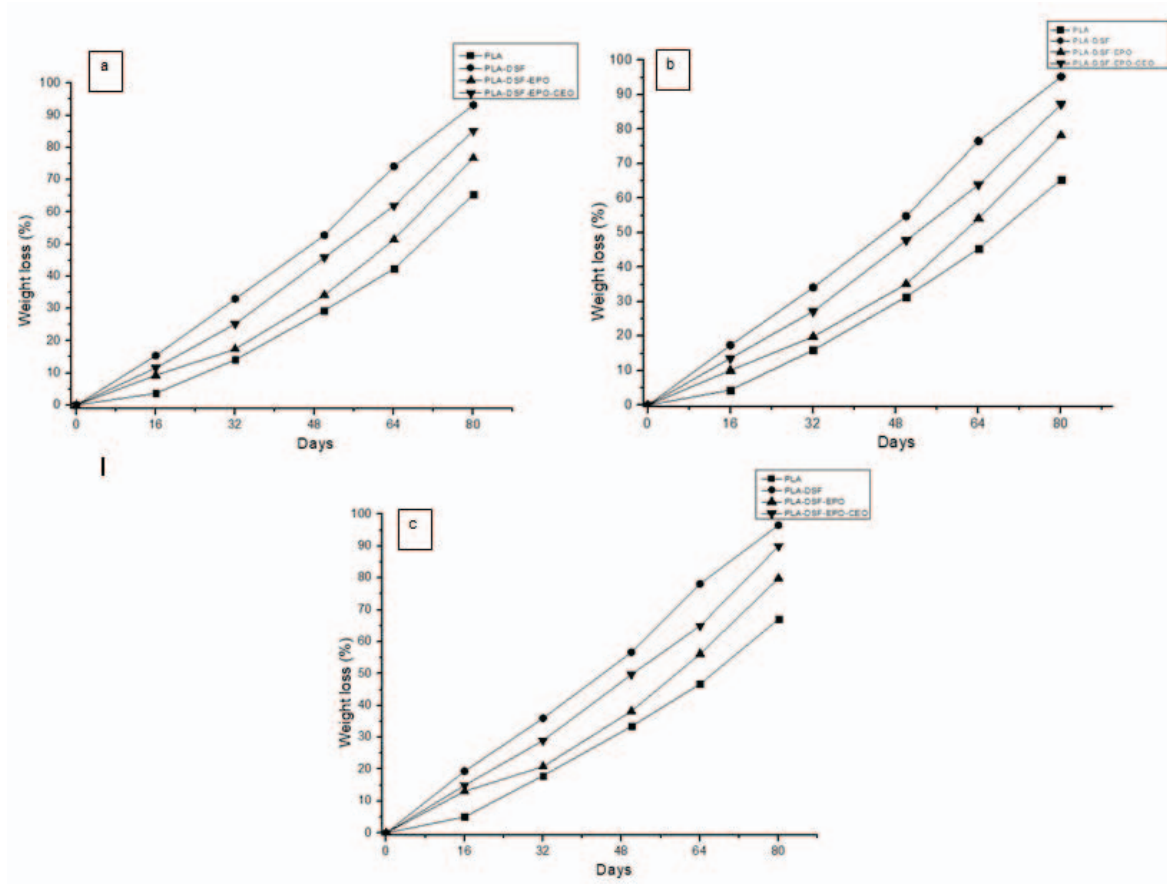


Fig. 3. Weight loss of PLA biocomposite for a) untreated sample, b) treated sample at condition 1 and c) treated sample at condition 2.

The weight loss experienced by the untreated PLA-DSF-EPO-CEO biocomposite after 80 days was 85.18% (Fig. 3(a)). This revealed that the degradability of the specimens dependent on the addition of CEO. There was a slight difference between the samples with and without CEO. The PLA biocomposite film with CEO degraded faster in the soil compared to the PLA-DSF-EPO specimen. Fig. 3(c) shows that the treated biocomposite (condition 2) with CEO degraded the fastest, followed by the treated biocomposite (condition 1) and untreated biocomposite. The presence of CEO in the PLA biocomposites weakened the specimens. This caused the degradation rate of the PLA biocomposite films to increase due to the weak bonding after buried in soil. Furthermore, some additive elements inside the specimens might have migrated into the soil and helped in the degradation process [27].

### 3.3. Surface Morphology

Fig. 4 and 5 illustrate the surface micrographs for the untreated and SCCO<sub>2</sub>-treated PLA-DSF-EPO-CEO films before and after 60 days of the soil burial degradation test. This confirmed that various changes had taken place on the surface of the biocomposite films. The results for the sample without SCCO<sub>2</sub> treatment are shown in Fig. 4, while the findings for the treated samples under conditions 1 and 2 are presented in Fig. 5. After the degradation process, more pores and visible ruptures on the surface were noted.

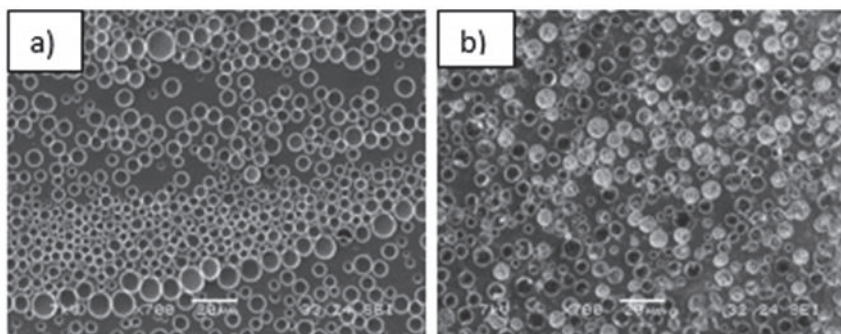


Fig. 4. The surface morphology for PLA-DSF-EPO-CEO films without treatment a) before and b) after 60 days of soil burial.

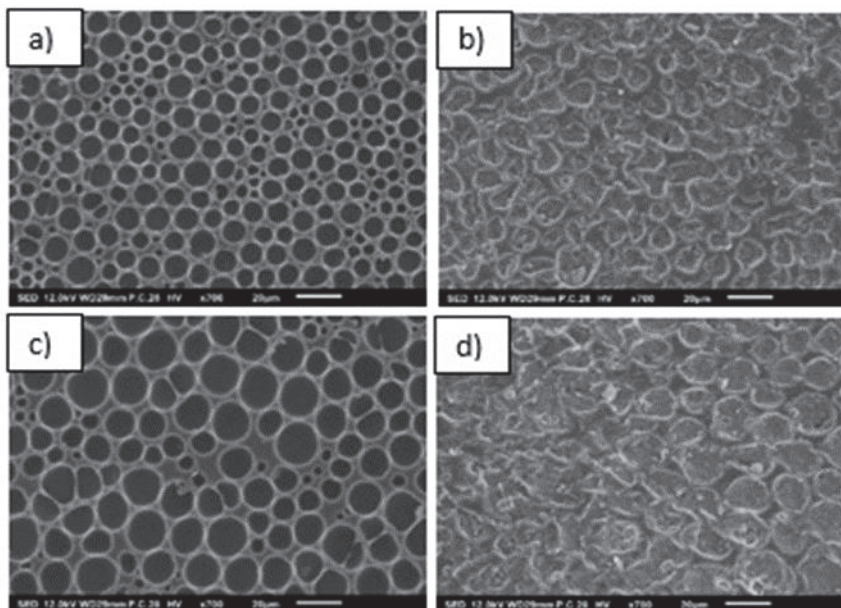


Fig. 5. The surface morphology for PLA-DSF-EPO-CEO films underwent SCCO<sub>2</sub> treatment a) before degradation (condition 1), b) after degradation (condition 1), c) before degradation (condition 2) and d) after degradation (condition 2).

The influence of SCCO<sub>2</sub> treatment with degradation time on the biocomposites was observed under SEM. More apparent physical changes had taken place within the surface of the biocomposites treated with SCCO<sub>2</sub> compared to the samples without SCCO<sub>2</sub>. Based on the observation, Fig. 5(b) and (d) showed more ruptures than Fig. 4(b). The surface of the untreated films was less disrupted unlike the treated samples after Day 60. Such changes in the treated samples were signs of the degradation of the PLA biocomposite films. According to Fig. 5, before the soil burial test, a high porosity was observed on the surface of the biocomposite after the SCCO<sub>2</sub> treatment. In contrast, after the burial in soil, all the films were rough and had numerous holes on the surface. Furthermore, the samples also physically changed. The weight loss results could be correlated with the SEM micrographs, as shown in Fig. 4 and 5.

### 3.4. Antimicrobial Analysis

Antimicrobial activity was investigated in two steps. Firstly, the antimicrobial activity of the CEO was examined using the agar diffusion method. This preliminary study was carried out to evaluate the antimicrobial effect of pure CEO; the results are presented in Fig. 6 (a-b). In the second step, CEO was incorporated into the PLA film. The effect of the antimicrobial activity of CEO in the PLA biocomposites was studied using the agar diffusion method and it was then tested against selected microorganisms. There is no agreement on the standard procedures to evaluate the effectiveness of antimicrobial activities [14]. An antimicrobial test was conducted after the PLA biocomposites had been treated with  $\text{SCCO}_2$ .

The antimicrobial activities of the untreated PLA biocomposite films incorporated with CEO against gram-positive (*Staphylococcus aureus*) and gram-negative (*Escherichia coli*) bacteria are shown in Fig. 6. Both bacteria represent the spoilage of the microorganism groups normally found in food products. The size of the inhibition zone around the disks determined the inhibitory activities of the specimen films [17]. Although the preliminary results of bacteria inhibition were satisfactory, showing that a complete inhibition of bacteria can be achieved by increasing the amount of CEO, the PLA biocomposites however became more brittle when the CEO content was increased. To overcome this problem, it was necessary to vary the content of the plasticizer. Nevertheless, this study focused only on the incorporation of 1 wt% of CEO.

The control samples without CEO negatively inhibit any of the tested bacteria, which resulted in no inhibition zones around the films. In Fig. 6 (a–b), all the films of the control samples were unable to stop the growth of the pathogens. In fact, bacteria colonies were formed on the agar. This result agreed with the findings by Ghasemlou et al. [28] on the plasticized corn starch films with essential oil. They reported that the control films negatively exhibited inhibition zone against the tested bacteria. This indicates that the main material used contained no antimicrobial agent, and therefore, the essential oil was incorporated into the polymer films. No clear zones appear show that the specimens were not inhibitory [17].

Fig. 6 (e–f) shows the inhibitory effect of films containing 1 wt% CEO against gram positive (*S. aureus*) and gram negative (*E. coli*) bacteria. All the films incorporated with CEO inhibited the growth of the two tested bacteria. The 1 wt% concentration of CEO resulted in a significant inhibition, with a diameter of  $15.1 \pm 0.5$  mm for *E. coli* and  $12.5 \pm 0.5$  mm for *S. aureus*. These results were significantly different from that of the control specimens. In Anuar et al. [1], the untreated PLA biocomposite film with 1 wt% of CEO showed an inhibition area of  $15.05 \pm 0.5$  mm for the *Bacillus subtilis* (gram-negative) and  $12.8 \pm 0.5$  mm for the *S. aureus*. There was a slight difference in the antimicrobial activity results between the treated and untreated samples. However, both samples still achieved the objective of inhibiting bacterial growth. This demonstrated that CEO had a strong antimicrobial activity towards both bacteria. The addition of 0.1 wt% of CEO to the PLA film is adequate to decrease the growth of the *S. aureus* [14]. The results of the current study were in agreement with those who also noticed a higher antimicrobial effect among biodegradable films incorporated with CEO [15]. It is important to note that the antimicrobial activity of the PLA film with CEO is based on preliminary studies that evaluated the antimicrobial activity of pure CEO, as in Fig. 6 (c–d).

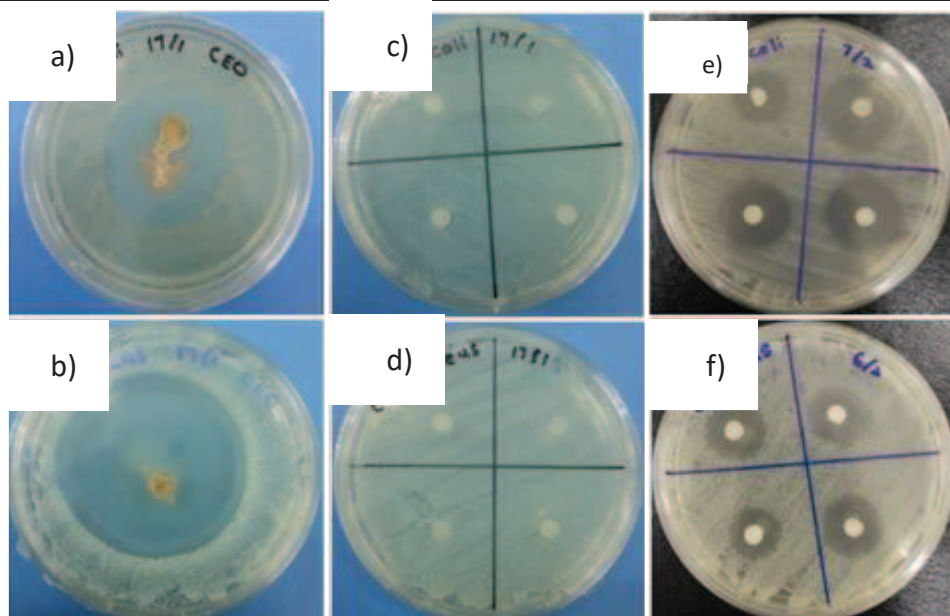


Fig. 6. The inhibition zone of a) control sample without CEO in *E-coli*, b) control sample without CEO in *S. aureus*, c) pure CEO in *E. coli*, d) pure CEO in *S. aureus*, e) sample incorporated CEO in *E-coli* and f) sample incorporated CEO in *S. aureus*.

Table 2 lists the results of the inhibitory effect of CEO incorporated into the bio-based polymer, which was lower than that of pure essential oil. The same outcome is observed as reported on polyvinyl alcohol (PVA)-cassava bagasse incorporated with essential oil [29,30]. According to Santos et al. [29] and Debiagi et al. [30], the processing surroundings caused a partial loss of the volatile components of the essential oil during the preparation of the biocomposite films. The gram-negative bacteria (*E. coli*) were more resistant than the gram-positive bacteria (*S. aureus*) towards the antibacterial treatment. The lower antimicrobial activity against gram-negative bacteria (*E. coli*) affects the external lipopolysaccharide wall close to the peptidoglycan cell wall. This limits the diffusion of hydrophobic compounds through the lipopolysaccharide layer. On the other hand, gram-positive bacteria (*S. aureus*) have a thick layer of peptidoglycan that may function as a preventive barrier against certain essential oil compounds [28].

Table 2: Antimicrobial activity of PLA biocomposite incorporated with CEO

Tested bacteria	Diameter of inhibitory zone (mm)		
	Control	1 wt% CEO	PLA biocomposite incorporated 1 wt% CEO
<i>S. aureus</i>	0±0	35.3±0.5	12.5±0.5
<i>E. coli</i>	0±0	32.7±0.2	15.1±0.5

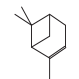
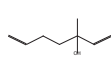
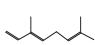
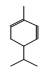
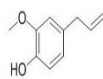
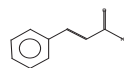
The active compound, cinnamaldehyde, expressed a high antimicrobial activity against gram-positive and gram-negative bacteria. The antimicrobial efficiency of essential oils is related to the concentration and proportion of the phenolic compound [30]. It is believed that the amount of CEO that is added has a role in increasing the inhibition zone of the bacteria. Various researches have been carried out on essential oils incorporated into biocomposite films used in the food packaging industry. Phenolic compounds disintegrate

the external cell membrane and mitochondria of bacteria, allowing them to become permeable, and leading to leakage of the cell wall. From the gas chromatography (GC) data on CEO presented in Fig. 7, the presence of the main phenolic and terpenoid compounds effectively reduced the zone inhabited by the *E. coli* and *S. aureus*. The high content of cinnamaldehyde and  $\alpha$ -eugenol in CEO through a GC analysis as reported by Bongiovanni et al. [31]. CEO yielded good antibacterial activity compared to thyme and lemongrass oils, and better antibacterial activity than other essential oils like rosemary and oregano [32].

### 3.5. Gas Chromatography

About six different elements with varying retention times were detected via the gas chromatography (GC) analysis (Fig. 7). The contents of the elements identified in pure CEO are tabulated in Table 3. These elements were identified through a retention time and mass spectral library search. The relative amount of each constituent was calculated according to the GC peak area. As seen in Table 3, the antimicrobial components were characterised by a dominant concentration of cinnamaldehyde (46.615%) and eugenol (16.345%). Other main constituents included  $\alpha$ -Pinene (2.901%), 3-methyl-hepta-1,6-dien-3-ol (9.064%), trans- $\alpha$ -Ocimene (8.709%), and  $\alpha$ -Phellandrene (0.865%), which acted as antibacterial and antifungal elements but were less effective in inhibiting the bacteria. Most CEO components are phenolic in nature and are volatile, and also consist of trace levels of terpenes with antibacterial activity [33].

Table 3: Composition of element content in the pure cinnamon essential oil (CEO)

R.T. (minutes)	Name Compound	Area %	Quant S/N	Area	MW	Structure	Molecular Formula
6.84524	$\alpha$ -Pinene	2.9105	3.8659	294004	136		C <sub>10</sub> H <sub>16</sub>
10.3362	3-Methyl-hepta-1,6-dien-3-ol	9.0646	4.5627	915667	126		C <sub>8</sub> H <sub>14</sub> O
15.4335	trans- $\alpha$ -Ocimene	8.7029	5.1193	879130	136		C <sub>10</sub> H <sub>16</sub>
8.90751	$\alpha$ -Phellandrene	0.86546	2.5648	87425	136		C <sub>10</sub> H <sub>16</sub>
14.9643	Eugenol	16.345	7.4453	1651138	164		C <sub>10</sub> H <sub>12</sub> O <sub>2</sub>
12.9065	Cinnamaldehyde, (E)-	46.615	20.201	4708802	132		C <sub>9</sub> H <sub>8</sub> O

Cinnamaldehyde and eugenol combinations are already being used as disinfectants in hospitals, especially for medical devices [34]. The experimental test enabled the evaluation and comparison of antimicrobial activity against bacteria commonly found in food products. With these findings, it can be concluded that CEO is suitable and more effective against the tested bacteria since it presents a wider inhibition zone with a lower concentration. It was hypothesised that this result could be due to the presence of cinnamaldehyde as an active compound against both gram-positive and gram-negative bacteria. Furthermore, this finding also presented an important approach in developing active packaging with a lower

concentration of active essential oil. Many studies on the antimicrobial activity of active films incorporated with other essential oils have indicated their potential for use in food packaging. As such, the effectiveness of antimicrobial films activated with CEO should be considered by the food packaging industry.

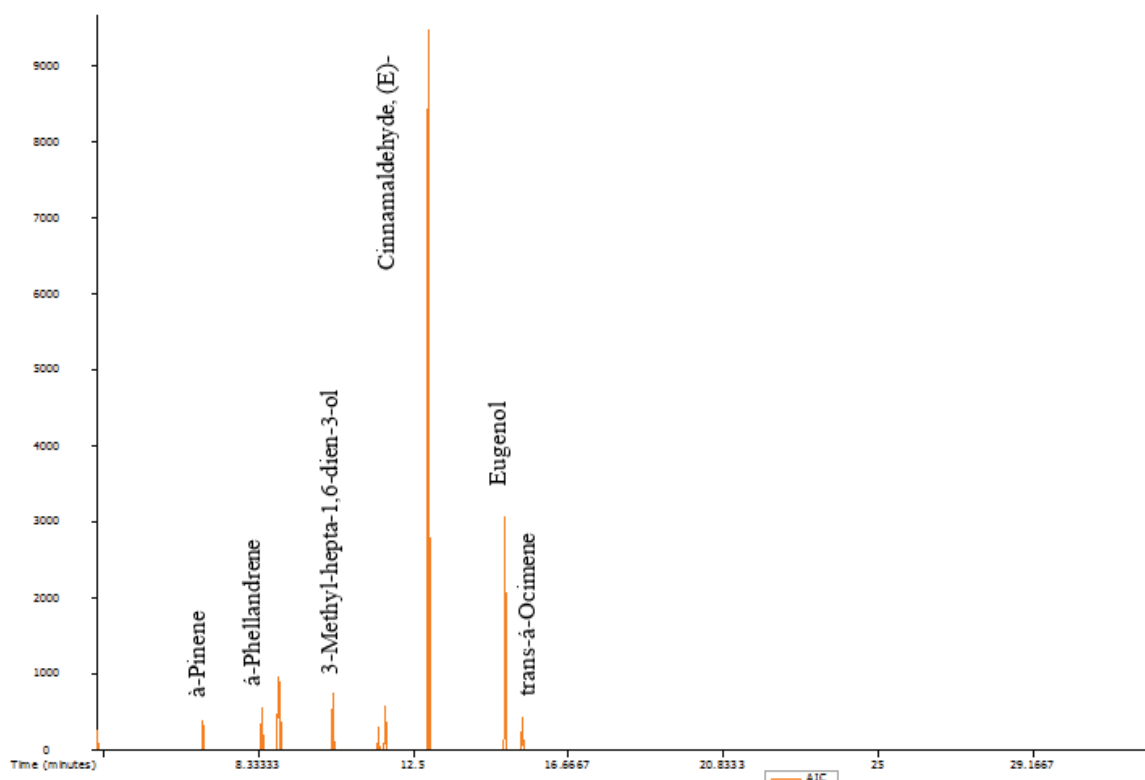


Fig. 7. Gas chromatography profile of cinnamon essential oil.

## 4. CONCLUSION REMARKS

The weight loss for PLA biocomposite was increased due to the presence of more porosity in the biocomposites. The water absorption evident that SCCO<sub>2</sub> treatment aids to reduce the water uptake of PLA biocomposite due to plasticizing effect. The plasticizer decreased the moisture transfer between the food and packaging, thus improving the shelf-life of packaged food. Only 1 wt% CEO has optimized the antimicrobial properties for active food packaging application. Besides that, the presence of aldehyde as a functional group in CEO was evident by using GC-MS/TOF. The use of CEO is very significant in this research as an antimicrobial agent for the biocomposites film. Based on the findings, SCCO<sub>2</sub> could be an interesting alternative treatment in the food packaging industry as compared to the conventional method.

## ACKNOWLEDGEMENT

The authors wish to thank the Ministry of Higher Education (MOE) for the funding provided through the Fundamental Research Grant Scheme (FRGS16-003-0502), Research Initiative Grant Scheme – Post-Doctoral Fellow (RPDF18-010-0010) from International Islamic University Malaysia (IIUM), Department of Science & Technology (DST)-ASEAN-India

Research Training Fellowship (RTF/2019/000083) for the equipment and facilities provided in making these studies a success.

## REFERENCES

- [1] Anuar H, Nur Fatin Izzati B, Sharifah Nurul Inani SM, Siti Nur E'zzati MA, Siti Munirah Salimah AB, Ali FB, Manshor MR. (2017) Impregnation of cinnamon essential oil into plasticised polylactic acid biocomposite film for active food packaging. *Journal of Packaging Technology and Research*, 1(3): 149-157.
- [2] Lithner D. (2011) Environmental and health hazards of chemicals in plastic polymers and products. PhD thesis. University of Gothenburg, Department of Plant and Environmental Sciences.
- [3] Thothong S, Jarerat A, Sriroth K, Tantatherdtam R. (2013) Degradation of porous starch granules and poly (butylene adipate-co-terephthalate) (PBAT) blends: Soil burial and enzymatic tests. *Advanced Materials Research*, 651: 12-17.
- [4] Nur Aimi MN, Anuar H, Manshor MR, Wan Nazri WB, Sapuan SM. (2014) Optimizing the parameter in durian skin fiber reinforced polypropylene composites by response surface methodology. *Industrial Crops and Products*, 54: 291-295.
- [5] Yussuf AA, Massoumi I, Hassan A. (2010) Comparison of polylactic acid/kenaf and polylactic acid/rise husk composites: The influence of the natural fibres on the mechanical, thermal and biodegradability. *Journal of Polymers and the Environment*, 18(3): 422-429.
- [6] Gunti R, Ratna Prasad AV, Gupta AVSSKS. (2016) Mechanical and degradation properties of natural fiber-reinforced PLA composites: Jute, sisal and elephant grass. *Polymer Composites*, 39(4): 1125-1136.
- [7] Kumar R, Yakubu MK, Anandjiwala RDY. (2010) Biodegradation of flax fibre-reinforced polylactic acid. *Express Polymer Letters*, 4(7): 423-430.
- [8] Wan Nazri WB, Ezdiani ZN, Romainor MM., Erma KS, Jurina J, Noor Fadzlina IZA. (2014) Effect of fibre loading on mechanical properties of durian skin fibre composite. *Journal Tropical Agriculture and Food Science*, 42(2): 169-174.
- [9] Manshor MR, Anuar H, Nur Aimi NM, Ahmad Fitrie MI, Wan Nazri WB, Sapuan SM, El-Shekeil YA, Wahid MU. (2014) Mechanical, thermal and morphological properties of durian skin fibre reinforced PLA biocomposites. *Material and Design*, 59: 279-286.
- [10] Ali F, Awale Fakhruddin RJ, Anuar H. (2016) Plasticizing poly (lactic acid) using epoxidized palm oil (EPO) for environmental friendly packaging material. *Malaysian Journal of Analytic Sciences*, 20(5): 1153-1158.
- [11] Silverajah VSG, Ibrahim NA, Yunus WM, Hassan HA, Woei CB. (2012) A comparative study on the mechanical, thermal and morphological characterization of poly (lactic acid)/epoxidized palm oil blend. *International Journal of Molecular Sciences*, 13: 5878-5898.
- [12] Chieng BW, Ibrahim NA, Wan Md Zin WY, Hussein MZ. (2014) Epoxidized vegetable oils plasticized poly (lactic acid): Mechanical, thermal, and morphology properties. *Journal Applied Polymer Science*, 130: 4576-4580.
- [13] Souza A, Dias AMA, Sousa HC, Tadini CC. (2013) Cassava starch composite films incorporated with cinnamon essential oil: Antimicrobial activity, microstructure, mechanical and barrier properties. *LWT - Food Science and Technology*, 54: 346-352.
- [14] Qin Y, Yang J, Xue J. (2015) Characterization of antimicrobial poly (lactic acid)/ poly (trimethylene carbonate) films with cinnamaldehyde. *Journal of Material Science*, 50(3): 1150-1158.
- [15] Erdohan ZÖ, Belgizar C, Turhan KNB. (2013) Characterization of antimicrobial polylactic acid-based films. *Journal of Food Engineering*, 119(2): 308-315.
- [16] Vazirian MA, Alehabib S, Hossein J, Mohammad RF, Toosi AN, Mahnaz K. (2015) Antimicrobial effect of cinnamon (*Cinnamomum verum* J. Presl) bark essential oil in cream-filled cakes and pastries. *Research Journal of Pharmacognosy*, 2(4): 11-16.
- [17] Wu J, Sun X, Guo X, Ge S, Zhang Q. (2017) Physicochemical properties, antimicrobial activity and oil release of fish gelatin films incorporated with cinnamon essential oil. *Aquaculture and Fisheries*, 2(4): 185-192.

- [18] Milovanovic S, Kuska R, Skoric-Lucic M, Kalagasidis-Krusic M, Frerich S, Zizovic, I, Ivanovic J. (2016) Swelling kinetics and impregnation of PLA with thymol under supercritical CO<sub>2</sub> conditions. *Tehnika*, 71(1): 16-20.
- [19] Patpen P, Russly AR, Rosnita AT, Khalina A. (2015) Mechanical properties and water absorption behaviour of durian rind cellulose reinforced poly (lactic acid) biocomposites. *International Journal on Advanced Science Engineering Information Technology*, 5(5): 343-348.
- [20] González A, Alvarez I, Cecilia I. (2013) Soy protein - Poly (lactic acid) bilayer films as biodegradable material for active food packaging. *Food Hydrocolloids*, 33(2): 289-296.
- [21] Souza A, Goto GEO, Mainardi JA, Coelho ACV, Tadini CC. (2014) Impregnation of cinnamaldehyde into cassava starch biocomposite films using supercritical fluid technology for the development of food active packaging. *Carbohydrate Polymers*, 102: 830-837.
- [22] Aranda-Garcia FJ, González-Núñez R, Jasso-Gastinel CF, Mendizábal E. (2015) Water absorption and thermomechanical characterization of extruded starch/ poly (lactic acid)/ agave bagasse fibre bioplastic composites. *International Journal of Polymer Sciences*, 2015: 1-7.
- [23] Emad AJA, Wan Md. Zain WY, Nor Azowa I, Mohd Zaki AR. (2010) Properties of epoxidized palm oil plasticized polylactic acid. *Journal Material Science*, 45: 1942-1946.
- [24] Seniha GF, Yagci Y, Tuncer EAY. (2006) Polymers from Triglyceride Oils. *Progress in Polymer Science*, 31: 633-670.
- [25] Amer ZJA, Saeed AQ. (2015) Soil burial degradation of polypropylene/ starch blend. *International Journal of Technical Research and Applications*, 3(1): 91-96.
- [26] Weng YX, Jin YJ, Meng QY, Wang L, Zhang M, Wang YZ. (2013) Biodegradation behaviour of poly (butylene adipate-co-terephthalate) (PBAT), poly (lactic acid) (PLA), and their blend under soil conditions. *Polymer Testing*, 32(5): 918-926.
- [27] Lardjane N, Belhaneche BN. (2009) Migration of additives in simulated landfills and soil burial degradation of plasticized PVC. *Journal of Applied Polymer Science*, 111(1): 525-531.
- [28] Ghasemlou M, Aliheidari N, Fahmi R, Shojaee-Aliabadi S, Keshavarz B, Cran MJ, Khaksar R. (2013) Physical, mechanical and barrier properties of corn starch films incorporated with plant essential oils. *Carbohydrate Polymers*, 98(1): 117-1126.
- [29] Santos SF, Novales MG. (2012) Essential Oils from Aromatic Herbs as Antimicrobial Agents. *Current Opinion in Biotechnology*, 23: 136-141.
- [30] Debiagi F, Kobayashi, Renata KT, Nakazato GP, Luciano A, Mali S. (2014) Biodegradable active packaging based on cassava bagasse polyvinyl alcohol and essential oils. *Industrial Crops and Products*, 52: 664-670.
- [31] Bongiovanni V, Colombo M, Laura C, Andrea T, Daniela C. (2017) Determining odour-active compounds in a commercial sample of cinnamomun cassia essential oil using GC-MS and GC-O. *Journal of Chromatography & Separation Techniques*, 8(1): 1-7.
- [32] Gende L, Floris I, Fritz R, Eguaras M. (2008) Antimicrobial activity of cinnamon (*Cinnamom zeylanicum*) essential oil and its main components against *Paenibacillus* larvae from Argentina. *B. Insectol*, 61(1): 1-4.
- [33] Adinew B. (2014) GC-MS and FT-IR analysis of constituents of essential oil from cinnamon bark growing in South-west of Ethiopia. *International Journal of Herbal Medicine*, 1(6): 22-31.
- [34] Goni P, Lopez P, Sanchez C, Gomez LR, Beceril R, Nerin C. (2009) Antimicrobial activity in the vapour phase of a combination of cinnamon and clove essential oils. *Food Chemistry*, 116: 982-989.



# DYNAMIC MODELING OF A SINGLE-LINK FLEXIBLE MANIPULATOR ROBOT WITH TRANSLATIONAL AND ROTATIONAL MOTIONS

DERMAWAN DERMAWAN<sup>1,2\*</sup>, HAMMADA ABBAS<sup>1</sup>, RAFIUDDIN SYAM<sup>1</sup>,  
ZULKIFLI DJAFAR<sup>1</sup> AND ABDUL KADIR MUHAMMAD<sup>2</sup>

<sup>1</sup>*Department of Mechanical Engineering, Hasanuddin University,  
Gowa-Makassar, Indonesia.*

<sup>2</sup>*Department of Mechanical Engineering, State Polytechnic of Ujung Pandang,  
Makassar, Indonesia*

\*Corresponding author: [dermawan@poliupg.ac.id](mailto:dermawan@poliupg.ac.id)

(Received: 26<sup>th</sup> August 2019; Accepted: 27<sup>th</sup> November 2019; Published on-line: 20<sup>th</sup> January 2020)

**ABSTRACT:** The flexible manipulator is widely used in space robots, robot arm, and manufacturing industries that produce micro-scale products. This study aims to formulate the equation of motion of a flexible single-link manipulator system that moves translationally and rotationally and to develop computational codes with the finite-element method in performing dynamic simulation on the vibration of the flexible manipulator system. The system of the single-link flexible manipulator (SLFM) consists of an aluminium beam as a flexible link, a clamp part to hold the link, a DC motor to rotate the drive shaft, a trajectory to transfer the link in translational motion, and a servo motor to rotate the link. Computational codes in time history response (THR) and Fast Fourier Transform (FFT) processing were developed to identify the dynamic behaviour of the link. The finite-element method and Newmark-beta are used in simulating the SLFM. Simulation using the finite-element method has displayed dynamic behaviour through a graph of FFT on free vibration and THR graph on forced vibration by the excitation force due to the translational and rotational motions of the system. FFT has also generated natural frequency values as  $f$  8.3 [Hz]. For translational and rotational motions, lateral deformation gets the maximum deviation at the value 0.0077 [m] and the minimum deviation -0.0085 [m] at  $t = 0$  [s]. While at time  $t = 0.5$  [s] due to the existence of the excitation force at the time, the maximum deviation at the value -0.009 [m], and the minimum deviation -0.0085 [m].

**ABSTRAK:** Pemanipulasi fleksibel banyak digunakan dalam robot angkasa, lengan robot, dan industri pembuatan yang menghasilkan produk skala-mikro. Kajian ini bertujuan mengformulasi persamaan pergerakan sistem manipulasi pautan-tunggal fleksibel yang bergerak secara realisasi dan putaran dan bagi membina kod pengkomputeran dengan kaedah unsur-terhingga dalam membuat simulasi dinamik pada getaran sistem manipulasi fleksibel. Sistem manipulasi pautan-tunggal fleksibel (SLFM) terdiri daripada alur aluminium sebagai pautan fleksibel, bahagian pengapit bagi memegang pautan, motor DC bagi memutar pandu aci, trajektori bagi memindahkan pautan dalam gerakan realisasi, dan motor servo bagi memutar pautan. Kod pengkomputeran dalam Sambutan Respons Masa (THR) dan proses Penjelmaan Fourier Pantas (FFT) telah dibina bagi mengenal pasti kelakuan dinamik pada pautan. Kaedah unsur-terhingga dan beta-Newmark telah digunakan dalam simulasi SLFM. Simulasi menggunakan kaedah unsur-terhingga menunjukkan kelakuan dinamik melalui graf FFT pada bebas getaran dan graf THR pada getaran paksaan melalui ujaan paksa bagi membentuk realisasi dan gerakan putaran pada sistem. FFT juga menghasilkan nilai frekuensi semula jadi sebagai  $f$  8.3 [Hz]. Bagi

realisasi dan gerakan putaran, sisihan perubahan bentuk maksimum ialah pada nilai 0.0077 [m] dan sisihan minimum -0.0085 [m] pada  $t = 0$  [s]. Sementara pada masa  $t = 0.5$  [s] bergantung pada ujaan paksa yang hadir pada masa tersebut, sisihan maksimum ialah pada nilai -0.009 [m], dan sisihan minimum ialah -0.0085 [m].

---

**KEYWORDS:** *dynamic modelling; single-link flexible manipulator; finite-element method; time history response; translational and rotational motions*

## 1. INTRODUCTION

In industrial applications and robotic systems, single-link flexible manipulators (SLFM) are expected to work optimally during operation. Researchers who study flexible manipulators for space can be found in many reputable journals, such as [1-6]. For the application of space robots, a manipulator robot is designed to lift relatively small objects such as rock samples and remove existing obstacles so that the manipulator must be able to carry out operations with better positioning accuracy. Lower weight aims to save load capacity and reduce the cost of rocket launches and reduce energy consumption. SLFM has limitations with frequent vibrations that cause system performance to be interrupted. Therefore, further research is needed to describe the dynamic conditions of the SLFM. Several studies have investigated the performance and control system of the SLFM. Qiu [7] reviewed two main parts of the flexible Cartesian manipulator (FCM), explicitly the control algorithm and validated it with the experiment. The FCM used Fiberglass colophony material. The FCM experiment only displayed translational motion along the  $Y$ -axis ( $O$ - $Y$ - $O$ ). Conversely, Shin and Rhim [8] conducted modelling with the Newtonian approach to horizontal translational motion ( $O$ - $X$ - $O$ ) on the flexible link. The modelling result showed the effect of lateral vibration and dynamic stiffness at varying frequencies of the beam. Yang et al. [9] designed an observation using partial differential equations (PDE) using kinetic energy and potential energy methods to predict vibration, unlimited dimensional condition by only requiring practical measurement values from a boundary position. From the simulation result, the vibration can be removed using PD control.

The research done by Ata et al. [10] is somewhat different. They used an Euler Bernoulli approach on SLFM, where a flexible beam is considered rigid and marked by a straight line that extends from point  $O$  to the end of the beam, called a virtual link (VL), which is perpendicular to the tangent vector line. The beam on VL moves rotationally. Still, on the SLFM, Muhammad et al. [12-15] carried out comprehensive simulations and experiments with the FEM, PD, and AF control approaches to vibration on the SLFM. They [16-18] also added a piezoelectric actuator on aluminium-based links, which generate stress on two Degrees of Freedom (DOF). Meanwhile, Mahto [18], still in the rotation movement of the SLFM, has investigated it using the finite-element method (FEM) approach with five DOF assuming the link manipulator as a Euler-Bernoulli beam.

A myriad of investigations on the flexible manipulator using FEM in analysing vibration has been reported in the literature such as essential modelling replacement in control algorithm [19], a multi-link flexible robotic manipulator with a smart piezoelectric transducer [20], vibration control of a single-link flexible composite manipulator [21]. Finite-element modelling with the piezo-integrated structure using Hamiltonian principles [22], and free vibration analysis on a thin-plate [23]. Based on several studies, in general, they researched the SLFM system with just one motion: translation or rotation. If the SLFM is applied in industry, it generally uses two movements simultaneously, that is to say, translational and rotational motions. The problem is the lack of research that combines

translational and rotational motions of the SLFM system, which results in inaccurate positioning. Therefore, this research will do a more in-depth study.

Several similarities were also identified with existing research, such as the use of Lagrange's equation, kinetic energy, and potential energy to derive the equation of motion [24]. The difference is, Bien's work focuses on the combination of translational and rotational movements of a two-link manipulator, where the first link moves horizontally, and the second link moves rotationally. Dermawan et al. [25] have found the equation of translational movement in SLFM using the finite-element method. Research from Muhammad et al. [17] as the primary reference in this research, that has formulated the equation of rotational motion at SLFM, becomes interesting to develop by combining translational and rotational movements.

The purpose of this study is to formulate the equation of motion and compose computational codes by FEM on the SLFM system that moves translationally and rotationally. This research used FEM in carrying out dynamic simulations of the SLFM system. The results of the simulation showed the vibration dynamics of the order by displaying a Time History Response (THR) and Fast Fourier Transform (FFT) processing of the system.

## 2. DYNAMIC MODELLING

Based on the kinematic model of the SLFM that moves translationally, as shown in Fig. 1, the position vector of point  $P$  moves translationally at the  $O$ - $Y$  coordinate. The link moves translationally in the horizontal direction at the coordinates  $O$ - $Y_p$  as far as  $Y$ , and  $v_p$  is the lateral deformation to point  $P$ . The base of the link experiences a positive displacement on the  $Y$ -axis as now as  $O$ - $y$ , the positive  $X$ -axis at position  $X_p = x_p$ , and the end of the link is a position vector  $P$ . The position vector  $r(x, t)$  at point  $P$  on the link at  $t = t$ , is represented in the  $O$ - $X$ - $Y$  coordinates.

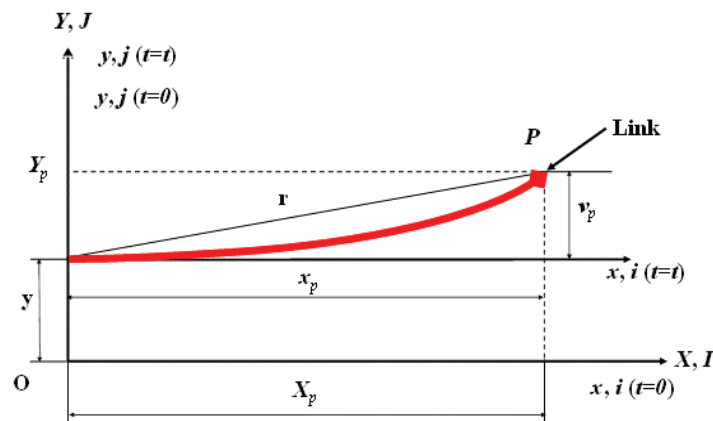


Fig. 1: The position vector of point  $P$  on the link that moves translationally.

The position vector of point  $P$  in the  $O$ - $X$ - $Y$  coordinates is

$$r(x, t) = X_p(x, t)\mathbf{I} + Y_p(x, t)\mathbf{J}, \quad (1)$$

where;

$$X_p(x, t) = x_p, \quad (2)$$

$$Y_p(x, t) = y + v_p. \quad (3)$$

The velocity vector of point  $P$  in the coordinates  $O$ - $x$ - $y$  is given with

$$\dot{\mathbf{r}}(x, t) = \dot{X}_p(x, t)\mathbf{I} + \dot{Y}_p(x, t)\mathbf{J}. \quad (4)$$

### 2.1 Equation of Motion using the Finite-Element Method

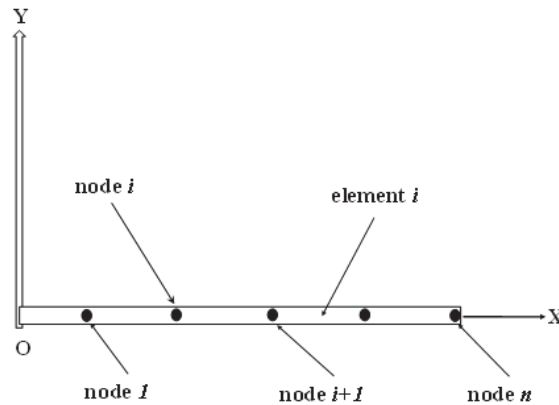


Fig. 2: The translational coordinate of the link.

This paper uses the finite-element method approach, where each partition on the link is presently divided into several elements. The aim is to find out the mass matrix ( $M$ ) and the stiffness matrix ( $K$ ), that will be used to simulate the dynamics of the system. The system dynamics model is a cantilever structure that is partitioned into six elements and six-node points. Fig. 2 show the translational coordinate  $X$ - $Y$  divided by one-dimension and two-node elements with four boundary conditions together at node  $i$  and  $i+1$ .

An element of the link is shown in fig. 3. The finite-element has two DOF, called the lateral deformation of the  $i$ -th element ( $v_i$ ) and slope ( $\varphi_i$ ). The physical properties of the system consist of the length of the link ( $L_i$ ), the cross-sectional area of the link ( $S_i$ ), and the moment of inertia ( $I_i$ ). Each element has mechanical properties, namely Young's modulus and mass density, which are denoted by  $E_i$  and  $\rho_i$ .

The nodal displacement vector is expressed by

$$\delta_i = [v_i, \varphi_i, v_{i+1}, \varphi_{i+1}], \quad (5)$$

with

$$v_i = a_1 + a_2x_i + a_3x_i^2 + a_4x_i^3. \quad (6)$$

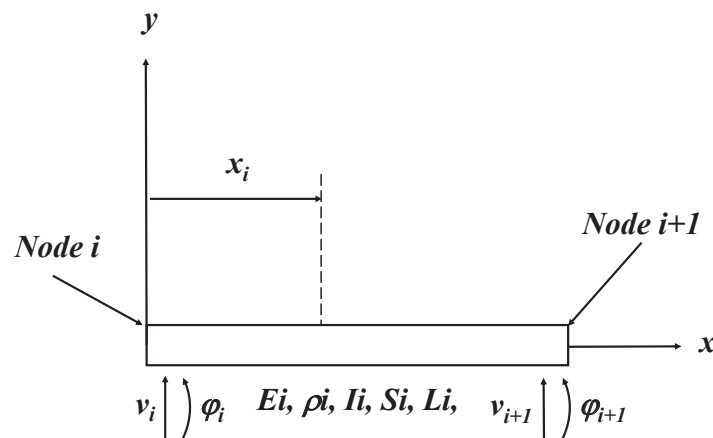


Fig. 3: Nodal displacement of the link.

In the discretization process, the equation of translational motion can be achieved as follows;

Acceleration of  $P$  can be written by

$$\dot{\mathbf{r}}^T \cdot \dot{\mathbf{r}} = \dot{x}_p^2 + \dot{y}^2 + \dot{v}_p^2 + 2\dot{y}\dot{v}_p. \quad (7)$$

The general articulation of kinetic energy ( $T$ ), with ( $V$ ) being the velocity, can be expressed by

$$T = \frac{1}{2} \int_v \rho \cdot V^2 dv. \quad (8)$$

Kinetic energy ( $T_i$ ) of the system is given by

$$T_i = \frac{1}{2} \int_{v_i} \rho_i \cdot \dot{\mathbf{r}}^T \cdot \dot{\mathbf{r}} \cdot dv_i. \quad (9)$$

So that kinetic energy of translation motion ( $T_{it}$ ) for the system can be written as

$$T_{it} = \frac{1}{2} m_i \dot{x}_p^2 + \frac{1}{2} m_i \dot{y}^2 + \frac{1}{2} \delta_i^T M_i \delta_i + \dot{y} f_{ti}^T \delta_i, \quad (10)$$

where

$$\dot{y} f_{ti}^T \delta_i = \frac{m_i}{12} [6 \quad l_i \quad 6 \quad -l_i]. \quad (11)$$

The potential energy ( $U_i$ ) of the system is

$$U_i = \frac{1}{2} \delta_i^T K_i \delta_i. \quad (12)$$

The dissipation function ( $R_i$ ) of the system is

$$R_i = \frac{1}{2} C_i \dot{\delta}_i^2. \quad (13)$$

The mathematical model of a dynamic system using the Lagrange's equation is written with

$$\frac{d}{dt} \left( \frac{\partial T}{\partial \dot{q}_k} \right) - \frac{\partial T}{\partial q_k} + \frac{\partial U}{\partial q_k} + \frac{\partial R}{\partial \dot{q}_k} = Q_k. \quad (14)$$

If we substitute variables from Eq. (14) as follows:

$$\frac{d}{dt} (M_i \dot{\delta}_i - \dot{y}(t) f_{ti}^T) + K_i \delta_i + \frac{\partial R}{\partial \dot{q}_k} + C_i \dot{\delta}_i = Q_k. \quad (15)$$

Furthermore,

$$M_i \ddot{\delta}_i - \ddot{y}(t) f_{ti}^T + C_i \dot{\delta}_i + K_i \delta_i = 0. \quad (16)$$

So that the equation of motion for the  $i$ -th element gives

$$M_i \ddot{\delta}_i + C_i \dot{\delta}_i + K_i \delta_i = \ddot{y}(t) f_{ti}^T. \quad (17)$$

Matrix  $M_i$ ,  $C_i$ ,  $K_i$ , and  $\ddot{y}(t) f_{ti}^T$  are the mass matrix, damping matrix, stiffness matrices, and excitation forces of the DC motor, respectively. Matrix  $M_i$ ,  $C_i$ ,  $K_i$  is an element of the equation contained in Eq. (17) is a representation of;

$$M_i = \frac{\rho_i s_i L_i}{420} \begin{bmatrix} 156 & 22L_i & 54 & -13L_i \\ 22L_i & 4L_i^2 & 13L_i & -3L_i^2 \\ 54 & 13L_i & 156 & -22L_i \\ -13L_i & -3L_i^2 & -22L_i & 4L_i^2 \end{bmatrix}, \quad (18)$$

$$K_i = \frac{E_i I_i}{L_i^3} \begin{bmatrix} 12 & 6L_i & -12 & 6L_i \\ 6L_i & 4L_i^2 & -6L_i & 2L_i^2 \\ -12 & -6L_i & 12 & -6L_i \\ 6L_i & 2L_i^2 & -6L_i & 4L_i^2 \end{bmatrix}, \quad (19)$$

$$C_i = \alpha \cdot K_i. \quad (20)$$

While the translational motion of the force vector is

$$f_{ti}^T = -\frac{\rho_i S_i L_i}{12} \{6, l_i, 6, -l_i\}. \quad (21)$$

The length of the  $i$ -th element is the length from the first element to  $i$ , with the symbols  $l_i$  and  $l_{i+1}$ .

Equation of translational motion of the SLFM with  $i$ -th element based on boundary conditions is written with;

$$M_n \ddot{\delta}_n + C_n \dot{\delta}_n + K_n \delta_n = \dot{y}(t) f_{tn}. \quad (22)$$

The kinetic energy of rotational motion ( $T_{ir}$ ) of the system has been formulated in [11] as follows

$$T_{ir} = \frac{7}{6} m_i l_i^2 \dot{\theta}^2 + \frac{1}{2} \delta_i^T M_i \dot{\delta}_i + \frac{1}{2} \delta_i^T \dot{\theta}^2 M_i \delta_i + \dot{\theta} f_{ri}^T \delta_i. \quad (23)$$

And then the rotational force vector is written with

$$\ddot{\theta}(t) f_n = \frac{\rho_i S_i L_i}{60} \{30l_{1-i} + 9l_i, 5l_{1-i} l_i + 2l_i^2, 21l_i, -5l_{1-i} l_i + 3l_i^2\}. \quad (24)$$

Equation of motion of the  $i$ -element is written by [12],

$$M_n \ddot{\delta}_n + C_n \dot{\delta}_n + (K_n - \dot{\theta}^2(t) M_n) \delta_n = \ddot{\theta}(t) f_n. \quad (25)$$

where  $\ddot{\theta}(t) f_{ri}^T$  the respective excitation forces.

To find the kinetic energy of the system, kinetic energy caused by translational and rotational motions is obtained by combining kinetic energy from translational motion and rotational motion so that the kinetic energy of translational and rotational motions ( $T_{itr}$ ) of the system will be obtained;

$$T_{itr} = T_{it} + T_{ir}. \quad (26)$$

From the discretization result of the kinetic energy of translational and rotational motions, then by substituting Eq. (10) and (23) into Eq. (26) becomes

$$T_{itr} = \frac{5}{3} m_i (\dot{x}_p^2 + \dot{y}^2 + l_i^2 \dot{\theta}^2) + \delta_i^T M_i \dot{\delta}_i - \frac{1}{2} \delta_i^T \dot{\theta}^2 M_i \delta_i - (\dot{y} f_{ti}^T + \dot{\theta} f_{ri}^T) \delta_i. \quad (27)$$

Applying Lagrange's equation, then substitution Eq. (27) to Eq. (14) gives

$$\frac{d}{dt} (2M_i \dot{\delta}_i - (\dot{y} f_{ti}^T + \dot{\theta} f_{ri}^T)) - \dot{\theta}^2 M_i \delta_i + K_i \delta_i + C_i \dot{\delta}_i = 0, \quad (28)$$

$$2M_i \ddot{\delta}_i - (\ddot{y} f_{ti}^T + \ddot{\theta} f_{ri}^T) + (K_i - \dot{\theta}^2 M_i) \delta_i + C_i \dot{\delta}_i = 0. \quad (29)$$

From the results of discretization using Lagrange's equation, the equation of translational and rotational motions for the  $i$ -element becomes

$$2M_i \ddot{\delta}_i + C_i \dot{\delta}_i + (K_i - \dot{\theta}^2 M_i) \delta_i = (\ddot{y} f_{ti}^T + \ddot{\theta} f_{ri}^T). \quad (30)$$

Finally, the equation of translational and rotational motions of the system can be written

$$2M_n \ddot{\delta}_n + C_n \dot{\delta}_n + (K_n - \dot{\theta}^2 M_n) \delta_n = (\dot{y} f_{t_n}^T + \ddot{\theta} f_{r_n}^T). \quad (31)$$

### 3. COMPUTATIONAL MODEL

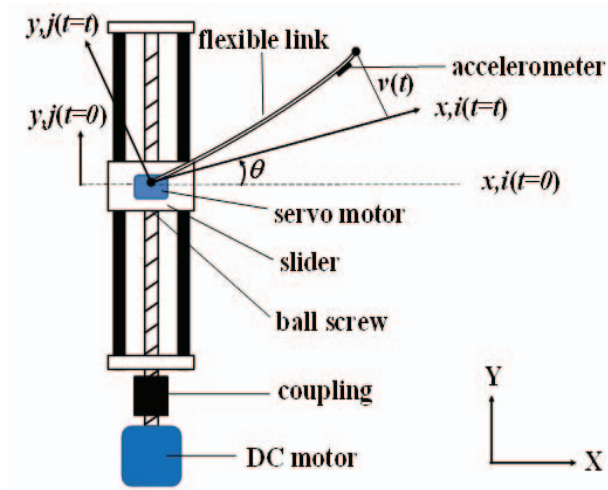


Fig. 4: Physical model of the SLFM.

Figure 4 shows the physical model of the SLFM robot. The SLFM consists of an aluminium beam, a track of the link, a clamp-part, a servo motor to rotate of the link, and a DC motor to make translational motion using a ball screw mechanism. The link, including the clamp-part, is more rigid than the link alone. Furthermore, at the end of the link, an accelerometer is installed to detect vibration that occurs in the system.

Figure 5 shows an illustration set-up of the SLFM system. On the microcontroller, there is a switch to regulate translational and rotational motions on the SLFM system. The switch consists of On-Off buttons, translational motion, translational and rotational motions, and direction of movement. There is a USB connector for connecting the vibration sensor accelerometer to a computer program.

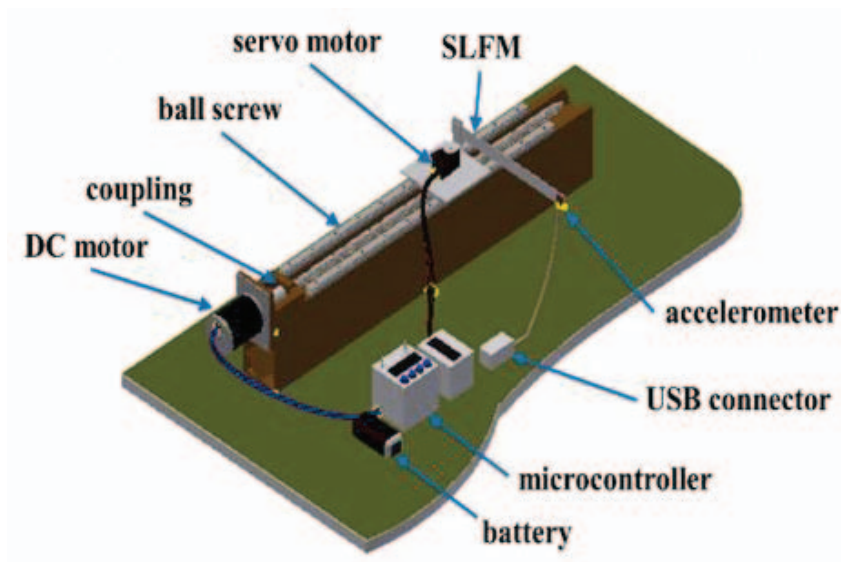


Fig. 5: Illustration set-up of the SLFM.

Table 1: Physical parameters of the SLFM.

Property	Symbol	Value
Total length [m]	$L$	$3.30 \times 10^{-1}$
Length of the link [m]	$l_i$	$3.00 \times 10^{-1}$
Breadth of cross section [m]	$b_i$	$2.50 \times 10^{-2}$
Height of cross section [m]	$h_i$	$1.00 \times 10^{-3}$
Cross-section area of the link [m <sup>2</sup> ]	$S_i$	$1.95 \times 10^{-5}$
Cross-section area moment of inertia Around $i$ -axis of the link [m <sup>4</sup> ]	$I_i$	$2.75 \times 10^{-12}$
Young's Modulus of the link [N/m <sup>2</sup> ]	$E_i$	$7.00 \times 10^{10}$
The mass density of the link [kg/m <sup>3</sup> ]	$\rho_i$	$2.70 \times 10^3$
The viscous damping ratio of the link	$\alpha$	$0.10 \times 10^{-3}$

## 4. RESULTS

### 4.1 Time History Response on Free Vibration

Figure 6 shows the time history response of lateral deformation  $V_p$  on free vibration. The lateral deformation was simulated using impulse force as an external force. In this section, the DC motor and servo motor have not moved. The computational code has been generated at a nodal point six on the THR of lateral deformation. The minimum deviation is at the value -0.009 [m], and the maximum difference is 0.0078 [m].

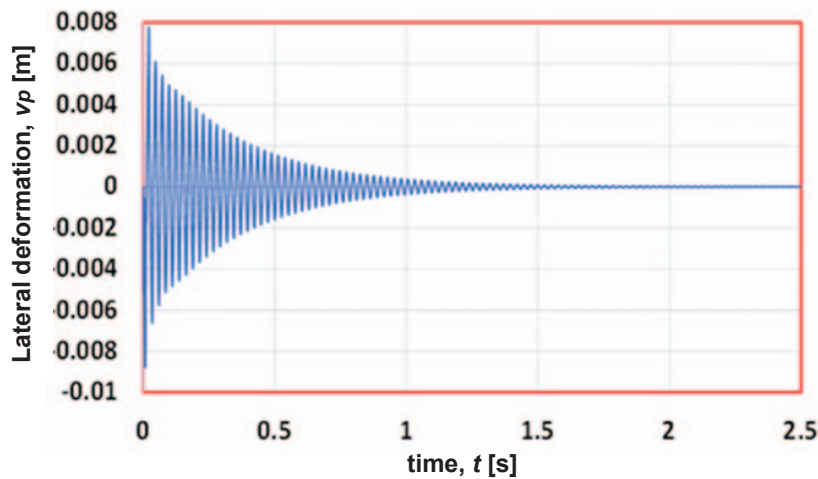


Fig. 6: THR on the free vibration of the SLFM.

### 4.2 Fast Fourier Transform Processing

The results obtained from simulation with free vibration on the system, are then transferred by the FFT process to get the value of the natural frequency of the magnitude. Figure 7 shows the result of a simulation of the natural frequency of the SLFM system. The FFT graph shows that the natural frequency ( $f$ ) is 8.3 [Hz]. When compared using the calculation method, a natural frequency of the order obtained is 9.1 [Hz], so it can be concluded that the simulation results can be validated correctly.



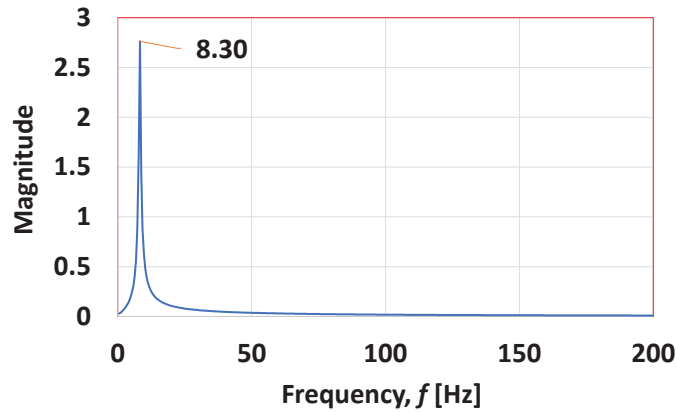


Fig. 7: The natural frequency of the SLFM.

### 4.3 Time History Response with Excitation Force on Translational Motion

Figure 8 shows the THR of lateral deformation with the excitation force of the SLFM system on the translational motion. Computational codes on THR of lateral deformation were developed based on the formulation explained in the previous section. In the calculation, the motor rotates the shaft within 2.5 seconds. This simulation calculates at a nodal point six of the link using the excitation force. The DC motor was operated within 2.5 seconds. It can be seen that the lateral deformation gets the minimum deviation at the value -0.0035 [m], and the maximum difference is 0.0032 [m] at  $t = 0$  [s] and  $t = 0.5$  [s] due to the existence of the excitation force at the time, the minimum deviation at the value -0.0037 [m]. The maximum deviation is 0.0034 [m].

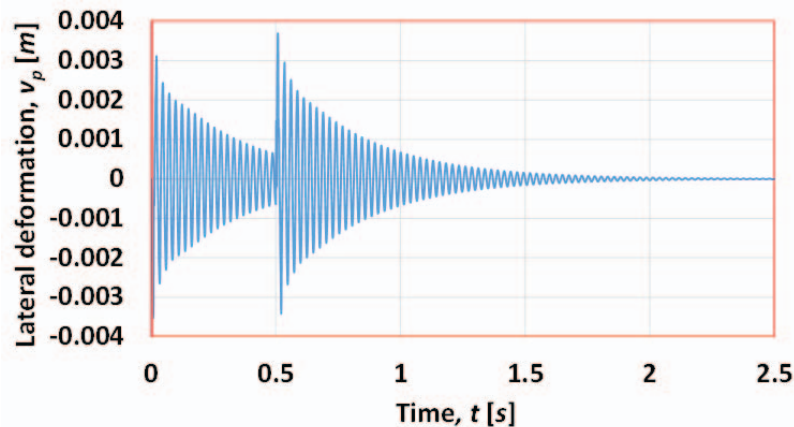


Fig. 8: THR on the system with excitation force experienced translational motion.

### 4.4 Time History Response with Excitation Force on Translational and Rotational Motions

The simulation results of translational and rotational motions obtain THR of lateral deformation using excitation forces on the system, as shown in Fig. 9. In this simulation, the DC motor for translational motion and servo motor rotates the link by the angle of  $\pi/2$  radians (90 degrees) within 2.5 seconds. It can be seen that the lateral deformation gets the maximum deviation is at the value 0.0077 [m], and the minimum difference is 0.0085 [m] at  $t = 0$  [s]. While, at time  $t = 0.5$  [s] due to the existence of the excitation force at the time, the maximum deviation at the value 0.009 [m], and the minimum difference is -0.0085 [m].

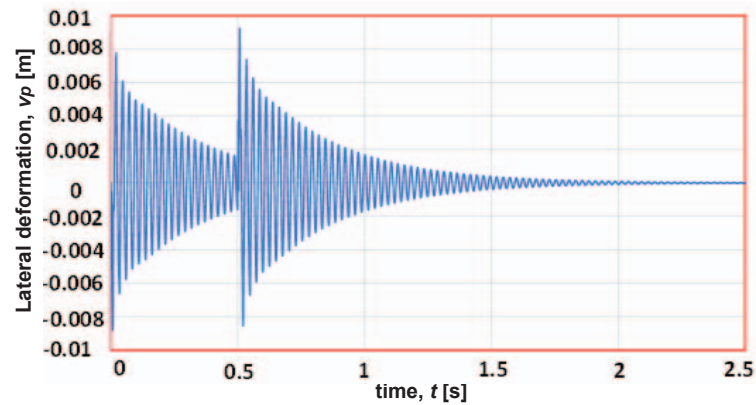


Fig. 9: THR on the SLFM with excitation force experienced translational and rotational motions.

## 5. DISCUSSION

This study focuses on the discretization of equations of motion in SLFM systems using FEM. When compared with research that has been done by Muhammad et al. [17], the results of simulations and experiments of rotational motion have the same tendency as shown on the THR graph. The damping factor and physical parameters determine vibration characteristics. The difference is that this study has installed vibration control in the system so that it produces smaller vibrations and voltages. Therefore, for further research, validation of the simulation results with the experimental method, and appropriate vibration control is needed to obtain high position accuracy.

## 6. CONCLUSION

This study has presented the dynamic modelling of the single-link flexible manipulator robot. The equation of motion for the single-link flexible manipulator that includes translational and rotational motion has been formulated using the finite-element method and the Lagrange equation. The computational code has been successfully developed and used in system dynamics simulations. The results are presented in the order of time history response and natural frequency with the FFT processing. For the translational and rotational motions, the lateral deformation is higher when compared to translational motion, and this is due to the presence of two kinetic energies that occur in the system, namely translational kinetic energy and rotational kinetic energy. This research indicates that vibrations that arise in SLFM that move translationally and rotationally are more significant when compared to the individual translational motion or rotational motion, due to the influence of the simultaneous movements that occur in the system. The presented dynamic model ignores the coupling effect and the action of the motor, therefore, this system requires experiment validation and vibration control for industrial applications and robotics.

## REFERENCES

- [1] Sabatini M, Gasbarri P, Monti R, Palmerini GB (2012). Vibration control of a flexible space manipulator during on orbit operations. *Acta Astronaut.* 73: 109–121. <https://doi.org/10.1016/j.actaastro.2011.11.012>.
- [2] Nanos K, Papadopoulos EG (2015). On the dynamics and control of flexible joint space manipulators. *Control Engineering Practice.* 45: 230–243. <https://doi.org/10.1016/j.conengprac.2015.06.009>.

- [3] Meng D, Wang X, Xu W, Liang B (2017). Space robots with flexible appendages: Dynamic modeling, coupling measurement, and vibration suppression. *Journal of Sound and Vibration*. 396: 30-50. <https://doi.org/10.1016/j.jsv.2017.02.039>.
- [4] Gasbarri P, Pisculli A (2015). Dynamic/control interactions between flexible orbiting space-robot during grasping, docking and post-docking manoeuvres. *Acta Astronaut*. 110: 225-238. <https://doi.org/10.1016/j.actaastro.2015.01.024>.
- [5] Borovin GK, Lapshin V (2018). Motion planning of a space robot. in IOP Conference Series: Materials Science and Engineering PAPER. doi:10.1088/1757-899X/468/1/012020.
- [6] Xu W, Meng D, Chen Y, Qian H, Xu Y (2014). Dynamics modeling and analysis of a flexible-base space robot for capturing large flexible spacecraft. *Multibody System Dynamics*. 32: 357-401. doi:10.1007/s11044-013-9389-0.
- [7] Qiu ZC (2012). Adaptive nonlinear vibration control of a Cartesian flexible manipulator driven by a ballscrew mechanism. *Mechanical Systems and Signal Processing*. 30: 248–266. <http://dx.doi.org/10.1016/j.ymsp.2012.01.002>.
- [8] Shin H, Rhim S (2015). Modeling and control of lateral vibration of an axially translating flexible link. *Journal of Mechanical Science and Technology*. 29: 191–198. <http://dx.doi.org/10.1007/s12206-014-1226-8>.
- [9] Yang H, Liu J, Lan X (2015). Observer design for a flexible-link manipulator with PDE model. *Journal of Sound and Vibration*. 341: 237–45. <https://doi.org/10.1016/j.jsv.2014.12.033>.
- [10] Ata AA, Fares WF, Sa'adeh MY (2012). Dynamic Analysis of a Two-link Flexible Manipulator Subject to Different Sets of Conditions. *Procedia Engineering*. 41: 1253–1260. <https://doi.org/10.1016/j.proeng.2012.07.308>.
- [11] Muhammad AK, Okamoto S, Lee JH (2014). Computer simulations on vibration control of a flexible single-link manipulator using finite-element method. in *The Nineteenth International Symposium on Artificial Life and Robotics 22-24 January 2014; Beppu, Japan*. pp. 381-386.
- [12] Muhammad AK, Okamoto S, Lee JH (2015). Finite Element Analysis for Active-force Control on Vibration of a Flexible Single-link Manipulator. *International Journal on Smart Material and Mechatronics (IJSMM)*. 2(2):106-109.
- [13] Muhammad AK, Okamoto S, Lee JH (2014). Comparison of proportional-derivative and active-force controls on vibration of a flexible single-link manipulator using finite-element method. *Artif Life Robotics*. 19: 375–381. <https://doi.org/10.1007/s10015-014-0186-5>.
- [14] Muhammad AK, Okamoto S, Lee JH (2015) Active-Force Control on Vibration of a Flexible Single-Link Manipulator Using a Piezoelectric Actuator. In: *Transactions on Engineering Technologies*. Edited by Yang GC, Ao SI, Huang X, Castillo O. Springer, Dordrecht; pp 1–15. doi:[https://doi.org/10.1007/978-94-017-9588-3\\_1](https://doi.org/10.1007/978-94-017-9588-3_1).
- [15] Muhammad AK, Okamoto S, Lee JH (2014). Comparisons of proportional and active-force controls on vibration of a flexible link manipulator using a piezoelectric actuator through calculations and experiments. *Engineering Letters*. 22(3): 8.
- [16] Muhammad AK, Okamoto S, Lee JH (2016). Comparison Between the One Piezoelectric Actuator and the Two Ones on Vibration Control of a Flexible Two-Link Manipulator Using Finite Element Method. *International Journal of Mechanical Engineering* 5(1): 27-44.

[http://www.iaset.us/view\\_archives.php?year=2016&jtype=2&id=67&details=archives](http://www.iaset.us/view_archives.php?year=2016&jtype=2&id=67&details=archives).

- [17] Muhammad AK, Okamoto S, Lee JH (2014). Computational Simulations and Experiments on Vibration Control of a Flexible Link Manipulator Using a Piezoelectric Actuator. In proceedings of the International MultiConference of Engineers and Computer Scientists IMECS 2014. 1: 12-14 March 2014; Hong Kong.
- [18] Mahto S (2014). Shape optimization of revolute-jointed single link flexible manipulator for vibration suppression. *Mechanism and Machine Theory*. 75: 150–160. <https://doi.org/10.1016/j.mechmachtheory.2013.12.005>.
- [19] Dubay R, Hassan M, Li C, Charest M (2014). Finite element based model predictive control for active vibration suppression of a one-link flexible manipulator. *ISA Transactions*. 53(5): 1609–19. <https://doi.org/10.1016/j.isatra.2014.05.023>.
- [20] Halim D, Luo X, Trivailo PM (2014). Decentralized vibration control of a multi-link flexible robotic manipulator using smart piezoelectric transducers. *Acta Astronautica*. 104(1): 186–196. <https://doi.org/10.1016/j.actaastro.2014.07.016>.
- [21] Yavuz Ş, Malgaca L, Karagülle H (2016). Vibration control of a single-link flexible composite manipulator. *Composit Structur*. 140: 684–691. <https://doi.org/10.1016/j.compstruct.2016.01.037>.
- [22] Parashar SK, von Wagner U, Hagedorn P (2013). Finite element modeling of nonlinear vibration behavior of piezo-integrated structures. *Computers & Structures*. 119: 37–47. <https://doi.org/10.1016/j.compstruc.2012.12.026>.
- [23] Kadioğlu F, Tekin G (2018). Mixed Finite Element Formulation for the Free Vibration Analysis of Viscoelastic Plates with Uniformly Varying Cross-Section. *International Journal of Mechanical Engineering and Robotics Research* 7(2): 235–239. <https://doi.org/10.18178/ijmerr.7.3.235-239>.
- [24] Bien DX, My CA, Khoi PB (2018). Dynamic Modeling and Control of a Flexible Link Manipulators with Translational and Rotational Joints. *VNU Journal of Science: Mathematics – Physics*. 34(1): 52–66. <https://doi.org/10.25073/2588-1124/vnumap.4240>.
- [25] Dermawan D, Abbas H, Syam R, Djafar Z, Muhammad AK (2019). Finite element analysis on vibration of a flexible single-link manipulator moved translationally. *IOP Conference Series: Materials Science and Engineering*. 619(1): 012050. <https://doi.org/10.1088/1757-899X/619/1/012050>.